



UNIVERSITAT DE
BARCELONA

Structural analysis for the improvement of SnO₂ based gas sensors

Àngel Diéguez Barrientos

ADVERTIMENT. La consulta d'aquesta tesi queda condicionada a l'acceptació de les següents condicions d'ús: La difusió d'aquesta tesi per mitjà del servei TDX (www.tdx.cat) i a través del Dipòsit Digital de la UB (diposit.ub.edu) ha estat autoritzada pels titulars dels drets de propietat intel·lectual únicament per a usos privats emmarcats en activitats d'investigació i docència. No s'autoritza la seva reproducció amb finalitats de lucre ni la seva difusió i posada a disposició des d'un lloc aliè al servei TDX ni al Dipòsit Digital de la UB. No s'autoritza la presentació del seu contingut en una finestra o marc aliè a TDX o al Dipòsit Digital de la UB (framing). Aquesta reserva de drets afecta tant al resum de presentació de la tesi com als seus continguts. En la utilització o cita de parts de la tesi és obligat indicar el nom de la persona autora.

ADVERTENCIA. La consulta de esta tesis queda condicionada a la aceptación de las siguientes condiciones de uso: La difusión de esta tesis por medio del servicio TDR (www.tdx.cat) y a través del Repositorio Digital de la UB (diposit.ub.edu) ha sido autorizada por los titulares de los derechos de propiedad intelectual únicamente para usos privados enmarcados en actividades de investigación y docencia. No se autoriza su reproducción con finalidades de lucro ni su difusión y puesta a disposición desde un sitio ajeno al servicio TDR o al Repositorio Digital de la UB. No se autoriza la presentación de su contenido en una ventana o marco ajeno a TDR o al Repositorio Digital de la UB (framing). Esta reserva de derechos afecta tanto al resumen de presentación de la tesis como a sus contenidos. En la utilización o cita de partes de la tesis es obligado indicar el nombre de la persona autora.

WARNING. On having consulted this thesis you're accepting the following use conditions: Spreading this thesis by the TDX (www.tdx.cat) service and by the UB Digital Repository (diposit.ub.edu) has been authorized by the titular of the intellectual property rights only for private uses placed in investigation and teaching activities. Reproduction with lucrative aims is not authorized nor its spreading and availability from a site foreign to the TDX service or to the UB Digital Repository. Introducing its content in a window or frame foreign to the TDX service or to the UB Digital Repository is not authorized (framing). Those rights affect to the presentation summary of the thesis as well as to its contents. In the using or citation of parts of the thesis it's obliged to indicate the name of the author.

0700557611



UNIVERSITAT DE BARCELONA



UNIVERSITAT DE BARCELONA
Departament d'Electrònica

STRUCTURAL ANALYSIS FOR THE IMPROVEMENT OF SnO₂-BASED GAS SENSORS

Ph. D.

Dissertation presented by
Angel Diéguez Barrientos
in partial fulfillment of the requirements for the
degree of Doctor of Philosophy in Physics

Supervisors: Dr. Albert Romano Rodríguez
Prof. Joan Ramón Morante i Lleonart

Barcelona, July 1999

BIBLIOTECA DE LA UNIVERSITAT DE BARCELONA



0700557611

UNIVERSITAT DE BARCELONA
Div. de Ciències Exp i Mat.
Afers Generals
E 29 JUL. 1999
NÚMERO: 69

45

Universitat de Barcelona
Facultat de Física
Departament d'Electrònica

STRUCTURAL ANALYSIS FOR THE IMPROVEMENT OF SnO₂ BASED GAS SENSORS

Memòria presentada per optar al títol de doctor en Ciències Físiques

Programa de doctorat: Micro i Optoelectrònica Física
Bienni: 93-95

Barcelona, juny de 1999

Autor: Angel Diéguez Barrientos
Directors de tesi: Joan Ramón Morante i Lleonart
Albert Romano Rodríguez
Tutor: Joan Ramón Morante i Lleonart

En Joan Ramón MORANTE i LLEONART, Catedràtic de la Facultat de Física de la Universitat de Barcelona, i n'Albert ROMANO RODRÍGUEZ, Professor Titular de la Facultat de Física de la Universitat de Barcelona,

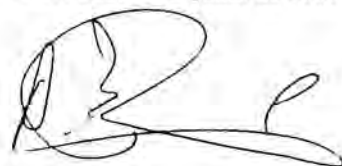
CERTIFIQUEN:

que la memòria "STRUCTURAL ANALYSIS FOR THE IMPROVEMENT OF SnO₂ BASED GAS SENSORS", que presenta n'Angel DIÉGUEZ BARRIENTOS per a optar al grau de Doctor en Ciències Físiques, s'ha realitzat sota la seva direcció.

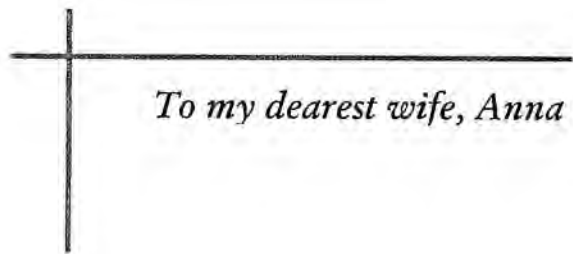
Barcelona, 20 de juliol de 1999



Dr. J.R. MORANTE i LLEONART



Dr. A. ROMANO RODRÍGUEZ



To my dearest wife, Anna

ACKNOWLEDGEMENTS

First of all and in a special form I am grateful to my advisors, **Prof. Joan Ramón Morante** and **Dr. Albert Romano**, for the guidance, insightful suggestions, support and collaboration that they have offered me during all the development of this work.

A special gratefulness is also required for some people of the Laboratory. A lot of thanks to **Dr. Albert Cornet**, for the comments during all my stay in the laboratory and especially moral support, and **Dr. Anna Vilà** because she is always there when someone needs her. I thank also to Dr. J.Ll. Alay for the XPS measurements, and the companionship of all the people of this new and dynamic Department.

An important part of this work has been carried out thanks to the NANOGAS project. I would like to thank at this respect Dr. Xavier Boutin of SAGEM, Dr. Ezio Cereda of CISE, and Dr. Bernd Schumann of BOSCH GmbH. Nevertheless, the most important part of the work has been performed out of the project thanks to the special collaboration with some partners. So, my best gratefulness, given the intensity of the collaboration, goes directed to all those people without which this work could not have been carried out. Especially I would like to thank their collaboration (and their samples) to the collaborators of the Universities of Tübingen and Brescia. I would like to thank the collaboration to **Prof. Wolfgang Göpel**, who unfortunately deceased on 14 June 1999, and **Prof. Giorgio Sverbeglieri**, directors of the groups of work of such universities. I direct my best thanks and regards to **Dr. Nicolae Bârsan**, to **Dr. Udo Weimar**, and to **Jürgen Kappler**, of the University of Tübingen, as well as to the **Dr. Cease Perego**, to **Dr. Paolo Nelli**, to **Dr. Luigi Sangaletti**, and to **Dr. Elisabetta Comini**, of the University of Brescia. I thank to all this people their collaboration, their sympathy, and their direct contribution to this thesis. Concretely, they have carried out all electrical measurements and fabrication of samples. I am sincerely grateful by the time Juergen Kappler, Dr. Nicolae Bârsan and Dr. Paolo Nelli have spent in preparing the samples for this work.

I wish also to acknowledge the EEC by the financial support through the BRITE-EURAM contract BRE2-CT94-0940 corresponding to the project 'NANOGAS'.

Finally, THANKS to my **family**. Thanks to my **mother** to be the best mother of the world, for the whole affection that I have received from her and to have taught me to be like I am. Thanks to my **father** for impel me to continue studying during years. And how not, thanks to **Anna**, to be the best person I know and the best wife that a man can wish. Thanks also to my **sisters**, Fina, Marta and Irene, they know all that a sister has to tolerate.

PREFACE AND OUTLINE

Current gas sensor technology, although meeting the minimum requirements in many instances, suffers for a number of limitations. Hence, there is currently a considerable volume of research being undertaken at many laboratories of different countries. In the past, all chemical sensors and catalyst were optimised empirically by a trial and error method. Today, however, systematic research and development is becoming increasingly important in order to improve sensors and to find new sensing principles. The obtaining of long term stable gas sensors with improved sensitivity, selectivity, and low cost for mass production passes through fundamental research and, therefore, through material characterisation to build new chemically sensitive devices or to improve existing ones. At this respect a wide programme on semiconducting gas sensors is funded under EEC BRITE/EURAM projects and is aimed at developing a wide range of both flammable and toxic gas sensors produced by both thick (screen printed) and thin (sputtered) film techniques. Advantages of such programme include a strong interaction between universities and sensor manufacturers. Under this programme the project '*NANOGAS: Nanoscaled Functional Materials for Long Term Stable Gas Sensors*' was developed. The active members of the project were the University of Barcelona, the University of Tübingen, the University of Brescia, BOSCH GmbH, CISE S.A., SAGEM, and, added at the final part of the project, the University of Ferrara.

All the content of the current work was developed under the NANOGAS project and this is the main reason to write it in English. So, people involved in the project can find a notorious review of part of the results of NANOGAS and the discussion that lack during the development of the project. Concretely this thesis includes most of the work performed in sensors and raw material based on SnO₂ we used. For consistency and in order not to extend too much the work, the part in which other materials like, TiO₂ and WO₃, were investigated is not included here.

The work is organised as follows. In *Chapter 1* an introduction to the different sensor devices, materials used and the operating principles of metal-oxide-semiconductor gas sensors is given. A special focus on SnO₂ is applied. *Chapter 1* contains all the required information to understand why gas sensors are needed, their fundamentals, and the current possibilities for improvement. Nevertheless, in the subsequent chapters (except in *Chapter 2*) a brief introduction related to the concrete objective of the chapter is included. So, a large background on metal-oxide-semiconductor gas sensors, and especially about those based on SnO₂ is presented. Moreover, the introduction reviews some confused details of the existing literature on the principles of operation of semiconductor gas sensors.

Chapter 2 consists in a quite detailed review of the techniques for structural analysis used to perform the investigations. The techniques included are Transmission and Scanning electron microscopies and the related analytical techniques, X-ray diffraction, X-ray photoelectron spectroscopy, and Raman and

Infrared spectroscopies. Such a detailed overview has been included because of several reasons. The most important is to give a compendium of most of the different techniques used in the laboratory in a unique work. Therefore, *Chapter 2* can be a good starting point for a person who begins in structural characterisation of materials for microelectronics in general. The work performed under the NANOGAS project was pioneer for the laboratory, but now more people is working on similar characterisation of nanoscaled materials for gas sensors and other fields. Special features related to nanoparticles have been so added in *Chapter 3*. Therefore, a complete background to the techniques of characterisation of nanometer sized materials is presented in *Chapters 2* and *3*. People interested only in the improvement of the gas sensors investigated in this work can skip *Chapter 2* and part of *Chapter 3*.

Chapters 3 and *4* include the whole experimental work performed as well as the discussion and conclusions to which we arrived. *Chapter 3* is related to tin dioxide thick film gas sensors. The method used to fabricate the sensing material was sol-gel. Sol-gel technology is a method to synthesise nanophase metal oxide particles in a colloidal suspension. Primary concerns in this process are the control of the size, the chemical composition, and the microstructure of the ultrafine particles. The sol-gel process can be varied through changes in solution chemistry and stabilisation techniques to produce the desired particle morphologies. Nevertheless, sol-gel processes are very complex and only partially understood. In this work the chemistry of the process is not considered. Nevertheless the aim of an important part of the dissertation is to optimise the SnO₂ powders obtained by sol-gel for application in gas sensing. This improvement of the raw material is done initially by calcination treatments and by the introduction of noble metal additives. As is commented in *Chapter 1*, these are the usual methods to improve sensor characteristics. However, a third technological parameter is introduced in the fabrication of the sensors, namely the grinding of the powders. In this respect, grinding is presented in a detailed way for the first time to the scientific community as a way to control the sensing properties of nanoparticles.

As a consequence of the detailed structural characterisation new knowledge about the structural properties of SnO₂ nanoparticles is added to the current knowledge. The methodology used to characterise the nanoparticles can be taken as a general way to act in characterising this material or similar. In fact, the acquired knowledge is being applied actually to other materials being analysed in the laboratory.

Chapter 4 has been dedicated entirely to thin film gas sensors. Because of the current interest in building integrated circuits and smart sensors and because since few years this was done by using thin films, the introduction has been made deliberately a little bit more extensive. Particularly a quite extensive review on methods for growing thin films is given. Two growing techniques have been analysed in this part of the thesis: *Ion Beam Assisted Deposition*, and *Reothaxial*

Growth and Thermal Oxidation. Both methods of growing SnO₂ thin films are currently of considerable interest. Nevertheless, this *Chapter* is dedicated in more detail to the last because of the availability of samples and the demonstrated effectiveness of sensors based in such technology. The first method surges from techniques such as electron or thermal evaporation of SnO₂. The last method, from the sputtering deposition of SnO₂. In these techniques it is usual to obtain a non-stoichiometric film, which is highly undesirable to fabricate gas sensors.

With the Ion beam Assisted Deposition of SnO₂ it is tried to approximate to the correct stoichiometry of the material by simultaneous bombardment with oxygen ions during the deposition. Nevertheless, some problems appear, related to the experimental conditions used to grow de SnO₂ films. These are discussed in the text and the conditions to obtain a good film for gas sensing improved.

In the Reothaxial Growth and Thermal Oxidation method, the oxidation step used in most sputtered films, after deposition, is included directly in the process. So, the Reothaxial Growth and Thermal Oxidation method is a simpler procedure that allows to obtain stoichiometric films. Nevertheless, the conditions for the deposition of Sn and the posterior oxidation have to be well controlled. So, when treating with this methodology, we will analyse in detail both steps, identifying the possible sources of drifts in the sensor response in the obtained layers. The results of the investigation can be extrapolated to other procedures for growing SnO₂ in which a thermal oxidation of Sn or of non-stoichiometric SnO₂ is performed.

In *Chapter 5* the main conclusions of the work are drawn briefly.

CONTENTS

1. Introduction: Devices, Materials and principle of operation of metal oxide semiconductor gas sensors

1.1	The interest in gas sensing	1
1.1.1	Environmental control	1
1.1.2	Security at home	5
1.1.3	Electronic noses.....	5
1.2	Gas sensors: devices and materials	9
1.3	Tin dioxide based semiconductor gas sensors	14
1.4	Gas detection in polycrystalline SnO ₂ gas sensors.....	16
1.4.1	SnO ₂ as sensing element.....	16
1.4.1.1	General scheme in the absence of gas	16
1.4.1.2	General scheme under the presence of gases	21
1.4.1.3	Temperature effects and reactive sites on SnO ₂	24
1.4.2	Definition of sensitivity in metal oxide semiconductor gas sensors	26
1.5	Sensor design of semiconductor (SnO ₂) gas sensors.....	29
1.5.1	Thin and thick film semiconductor gas sensors	29
1.5.2	Microstructure of the film and grain size effects.....	30
1.5.3	Introduction of noble metal additives	34
1.6	References	38

2. Structural characterisation techniques

2.1	Electron microscopy	53
2.1.1	Some notes on the interaction of electrons with matter	54
2.1.1.1	Elastic scattering	55
2.1.1.2	Inelastic scattering	57
2.1.2	Scanning electron microscopy	59
2.1.3	Transmission electron microscopy.....	61
2.1.3.1	Selected area diffraction	62
2.1.3.2	Bright field and dark field imaging.....	63
2.1.3.3	Mass-thickness contrast	70
2.1.3.4	Phase contrast and high resolution TEM.....	70
2.1.4	Electron dispersive X-ray analysis and electron energy loss spectroscopy	77
2.1.4.1	Energy dispersive X-ray spectroscopy.....	77
2.1.4.2	Electron energy loss spectroscopy	78
2.2	X-ray diffraction	81

2.2.1	Methods for acquiring an X-ray powder diffraction pattern	82
2.2.2	Analysis of the spectrum	84
2.2.2.1	Quantitative analysis of crystalline phases	85
2.2.2.2	Grain size evaluation in polycrystalline samples	86
2.3	X-ray photoelectron spectroscopy	89
2.3.1	The XPS spectrometer	89
2.3.2	The XPS spectrum	91
2.4	Optical spectroscopic techniques	93
2.4.1	Infrared spectroscopy	94
2.4.1.1	Description of infrared absorption	94
2.4.1.2	Instrumentation for infrared spectroscopy	97
2.4.2	Raman spectroscopy	100
2.4.2.1	Description of the Raman effect	100
2.4.2.2	Instrumentation for micro-Raman spectroscopy	103
2.4.3	Infrared and Raman allowed vibrations	104
2.5	Notes on specimen preparation techniques	106
2.6	Equipment used in this work for the structural characterisation	111
2.7	Further readings	114

3. On the investigation of fundamental properties of SnO₂ nanoparticles and improvement of stability and selectivity of sol-gel fabricated SnO₂ thick film gas sensors

3.1	Sol-gel fabrication of thick film gas sensors	120
3.1.1	The preparation of SnO ₂ by the sol-gel route	121
3.1.2	Printing versus dipping	122
3.1.3	Preparation of powders and sensors for this work	124
3.1.3.1	Powder preparation	124
3.1.3.2	Fabrication of the sensors	127
3.2	Structural, vibrational and, electronic properties of SnO ₂	129
3.2.1	Crystalline structure	129
3.2.2	Vibrational structure	130
3.2.3	Electronic properties	132
3.2.4	Interrelating structure and gas sensing; Defects and surface structure of SnO ₂	133
3.3	Effect of calcination temperature on the properties of SnO ₂ nanoparticles	135
3.3.1	General evolution	135
3.3.2	Particular aspects of the FTIR spectra	143
3.3.2.1	Influence of morphology and aggregation on the spectra	143

3.3.2.2	Water desorption.....	146
3.3.3	The complete Raman spectrum of nanometric SnO ₂ particles.....	148
3.3.3.1	Classical modes of SnO ₂	151
3.3.3.2	Modes activated by disorder in SnO ₂ nanoparticles	153
3.3.3.3	Low frequency modes of SnO ₂ nanoparticles	156
3.3.4	Comparison of grain size obtained by different techniques	161
3.4	The addition of noble metals	163
3.4.1	Influence of noble metal additives and calcination on the sensor response	164
3.4.1.1	Sensor resistance	164
3.4.1.2	Sensor response.....	172
3.4.1.3	Sensor stability.....	174
3.4.2	Distribution of noble metal additives	174
3.4.2.1	Transmission electron microscopy.....	175
3.4.2.2	Raman spectroscopy	177
3.4.2.3	X-ray photoelectron spectroscopy	179
3.5	Improvement of the sensor characteristics by means of grinding treatments	181
3.5.1	Microstructure changes induced by grinding treatments.....	184
3.5.1.1	Overview of the influence of grinding	185
3.5.1.2	Origin of particle size reduction by grinding after calcination.....	186
3.5.1.3	Origin of particle size reduction by grinding before calcination.....	187
3.5.2	Influence of grinding on the electrical characteristics of sensors	188
3.5.2.1	Influence of grinding on the electrical resistance.....	190
3.5.2.2	Influence of grinding on sensor response.....	191
3.6	Conclusions.....	195
3.7	References.....	198

4. Improvement of the stability of highly porous SnO₂ thin film gas sensors

4.1	Introduction.....	206
4.1.1	Justification of the use of thin film gas sensors.....	206
4.1.2	Low power consumption miniaturised gas sensors.....	207
4.1.3	Importance of the stability of gas sensors.....	208
4.1.4	Usual methods for SnO ₂ thin film gas sensor fabrication.....	209
4.1.4.1	Chemical methods	210

4.1.4.2	Physical methods.....	212
4.1.5	Today's modifications for improvement of thin films	214
4.2	The deposition assisted with ions: The IBAD technique	220
4.2.1	Description of the substrates	221
4.2.2	Influence of the deposition rate and final annealing on the film characteristics	223
4.2.2.1	Characteristics of the as-obtained films.....	224
4.2.2.2	Characteristics of the films after annealing	226
4.2.3	Optimisation by substrate heating during deposition	228
4.2.4	Introduction of noble metals as catalysts.....	229
4.3	The improvement of the sputtering technique: The RGTO technique.....	233
4.3.1	General characteristics of the growth of SnO ₂ RGTO films	234
4.3.1.1	Substrates used for RGTO growth.....	234
4.3.1.2	Parameters for Sn deposition	235
4.3.1.3	The thermal oxidation cycle in RGTO	235
4.3.2	Initial investigation of SnO ₂ thin films grown by the RGTO technique	236
4.3.2.1	Experimental results about the deposition of Sn.....	236
4.3.2.2	Kinetics of droplet nucleation.....	241
4.3.2.3	Morphology of the RGTO films after a complete oxidation cycle	246
4.3.2.4	Degree of oxidation after 30h in the oxidation cycle	250
4.3.3	Structural characterisation of the thermal oxidation of tin	251
4.3.3.1	Formation of the spongy agglomerates	253
4.3.3.2	The thermal oxidation of Sn: XRD and Raman spectroscopies.....	257
4.3.3.3	The thermal oxidation of Sn: Connection with the formation of agglomerates	261
4.3.3.4	Influence of the temperature of deposition of tin in the final film.....	262
4.3.3.5	Influence of an incomplete oxidation on gas sensor stability.....	267
4.3.4	The multilayer RGTO technique.....	271
4.3.4.1	Description of film formation	272
4.3.4.2	Improvement of the sensor characteristics with multilayered RGTO systems	274
4.4	Conclusions.....	277
4.5	References.....	279

5.	Conclusions	295
----	--------------------------	-----

CHAPTER 1

INTRODUCTION:
DEVICES, MATERIALS AND PRINCIPLE OF
OPERATION OF METAL OXIDE
SEMICONDUCTOR GAS SENSORS

1.1 The interest in gas sensing

Nowadays there is a great effort in building systems and microsystems with combined electronics and sensors. Sensors systems, including sampling, transduction, and signal handling, are the key elements in the progress towards new functionalities and sensor automation. Applications of these systems include environment, security, health care, home systems, smart buildings, transportation, telecommunications, discrete manufacturing, process industries and so on.

More specifically, a market dedicated to gas sensors is also opened in order to satisfy some of the commented basic socio-economical needs such as health, environment, and safety. Gas sensing is a continuously growing field. New applications are found from year to year and the needs for current and past applications are continuously increasing. Nevertheless, compared to the senses of sight, hearing, and touch, scientists know relatively little about how humans smell and taste. In this respect gas sensing is a relatively new field in which a lot of work can be done.

Gas sensors are known basically by their application in environmental control and security at home and closed places. Without being a direct application of gas sensors, but an instrument in which gas sensors are the fundamental component, they are also known by the multiple applications of electronic noses. In the following these fields of application of gas sensors are discussed.

1.1.1 Environmental control

Nowadays, a variety of air pollutants have known or suspected to have harmful effects on human health and on the environment. By observing table I, it can be seen that these pollutants are principally the products of combustion, power generation or motor vehicle traffic. Pollutants from these sources may not only be a problem in the immediate vicinity of their sources but can travel long distances, chemically reacting in the atmosphere to produce secondary pollutants such as acid rain or ozone.

Contamination of the ambient in populated areas is, evidently, consequence of human activity (see the origin of pollutants in table I and the comparison of their concentration in clean and populated areas in table II). As an immediate result, the atmospheric air all over the world contains now a variety of artificially produced chemical components, which make the environment getting worst in comparison with clean areas. The most important pollutants, their harmful effect to the environment and human health, and their concentration in clean or populated areas are in presented in table II. As it is clear from this table, except for CO₂ and CH₄ the concentration of air pollutants is in the sub ppm range, which require extremely

sensitive sensors. As the gases to be controlled do not appear individually, sensors have to be also highly selective.

So, major reasons for the need of gas sensors are monitoring of environmental pollutants and controlling their emission. At this respect, the market, based on the new regulations, demands a higher reliability in domestic and environmental gas sensors for the detection of combustible and toxic gases.

Automobiles and combustion facilities are the two major contaminants of the atmosphere. In the case of automobiles, for example, new legislation in the European Union and the United States will force that the future automotive exhaust emission must drop substantially from its actual levels. In a car, the less complete the combustion of fuel in the working cylinder, the higher is the emission of toxic substances in the exhaust gas. Of the exhaust gas, about 1% is harmful to the environment. This harmful part of the exhaust consists of carbon monoxide, CO, oxides of nitrogen, NO_x, and hydrocarbons, HC. Concentration of these components in the exhaust strongly depends on the type of engines and operating conditions, but could be in the order of several % for CO, ~1000ppm of HCs, and ~100ppm of NO_x [1]. To see the importance of car emissions, it is interesting to note that more than the 40% of the NO_x emissions are produced in Europe by automobiles (table I, II). So, it is clear the importance to reduce emissions in this particular case.

As in most cases, emissions can be reduced by obtaining a complete combustion. In automobiles, this is aided by using a *lambda probe*, which measures oxygen in the exhaust system of the car. Since the amount of oxygen in the exhaust gas indicates how complete the combustion of the air-fuel mixture in the cylinders is, oxygen is a good representative gas of the combustion process. Feedback from the sensor controls the amount of fuel injected into the engine, assuring optimum air/fuel mixture for complete combustion, and therefore the lowest possible emissions and gasoline usage. Similar procedures are encouraged to control important emissions.

From the point of view of domestic and industry emissions, coal has been substituted in many countries by natural gas. This leads to a decrease of the SO₂ emissions. At the same time it opens a new field for gas sensing. In this respect, a current important application in the field of gas sensing is the monitoring of the satisfactory combustion performance of natural gas boilers, and substantial effort is currently being done at this respect. Combustion of natural gas gives rise to a complex mixture of gases and any new developments in gas sensing must consider cross specificity between gas species. In this aspect, the technique of monitoring the ratio of CO to CO₂ in the combustion products of natural gas has been shown to provide a suitable measure of whether a gas boiler requires cleaning and adjustment. However, some other gases as CH₄, CO₂, CO, O₂, H₂, NO_x and H₂O, result also in the combustion and could be also of interest. Further applications in this field is the detection of gas leaks by using a leak tracer incorporating a solid state gas sensor.

<i>Origin</i>	<i>SO₂</i>	<i>NO_x</i> (<i>NO₂</i>)	<i>NMVOC</i>	<i>CH₄</i>	<i>CO</i>	<i>CO₂/1000</i>	<i>N₂O</i>	<i>NH₃</i>
1 Public power, cogeneration and district heating	62.48	20.58	0.52	0.29	0.41	25.20	4.73	0
2 Commercial, institutional and residential combustion	3.72	1.82	2.88	1.31	17.99	11.29	1.29	0
3 Industrial combustion	23.42	13.69	0.61	0.23	8.19	24.68	3.35	0
4 Production processes	2.85	0.84	3.88	0.13	4.84	5.98	3.48	3.02
5 Extraction and distribution of fossil fuels	0	0	3.04	20.64	0	0	0	0
6 Solvent use	0	0	15.95	0	0	0	0	0
7 Road transport	3.29	42.99	25.33	0.41	56.90	19.23	1.18	0.32
8 Other mobile sources and machinery	2.68	18.37	2.04	0.05	2.35	5.08	0.17	0
9 Waste treatment and disposal	1.55	1.27	2.60	20.59	6.55	3.02	0.25	0
10 Agriculture	0	0.07	4.00	29.33	2.53	5.49	30.65	96.66
11 Nature	0	0.36	39.14	27.01	0.24	—	54.88	0
TOTAL	2060904	1227684	1969894	3163868	4812840	261006	195740	344469

Table 1: Atmospheric emissions data (partials in percent and total in tones) in 1994 for Spain. These data are representative of atmospheric emissions in Europe. Key to Pollutant: SO₂ - Sulphur oxides as sulphur dioxide; NO_x - Nitrogen oxides as nitrogen dioxide; NMVOC - Non-methane volatile organic compounds; CH₄ - methane; CO - carbon monoxide; CO₂ - carbon dioxide; N₂O - nitrous oxide; NH₃ - ammonia. Data after [2].

Pollutant	Main origin	Environment	Effect	Concentration (ppb)	
				Cities	Clean
SO ₂	Power stations burning fossil fuels	H ₂ O+SO ₂ →Acid rain	Asthma Chronic bronchitis	10	0.5
CO	Vehicle exhaust		Reduction of the oxygen-carrying capacity of the blood		
CO ₂	Power stations burning fossil fuels	Warming effect (Greenhouse effect)		390·10 ³	350·10 ²
NO _x (NO+ NO ₂)	Vehicle exhaust Power stations	NO _x +HC+sunlight→ photochemical pollutants (eg. Ozone)	Asthma Breathing difficulties	50	1
CH ₄	Landfill sites Farm animals Venting from coal mines	Warming effect (Greenhouse effect)		2·10 ³	1.8·10 ²
HC	Vehicle exhaust Combustion of petrol Evaporation of solvents Aerosols	Ozone formation	Cancer (eg. Benzene and 1,3-butadiene)	3	1
N ₂ O		Acid rain		2	0.5
O ₃	Secondary from sunlight+HC+NO ₂	Increase of corrosion	Breathing difficulties	100	40

Table 11: Main pollutants and their human and environmental effects. Concentrations in clean and populated areas were extracted after [3].

1.1.2 Security at home

At home, safety sensors are intended to protect a household from dangerous situations. In the case of chemical sensors the danger signal arises due to an elevated concentration of some gas (flammable or toxic) in the atmosphere. In some countries, safety sensors (such as those related with electrical and thermal distribution) are used in domestic premises [4]. However, chemical sensors are not widely employed for this purpose already. Indeed, the use of safety sensors for gases in domestic environment is not imposed by law in any country, being mandatory the use of such detectors in large burners (Japan) or left to the responsibility of the manufacturers to adopt it for their products (US) [4]. Nevertheless, this situation could change in the following years, and the corresponding normative has been already developed or is in course [5].

At home, safety sensors present a major problem, namely the interference with volatile organic compounds coming from solvents and cleaning products. Therefore, highly selective sensors are needed in order to avoid false alarms.

In this respect, it is worth to comment that the measurement of a known gas can be made with only one sensor. Nevertheless, the problems arise with the presence of interfering gases or when the sensor is used in an unknown ambient. When the interest is to measure the detailed concentration of more than one gas simultaneously, this can not be performed by using a unique sensor also. In all these cases a more sophisticated system is needed.

1.1.3 Electronic noses

With a different aim, more recent applications of gas sensing appear from the development of electronic noses. Electronic noses, also called artificial noses, flavour sensors or aroma sensors, are a new concept of sensor application, which tries to mimic the human olfactory system by using an array of electronic chemical sensors with partial specificity and appropriate pattern-recognition electronics [6]. If well it is true that electronic noses can be used for environmental control and sensing at home, it is a sophisticated system usually used for more specific purposes.

The major differences between electronic noses and standard analytical chemistry equipment are that electronic noses produce a quantitative output, can often be easier to automate, and can be used in real-time analysis. The advantages are exploited especially when sensors are not very selective. Advantages include compactness, portability, real-time analysis and automation.

The sensing component of the electronic nose can be formed by an array of several different sensing elements (e.g. chemical sensors), where each element measures a different property of the sensed chemical (which can be a complex mixture of gases), or it can be a single device (e.g. spectrometer) that produces an

array of measurements for each chemical. When using a certain number of chemical sensors, the easiest design consists in building an array of sensors, where each sensor in the array is designed to respond to a specific chemical. With this approach, the number of unique sensors must be at least as large as the number of chemicals being monitored. On the other hand, the use of artificial neural networks allows, when combined with a sensor array, the use of a lower number of sensors in the array that the number of detectable chemicals. Hence, the latter is the system usually selected.

Odour classification using an electronic nose is schematised in figure 1. The active material of each sensor i (where $i=1$ to n and n is the total number of sensors in the array) converts the chemical input of odour j into a time-dependent electrical signal $V_{ij}(t)$. The response pattern from the array is then a vector, X_j , which can be analysed using a suitable data processing technique. This process is known as pattern recognition (PARC) in odour sensing and in practice usually involves the selection of a preprocessing algorithm, x_{ij} , e.g. the normalisation of the array output to reduce experimental variation. Electronic nose technology is, at present, application specific. That is to say that each application requires a specific experimental protocol and PARC technique.

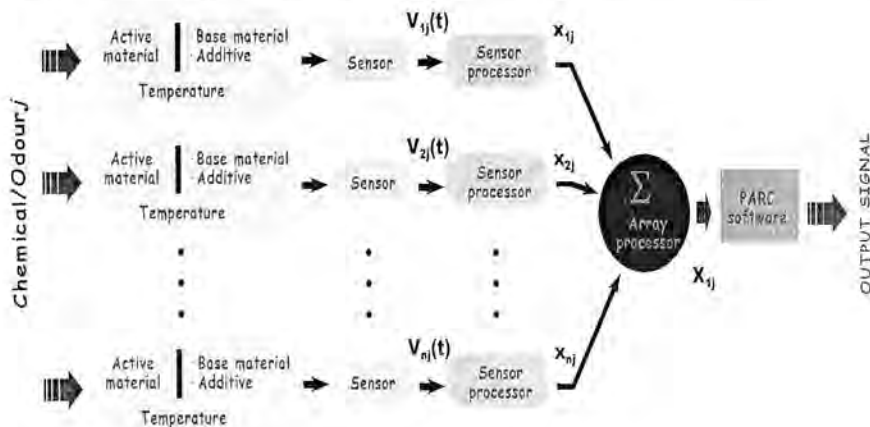


Figure 1: Schematic representation of odour classification using an electronic nose.

For chemical recognition the artificial neural network has to be previously trained. During the training process, various chemicals with known mixtures are presented to the system and a database of signatures is built up. This database of labelled signatures is used to train the pattern recognition system. With a neural network, the intense computation takes place during the training process. Once the artificial neural network is trained for chemical vapor recognition, operation consists

of propagating the data through the network. Since the computation involved during this operation consists of vector-matrix multiplication and application of look-up tables, unknown chemicals can be rapidly identified.

Many artificial neural networks configurations and training algorithms have been used to build electronic noses including backpropagation-trained, feed-forward networks, fuzzy ARTmaps, Kohonen's self-organising maps (SOMs), learning vector quantisers (LVQs), Hamming networks, Boltzmann machines, and Hopfield networks. Although each sensor of the system is designed for a specific chemical, each responds to a wide variety of chemicals. Nevertheless, collectively, the entire system responds with unique signatures (patterns) to different chemicals.

Currently, the field of application of electronic noses is already substantially large. For example, electronic noses can be applied successfully to [7-9]:

- Environmental monitoring, including analysis of fuel mixtures [10], and identification of household odours [11]. Potential applications in this field include identification of toxic wastes, air quality monitoring, and monitoring factory emissions.

- Medicine applications, as an electronic nose can examine odours from the body and serve to identify possible problems. For example, odours in the breath can be indicative of gastrointestinal problems, infections, Infected wounds and tissues emit distinctive odours that can be used for diagnosis, and odours coming from body fluids can indicate liver and bladder problems [12, 13]. Futuristic applications of electronic noses in medicine could be, for example, the development of telesurgery [14]. Applications of electronic noses to medical diagnosis is not restricted only to humans. As example, Elliot-Martin et al. [15] used an electronic nose based on semiconductor gas sensors to diagnose ketosis in cows through breath analysis.

- Food industry, which constitutes the largest market for electronic noses. In this case electronic noses allow to increase or replace panels of human experts, or to reduce the amount of analytical chemistry that is required in food production. Applications include quality assessment in food production and inspection of food quality by odour, control of food cooking processes, inspection of fish, monitoring of fermentation processes, monitoring of beverage odours, automated flavour control, etc. Table III shows a brief recompilation of different artificial noses applied to the food industry.

Application	Instrumental System	Sensor technology	Ref.
<i>Meat</i>	Alabaster-UV	1 MOS, IUV	[16]
	FOX 2000	6 MOS	[17-21]
	FOX 3000	12 MOS	[22]
	NST 3210	10 MOSFET, 4 MOS, 1 IR	[23]
	AromaScan	32 CP	[24]
<i>Fish</i>	Laboratory-made	2-6 MOS	[25]
	NST 3210	10 MOSFET, 4 MOS, 1 IR	[26]
<i>Cheese</i>	QMB6	6 BAW	[27]
	AromaScan A20S	20 CP	[28, 29]
	FOX 3000	12 MOS	[30]
<i>Grains</i>	CPS	4 amperometric	[31]
	NST 3210	10 MOSFET, 4 MOS, 1 IR	[32, 33]
<i>Peach</i>	Laboratory-made	MOS	[34]
<i>Blueberry</i>	Laboratory-made	2 MOS	[35]
<i>Tomato</i>	Laboratory-made	8 QMB	[36]
<i>Vegetable oils</i>	MOSES	8 MOS, 8 QMB	[37]
<i>Coffee</i>	FOX 3000	12 MOS	[38]
<i>Beer</i>	Laboratory-made	12 CP	[39]
	AromaScan A20S	20 CP	[40]
			[41]
<i>Alcoholic beverages</i>	Laboratory-made	5 BAW	[42]
		MOS	[43]
		CP	[44-46]
	Laboratory-made	8 SAW	[47]
<i>Flavours</i>	Laboratory-made		[48]
<i>Packaging</i>	FOX 2000	6 MOS	[49]
	NST 3210	10 MOSFET, 4 MOS, 1 IR	[50]
	AromaScan A32S	32 CP	[51]
	MOSES II	8 MOS, 8 QMB	[52]

Table III: Applications of electronic noses to food. The types of sensors are MOS= metal oxide semiconductor; CP= conducting polymer; BAW= bulk acoustic wave; SAW= surface acoustic wave; QMB= quartz microbalance; MOSFET= metal oxide semiconductor field effect transistor. The suppliers for the electronic noses are: AromaScan, AromaScan plc., Electra House, Electra Way, Crewe CW1 1WZ, UK; FOX, Alpha MOS, 3 Av. Didier Daurat, F-31400 Toulouse, France; NST 3210, Nordic Sensor Technologies AB, Teknikringen 6, SE-583 30, Linköping, Sweden; QMB6, HKR-Sensorsysteme, Gotzinger Str. 56, D-81371 München, Germany; MOSES II, Lennartz electronic, GSG GmbH, Karlsburgstr. 6, D-76227 Karlsruhe, Germany.

1.2 Gas sensors: devices and materials

The gas detection can be carried out thanks to a wide range of physical, chemical, electrochemical and optical principles. It is true that some devices, like for example gas chromatographs, have a very high reliability in gas detection. However, these devices present also a high final cost, require off-line operations (calibration, maintenance, etc), and the need of sample preparing. In the case of other transducers as those based on infrared technology, there exist, in addition, others inconveniences, such as the limited range of measurement in the low ppm region [34].

Excluding these large and complicated devices from the discussion, various types of gas sensors are available in the market. Others are currently only under development at laboratories around the world. Nevertheless, investigation is directed, rather than to new sensors, to increase the characteristics of existing sensors. Ideal sensors should present:

- high sensitivity towards chemical compounds
- high selectivity (low cross sensitivity)
- high stability
- low sensitivity to humidity and temperature
- high reproducibility and reliability
- short reaction and recovery time
- be robust and durable
- easy calibration
- small dimensions (portability)

These characteristics have given rise to a topic in gas sensors, i.e., the rule known as the six 'S' of sensors: Sensitivity, Selectivity, Speed of response, Stability, Size/Shape, and \$/cost.

Among the large variety of sensors developed, the market is dominated thoroughly by metal oxide semiconductor gas sensors, usually known simply as semiconductor gas sensors. The main reason for this fact is their low cost in front of other options. So, these devices are by far the most important ones. In this work, *Chapter 3* and *Chapter 4* are dedicated completely to particular aspects of this type of sensor. In *Chapter 1*, semiconductor gas sensors, specially those fabricated using SnO₂ will be treated in detail in parts *1.3*, *1.4*, and *1.5*.

Together with semiconductor gas sensors, there exist a large variety of devices fulfilling some of the characteristics of ideal gas sensors, the most important of which are presented in table IV, where the detection principles of each type of sensor is briefly outlined. Nevertheless, it is not the objective of this part of the *Chapter* neither to describe the different types of sensors in deep, nor to explain why

some materials are used. For such a detailed overview the reader is referred to more specialised work of other authors [53] and the extensive number of references presented therein.

For each of the sensor types presented in table IV there are different materials to be used as the sensing active part. Highlighted materials are semiconductor oxides like SnO_2 , ZnO , TiO_2 , WO_3 , and Ga_2O_3 , or phthalocyanines, like PbPc , and CuPc , for conductance sensors, Y_2O_3 stabilised ZrO_2 for solid-electrolyte sensors, Pd/ThO_2 as catalyst dispersed on $\gamma\text{-Al}_2\text{O}_3$ in pellistors, SiO_2 , Si_3N_4 , Al_2O_3 , Ta_2O_5 , or polymeric membranes for the gate material in ISFETs, thin Pd gates in MOSFETs, and phthalocyanines, Hg, ZnO , LiNbO_3 , and more complex materials to act as chemical interface in mass-sensitive devices. For a complete survey on materials for gas sensors the reader is referred again to the references presented in table IV.

Because of their current interest, metal oxide semiconductor (MOS), metal oxide semiconductor field effect transistors (MOSFET), conducting organic polymers (CP), and piezoelectric crystals (BAW, SAW, QMB) require special attention, as they are the most mentioned in recent publications and, therefore, which are considered the ones with the highest expectations. As has been commented, semiconductor gas sensors will be treated in detail in sections below and in the remaining of the work. Now, MOSFET sensors, mass-sensitive sensors, and CP sensors will be explained briefly.

Metal oxide semiconductor field-effect transistor sensors

MOSFET sensors operation relies on a change of the electrostatic potential. The most important of these devices is the hydrogen sensitive PdMOS (Palladium metal oxide semiconductor) device, reported for the first time in 1975 by Lundström et al. [54]. The structure of a MOSFET gas sensor is similar to that of the MOSFET transistor. There exist three contacts, two of which allow the carriers in (source) and out (drain), and the third, the gate, acts regulating the current through the transistor. The MOS structure is formed by a silicon semiconductor, a silicon oxide insulator and a catalytic metal (usually Pd, Pt, Ir, or Rh), acting as gate. As it is needed a high temperature of operation to improve the catalytic activity of the gate, and Si is intrinsic at these temperatures ($T > 125^\circ\text{C}$) and hence can not act as a MOSFET, Silicon is currently being substituted by SiC.

The gate structure of a MOSFET sensor is either a thick, dense metal film (100-200nm) or a thin, porous metal film (6-20nm). The sensitivity and selectivity of MOSFET sensors may be influenced by the operating temperature (50-200°C), and the composition and microstructure of the metal gate [54, 55]. MOSFET sensors have a relatively low sensitivity to moisture and are thought to be very robust. However, a high control is needed to obtain high quality and reproducibility.

In the MOSFET sensor, the gate and the drain contacts are shortcut, giving a diode mode transistor. The applied voltage on the gate and drain contact creates an

electric field, which influences the conductivity of the transistor. When polar compounds interact with the gate, the electric field and, thus, the current flowing through the sensor are modified. In the case of thick gate MOSFET sensors, the thick, continuous metal gate responds almost exclusively to molecules that dissociate hydrogen on the catalytic metal surface. The dissociated hydrogen atoms diffuse rapidly (microseconds) through the metal, causing a dipole layer at the metal-insulator interface, leading to a potential change in the gate of the transistor. Detection of molecules such as ammonia or carbon monoxide is not possible with such a layer since no hydrogen atoms are released. If the metal gate is thin, the most probable mechanism is explained by the contribution of voltage shifts at the surface of the metal due to the adsorption and chemical reactions, at the metal-insulator interface due to hydrogen diffusion through the metal, and at the insulator surface due to reactions on the oxide metal surface of polar molecules or charges, which directly react with the oxide metal, or diffuse out on this surface [54, 55].

Piezoelectric crystal sensors

Piezoelectric sensors are made of tiny discs, usually quartz, lithium niobate (LiNbO_3) or lithium tantalate (LiTaO_3), coated with materials such as chromatographic stationary phases, lipids or any non-volatile compound thermally and chemically stable [56, 57]. When an alternating electrical potential is applied at room temperature, the crystal vibrates at a very stable frequency, defined by its mechanical properties. Upon exposure to gases, the coating absorbs certain molecules, which increases the mass of the sensing layer and, hence, decreases the resonance frequency of the crystal. This change can be monitored and related to the volatile present.

The crystals may be made to vibrate in a bulk acoustic wave (BAW) or in a surface acoustic wave (SAW) mode by selecting the appropriate combination of crystal cut and type of electrode configuration. In BAW sensors 3-dimensional waves travel through the crystal, while in SAW sensors 2-dimensional waves (Rayleigh, Love and Bluestein-Gulyaev) propagate along the surface of the crystal at a depth of approximately one wave length.

The principle of BAW sensors was introduced by King in 1964 with his Piezoelectric Sorption Detector [58]. These devices are also called 'quartz crystal microbalance' (QCM or QMB) because, similar to a balance, their responses change in proportion to the amount of mass adsorbed. BAW sensors vibrate at a frequency of 10-30MHz. Their thin coating (10nm-1 μ m) is deposited by spin-coating, airbrushing or inkjet printing. More than 10 years later, in 1979, the first gas sensor based on a SAW oscillator was introduced by Wohljen and Dessy [59-61]. However, the use of such a sensor was first reported by Martin et al. in the 1980s [62]. These devices operate at a higher frequency than BAW sensors, i.e., 100MHz-1GHz. The manufacturing technique includes photolithography and airbrushing, and

is fully compatible with planar integrated circuits fabrication, especially planar silicon technology.

Since piezoelectric sensors may be coated with an unlimited number of materials, they present the best selectivity [63]. However, the coating technology is not yet well controlled, which includes poor batch-to-batch reproducibility. SAW sensors, though limited by the noise caused by their high operating frequency, are more sensitive than BAW sensors. However, both sensors require a higher concentration of volatiles to reach response levels comparable to other sensor types [63].

Conducting organic polymer sensors

Conducting organic polymer (CP) sensors have been under development from approximately 10 years [64]. These sensors comprise a substrate (eg. fiber-glass or silicon), a pair of gold-plated electrodes, and a conducting organic polymer such as polypyrrole, polyaniline or polythiophene as the sensing element. The polymer film is deposited by electrochemical deposition between both electrodes, previously fixed to the substrate [63, 65].

Like semiconductor gas sensors, the operation principle of CP gas sensors relies on changes of the resistance by the adsorption of gas. However, their operating mechanism is more complex and not yet well understood. It seems that, as the conducting polymer is grown out of a solution, the deposited film contains cation sites balanced by anions from the electrolyte and the solvent residue. The cation sites probably consist of polarons or bipolarons, which are small regions of positive charge in the polymer chain, providing mobile holes for electron transport. When a voltage is passed across the electrodes, a current passes through the conducting polymer. The addition of volatile compounds to the surface alters the electron flow in the system and therefore the resistance of the sensor.

In general, these sensors show good sensitivities, especially for polar compounds. However, these sensors are not yet widely marketed because of their low operating temperature (<50°C) makes them extremely sensitive to moisture, currently present a lifetime of only 9-18 months, the difficulty of producing good batch-to-batch reproducibility, and the pronounced drift of their response.

Sensor type	Monitored variable*	Principle*
Conductance sensor Semiconductor gas sensor Conducting polymer sensor Capacitive sensor	$\Delta\sigma, \Delta i, \Delta v$	$\sigma = f(p_i)$
FET sensor MOSFET	$\Delta\phi, \Delta\sigma, \Delta i, \Delta v$	$C = f(p_i)$ $ Y = G + i\omega C = f(p_i)$ $\Delta V = f(p_i)$ $I_o = f(p_i)$ $\Delta\phi = f(p_i)$
Mass-sensitive sensors Quartz microbalance QMB Surface acoustic wave SAW	$\Delta m, \Delta f$	$\Delta f = -f_o \frac{\Delta m}{m} = f(p_i)$
Calorimetric sensor Pellistors or catalytic sensors Pyroelectric sensors Seebeck effect sensors Thermal conductivity sensors	$\Delta T, \Delta q, \Delta i, \Delta v$	$\Delta P = f(\Delta T)$ $\Delta V = f(\Delta T)$
Fiber optic chemical sensor	$\Delta n, \Delta\phi, \Delta i, \Delta v$	$\Delta n = f(p_i)$ $\Delta\phi = f(p_i)$
Electrochemical sensor	$\Delta i, \Delta v$	$E = E_o + \frac{RT}{nF} \ln(a_i)$

Table IV: Schematic information about the different types of existing gas sensor devices. (*) V=voltage, I=current, P=power, σ =conductivity, ϕ =work function, f_o =frequency, n =refraction index, φ phase, and m =mass, p_i partial pressure of component i , f_o resonance freq. of the oscillating quartz, E electrochemical potential, F Faraday constant, R gas constant, a_i activity of ion i , n number of electrons involved in the potential-determining reaction

1.3 Tin dioxide based semiconductor gas sensors

The most widely known gas sensor is the semiconductor tin dioxide sensor, originally developed in Japan over 30 years ago. As commented previously, because of its lower price in front of the other devices, it is currently the more widely used gas sensor for the identification of gases. After Brattain and Bardeen demonstrated already in 1953 [81] that gas adsorption at the surface of Ge lead to a significant variation of the conductance, the first built structure to be used as gas sensor, making use of this phenomena, has been usually attributed to Seiyama (ZnO sensor) and Taguchi in 1962 [82, 83].

Commercially available MOS sensors consist mainly of a cylindrical or flat ceramic substrate heated by wire and coated by a metal oxide semiconducting film. The metal oxide coating may be either n-type (ZnO, SnO₂, TiO₂, Fe₂O₃, etc) or p-type (NiO, CoO, etc), presenting the former a decrease of conductivity to oxidising gases and the latter to reducing gases. The film deposition technique further divides each sensor type into thin (6-1000nm) or thick (10-300µm) film sensors.

The first semiconductor gas sensors based on SnO₂ were developed later in 1970 by Taguchi [84]. Initially they were known as Taguchi or Figaro sensors (the inventor and the name of the company that commercialised the sensors, respectively). Since that moment SnO₂ has become the most investigated material for MOS sensors.

The main reason to select SnO₂ as gas sensitive material is the high reactivity to gases observed at relatively low operating temperature. The high reactivity to reducing gases arises from the easy adsorption of oxygen at its surface, thanks to the natural non-stoichiometry of SnO₂.

The principle of operation of SnO₂-based semiconductor gas sensors lies on detecting the conductivity changes experienced by the n-type material when surface chemisorbed oxygen reacts with reducing gases, such as methane or CO. In the simpler schematisation of the detection mechanism, it could be said that in clean air the conductivity is low because the conduction electrons are bound to surface oxygen, whereas in the presence of a reducing gas, electrons are no longer bound to the surface states and the conductivity increases. Therefore, the adsorption of gaseous species controls the surface and grain boundary resistance of the oxide. As gas adsorption is related to the surface of the material, polycrystalline and even nanocrystalline structures are preferred.

As for other metal-oxide semiconductor gas sensors, SnO₂ gas sensors are fabricated currently either by thick or thin film technologies. In thick film technology, which will be treated in more detail in *Chapter 3*, the fabrication of the sensor can be performed by the obtaining of a SnO₂-based paste, which is painted or printed on a cylindrical or planar Al₂O₃ substrate, or by pressing and sintering pellets. Thin film technology, treated in detail in *Chapter 4*, uses techniques such as sputtering or electron beam evaporation to deposit a thin and polycrystalline film of

SnO₂ onto an electrically and thermal insulating substrate. In the case of thin films a different densification of the film can be obtained by using different deposition techniques, whilst thick films are always porous bodies or layers. Although sensors fabricated by these methods there exist commercially, at present, the larger part of commercially available SnO₂ gas sensors are of the Taguchi type of the Japanese Figaro Inc. These sensors are thick film devices in which the SnO₂ sintered material is deposited onto a cylindrical Al₂O₃ substrate, which has usually Pt electrodes on, and a filament, that acts as a heater, inside. Later, in *Chapter 3*, it is presented an image of such type of sensor.

In general, although thick film gas sensors present a higher power consumption, they are more robust, less susceptible to contamination and more sensitive. Thick film technology offers important advantages such as high productivity and automation, the time required to pass from prototypes to products being very short [85]. Although hybrid integrated circuits can be done by using thick film technologies, current tendencies in commercial sensors are focussed in the increase of the integration of the sensors, using the maximum number of steps compatible with typical semiconductor processes, and reduce power consumption. Both in most cases imply the use of thin film technologies.

Either in thick or thin film sensors, aims are focussed in obtaining sensors with long-term stability, better sensitivity and stability. Higher sensitivity and selectivity passes in some cases by selecting a different basic oxide (eg.: in the detection of oxidising gases, to which SnO₂ is not very sensitive, WO₃ is being recently used), by adding catalytic additives to SnO₂, such as Pt, Pd or Au, or by changing the operation temperature. Selectivity can also be altered by strict control of the particle size of the film. Nevertheless, semiconductor gas sensors are usually less selective than other technologies such as CP, BAW, SAW, or MOSFET. As semiconductor gas sensors usually operate at high temperatures (200-650°C), long-term stability requires lowering of the operation temperature or ageing before the use of the sensor. The operation temperature can be decreased by introducing catalytic noble metals in the film.

Finally, the high operating temperature of some semiconductor gas sensors makes them inappropriate in environments containing large amounts of potentially flammable chemicals. Furthermore, they may be poisoned by irreversible binding to compounds, such as sulphur or weak acids, and are extremely sensitive to ethanol, which 'blinds' them to any other volatile compound of interest.

1.4 Gas detection in polycrystalline SnO₂ gas sensors

Gas detection is a complicated field. However, basic understanding of the behaviour of SnO₂ polycrystalline gas sensors can be acquired with elemental concepts of electronics, chemistry and materials sciences. It is the objective of this part of the chapter to analyse the basic principles of gas detection of polycrystalline SnO₂-based sensors.

1.4.1 SnO₂ as sensing element

The bulk of SnO₂ is known to have oxygen vacancies, which electronically act as electron donors, giving rise to the n-type conductivity of the material. Because of its wide band gap, the hole contribution to the conductivity is usually ignored. In the same way, it is unambiguously agreed that the conductance change on exposure to gases arises mainly through a surface phenomenon on the SnO₂ grains. SnO₂ is a good sensing material for reducing gases.

Following Yamazoe [86], chemical sensing is composed of two parts, i.e., the reception function, which recognises or identifies a chemical substance, and the transducer function, which translates the chemical signal into an output signal. On a first view, while the former is performed by the surface of each semiconductor particle, the whole microstructure of the active sensing element is involved in the latter.

In order to understand how the receptor functional part of the sensing process takes place on polycrystalline SnO₂ films, the different factors affecting the electronic structure of the surface part of the grains will be considered in the following sections.

1.4.1.1 General scheme in the absence of gas

As has been commented above, the n-type conductivity of SnO₂ arises from the existence of the native donor levels of 0.03-0.034eV and 0.14-0.15eV below the conduction band edge, which are generally thought to result from single and doubly ionisation of oxygen vacancies [87, 88]. At temperatures below ~400°C the concentration of such bulk oxygen vacancies, N_D , can be considered constant, independent of temperature and oxygen partial pressure. On the other hand, SnO₂ presents a negligible concentration of electronic band-gap states at their geometrically ideal surfaces, which has been claimed as one of the more important practical reasons for choosing SnO₂ for semiconductor gas sensors [89, 90]. So, as the oxygen vacancy concentration is frozen, the position of the Fermi level is fixed at a certain position between the conduction band edge and the intrinsic Fermi level

position, which would be near the mid of the band gap (depending on the effective mass of electrons and holes).

The case of a polycrystalline material, which is formed by small crystals with different crystallographic orientations, is substantially different from the above scheme because:

□ First, the regions of connection between grains (grain boundaries) are formed by several layers of atoms displaced from their original positions, allowing the coupling between the crystalline lattices of both crystals. As a consequence of the natural disorder of grain boundaries, the local band structure of the material results substantially modified by the appearance of interfacial energetic levels than are situated in the band gap region. These levels can be electrically active, being the acceptor or donor level conditioned by their origin.

□ Second, ideal surfaces with negligible band gap states exist in a single crystalline specimen and constitute the more abundant surfaces in polycrystalline specimens with large grain sizes. However, as grain size is reduced, the reduction of the quantity of such ideal surfaces is expected as well. In the limit, when treating with nanoparticles, these ideal surfaces do not exist. As a consequence, the presence of unreconstructed surfaces is expected to increase and, hence, the number of dangling bonds and surface vacancies. These can also induce acceptor or donor levels at the surface of the grains.

The existence of surface or interface traps acting as acceptors or donors, each of them having a certain density of states and certain parameters of emission and capture, makes that in the thermodynamic equilibrium at each temperature, the Fermi level position be determined by this region. Free carriers would be trapped or emitted at/from the corresponding levels, making the acceptor/donor levels to be negatively/neutrally charged when they are situated below the Fermi level position or neutrally/positively charged when situated above. The charge trapped at grain boundaries/surfaces is compensated by opposite charged depletion regions surrounding the grain boundaries/surfaces. However, a direct association between the created states, their activity, their location in the band gap, and the type of defects from where they are caused can not be predicted a priori. Nevertheless, for an n-type semiconductor, in the case of grain boundaries the position of the Fermi level in the grain boundary has to be lower than the corresponding position in the bulk material.

As can be seen in figures 2 and 3, from Poisson's equation, the charge in the depletion regions causes curvature of the energy bands, leading to potential barriers (doubly Schottky barrier at an interface), which prevents the movement of any remaining majority free carriers from one grain to another.

One usually starts with the one-dimensional Poisson's equation under depletion conditions:

$$\frac{d^2\varphi(x)}{dx^2} = -\frac{dE}{dx} = -\frac{\rho(x)}{\varepsilon} \quad (1)$$

where $\varphi(x)$ is the electrostatic potential at distance x from the surface/interface plane, ρ is the charge density at the same position, and ε the dielectric constant of the semiconductor.

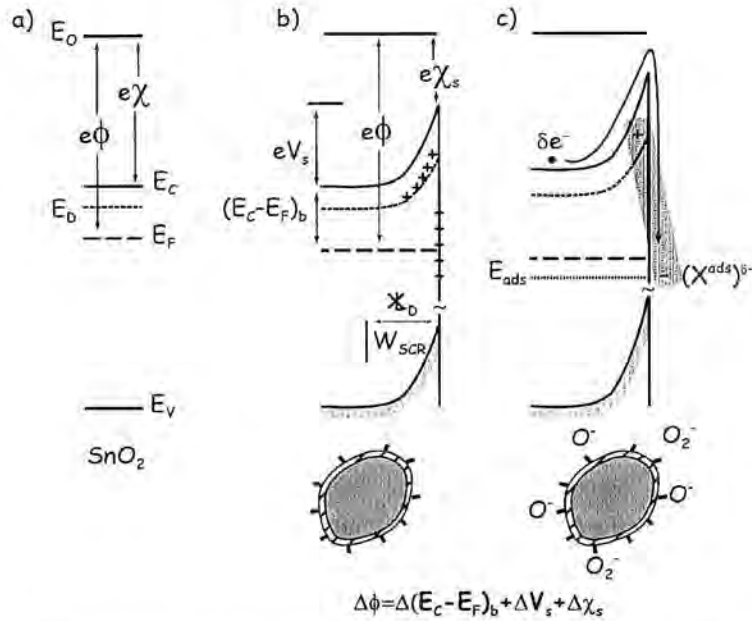


Figure 2: a) Typical energy band diagram of an n-type semiconductor like SnO_2 . E_0 is the vacuum level, E_C and E_V the conduction and valence band edges, E_F the Fermi level position, E_D the position of the donor level, and ϕ and χ the work function and electron affinity, respectively. b) Modifications in the case of the same material in polycrystalline form. As a consequence of the existence of surface traps a depletion region and a potential barrier are created near the surface. It is remarked that the width of the depletion region is not the Debye length, as defined by some authors. c) Polycrystalline material with oxygen adsorbed. As will be commented later in the text, oxygen ionosorption will produce the appearance of inter bandgap levels, modification of barrier height and depletion region, and modification of the electron affinity as a consequence of the creation of dipoles between ionosorbed charges and uncompensated charges in the depletion region.

For grain sizes large enough to have neutral regions inside, one can consider the contour conditions $\varphi|_{x=0} = V_s$, and $d\varphi/dx|_{x=W} = 0$, being V_s the barrier height and W the width of the space charge region. Under abrupt approximation the

net charge density in the depletion region ($0 < x < W$) is $\rho(x) = eN_D$, being N_D the density of donor states in the bulk of the semiconductor, and by solving the Poisson's equation the width of the depletion region is given by:

$$W = \sqrt{\frac{2\epsilon V_s}{eN_D}} \quad (2)$$

and the charge per unit of area appearing in the depletion region will be given by:

$$Q_{SCR} = eN_D W = \sqrt{2\epsilon e N_D V_s} \quad (3)$$

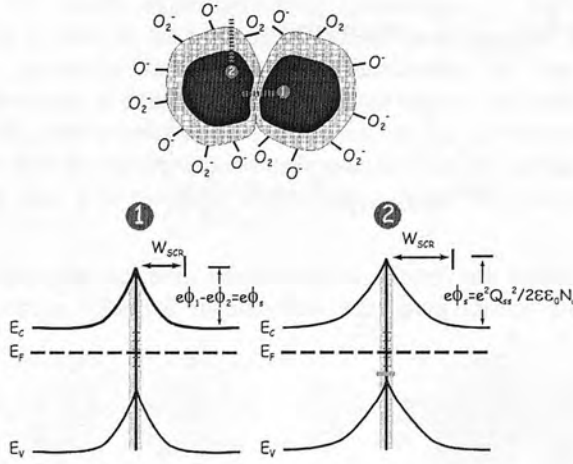


Figure 3: Surface or interface traps create a potential barrier and a depletion region. Under gas adsorption, as grain boundaries are less exposed, strictly barrier height should be different at grain boundaries and at surfaces, as shown in this figure. In any case, barrier height is given by the total charge of the surface/interface and the concentration of free carriers in the semiconductor.

By considering only the surface states (not considering the potential contact between two grains) and applying the charge neutrality,

$$\sqrt{2\epsilon e N_D V_s} = Q_{ss} = e \int N_{ss}(E) f_{ss}(E, E_F) dE \quad (4)$$

which gives a barrier height:

$$eV_s = \frac{Q_{ss}^2}{2\epsilon N_D} = \frac{e^2}{2\epsilon N_D} \left[\int N_{ss}(E) f_{ss}(E, E_F) dE \right]^2 \quad (5)$$

where N_{ss} is the net surface density of charged states per energy unit, and f_{ss} is the probability of occupancy of the boundary levels given by the Fermi-Dirac statistics.

In order to calculate the expression for the barrier height it is necessary to introduce some model for the distribution of interface/surface states, $N_{ss}(E)$. So, for example, it can be considered a density of states independent of the energetic position, $N_{ss}(E)=N_{ss}$, with $f_{ss}(E,E_F)=0$ for $E>E_F$ and $f_{ss}(E,E_F)=1$ for $E<E_F$, which gives:

$$eV_s = \frac{e^2 N_{ss}^2 (E_F - E_V)^2}{2\epsilon N_D} \quad (6)$$

or a density of states localised in E_{ss} , $N_{ss}(E)=N_{ss}\delta(E-E_{ss})$, $f_{ss}(E) = \left[\exp\left(\frac{E-E_F}{kT}\right) + 1 \right]^{-1}$, which gives:

$$eV_s = \frac{e^2 N_{ss}^2}{2\epsilon N_D} \left[\frac{1}{1 + \exp\left(\frac{E_{ss} - E_F}{kT}\right)} \right]^2 \quad (7)$$

For a state well below the Fermi level (it is considered that only one effective and totally filled state exists) gives the well known Schottky equation for planar geometry,

$$eV_s = \frac{e^2 N_{ss}^2}{2\epsilon N_D} \quad (8)$$

The explained scheme should be the initial step to begin the analysis of the gas sensing mechanism in SnO_2 . Nevertheless, this situation is normally skipped because:

- i) the large quantity of unknowns and uncertainty of parameters,
- ii) this situation would be only important for very small grains, where the density of interface traps is not negligible because of the existence of non-perfect surfaces, and
- iii) except for the case in which the Fermi level is pinned by a large density of surface states of any type, the more realistic situation in which the surface of the grains is covered by oxygen ions, dominates the height of potential barriers, and hence, the conduction of electrons from grain to grain.

1.4.1.2. General scheme under the presence of gases

As it will be shown, if one does not consider the kinetics of the reactions taking place at the surface of the semiconductor particles, the general picture when SnO_2 is in a certain atmosphere is the same as above. The rigor in the treatment of solid-gas interfaces is sacrificed in the discussion.

When the SnO_2 is exposed to an atmosphere at moderate temperatures, two things can occur, namely, gas adsorption due the high reactivity of the SnO_2 surface or reaction of interaction of the gas molecules with the molecules ionosorbed already at the SnO_2 surface. Gas adsorption, understood as a direct chemical interaction between the gas molecules and the semiconductor surface, is accompanied by charge exchange. Such interchange is interpreted from the electronic point of view as the creation of an inter-band-gap level whose occupation probability is given by the Fermi-Dirac distribution function (figure 4). Its behaviour as acceptor or donor will depend on the type of molecule adsorbed. Thus, oxygen and NO_2 create acceptor levels, as they capture electrons from the bulk of SnO_2 in order that the adsorption can take place, while H_2 or CO introduce donor levels because they give electrons to the SnO_2 through the creation of an oxygen vacancy.

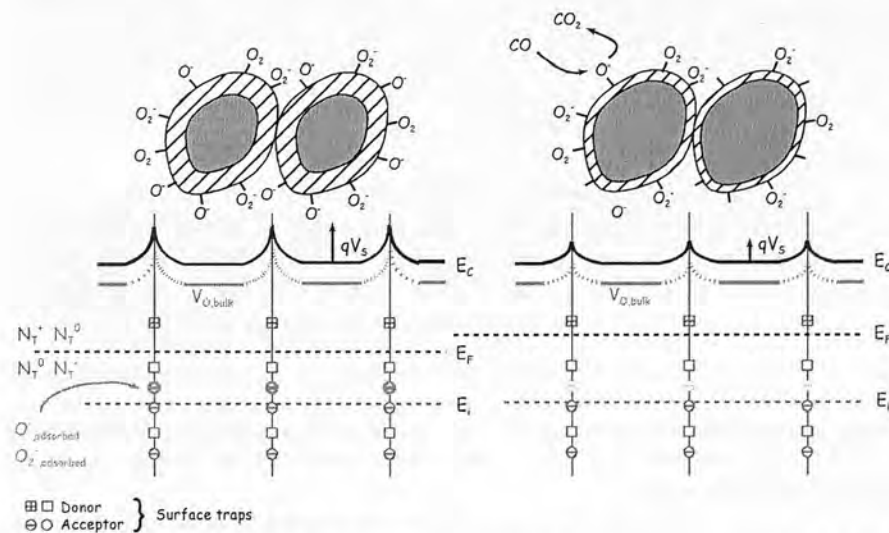


Figure 4: Schematic picture of gas adsorption (very simple). Oxygen creates acceptor levels, which take away electrons from the bulk of the semiconductor. Upon reducing gas arrival, like CO , oxygen ionosorbed can be taken from the surface (as shown in this image) or can be taken from the semiconductor. In any case the behaviour is such as if a donor level was created.

On the other hand, reaction of molecules in the gas phase with those existing already on the semiconductor surface is interpreted as the annihilation of the previously created inter-band-gap states (figure 4). Nevertheless in most cases there is not a direct relationship between the presence of a certain gas in the ambient and the type of level created/annihilated because some intermediate reactions can occur [91].

There are well accepted two types of adsorptions: physisorption and chemisorption. Usually their separation arises because of the different strength of the binding. Physisorption is considered when the energy of the bond is of the order of 0.01-0.1eV, while chemical adsorption is considered when the adsorbed molecules are bound to the semiconductor with bonding energy as large as 1eV. Such difference actually is due to the underlying adsorptive forces. Physisorption is caused by dispersion forces, forces of electrostatic nature and electrical image forces, whereas chemisorption is based on the stronger covalent forces (overlapping between the adsorbate and adsorbent wave functions) and, hence, is connected with a partial electron transfer between adsorbent and adsorbate [92]. According to the Charge Transfer Model (CTM) the physisorbed state acts as a precursor for the chemisorbed one and both states are identified with the same electronic system and, thus, the same Fermi-Dirac statistics. Nevertheless, from a quantum-chemical point of view (Volkenstein model), Geistlinger [92] remarks the inconsistency of such assumption, establishing that physical and chemical adsorption represent electron states of different configurations and, hence, have associated different electronic levels, whose occupancy is given by different Fermi-Dirac statistics. Physisorption is associated to a neutral state for adsorption, while chemisorption to a charged one. Between both states there is a kinetic interaction similar to that between the gas phase and the chemisorbed species.

It is only after chemisorption that the charge displacement occurs between the gas and the semiconductor surface. This interchange of charge gives rise to a band bending in the surface region (equation 5), to a change of the surface conductivity, and to a change in the electron affinity $\Delta\chi$, due to the creation of dipoles at the surface [93], i.e., to a total work function change given by (figure 2):

$$\Delta\Phi = -\Delta(eV_s) + \Delta\chi + \Delta(E_C - E_F)_{bulk} \quad (9)$$

Chemisorption may also produce changes in the surface mobility, as ionosorbed molecules play an important role in electronic conduction as charged scattering centres at the surface [94].

Once the surface of the semiconductor is occupied by adsorbed molecules, new molecules trying to adsorb experience a new environment in such a way that the amount of total ions adsorbed is limited to a coverage of $\sim 10^{-2}$ - 10^{-3} monolayers for electrostatic reasons (Weisz limitation) [95]. To understand this principle one can consider oxygen chemisorption as example. In this case, the positive charge appearing in the semiconductor surface as a consequence of adsorption causes a

band bending of up to about 1eV and depletion layer thickness of about 10^{-6} to 10^{-5} cm [91]. With growing surface density of ionosorbed oxygen, the band bending of the depletion layer increases, lifting the level of surface acceptors above the Fermi level, thus limiting the adsorption of new arriving oxygen molecules. By this scheme it seems evident that this limitation could be overcome if acceptor levels are introduced by other gases. However, it is worth to comment that because of the existence of interface traps the Fermi level can be pinned, making the material insensitive to the adsorption of certain ions.

If the coverage of the surface of the semiconductor by ionosorbed species is θ , then the barrier height is related to the square of the surface charge ($N_{ss}\theta$)² through the Schottky relation (equation 8). In general the coverage will be determined by the gas pressure P and there will be additional charges (Q_0) as a consequence of filled states resulting from traps at the surface/interface:

$$eV_s = \frac{e^2(Q_0 + N_{ss}\theta(P))^2}{2\epsilon N_D} \quad (10)$$

The conductivity in the surface region is then given by

$$\sigma = \sigma_n + \sigma_p = e\mu_n n_{bulk} e^{-eV_s/kT} + e\mu_p p_{bulk} e^{eV_s/kT} \quad (11)$$

Although holes can be neglected in the bulk conductivity, their contribution to surface conductivity when a high density of negative ions are absorbed may not be negligible, as with the increase of the height of the surface barrier, the hole contribution increases as well, while the electron term decreases [96]. Such conditions can occur in an oxygen rich ambient or with low concentration of reducing gases, or in an atmosphere containing another oxidising gas such as NO_2 , as NO_2 is a strong acceptor on SnO_2 than oxygen, presumably with a surface state energetically below the state of adsorbed oxygen (by adsorption of NO_2 , it is reduced to NO by the oxidation of donors, i.e., the refilling of oxygen vacancies with oxygen atoms) [91].

In most cases, however, the holes contribution is negligible. If, in addition, the grains forming the polycrystalline SnO_2 are large enough to consider that they are formed by a surface depletion region and a neutral interior one, conductance can be considered dependent only on the surface conductivity of electrons, and may be described by [97]:

$$G = G_0 e^{-eV_s/kT} \quad (11)$$

where G_0 is a factor which includes the bulk intragranular conductance and geometrical effects. Under real atmospheric conditions barrier height depends on the temperature, and partial pressure of oxygen and reducing gases, $eV_s = eV_s(T, p_{O_2}, p_R)$ [98], as indicated in equation 10. In this way, it is usual to find in the literature

dependencies of the conductivity on the partial pressure of gases, mainly of oxygen. By using the charge transfer model Clifford proposed a theoretical model [92, 99], connecting the partial pressure P_x of the gas phase with the concentration of physisorbed species, X_{phys} , and applying the mass-action law to the catalytic surface reaction,



succeeding in describing from a uniform point of view the numerous power laws for the conductivity which are experimentally observed:

$$\sigma \propto A e^{-E_A/kT} P_x^{-1/m} \quad (13)$$

where E_A is the activation energy which represents the sensitivity of the electrical conductivity to the temperature changes and $1/m$ represents the sensitivity of the conductivity to the changes in the partial pressure of the gas x [100].

Typically, conductivity is related to the partial pressure of oxygen and usual values of m are 6, 4, and 2, each of them depending on the species ionosorbed. At high temperatures, m is generally equal to 6, corresponding to conductivity changes due to the concentration of oxygen vacancies [91, 101]. However, near room temperature oxygen vacancies are frozen in and isothermal conductance changes are due to chemisorption. In this case, if the mass-action is applied to O chemisorption m results to be 2 [92]. When charge-compensating substitutional impurities are present m can take the value $m=4$ [101]. However, this value depends on the type of impurity [100].

1.4.1.3 Temperature effects and reactive sites on SnO_2

Although it is not direct from the above scheme, temperature has pronounced effects on the sensitivity of SnO_2 gas sensors. The temperature of operation influences the physical properties of semiconductors (change of the free carrier concentration, Debye length, ...), but has also other important influences, because every reaction taking place at the surface of the semiconductor, as well as the most probable species adsorbed and, hence, the reaction sites are temperature dependent. So, temperature specially affects those properties related to the processes occurring at the surface of the sensor. For example, adsorption and desorption processes are temperature activated processes, as well as surface coverage by molecular and ionic species, chemical decomposition and other reactions. In this way, dynamic properties of the sensors such as response time and recovery, and the static characteristics of the sensor depend on the temperature of operation [102]. Reactive sites are also temperature dependent. The traditional methods for characterisation of the nature of reactive sites on oxide surfaces and the prevailing species at each temperature are temperature programmed desorption spectroscopy

(TPD), electron spin resonance spectroscopy (EPR), photodesorption methods, and chemical modification of the surface usually called poisoning [103]. By considering both surface species and surface reactions a temperature for which the sensitivity of a semiconductor gas sensor is maximum is always observed.

Because of the natural non-stoichiometry of SnO_2 , it presents an n-type character. Therefore the species who tend to trap electrons from the semiconductor are those who are easily adsorbed. This implies that under usual operating conditions the surface of SnO_2 is mainly covered by oxygen and water species, usual operating conditions understood as an ambient such as synthetic air (79% N_2 + 21% O_2), in which some small quantity of other gas is introduced, and certain humidity conditions. So, the oxygen available as well as the different species resulting from water are crucial for the understanding of the operating behaviour.

At room temperature the forms of adsorbed oxygen which are generally accepted are electrically neutral molecular oxygen, O_2 , and the negatively charged oxygen species O^{2-} , O^- , and O_2^- [104]. The adsorption of the molecular form is evidently not accompanied by changes in the electrical conductivity of the oxide. The ionic species, however, strongly influence the conductivity, as they behave as surface acceptor centres, taking electrons from the bulk of SnO_2 and creating potential barriers at the surface.

It is known that at room temperature oxygen is adsorbed partially in the irreversible ionic form and partially in the reversible molecular form and that the molecular form was found to be present even at 100°C , even though at this temperature physical adsorption is not likely to occur.

Adsorbed oxygen species transform at the surface of an oxide according to the general scheme $\text{O}_{2\text{ ads}} \rightarrow (\text{O}_{2\text{ ads}})^- \rightarrow (\text{O}_{\text{ads}})^- \rightarrow (\text{O}_{\text{lattice}})^{2-}$, in which they are gradually becoming richer in electrons. According to Yamazoe et al. [105], oxygen desorbs with a maximum temperature of desorption as physisorbed O_2 at 80°C , as O_2^- at 150°C , and O^- or O^{2-} at 520°C . At temperatures higher than 600°C the thermal reduction of the SnO_2 occurs and lattice oxygen is desorbed.

At room temperature the equilibrium of the $(\text{O}_{2\text{ ads}})^-$ coverage with gaseous O_2 is approached slowly. With increasing temperature $(\text{O}_{2\text{ ads}})^-$ converts to $2(\text{O}_{\text{ads}})^-$ by taking one electron from the bulk in the reaction $(\text{O}_{2\text{ ads}})^- + e^- \rightarrow 2(\text{O}_{\text{ads}})^-$, which, at constant oxygen coverage, causes an increase of surface charge density with corresponding variations of band bending and surface conductivity. Above c.a. 450K the $(\text{O}_{\text{ads}})^-$ ions are found as the prevailing species. Such ions are very reactive and more than the $(\text{O}_{2\text{ ads}})^-$ ions [91]. On the other hand, the O^{2-} species, which is the least stable form of oxygen in the gas phase, becomes stabilised only in the crystal lattice by the electric field created by its neighbouring cations, i.e., by the Madelung potential of the lattice. The formation of O^{2-} species involves the conduction of electrons to the adsorption center because four electrons are needed to transform one O_2 molecule into two O^{2-} ions.

Water can be adsorbed in two states: molecular water, H_2O , and hydroxyl groups, OH^- . Adsorption of water vapour always produces a large increase in electronic conductivity in SnO_2 . Isolated OH^- at the surface show higher effect in conductivity than molecular H_2O . Molecular adsorbates are entirely desorbed by evacuation at $150^\circ C$ while surface hydroxyl groups are slowly desorbed beginning at $250^\circ C$ but are not entirely desorbed after evacuation at $500^\circ C$ [105]. The temperature of the desorption maximum is found at $110^\circ C$ for molecular H_2O and at $400^\circ C$ for OH^- .

So, it is clear that when a gas is introduced in the ambient atmosphere, its reactivity will depend on the species ionosorbed. If, for example, OH^- groups or a certain ionic oxygen species is adsorbed, there will be less sites for other negative species adsorption such as NO_2 (Weisz limitation and occupation of possible adsorption sites). On the other hand, reducing gases like H_2 or CO consume oxygen, lowering the barrier height. This oxygen can be present in two ionic forms at the surface of the SnO_2 , or can be incorporated in the lattice. The type of oxygen involved in the reaction will depend on the temperature of operation of the sensor.

The state of the surface is evidently gas dependent. In general most target gases are detected via the influence that they have on the oxygen stoichiometry of the surface. In this way, CO for example, can reduce the surface of SnO_2 taking oxygen ionosorbed and, thus, giving electrons to the bulk of the semiconductor, decreasing barrier height and increasing surface conductance. In this case, CO_2 , the reaction product, leaves the surface and returns to the gas phase. On the other hand, reactions between the surface oxygen ions and hydrocarbons or hydrogen generally produce water vapour as one of the reaction products, thus changing completely the surface of the semiconductor and taking active part in the chemisorption processes [106].

It is evident that gas detection with semiconductor gas sensors can not be completely explained by only taking into account the charge transfer occurring at the surface of the semiconductor. Charge transfer only explains the situation in equilibrium and surface reactions have to be considered for a detailed understanding of the response to different gases. Indeed, it has been demonstrated that in porous sensors besides reactivity, diffusivity of gases or more precisely, difference in diffusivity between a target and oxygen gas, is an important factor determining the sensitivity of the sensor [107]. This makes the sensing properties of semiconductor gas sensors (especially thick films) to be dependent on the molecular size of the sensed gases and of temperature, as all diffusion mechanisms are highly temperature dependent.

1.4.2 Definition of sensitivity in semiconductor gas sensors

As has been explained, exposure of SnO_2 gas sensors to gases produces changes in the conductivity of the semiconductor, mainly via change in the density

of free carriers in the bulk, the appearance of surface potential barriers and change in the surface mobility. In principle the same occurs for any other metal oxide semiconductor gas sensor. Whatever be the origin of such changes, i.e., surface reactions or direct reaction with the surface structure of the semiconductor, these changes are monitored in a real sensor through changes in the resistance, which is used to define sensor sensitivity.

Sensitivity is defined by the resistance (or conductance) change when the sensor is exposed to a gas with respect to the resistance that the sensor presents in a reference gas, usually air or synthetic air (figure 5). The most usually used expression for an n-type gas sensitive material like SnO₂ are:

$$S = \frac{R_{air}}{R_{gas}} \quad (14)$$

for oxidising gases like NO₂, and

$$S = \frac{R_{gas}}{R_{air}} \quad (15)$$

for reducing gases like CO. In this way sensitivity should be always larger than 1.

Nevertheless, sometimes sensitivity is also defined as

$$S = \frac{R_{gas} - R_{air}}{R_{air}} \quad (15)$$

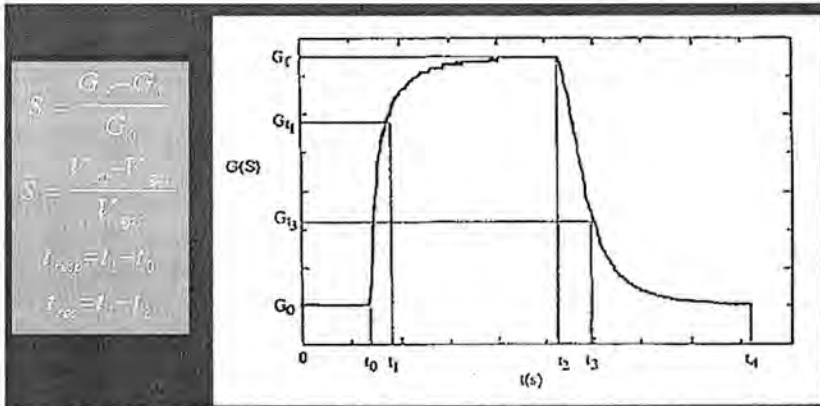


Figure 5: Definition of sensitivity and response and recovery times. Definitions are given for conductance or voltage changes. It is obvious the equivalent definitions for resistance changes.

Because it is difficult to clean completely the surface of the sensor of adsorbed molecules after a measurement, on the last times, some people prefers to

measure sensitivity with respect to a low concentration of the target gas. Resistance changes rapidly with increasing concentration of a target gas in air and slowly after some certain concentration is present in the ambient. So, a small quantity of uncontrolled gas in the chamber, or at the surface of the sensor, can produce a large error in the measurement of sensitivity.

1.5 Sensor design of semiconductor (SnO_2) gas sensors

The first step in sensor design is evidently to select the active material, sensor configuration and the mode of operation. By sensor configuration one can understand thick, thin film, geometry of the sensor, and shape and location of the heater and electrodes [108-110], as well as material for the heater and electrodes [111-113]. The mode of operation can be mainly DC or pulsed (transient). The first is the usual method, while the second is used to take advantage of the rate of some reactions. The connection of the sensor in hybrid integrated circuits or in a sensor array is more adequately part of the entire system design.

The improvement of SnO_2 gas sensor, as well as of any other semiconductor gas sensor, passes in most cases through the optimisation of the material. Indeed, material properties have influence in almost all the properties of the sensor, including sensor sensitivity, stability, speed of response, etc. As sensing is a surface process, it is directly related to the surface properties. Therefore an important goal is to control the semiconductor surface, up to now done usually via the introduction of additives promoting some catalytic activity. In addition, additives can sometimes modify the temperature of maximum sensitivity, which is very important if lowers, mainly in increasing stability and selectivity. In fact, depending on temperature and partial pressures, sensors may be designed with their principle based upon physisorption, chemisorption, surface, or bulk defect reactions [93], according to the explained in 1.4.1.3. As has been previously commented, of particular importance are the dependence with temperature of the presence of the corresponding oxygen species and water at the surface of SnO_2 .

Microstructure control and introduction of additives are so important in sensor properties that will be considered below in detail.

1.5.1 Thin and thick film semiconductor gas sensors

Being gas detection mainly a surface process, the first and probably most important characteristic of a semiconductor gas sensor comes from the distinction between thin and thick film semiconductor gas sensors. In general, a SnO_2 thin film is formed by finely dispersed particles of very small size very densely packed, forming a quasi-continuous layer. On the contrary, a thick SnO_2 film is composed of poorly bounded grains of variable sizes. It is evident that the last structure presents a higher effective surface area for gas adsorption and, hence, larger changes of resistance are expected under the adsorption of different gases. On the other hand, depending on the temperature, the degree of filling of the surface states of the semiconductor by the gas molecules and other characteristics of the system, the adsorbed molecules can leave back in the gas phase if overcome some potential barrier determined usually as the heat of adsorption [114]. Therefore, the larger is the effective surface area, the lesser will be the rate through which the steady state is

obtained. As a first approximation and according to what is intuitively expected, this implies that thin film gas sensors will have a higher speed of response, because in thin films gas molecules are adsorbed only at the surface of the entire structure. Nevertheless, it is only true if gas does not try to penetrate into the film. In this case, an initial rapid response takes place, but the sensor does not reach a stable value of the resistance because of the difficulty of gas diffusion imposed by the structure of the film. On the other hand, in thick films, gas follows different percolation paths through the entire thickness of the film. As the injection of electrons from the surface crystallites to the conduction band can be fast, speed of response would be limited by the gas diffusion into the grain boundaries [115] and thus by thickness [116].

1.5.2 Microstructure of the film and grain size effects

One usually considers a thin film as a densely packed film in which intergrain effects can be neglected (figure 6). However, it is obvious that thin films with porous structure are also included in the category of thin films. Nevertheless, such porous films respond in the same way as porous thick films, which will be considered later.

In a densely packed thin film, under gas adsorption a depletion region near the surface appears, in which conductance is much smaller than that of the remainder of the film. In this case the behaviour of the conductance is that of a bulk trap limited conductance in a layer of variable width (film thickness – width of the SCR), in which the activation energy for conductance would be the donor energy E_D [117]. Depending on the coverage by ionosorbed species and film thickness, the whole film can be depleted of electrons. In this case conductance is surface trap limited, i.e., the conductance is determined by the equilibrium between conduction band states and surface states. The activation energy for the conductance would be the surface state energy E_S [117]. In this case, conductance is directly affected by surface reactions.

According to the mechanism of gas detection in the explained structure, densely packed thin films have to be classified as field effect sensors, rather than as conductance sensors.

The case of a porous body (thick film) is qualitatively different (figure 7). The porous body is formed by low-resistance paths through the bulk of the crystallites, alternating with higher resistance constrictions at the points of contact. Several cases may be considered depending on the microstructure of the film [117]:

i) Film formed by grains interconnected by grain boundaries: This is the typical situation described in thick films. The bulk of each grain can be considered neutral such that an ohmic behaviour is expected. At grain boundaries charge is trapped from the ambient and depletion regions develop. The conductivity would be

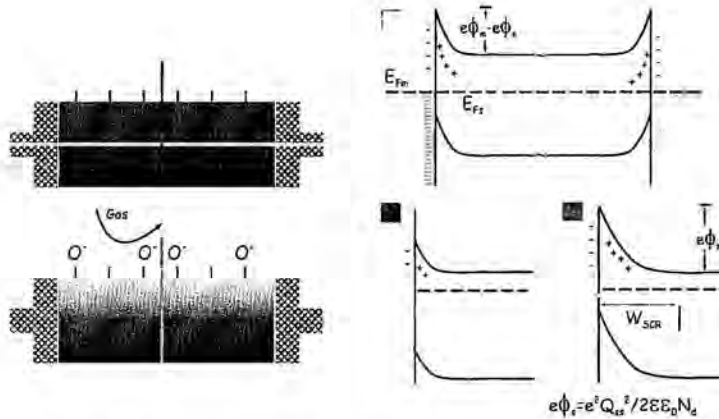


Figure 6: Gas detection in a densely packed thin film. A scheme of the film and the corresponding approximate energy band diagram is shown under the absence of gases and in an oxygen rich atmosphere.

limited by charge transport across Schottky barriers by thermoionic emission, or less usually, by tunneling. The activation energy for conductance would be the barrier height and would be directly affected by the charge and fractional coverage of the surface species and, hence, a function of the composition of the gaseous atmosphere, because barrier height is determined by the square of the surface charge (equations 5 and 10).

Resulting from the different grain size and shape of the particles forming the porous film and from the different number of neighbouring particles in contact with a certain particle (coordination number), one expects that the measured conductance is determined by a network of barriers differing in their height [118-121], i.e., the conductance is generally affected by the percolation mechanism, which depends on the barrier-height distribution and on the average coordination number of the network. Nevertheless, by assuming a fixed uniform distribution for the barrier with energies between the values eV_{s1} and eV_{s2} , it has been found that the activation energy of conductance is very accurately constant in the temperature range 350-900K for different network coordinations. However, in case that $\Delta V = V_{s2} - V_{s1}$ is large, the activation energy has a strong dependence on the coordination number of the network.

It is important to note that depending on grain size and coverage by negatively charged species, individual particles can be completely depleted electrons. For very small particles, grain boundary traps can themselves give rise to a completely depleted grain. In this case the boundary conditions applied to solve the Poisson's equation are no longer valid, because there is not any neutral region in the grain. It is evident that in this case conductance is not dependent upon barrier

height but on excitation from grain boundary traps. In the limit, for very small particles, the solution of the Poisson's equation with the adequate boundary conditions would result in a flat band condition at which conductivity is determined by the difference between the conduction band edge and the Fermi level position [122]:

$$\sigma = \sigma_0 e^{-[E_C - E_F]_{bulk}/kT} \quad (16)$$

The flat band condition occurs when nanoparticle size is lower than $2W_{SCR}$, where W_{SCR} is the width of the space charge region in the grain. It is clear that the condition $2L_D$ (where L_D is the Debye length, $\sim 3\text{nm}$ for SnO_2), presented usually in the literature, is not really correct.

L_D is defined as:

$$L_D = \sqrt{\frac{\epsilon kT}{e^2 N_D}} \quad (17)$$

and corresponds, by definition, to the distance of rearrangement that free carriers travel in order to shield a perturbing electric field created by a certain charge density [123]. Nevertheless, the Debye length can be associated to the ability of the semiconductor to evacuate free carriers and can be related to the width of the depletion region through:

$$W = L_D \sqrt{\frac{2eV_s}{kT}} \quad (18)$$

expression which we suppose is the origin of the confusion.

ii) *Film formed by grains interconnected by necks*: in this case, surface states corresponding to the gas species adsorbed cause a depletion zone extending to a certain depth. The conductivity would be largely that of the undepleted layer in the center of the neck and would be determined by activation of electrons from donor states in the bulk (bulk-trap limited regime with activation energy E_D), and would be affected by the gaseous atmosphere through changes in the effective channel width only. In this case electrons will move through a channel formed inside each neck from grain to grain. If the neck is closed, the depletion zones from the two surfaces overlap, leaving a higher-resistance ohmic path through the centre. In this case the conductance would be determined by activation of electrons from surface states into the conduction band (surface-trap-limited regime with activation energy E_S), and would be directly affected by the influence of the gaseous atmosphere on the occupancy of the surface states. In fact, the closed-neck structure has an activation energy related directly to the surface states and, hence, dependent, for example, on the main species of oxygen chemisorbed. The controlling mechanisms (open or closed neck) would be determined by the microstructure of the film as well as for

the gas concentration. The change as a consequence of gas adsorption from an open neck configuration to a closed neck one would give rise to a pronounced effect on conductivity and, thus, to the best microstructure to measure sensitivity.

Several authors [124-128] have reported the existence of two regions of sensitivity depending on grain size. By considering both grain boundaries and necks it has been shown that for large grain sizes, where conductivity is dominated by grain boundary contacts, sensitivity is practically independent of grain size. On the other hand, for very small sizes, where mainly necks control conductivity, sensitivity is strongly dependent of nanoparticle size. In this region sensitivity increases with the decrease of grain size. This effect is usually attributed to the high dependence of electron transport at any place inside the particle under a surface effect such as gas adsorption. The depletion of electrons by gas adsorption makes to pinch-off the individual grains and produces a considerable increment of resistance. Nevertheless, due to the dispersion of sizes of the nanoparticles forming the sensor, this pinch-off does not occur in all the particles simultaneously and this is why sensitivity changes rapidly but not suddenly.

According to the expression of the width of the depletion region (of if preferred, of the Debye length), the addition of impurities, such as for example In, Al, Sb or Bi, changes the donor/acceptor ratio, allowing control of the closed neck condition for larger grain sizes than in the case of the pure SnO_2 [124, 125].

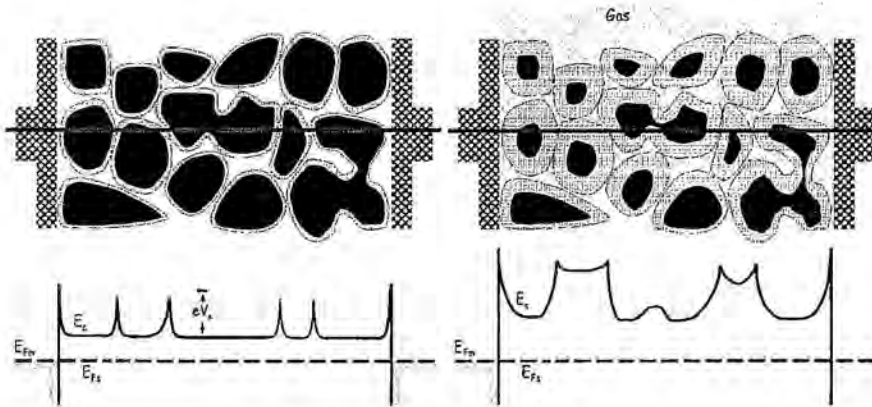


Figure 7: General scheme of a porous sensor containing both grain boundaries and necks under the absence of gases (left) or with a low pressure of oxygen and under high content of oxygen in the atmosphere (right). The band diagram is represented approximately in the lower part of each case. Note the complex evolution under gas adsorption as a consequence of the microstructure. It is schematically shown the idea that the gas does not penetrate the whole film.

Finally, it is remarkable that apart from the above geometric considerations, the behaviour of nanoparticles as sensing elements has to be considered far from the behaviour of large particles of single-crystals from a kinetic point of view (physisorption involved). On one hand, it is well known from single crystal studies

that the kinetics of reactions may be very different on different crystal faces. So, in general one can not expect that the kinetics on nanometer particles can be directly represented by the kinetics on a single surface. Going farther, nanometer particles can not even be represented by a superposition of the kinetics from different crystal faces because the coupling of the kinetics on adjacent facets by surface diffusion [129].

1.5.3 Introduction of noble metal additives

To modify or control the surface properties of the SnO_2 , introduction of noble metal additives, such as Pt or Pd, is usually performed. Other metals, as Ag, Al, Cu, Ni, Au, Sb, etc, and some oxides have also been experimented. The most important effects of noble metal addition consist in increase the maximum sensitivity and rate of response, as well as lowering of the temperature of maximum sensitivity [107, 126, 130, 131]. All these effects arise as a consequence of the promoting catalytic activity when loading with noble metals. The different mechanisms used to explain the results presented in the literature are commented in the following.

Under noble metal loading it is expected that it forms clusters at the surface of SnO_2 , such as those observed in the case of Pt [132, 133] and in the case of Pd [134, 135]. Depending on the noble metal deposited, the loading, and the interacting gas, these clusters will be in metallic or oxidised forms. In any case, the contact of the additive with the semiconducting oxide creates a barrier that is fully characterised by the electron affinity of the semiconductor, the work function of the metal and the density of surface states of the semiconductor that are located inside the energy band gap (figure 8). All of these three contributions create a Schottky barrier through the formation of a depletion region in the semiconductor surface in contact with the cluster. Eventually, the surface states created by the presence of the additive can pin the Fermi level of the semiconductor to that of the additive.

Two mechanisms have been proposed to explain the observed results [136, 126], i.e., chemical and electronic sensitisation (figure 9):

i) *Chemical sensitisation*: The metal, located at the semiconductor surface forming small clusters, facilitates the catalytic processes on the semiconductor surface. The action of the additive is in general two-fold [137]: i) the metallic cluster presents a higher sticking coefficient to gases than the semiconductor, and ii) on the cluster nearly all the gas molecules are dissociated, the products being spilt-over the semiconductor support. By this mechanism a gas like H_2 is activated by a metal and the activated fragments (H) are spilled-over to the semiconductor surface to react with the adsorbed oxygen. This type of sensitisation is likely to be operative for example in Pt-loaded SnO_2 , which is known to remain in the metallic form under most reaction conditions. It is worth to mention that spill-over consists generally in the adsorption on the catalyst followed by diffusion from the catalyst to the support.

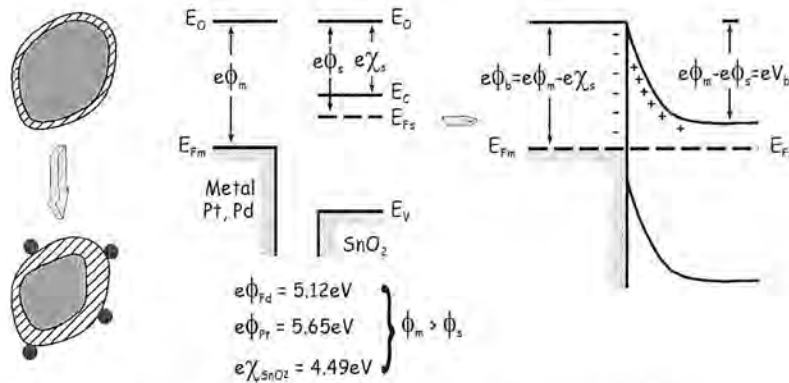


Figure 8: Effects of noble metal introduction. It is given a schematic representation of the energy diagram of SnO₂ and a metal like Pt or Pd. After contact of the semiconductor and the metal a Schottky barrier appears as a consequence of the different work functions, between others (right).

Because the activation energy for desorption is much higher than for diffusion, the support can act as source of reactant supply. However, the opposite case or both can also occur. Moreover, normally the support is assumed to be catalytically inactive, but not always.

It is evident why selectivity and lowering of the temperature of operation are obtained by means of the spill-over mechanism. One can consider, for example, the case of hydrogen. Oxides are not very active in hydrogen activation. However, deposited Pt can activate hydrogen, which subsequently migrates to the oxide surface by spill-over mechanism. In this way reactions that occur on the oxide surface and need hydrogen can proceed at lower temperatures and are favoured over reactions that do not consume hydrogen. It has to be noted, however, that some additives improve sensitivity to some gases, and hence, selectivity. Nevertheless, this not implies the obtaining of a selective sensor.

ii) *Electronic sensitisation*: In this case there is no mass transfer between the foreign particles and semiconductor. Instead, there is an electronic interaction between both through the space charge created in the semiconductor by the presence of the surface clusters. Additives at the surface of the semiconductor act as receptors while the semiconductor acts as a transducer of the changes taking place at the surface under gas adsorption. This type of sensitisation has so far been observed in SnO₂ elements impregnated with Ag, Pd, and Cu, which form stable metal oxides when exposed to air. The electronic interactions actually appear between the metal oxides and SnO₂, and disappear when the oxides are converted to metals (Ag and Pd) or a sulfide (CuS) on exposure, for example, to H₂ or H₂S, respectively. The chemical state of the particles changes on contact with a gas, inducing the corresponding change in the electronic state of the semiconductor. This change

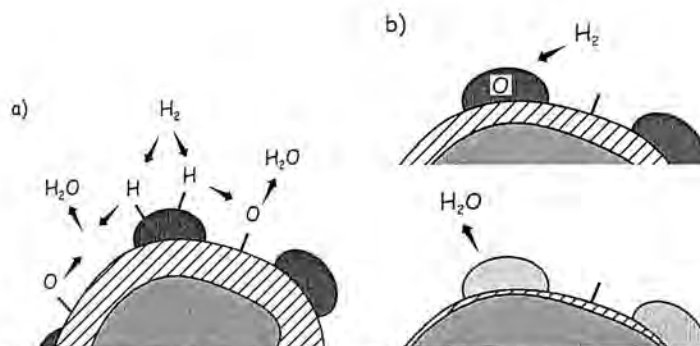


Figure 9: Scheme of the mechanisms of spill-over (a) and electronic sensitisation (b).

resulting from the change in the oxidation state of the surface cluster is often very drastic, giving rise to high gas sensitivity.

In spite the above mechanisms are the most accepted ones to explain most of the investigations, some authors propose other mechanisms to explain their results. Thus, for example, it has been claimed that under certain conditions for the distribution and size of the metallic clusters, tunneling occurs between the discrete islands [138], dominating the normally considered thermoionic emission carrier transport. Other authors consider that in some cases the effect that the depletion region created by the presence of additives at the surface of the semiconductor has on decreasing the effective grain size is more relevant [139]. Finally, it has been claimed also that improved response to gas with noble metal loading can arise mainly through the interaction of the gas molecules with the electron states introduced near the valence band edge by the additive, i.e., via the control of the population of such states and the consequent change of the band bending [140].

Actually, one has to observe that all the above mechanisms are present at the same time. However, several factors determine their activity and a concrete mechanism may be dominant in some case. Thus, in general, for a given additive, its distribution through the support and loading will have important effects on the device response in addition to that arising from the nature of the catalytic material itself [131, 140, 141]. Indeed, it has been observed that the maximum gas sensitivity depends, for a given metal additive, even on the loading method (fixation, impregnation, metal evaporation...) [142] and that the general response is influenced not only by the chemical state of the catalyst but also by its crystalline structure [143, 144]. On the other hand, the temperature of operation of the sensor can also determine the real function of the additive as, for example, spill-over can only occur at certain temperatures, which may depend on the gas.

The case of Pt and Pd are especially important, as they are the most usually employed additives on SnO_2 . Pt is always expected to be in metallic form. However, it can be covered by an oxygen layer, such that, depending on the size of the

metallic cluster deposited, it can be considered completely in oxidised form and not in metallic form. On the other hand, Pd is always assumed to be in oxidised form. Nevertheless, the final chemical state of Pd would depend on the different gases present in the ambient and on the loading performed.

The evolution of the chemical state of the additive would depend, in any case, of the present gases, which can infer a dynamic behaviour to the catalyst. As example it can be considered the dissociative adsorption of CH_4 on Pd supported catalysts. While methane is known to adsorb dissociatively on supported and unsupported Pd metal [145], it does not adsorb on oxygen-covered Pd [146]. Indeed, it seems that the dissociative adsorption of CH_4 on Pd is progressively inhibited by the presence of adsorbed oxygen [143], the sticking coefficient for dissociative adsorption decreasing linearly with increasing oxygen coverage. It has been observed that metallic Pd greatly enhances the rate of reduction of PdO by CH_4 [143, 147], and once formed the fragments of the dissociative adsorption of CH_4 (viz, CH_3 and H) spill over onto the Pd/PdO interface and rapidly reduce the oxide. In other case as for example of H_2 , it reduces the surface of PdO so quickly that it occurs in a shellwise fashion.

From this dynamic properties of the Pd additive it can be deduced that a mixture of gases like H_2 and CH_4 could be used to enhance the response to CH_4 because of the rapid reduction of PdO by H_2 .

1.6 REFERENCES

- [1] H. Nakagawa, S. Okazaki, S. Asakura, K. Fukuda, H. Akimoto, S. Takahashi, and T. Shigemori, An automated car ventilation system, *Techn. Digest of the 7th international meeting of Chemical Sensors, Beijing, July 27-30 (1998)*, pp. 187-189.
- [2] CORINAIR 94 in <http://www.aeat.co.uk/netcen/corinair/94/>
- [3] N. Yamazoe, G. Sakai, Sensors for environmentally concerned gases. Trends in reserch for environmental gas sensors, *Trans. Of Inst. Elec. Eng. Of Japan 118E*, 60-63 (1998).
- [4] N. Minnaja, Safety sensors, in: Sensors for domestic applications. De. By A. D'Amico, and G. Sberveglieri, World Scientific Publishing Co, Singapore, pp.107-114.
- [5] In US: Underwrites Laboratories Inc., Simple and multiple station Carbon monoxide detectors, US April 1992.
In UK: Technical Comitee GEL/31, Specification for Carbon Monoxide detectors (electrical) for domestic use, BS 7860:1996, British Standard, March 1996.
In Europe (under development): Normative of the Technical Comitee Gas Detectors (TC116) of the European Comitee for Electrochemical Standardization (CENELEC): Electrical apparatus for the detection of combustible gases in domestic premises, PR50194, final draft European Standard, July 1997; and Electrical apparatus for the detection of carbon monoxide in domestic premises, PR50291, final draft European Standard, August 1997.
- [6] J.W. Gardner, and P.N. Bartlett, A brief history of electronic noses, *Sensors and Actuators B 18-19*, 211-220 (1994).
- [7] P.E. Keller, L.J. Kangas, L.H. Liden, S. Hashem, and R.T. Kouzes, Electronic noses and their applications, *IEEE Tac 95 Conf. Proc.*, Portland, OR (USA), 1995.
- [8] E. Schaller, J.O. Bosset, and F. Escher, Electronic noses and their application to food, Review, *Food Science and Technology 31(4)*, 305-316 (1998).
- [9] A. Hierlemann, M. Schweizer-Berberich, U. Weimar, G. Kraus, A. Pfau, and W. Göpel, Pattern recognition and multicomponent analsis, in H. Baltes, W. Göpel, and J. Hesse (Eds.), *Sensors (Update) vol 2*, Weinheim, VCH, pp.119-180 (1996).
- [10] R.J. Lauf, and B.S. Hoffheins, Analysis of liquid fuels using a gas sensor array, *Fuel 70*, 935-940 (1991).

- [11] P.E. Keller, R.T. Kouzes, and L.J. Kangas, Three neural network based sensor systems for environmental monitoring, *IEEE Electro 94 Conf. Proc.*, Boston, MA (USA), 1994, pp. 378-382.
- [12] S. Ehrmann, J. Jüngst, J. Goschnick, and D. Everhard, Application of a gas sensor microarray to human breath analysis, , *Techn. Digest of the 7th international meeting of Chemical Sensors, Beijing, July 27-30 (1998)*, pp. 214-216.
- [13] C. Di Natale, A. Macagnano, R. Paolesse, A. Mantini, and A. D'Amico, Electronic nose approach to the human skin odour analysis, , *Techn. Digest of the 7th international meeting of Chemical Sensors, Beijing, July 27-30 (1998)*, pp. 148-150.
- [14] P.E. Keller, R.T. Kouzes, L.J. Kangas, and S. Hashem, Transmission olfactory information for telemedicine, *Interactive Technology and the New Paradigm for Healthcare*, Ed. by R.M. Satava, K. Morgan, H.B. Sieburg, R. Matteus, and J.P. Christensen, IOS Press., Amsterdam, 1995, pp. 168-172.
- [15] R.J. Elliot-Martin, T.T. Mottranm, J.W. Gardner, P.J. Hobbs, and P.N. Bartlett, Preliminary investigation of breath sampling as a monitor of health in dairy cattle, *J. Agric. Engng. Res.* **67**, 267-275 (1997).
- [16] J.L. Berdagué, and T. Talou, Exemples d'application aux produits carnés des senseurs de gaz à semi-conducteurs, *Sciences de Aliments* **13**, 141-148 (1993).
- [17] J.L. Berdagué, G. Vernat, and V. Rossi, Revue. Caractérisation instrumentale de la qualité des matières premières et des aliments par analyse des composés volatils, *Viandes et Produits Carnés* **14**, 135-138 (1993).
- [18] V. Rossi, R. Talon, and J.L. Berdagué, Rapid discrimination of Micrococcaceae species using semiconductor gas sensors, *J. Microbiological Methods* **24**, 183-190 (1995).
- [19] V. Rossi, C. Garcia, R. Talon, C. Denoyer, and J.L. Berdagué, Discrimination rapide par senseurs de gaz à semi-conducteurs. Application aux produits carnés secs et aux souches bactériennes, *Viandes et Produits Carnés* **16**, 21-24 (1995).
- [20] V. Vernat-Rossi, C. Garcia, R. Talon, C. Denoyer, and J.L. Berdagué, Rapid discrimination of meat products and bacterial strains using semiconductor gas sensors, *Sensors and Actuators B* **37**, 43-48 (1996).
- [21] L. Moy, G. Vasic, J.L. Berdagué, and V. Rossi, Transient signal modeling for fast odour classificaton, in: P. Etiévant, and P. Schreier (Eds.), *Proceedings of Bioflavour 95*. Dijon: INRA éditions, pp. 55-58 (1995).

- [22] R. Van Dijk, Quality control in the meat industry using gas sensor arrays, *Olfaction and Electronic Nose, 3rd International Symposium, Toulouse* (1996).
- [23] F. Winqvist, E.G. Hörnsten, H. Sundgren, and I. Lundström, Performance of an electronic nose for quality estimation of ground meat, *Measurement Science Technology* **4**, 1493-1500 (1993).
- [24] V.P. Shiers, P.J. Farnell, W.C. Blackburn, and D. Kilcast, Comparison of electronic nose, sensory panel and microbiological analysis for the detection of spoilage in modified-atmosphere-packed minced beef, *Leatherhead report 734* (1996).
- [25] R. Olafsson, E. Martinsdottir, G. Olafsdottir, P.I. Sigfusson, and J.W. Gardner, Monitoring of fish freshness using tin oxide sensors, in: J.W. Gardner, and P.N. Bartlett (Eds.), *Sensors and Sensory Systems for an Electronic Nose*, Dordrecht, Kluwer Academic Publishers, pp. 257-272 (1992).
- [26] F. Winqvist, H. Sundgren, and I. Lundström, A practical use of electronic noses: quality estimation of cod fillet bought over the counter, *Transducers '95, Eurosensors IX, The 8th International Conference on Solid-State Sensors and Actuators, and Eurosensors IX, Stockholm, Sweden, (June 25-29)*, **1**, 695-697 (1995).
- [27] Anonymous. Elektronische Nasen, *Die Ernährungsindustriek* **6**, 54-55 (1996).
- [28] M. Zannoni, Preliminary results of employ of an artificial nose for the evaluation of cheese, *Scienza e Tecnica Lattiero-Casearia* **46**, 277-289 (1995).
- [29] K.C. Persaud, and P.J. Travers, Arrays of broad specificity films for sensing volatile chemicals, in E. Kress-Rogers (Ed.), *Handbook of Biosensors and Electronic Noses*, Frankfurt, CRC Press, pp. 563-592 (1997).
- [30] R. Mariaca, and J.O. Bosset, Instrumental analysis of volatile (flavour) compounds in milk and dairy products, *Lait* **77**, 13-40 (1997).
- [31] J.R. Stetter, M.W. Findlay, K.M. Schroeder, C. Yue, and W.R. Penrose, Quality classification of grain using a sensor array and pattern recognition, *Analytica Chimica Acta* **284**, 1-11 (1993).
- [32] T. Börjesson, T. Eklöv, A. Jonsson, H. Sundgren, and J. Schnürer, Electronic nose for odor classification of grains, *Cereal Chemistry* **73**, 457-461 (1996).
- [33] A. Jonsson, F. Winqvist, J. Schnürer, H. Sundgren, and I. Lundström, Electronic nose for microbial quality classification of grains, *International Journal of Food Microbiology* **35**, 187-193 (1997).

- [34] E. Moltó, E. Selfa, J. Ferriz, E. Conesa, and A. Gutierrez, An aroma sensor for assessing peach quality, *J. Agric. Engng. Res.* **72**, 311-316 (1999).
- [35] J.E. Simon, A. Hertzroni, B. Bordelon, G.E. Miles, and D.J. Charles, Electronic sensing of aromatic volatiles for quality sorting blueberries, *J. Food Sci.* **61**, 967-969 (1996).
- [36] C. Di Natale, A. Macagnano, R. Paolesse, E. Tarizzo, A. D'Amico, F. Davide, T. Boschi, M. Faccio, G. Ferri, F. Sinesio, F.M. Bucarelli, E. Moneta, and G.B. Quaglia, A comparison between an electronic nose and human olfaction in a selected case study, *Proc. of the 1997 International Conference on Solid-State Sensors and Actuators, Chicago, June 16-19 (1997)*, pp. 1335-1338.
- [37] M. Schweizer-Berberich, M. Frank, T. Hermle, H. Ulmer, J. Mitrovics, U. Weimar, and W. Göpel, Quality tests of electronic noses: The influence of sample dilution and sensor drift on the pattern recognition for selected case studies, *Techn. Digest of the 7th international meeting of Chemical Sensors, Beijing, July 27-30 (1998)*, pp.139-141.
- [38] J.W. Gardner, H.V. Shurmer, and T.T. Tan, Application of an electronic nose to the discrimination of coffees, *Sensors and Actuators B* **6**, 71-75 (1992).
- [39] T.C. Pearce, J.W. Gardner, S. Friel, P.N. Bartlett, and N. Blair, Electronic nose for monitoring the flavour of beers, *Analyst* **118**, 371-377 (1993).
- [40] J.B. Tomlinson, I.H.L. Ormrod, and F.R. Sharpe, Electronic aroma detection in the brewery, *J. Am. Soc. of Brewing Chemists* **53**, 167-173 (1995).
- [41] J.W. Gardner, E.L. Hines, and M. Wilkinson, Application of artificial neural networks to an electronic olfactory system, *Measurement Science and Technology* **1**(5), 446-451 (1990).
- [42] H.H. Wang, Assessment of solid state fermentation by a bioelectronic artificial nose, *Biotechnology advances* **11**, 701-710 (1993).
- [43] C. Di Natale, F.A.M. Davide, A. D'Amico, G. Sberveglieri, and P. Nelli, Complex chemical pattern recognition with sensor array: the discrimination of vintage years of wine, *Sensors and Actuators B* **24-25**, 801-804 (1995).
- [44] H. Nanto, T. Kawai, H. Sokooshi, and T. Usuda, Aroma identification using a quartz-resonator sensor in conjunction with pattern recognition, *Sensors and Actuators B* **14**, 718-720 (1993).
- [45] J.V. Hatfield, P. Neaves, P.J. Hicks, K. Persaud, and P. Travers, Towards an integrated electronic nose using conducting polymer sensors, *Sensors and Actuators B* **18**, 221-228 (1994).
- [46] J.M. Slater, J. Paynter, and E.J. Watt, Multilayer conducting polymer gas sensor arrays for olfactory sensing, *Analyst* **118**, 379-384 (1993).

- [47] Y. Yanming, Y. Pengyuan, and W. Xiarou, Electronic nose based on SAWs array and the nose's odor identification capability, *Techn. Digest of the 7th international meeting of Chemical Sensors, Beijing, July 27-30 (1998)*, pp. 145-147.
- [48] T. Moriizumi, T. Nakamoto, and Y. Sakuraba, Pattern recognition in electronic noses by artificial neural network models, *Sensors and Sensory Systems for an Electronic Nose*, Ed. by J.W. Gardner, and P.N. Barlett, Amsterdam, The Netherlands, Kluwer Academic Publishers, pp. 217-236 (1992).
- [49] C. Bohatier, V. Bernat-Rossi, C. Breysse, J. Thebault, and J.L. Berdagué, Caractérisation d'un emballage défectueux par analyse de sa fraction volatile, *Industries Alimentaires et Agricoles* **112**, 849-852 (1995).
- [50] M. Holmberg, F. Winqvist, I. Lundström, J.W. Gardner, and E.L. Hines, Identification of paper quality using electronic nose, *Sensors and Actuators B* **26-27**, 246-249 (1995).
- [51] S.S. Schiffman, B.G. Kermani, and H.T. Nagle, Analysis of medication off-odors using an electronic nose, *Chemical Senses* **22**, 119-128 (1997).
- [52] H. Ulmer, J. Mitrovics, U. Weimar, and W. Göpel, Detection of off-odors using a hybrid modular sensor system, *Proc. of the 1997 International Conference on Solid-State Sensors and Actuators, Chicago, June 16-19 (1997)*, pp. 555-558.
- [53] Chemical and Biological Sensors, Part I, vol 2, Ed. by W. Göpel, T.A. Jones, M. Kleitz, J. Lundström, and T. Seiyama, VCH, Weinheim (FRG), 1991. Included in the series *Sensors: A Comprehensive Survey*, Ed. by W. Göpel, J. Hesse, and J.N. Zemel, VCH, Weinheim (FRG), 1991.
- [54] I. Lundström, S. Shivaraman, C. Svensson, and L. Lundkvist, Hydrogen-sensitive MOS field-effect transistor, *Appl. Phys. Lett.* **26**, 55-57 (1975).
- [55] I. Lundström, A. Spetz, F. Winqvist, U. Ackelid, and H. Sundgren, Catalytic metals and field-effect devices- a useful combination, *Sensors and Actuators B* **1**, 15-20 (1990).
- [56] M.S. Nieuwenhuizen, and A.J. Nederlof, Silicon based surface acoustic wave gas sensors, in *Sensors and Sensory systems for an Electronic Nose*, Ed. by J.W. Gardner, and P.N. Bartlett, Dordrecht, Kluwer Academic Publishers, (1992), pp. 131-145.
- [57] G. Guilbault, and J.M. Jordan, Analytical uses of piezoelectric crystal: a review, *Critical Reviews in Analytical Chemistry* **19**, 1-28 (1988).
- [58] W.H. King, Piezoelectric Sorption Detector, *Analytical Chemistry* **19**, 1735-1739 (1964).
- [59] H. Wohljen, and R. Dessy, Surface acoustic wave probe for chemical analysis. I. Introduction and instrument description, *Analytical Chemistry* **51**, 1458-1465 (1979).

- [60] H. Wohljen, and R. Dessy, Surface acoustic wave probe for chemical analysis. II. Gas chromatography detector, *Analytical Chemistry* **51**, 1465-1470 (1979).
- [61] H. Wohljen, and R. Dessy, Surface acoustic wave probe for chemical analysis. III. Thermomechanical polymer analyzer, *Analytical Chemistry* **51**, 1470-1478 (1979).
- [62] S.J. Martin, S.K. Schwartz, R.L. Gunshor, and R.F. Pierret, Surface acoustic wave resonators on a ZnO-on-Si layered medium, *J. Appl. Phys.* **54**, 561-569 (1983).
- [63] P. Mielle, Electronic noses: towards the objective instrumental characterization of food aroma, *Trends in Food Science & Technology, Special Issue on Flavour Perception*, **7**, 432-438 (1996).
- [64] D. Hodgins, The electronic nose: Sensor array-based instruments that emulate the human nose, in *Techniques for analyzing food aroma*, Ed. by R. Marsilli, New York, Marcel Dekker Inc., 1997, pp. 331-371.
- [65] M.E. Amrani, K.C. Persaud, and P.A. Payne, High-frequency measurements of conducting polymers: development of a new technique for sensing volatile chemicals, *Measurement Science and Technology* **6**, 1500-1507 (1995).
- [66] A.M. Azad, S.A. Akbar, S.G. Mhaisalkar, L.D. Birkefeld, and K.S. Goto, Solid-state gas sensors: A review, *J. Electrochem. Soc* **139**(12), 36903704 (1992).
- [67] W. Göpel, and K.D. Schierbaum, Electronic conductance and capacitance sensors, in *Chemical and Biological Sensors, Part I*, vol 2, Ed. by W. Göpel, T.A. Jones, M. Kleitz, J. Lundström, and T. Seiyama, VCH, Weinheim (FRG), 1991. pp 430-466.
- [68] D.E. Williams, Conduction and gas response of semiconductor gas sensors, in *Solid State Gas Sensors*, Ed. by P.T. Moseley, and B.C. Tofield, Adam Hilger, Bristol (UK), 1987, pp. 71-123.
- [69] I. Lundström, A. van der Berg, B.H. van der Schoot, H.H. van der Vlekkert, M. Armgarth, and C.I. Nylander, Field effect chemical sensors, in *Chemical and Biological Sensors, Part I*, vol 2, Ed. by W. Göpel, T.A. Jones, M. Kleitz, J. Lundström, and T. Seiyama, VCH, Weinheim (FRG), 1991. pp 469-528
- [70] M.S. Nieuwenhuizen, and A. Venema, Mass-sensitive devices, in *Chemical and Biological Sensors, Part I*, vol 2, Ed. by W. Göpel, T.A. Jones, M. Kleitz, J. Lundström, and T. Seiyama, VCH, Weinheim (FRG), 1991. p. 647-680.
- [71] M. Faccio, G. Ferri, F. Mancini, and P. Di Rosa, Resonating quartz sensors, in *Sensors for domestic applications*, Ed. by A. D'Amico, and G. Sberveglieri, World Scientific Publishing Co., Singapore, 1995, pp.71-86.

- [72] J.W. Grate, and G.C. Frye, Acoustic wave sensors, in *Sensors (Update)*, vol 2, Ed. by W. Göpel, J. Hesse, and J.N. Zemel, VCH, Weinheim (FRG), 1996, p. 38-83.
- [73] C. Caliendo, and E. Verona, Surface acoustic wave sensors, in *Sensors for domestic applications*, Ed. by A. D'Amico, and G. Sberveglieri, World Scientific Publishing Co., Singapore, 1995, pp. 87-104.
- [74] P.T. Walsh, and T.A. Jones, Calorimetric chemical sensors, in *Chemical and Biological Sensors, Part I*, vol 2, Ed. by W. Göpel, T.A. Jones, M. Kleitz, J. Lundström, and T. Seiyama, VCH, Weinheim (FRG), 1991. pp 531-572
- [75] E. Jones, The pellistor catalytic gas setector, in *Solid State Gas Sensors*, Ed. by P.T. Moseley, and B.C. Tofield, Adam Hilger, Bristol (UK), 1987 ,pp. 17-31.
- [76] O.S. Wolfbeis, G. Boisdé, and G. Gauglitz, Optochemical sensors, in *Chemical and Biological Sensors, Part I*, vol 2, Ed. by W. Göpel, T.A. Jones, M. Kleitz, J. Lundström, and T. Seiyama, VCH, Weinheim (FRG), 1991. p. 575-645.
- [77] G. Gauglitz, Opto-chemical and opto-immuno sensors, in *Sensors (Update)*, vol 1, Ed. by H. Baltes, W. Göpel, and J. Hesse, VCH, Weinheim (FRG), 1996, p. 1-45.
- [78] A.G. Mignani, and A.M. Scheggi, Fiber optic sensors, fundamentals and domestic applications, in *Sensors for domestic applications*, Ed. by A. D'Amico, and G. Sberveglieri, World Scientific Publishing Co., Singapore, 1995, pp. 14-23.
- [79] H.D. Wiemhöfer, and K. Cammann, Specific features of electrochemical sensors, in *Chemical and Biological Sensors, Part I*, vol 2, Ed. by W. Göpel, T.A. Jones, M. Kleitz, J. Lundström, and T. Seiyama, VCH, Weinheim (FRG), 1991. p. 160-189.
- [80] C.M. Mari, Non-Nerstian solid state sensor for home applications, in *Sensors for domestic applications*, Ed. by A. D'Amico, and G. Sberveglieri, World Scientific Publishing Co., Singapore, 1995, pp. 61-70.
- [81] W.H. Brattain, and J. Bardeen, *Bell Systems Tech. J.* **32**, 1 (1953).
- [82] T. Seiyama, A. Kato, K. Fujiishi, and M. Nagatani, A new detector for gaseous components using semiconductive thin films, *Anal. Chem.* **34**, 1502-1503 (1962).
- [83] N. Taguchi, *Jpn. Patent 45-38200*, 1962.
- [84] N. Taguchi, *UK Patent 1280809*, 1970; and K. Tagushi, *US Patent 3631 436*, 1970.
- [85] M. Prudenziati, Thick-film technology, *Sensors and Actuators A* **25-27**, 227-234 (1991).

- [86] N. Yamazoe, New approaches for improving semiconductor gas sensors, *Sensors and Actuators B* **5**, 7-19 (1991).
- [87] S. Samson, and C.G. Fonstad, Defect structure and electronic donor levels in stannic oxide crystals, *J. Appl. Phys.* **44**, 4618-4621 (1973).
- [88] C.G. Fonstad and R.H. Rediker, Electrical properties of high-quality stannic oxide crystals, *J. Appl. Phys.* **42**, 2911-2918 (1971).
- [89] W. Göpel, Chemisorption and charge-transfer at ionic semiconductor surfaces: implications in designing gas sensors, *Prog. Surf. Sci.* **20**, 9-103 (1985).
- [90] K.D. Schierbaum, Engineering of oxide surfaces and metal/oxide interfaces for chemical sensors: recent trends, *Sensors and Actuators B* **24-25**, 239-247 (1995).
- [91] D. Kohl, Surface processes in the detection of reducing gases with SnO₂-based devices, *Sensors and Actuators* **18**, 71-113 (1989).
- [92] H. Geistlinger, Electron theory of thin-film gas sensors, *Sensors and Actuators Bk 17*, 47-60 (1993).
- [93] W. Göpel, Solid-state chemical sensors: atomistic models and research trends, *Sensors and Actuators* **16**, 167-193 (1989).
- [94] M. Kanamori, K. Suzuki, Y. Ohya, and Y. Takahashi, Analysis of the change in the carrier concentration of SnO₂ thin film gas sensor, *Jpn. J. Appl. Phys.* **33**, 6680-6683 (1994).
- [95] P.B. Weisz, Effects of electronic charge transfer between adsorbate and solid on chemisorption and catalysis, *J. Chem. Phys.* **21**, 1531-1538 (1953).
- [96] N. Bârsan, R. Grigorovici, R. Ionescu, M. Motronea, and A. Vancu, Mechanism of gas detection in polycrystalline thick film SnO₂ sensors, *Thin Solid Films* **171**, 53-63 (1989).
- [97] S.R. Morrison, Measurement of surface state energy-levels of one-equivalent adsorbates on ZnO, *Surf. Sci.* **27**, 586-602 (1971).
- [98] V. Lantto, and P. Romppainen, Electrical studies on the reactions of CO with different oxygen species on SnO₂ surfaces, *Surf. Sci.* **192**, 243-264 (1987).
- [99] P.K. Clifford, Homogeneous semiconducting gas sensors: a comprehensive model, *Proc. 1st Int. Conf. Chemical Sensors, Fukuoka, Japan, 1983*, pp. 135, and P.K. Clifford and D.T. Tuma, Characteristics of semiconducting gas sensors, 1: Steady state gas response, *Sensors and Actuators* **3**, 233-254 (1983), 2: Transient response to temperature change, *Sensors and Actuators* **3**, 255-281 (1983).
- [100] Y. Xu, X. Zhou, and O.T. Sorensen, Oxygen sensors based on semiconducting metal oxides, *Techn. Digest of the 7th international meeting of Chemical Sensors, Beijing, July 27-30 (1998)*, pp. 426-430.

- [101] J.F. McAleer, P.T. Moseley, J.O.W. Norris, and D.E. Williams, Tin dioxide gas sensors, *J. Chem. Soc., Faraday Trans. 1* **83**, 1323-1346 (1987).
- [102] J. Mizsei, How can sensitive and selective semiconductor gas sensors be made?, *Sensors and Actuators B* **23**, 173-176 (1995).
- [103] D.E. Williams, and K.F.E. Pratt, Classification of reactive sites on the surface of polycrystalline tin dioxide, *J. Chem. Soc., Faraday Trans.* **94**, 3493-3500 (1998).
- [104] A. Bielanski, and J. Haber, Oxygen in catalysis on transition-metal oxides, *Catal. Rev.* **19** (1), 1-41 (1979).
- [105] N. Yamazoe, J. Fuchigami, M. Kishikawa, and T. Seiyama, Interactions of tin oxide surface with O₂, H₂O and H₂, *Surf. Sci* **86**, 335-344 (1979).
- [106] P.T. Moseley, and D.E. Williams, Oxygen surface species on semiconducting oxides, in *Techniques and mechanisms in gas sensing, Adam Hilger series on sensors, Ed. by Pt. Moseley, J. Norris, and D.E. Williams, Adam Hilger, Bristol, UK* (1991) pp. 47-60.
- [107] Y. Shimizu, T. Maekawa, Y. Nakamura, and M. Egashira, Effects of gas diffusivity and reactivity on sensing properties of thick film SnO₂ based sensors, *Sensors and Actuators B* **46**, 163-168 (1998).
- [108] W. Olthuis, W. Streekstra, and P. Bergveld, Theoretical and experimental determination of cell constants of planar-interdigitated electrolyte conductivity sensors, *Sensors and Actuators B* **24-25**, 252-256 (1995).
- [109] A. Götz, Integrated microsensors for microsystems with applications in biomedicine and environmental control, *Ph. D., Universitat Autònoma de Bellaterra, Facultat de Ciències*, November 1997.
- [110] M. Bauer, N. Bârsan, K. Ingrisch, A. Zeppenfeld, I. Denk, B. Schuman, U. Weimar, and W. Göpel, Influence of measuring voltage, geometry and electrodes on the characteristics of thick film SnO₂ gas sensors, *Proceedings of the 11th European Microelectronics Conference, Venice, May 1997*, 37-44.
- [111] R. Ionescu, and A. Vancu, Polarization effects in SnO₂ thick-film sintered sensors, *Phys. Stat. Sol. A* **151**, 135-142 (1995).
- [112] A. Ylinampa, V. Lantto, and S. Leppävuori, Some differences between Au and Pt electrodes in SnO₂ thick-film gas sensors, *Sensors and Actuators B* **13-14**, 602-604 (1993).
- [113] K. Fukui, and M. Nakane, Effects of tin oxide semiconductor-electrode interface on gas sensitivity characteristics, *Sensors and Actuators B* **13-14**, 589-590 (1993).
- [114] V.M. Aroutiounian, and G.S. Aghababian, To the theory of semiconductor gas sensors, *Sensors and Actuators B* **50**, 80-84 (1998).
- [115] V. Demarne, A. Grisel, R. Sanjinés, D. Rosenfeld, and F. Lévy, Electrical transport properties of thin polycrystalline SnO₂ film sensors, *Sensors and Actuators B* **7**, 704-708 (1992).

- [116] G. Martinelli, and M.C. Carotta, Sensitivity to reducing gas as a function of energy barrier in SnO₂ thick-film gas sensor, *Sensors and Actuators B* **7**, 717-720 (1992).
- [117] J.F. McAleer, P.T. Moseley, J.O.W. Norris, and D.E. Williams, Tin dioxide gas sensors, *J. Chem. Soc., Faraday Trans. 1* **83**, 1323-1346 (1987).
- [118] P. Römppainen, and V. Lanto, The effect of microstructure on the height of potential energy barriers in porous tin dioxide gas sensors, *J. Appl. Phys.* **63**(10), 5159-5165 (1988).
- [119] J. Sinkkonen, DC conductivity of a random barrier network, *Phys. Stat. Sol. B* **102**, 621-627 (1980).
- [120] R. Botter, T. Aste, and D. Beruto, Influence of microstructures on the functional properties of tin oxide-based gas sensors, *Sensors and Actuators B* **22**, 27-35 (1994).
- [121] S.R. Morrison, Semiconductor gas sensor, *Sensors and Actuators* **2**, 329-341 (1982).
- [122] K.D. Schierbaum, U. Weimar, W. Göpel, and R. Kowalkowski, Conductance, work function and catalytic activity of SnO₂-based gas sensors, *Sensors and Actuators B* **3**, 205-214 (1991).
- [123] R.F. Pierret, Semiconductor device fundamentals, Addison-Wesley Publishing Company Inc., Massachusetts (USA), 1996, pp. 749-750.
- [124] Ch. Xu, J. Tamaki, N. Miura, and N. Yamazoe, Correlation between gas sensitivity and crystallite size in porous SnO₂-based sensors, *Chem. Lett*, 441-444 (1990).
- [125] Ch. Xu, J. Tamaki, N. Miura, and N. Yamazoe, Grain size effects on gas sensitivity of porous SnO₂-based elements, *Sensors and Actuators B* **3**, 147-155 (1991).
- [126] N. Yamazoe, New approaches for improving semiconductor gas sensors, *Sensors and Actuators B* **5**, 7-19 (1991).
- [127] N. Bársan, Conduction models in gas-sensing SnO₂ layers: grain-size effects and ambient atmosphere influence, *Sensors and Actuators B* **17**, 241-246 (1994).
- [128] X. Wang, S.S. Yee, and W.P. Carey, Transition between neck-controlled and grain-boundary controlled sensitivity of metal-oxide gas sensors, *Sensors and Actuators B* **24-25**, 454-457 (1995).
- [129] V.P. Zhdanov, and B. Kasemo, Kinetics of rapid heterogeneous reactions on the nanometer scale, *J. Catal.* **170**, 377-389 (1997).
- [130] N. Yamazoe, Y. Kurokawa, and T. Seiyama, Effects of additives on semiconductor gas sensors, *Sensors and Actuators* **4**, 283-289 (1983).
- [131] J.F. McAleer, P.T. Moseley, J.O.W. Norris, D.E. Williams, and B.C. Tofield, Tin dioxide gas sensors: Part 2.- The role of surface additives, *J. Chem. Soc., Faraday Trans. 1* **84**(2), 441-457 (1988).

- [132] M. Labeau, M. Vallet-Regi, V. Ragel, J. Román, J. Martínez, J. Peña, E. García, A. Varela, B. Gautheron, and J.M. González-Calbet, SEM and TEM study of metallic nanoparticles dispersed on SnO₂, *Proc. of the 9th European Conference on Electron Microscopy, vol 2, EUREM92, Granada, Spain, pp. 655-656 (1992).*
- [133] M. Labeau, B. Gautheron, F. Cellier, M. Vallet-Regi, E. García, and J.M. González-Calbet, Pt nanoparticles dispersed on SnO₂ thin films: a microstructural study, *J. Sol. Stat. Chem.* **102**, 434-439 (1993).
- [134] S. Matsushima, J. Tamaki, N. Miura, and N. Yamazoe, TEM observation of the dispersion state of Pd on SnO₂, *Chem. Lett.* 1651-1654 (1989).
- [135] M. Labeau, B. Gautheron, G. Delabouglise, J. Peña, V. Ragel, A. Varela, J. Román, J. Martinez, J.M. González-Calbet, and M. Vallet-Regi, Synthesis, structure and gas sensitivity properties of pure and doped SnO₂, *Sensors and Actuators B* **15-16**, 379-383 (1993).
- [136] Sh. Matsushima, Y. Teraoka, N. Miura, and N. Yamazoe, Electronic interaction between metal additives and tin dioxide-based gas sensors, *Jpn. J. Appl. Phys.* **27**(10), 1798-1802 (1988).
- [137] D. Kohl, The role of noble metals in the chemistry of solid-state gas sensors, *Sensors and Actuators B* **1**, 158-165 (1990).
- [138] C.A. Papadopoulos, and J.N. Avaritsiotis, A model for the gas sensing properties of tin oxide thin films with surface catalysts, *Sensors and Actuators B* **28**, 201-210 (1995).
- [139] D.S. Vlachos, C.A. Papadopoulos, and J.N. Avaritsiotis, On the electronic interaction between additives and semiconducting oxide gas sensors, *Appl. Phys. Lett.* **69**(5), 650652 (1996).
- [140] G.S. Henshaw, R. Ridley, and D.E. Williams, Room-temperature response of platinumised tin dioxide gas-sensitive resistors, *J. Chem. Soc., Faraday Trans.* **92**(18), 3411-3417 (1996).
- [141] R. Pestman, R.M. Koster, J.A.Z. Pieterse, and V. Ponc, Reactions of carboxylic acids on oxides, 1. Selective hydrogenation of acetic acid to acetaldehyde, *J. Catal.* **168**, 255-264 (1997).
- [142] I. Kocemba, and T. Paryjczak, Metal films on a SnO₂ surface as selective gas sensors, *Thin Solid Films* **272**, 15-17 (1996).
- [143] J.N. Carstens, S.C. Su, and A.T. Bell, Factors affecting the catalytic activity of Pd/ZrO₂ for the combustion of methane, *J. Catal.* **176**, 136-142 (1998).
- [144] E. Garbowski, C. Feumi-Jantou, N. Mouaddib, and M. Primet, Decomposition of CH₄ over supported Pd catalysts, *Appl. Catal. A* **109**, 277-291 (1994).
- [145] F. Solymosi, A. Erdöhelyi, Cserényi, and Felvégi, Catalytic combustion of methane over palladium supported on alumina catalysts. Evidence for surface reconstruction of particles, *J. Catal.* **147**, 272-278 (1994).

- [146] M. Valden, J. Pere, N. Xiang, and M. Pessa, Influence of preadsorbed oxygen on activated chemisorption of methane on Pd(110), *Chem. Phys. Lett.* **257**, 289-296 (1996).
- [147] S.C. Su, J.N. Carstens, and A.T. Bell, A study of the dynamics of Pd oxidation and PdO reduction by H₂ and CH₄, *J. Catalysis* **176**, 125-135 (1998).

CHAPTER 2

STRUCTURAL CHARACTERIZATION
TECHNIQUES

The idea of making this *Chapter* is not only as a necessary accessory for the comprehension of the work by an unexperienced reader in structural characterization or persons usually involved in electrical characterization, but, in some way, to include an entire description of a group of basic structural characterization techniques in a clear way. For that, the fundamentals of the different techniques are treated, introducing in occasions the related physical phenomena and trying to explain in an intuitive way how to interpret the results, when it is possible. Additionally, the instrumentation required in each case is described basically, without entering in any case in great detail. For a reader interested in more details, a group of additional readings have been added at the end of the chapter. However, it has been sought that an experienced reader in the study of materials can acquire some basic knowledge that will allow him to go into more detail in the different techniques. The extension of the *Chapter* is justified by the fact that all the techniques reviewed have been intensive and extensively used through the work. Concretely a special emphasis is made in the sections dedicated to electron microscopy, especially of transmission, since, with a large difference, it is the most complicated technique. In other techniques also very important along the work, as Raman spectroscopy, a briefer introduction is made, which extends to more complex concepts of great importance for discussion during the development of *Chapter 3*.

The *Chapter* is divided in four main parts. The first one treats the *interaction of electrons with matter* and the information that this interaction supplies. According with this, some detailed explanation of *scanning and transmission electron microscopies* is given. As related techniques, in this part of the chapter are included those 'sub-techniques' giving chemical (analytical) information, i.e., *X-ray dispersive spectroscopy* and *electron energy loss spectroscopy*.

The second and third parts of the chapter deal with techniques related with X-rays. Although in both, *X-ray diffraction* and *X-ray photoelectron spectroscopy*, X-rays are utilized to obtain information of the sample, as the type of information and the principles of the technique are completely different, they are treated independently.

Next, some notes about the most widely used and important spectroscopical techniques related to optical phenomena associated with the vibrational structure of matter are discussed. These include *infrared spectroscopy* and *Raman scattering*, and will be of fundamental importance in the rest of the work, specially the last.

Finally, a brief description of sample preparation for all the techniques is given. Instead of explaining them in the corresponding part of the *Chapter*, it has been preferred to discuss them all at the end in order to emphasise the advantages of

some techniques, in front of others, also from the point of view of sample preparation.

It will be observed that no references are inserted in this chapter. As all the information provided in this chapter is the result of a large quantity of readings, it has been preferred to give a complete set of additional readings at the end of the chapter.

2.1 Electron microscopy

Since Hooke discovered the light-optical microscope, researchers have sought to improve the capability of the instrument to resolve more and more closely spaced objects. However, in spite of the high degree of improvement obtained during several centuries, Abbe discovered that diffraction was the ultimate limit that prevented one from pushing the resolution limit d beyond the limit:

$$d \approx 1.22 \frac{\lambda_o}{\sin \theta} = 1.22 \frac{\lambda_{vac}}{n \sin \theta} \quad (1)$$

where λ_o and $\lambda_{vac} = n\lambda_o$ are the wavelength of the light at the object and in the vacuum, respectively, and $n \sin \theta$ the numerical aperture.

So, at the beginning of this century the light microscope reached its best possible optical performance and further progress could only be made by shortening the wavelength of the light. However, after in 1923 Louis de Broglie showed that a wavelength is associated with a moving particle (equation 2), electrons in particular, and in 1927 Hans Busch demonstrated that an axially symmetric electromagnetic field acts on electrons like a glass lens on light rays, the barrier imposed by the wavelength limitation was overcome.

$$\lambda = \frac{h}{p} = \frac{h}{\left[2m_o eV \left(1 + \frac{eV}{2m_o c^2} \right) \right]^{1/2}} \quad (2)$$

λ electron wavelength

V acceleration voltage of EM

m_o electron rest mass

h Planck's constant

e electron charge

This was quickly applied by M. Knoll and E. Ruska, who in 1931 invented the electron microscope, surpassing the resolution of the light microscope. This result and the following improvements of lowering the limit of resolution resulted primarily from the extremely small wavelength of the electrons rather than from the quality of the electron lenses. Indeed even the best objective lenses of present-day electron microscopes are still poor compared with the sophisticated complex objectives of light microscopes.

In general, an electron microscope is an instrument that takes advantage of the physical-atomic phenomena produced when a beam of electrons, coming from a source that accelerates and directs them toward condenser lenses, bombards a specimen. From the phenomena that occur, the electron microscope obtains micro-morphological and, sometimes, also micro-analytical information.

Judged by its widespread use in all branches of science and more appropriately by the importance of the information which it has provided, the electron microscope might be claimed as one of the most significant scientific instrument invented in the twentieth century, and the tendency to regard any form of

microscopy as merely 'to take pictures' should be avoided in general by all material and biological scientists.

To understand the operation of electron microscopes, some notes on the interaction of electrons with matter and some nomenclature concepts are given in the following.

2.1.1 Some notes on interaction of electrons with matter

If a beam of electrons is directed to a solid target, the electrons pass either undeviated or they are scattered and are then adsorbed, reflected or transmitted. Moreover, electrons, as an ionising radiation, produce a wide range of secondary signals from the specimen. Fig. 1 is a schematic diagram of the principal interactions that can occur, indicating the events of interest to electron microscopy (transmission and scanning) and the analytical techniques (X-ray microanalysis and electron energy loss spectroscopy).

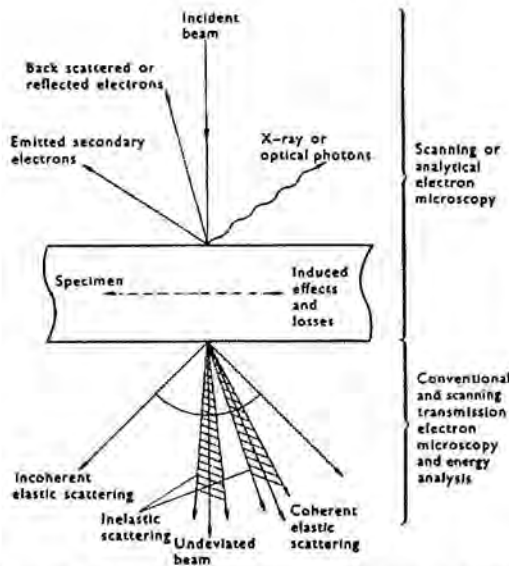


Figure 1: Main interactions of electron with matter related to structural characterization of materials and techniques. After Reading [1].

Electron scattering can be grouped in *elastic* and *inelastic* scattering. The former results from an interaction with no loss of energy (a small loss occurs because of the change in momentum on scattering by the atom) and the later with some measurable loss of energy. In this case we tend to consider electrons as particles and scattering to involve some interaction like billiard balls colliding. However, we can also separate scattered electrons into *coherent* and *incoherent*, which refers to their wave nature. These distinctions are related, since elastic electrons are usually coherent and inelastic

electrons are usually incoherent. When the incident electron waves are coherent (in phase), coherently scattered electrons are those that remain in phase and incoherently scattered electrons those that have no phase relationship after interacting with the specimen. In the case that electrons are scattered in the direction

of the electron beam we call them *forward-scattered* electrons. This scattering, which is employed in transmission electron microscopy, includes elastic scattering, Bragg scattering, the events called diffraction, refraction, and inelastic scattering. However, *back-scattered* electrons are very important also, because they are used in an important imaging mode in scanning electron microscopy.

2.1 1.1 Elastic scattering

It is convenient to divide elastic scattering mechanisms into two principal forms: electron scattering from isolated single atoms and collective scattering from many atoms together within the specimen. In the situation of interaction of a single

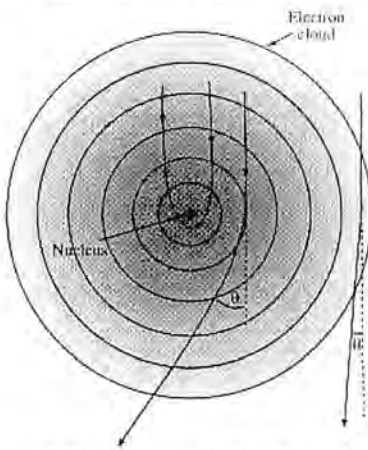


Figure 2: Elastic scattering, After Reading [3].

electron with an isolated atom, elastic scattering can occur in one of two ways, both involving Coulomb forces. As shown in fig. 2, the electron may interact with the electron cloud, resulting in a small angular deviation. Alternatively, if an electron penetrates the electron cloud and approaches the nucleus, it will be strongly attracted and may be scattered through a larger angle.

The chance that a particular electron undergoing any kind of interaction with an atom is determined by an interaction *cross section*, which can be defined in terms of the *effective radius* of the scattering center, r

$$\sigma = \pi r^2 \quad (3)$$

where r has a different value for each scattering process. In the case of elastic scattering, which is the most important in transmission electron microscopy image and diffraction pattern formation, the electron-electron and electron-nucleus cross sections can be easily expressed by,

$$\sigma_{electron} = \pi r_e^2 = \pi \left(\frac{e}{V\theta} \right)^2 \quad (4)$$

$$\sigma_{nucleus} = \pi r_n^2 = \pi \left(\frac{Ze}{V\theta} \right)^2 \quad (5)$$

where V is the potential of the incoming electron, which is scattered through an angle larger than θ by atoms of atomic number Z . This expression is useful because

it indicates the general behaviour of electrons in the electron microscope; i.e., usually electrons scatter less at high kV and high angles, and are scattered more by heavier atoms than light atoms. Thus, it can be observed that the dependence on θ , on the electron beam energy and on the atomic number Z , control a important part of the image contrast in electron microscopy.

The second principal form of elastic scattering occurs when the electron wave interacts with the specimen as a whole. The best known form of this interaction, diffraction, is particularly important at low angles. Following the original approach of Huygens for the diffraction of visible light, each atom in the specimen can be imagined acting as a source of 'secondary' spherical wavelets, as illustrated in fig. 3, understanding the electron beam as a wave, rather than as a particle. These wavelets reinforce one another on a few angular directions and cancel in all others. Thus, the low-angle elastic scattering distribution is modified by the crystal structure of the specimen, and intense diffracted beams emerge at certain specific angles.

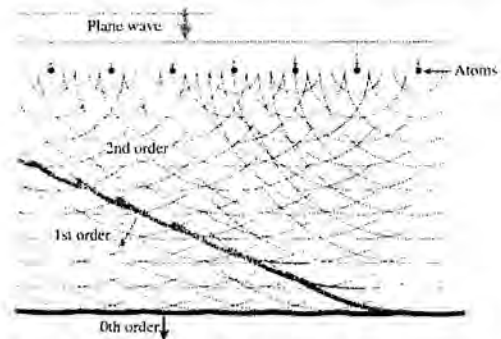


Figure 3: Diffraction. After Reading [3].

As the specimen contains N atoms/unit volume, the total cross section for scattering from the specimen can be defined as,

$$Q_T = N\sigma_T = \frac{N_o\sigma_T\rho}{A} \quad (6)$$

where N_o is Avogadro's number and A is the atomic weight of the atoms in the specimen which has a density ρ (so $NA=N_o\rho$). Thus Q can be regarded as the number of scattering events per unit distance that the electron travels through the specimen. If the specimen has a thickness t , then the probability of scattering by the specimen is given by:

$$Q_T t = \frac{N_o\sigma_T(\rho t)}{A} \quad (7)$$

The product of ρ and t is called the 'mass-thickness' of the specimen (e.g. doubling ρ produces the same effect as doubling t) and equation (7) is an important expression, since it contains all the variables that affect the scattering probability from a real specimen. It will be used when considering how certain kinds of image contrast arise in transmission electron microscopy.

2.1.1.2 Inelastic scattering

As has been commented, when the high-energy electron encounters an atom, it first penetrates the outer, loosely bound electron cloud, then it passes the inner, more tightly bound core shell electrons, and finally it may encounter the nucleus. As a general rule of thumb, the deeper the electron penetrates into the atom, the higher the energy that may be lost. When electrons loss energy, we are treating with inelastic processes, which can be separated into three components:

- Processes that generate X-rays
- Processes that generate other (secondary) electrons
- Processes that result from collective interactions with many atoms

In order to generate characteristics *X-rays*, a high-energy electron beam must penetrate through the outer electron shells and interact with the inner-shell (or core) electrons. If more than a critical amount of energy is transferred to an inner-shell electron, that electron is ejected; that is, it escapes from the attractive field of the nucleus, leaving a hole in the inner shell. When this happens the atom is left in an excited state and we describe it as 'ionized'. The ionized atom can return to its lowest energy (ground state) by filling in the missing electron with one from the outer shells. It is this transition which is accompanied either by the emission of an

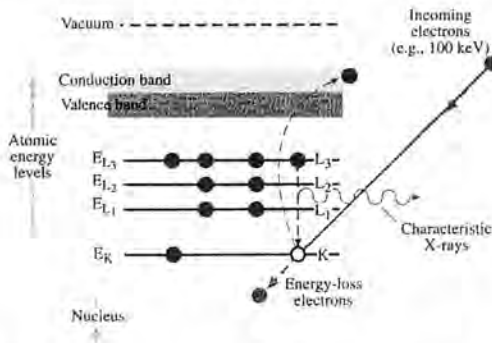


Figure 4: Generation of X-rays. After Reading [3].

X-ray or an Auger electron. The process of X-ray emission is shown schematically in fig. 4. Auger electron detection is rather specialized and usually carried out in a dedicated Auger electron spectrometer (AES) and will not be used in this work.

To generate an X-ray, the electron beam has to transfer an amount of energy larger than a critical value to the inner-shell electron to ionize the atom. Atoms with higher Z have more

protons and, therefore, have a higher critical ionization energy. According with H. Moseley,

$$\lambda = \frac{B}{(Z - C)^2} \quad (8)$$

where B and C are constants. As an X-ray is a photon of electromagnetic energy travelling at the speed of light in vacuum, relativistic corrections have not to be done as energy increases and, $E = h\nu = \frac{hc}{\lambda}$ and $\lambda = \frac{1.24}{E}$, where the wavelength, λ , is in nm and the energy, E , in keV.

Secondary electrons (SEs) are electrons in the specimen that are ejected by the beam electron. They can be discussed as three distinct groups:

- If the electrons are in the conduction or valence bands, then it does not take much energy to eject them, and they are called 'slow SEs' with energies typically below ~50eV.
- If the electrons are strongly bound inner-shell electrons, they are less readily ejected, but when they are thrown out of their shells they can have a significant fraction (up to about 50%) of the beam energy, and they are then called 'fast secondary electrons' or FSEs.
- If the electrons are ejected to compensate the energy loss of an electron that passes from an outer-level to a lower energetic level to fill a vacancy created previously, they are called Auger electrons.

Usually slow SEs are assumed to be free electrons, i.e., they are not associated with a specific atom and, so, they contain no specific elemental information. But because slow SEs are weak they can only escape if they are near the specimen surface. So, we use them in scanning electron microscopes to form images of the specimen surface. Fast SEs, which should be an order of magnitude more probable than slow SEs, are high-energy electrons that are generated in the specimen; they are high energy because they receive a large fraction of the beam energy. At the low beam energies used in a scanning electron microscope, FSEs are not a problem. However, in a transmission electron microscope, FSEs can have energies of ~50-200keV, in which case they will not only travel significant distances within the specimen, but they may also escape from deep distances within the specimen, degrading the spatial resolution of microanalysis in analytical electron microscopes and generating significant amounts of X-rays, which can cause problems in quantifying X-ray data. So, FSEs are not an image resolution problem, but rather a problem for chemical analysis.

Collective excitations occurring due to the electron beam include the generation of *plasmons* and *phonons*. Plasmons are collective oscillations of free electrons that occur when the beam electron passes through the free electron 'gas'. The plasmon energy is a function of the free-electron density and this changes with composition, so the plasmon excitation process is chemically dependent, although we rarely use it for microanalysis. Phonons are oscillations where all the atoms in the crystal lattice vibrate collectively. Such vibrations of the atoms are equivalent to specimen heating. One can reduce the number of phonons by cooling the specimen. Typically a phonon vibration causes a very small energy loss of <0.1eV, but the phonon scattered electrons are scattered out to quite large angles (5-15mrads versus

the typical angle of the transmitted beam $\sim 10\text{mrad}$ in a transmission electron microscope), and these electrons account for the diffuse background intensity present between the Bragg spots in diffraction patterns. Phonon scattered electrons carry not useful microchemical information, nor contrast useful to the microscopist.

2.1.2 Scanning electron microscopy

The idea of forming a focused electron probe and using the secondary emission to image surface topography of materials was first realized by Zworykin. The formation of the image in a scanning electron microscope (SEM) is schematically described in fig. 5.

By the focussing action of a strong convergent lens, an electron probe is formed and scanned over the surface of a thick sample (not electron transparent). Secondary electrons produced are then collected by a detector connected to a scintillator, so that the resulting photocurrent is amplified and recorded with respect to the position of the probe, thereby forming the scanned image of the surface.

It is usual in scanning electron microscopy to employ incident electron beams in the range $0.5\text{--}40\text{keV}$. The principal modes of contrast depend upon the detection of two categories

of electrons (figure 6). First, the reflected primary or back scattered electrons, with energies $\geq 50\text{eV}$, which are scattered from atoms within a shallow depth in the specimen ($\sim 1\mu\text{m}$), and second, emitted secondaries with energies $\leq 50\text{eV}$ but greater than the work function of the specimen surface. The last ones are obtained as an ionization product and because of their relatively low energies must be formed at very shallow depths ($\sim 0.1\mu\text{m}$). As electrons are scattered by the atomic potential $V(r)$, determined by the nuclear and electron cloud Coulomb potentials, it is clear that the characteristics of both reflected and secondary electrons are sensitive to variations in atomic number (hence composition) and topography. However, the reflective mode is much more efficient in detecting atomic number contrast while

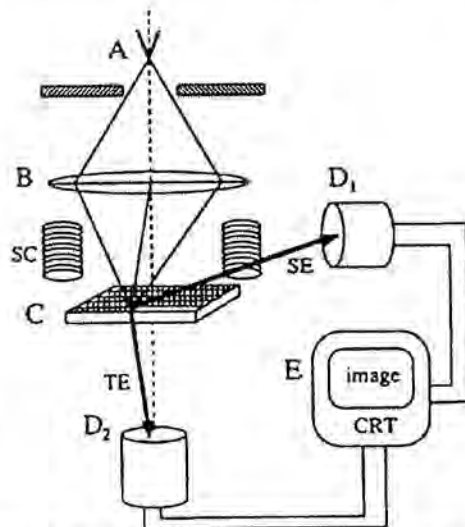


Figure 5: Scheme of a SEM apparatus. After Reading [5].

the emissive mode is used when topographical information is required. When used in the emissive mode topographic contrast is so strong that it may dominate any other contrast mechanism. An example of the same image taken with secondary and back-scattered electrons is presented in figure 7.

The resolution in the SEM, in the simplest terms, is related to the size of the electron probe that contains sufficient amount of current, which, to a certain extent, is dictated by the spherical and chromatic aberrations as well as the diffraction limitation. Resolution in SEM, however, is deteriorated by the interaction of the probe with the sample, and the subsequent beam spreading. This limitation becomes more evident at high emission voltages (20-30kV), which are necessary to obtain sufficient brightness in conventional electron sources. The use of high-brightness field emission sources in SEM allows the use of lower voltages (1-5kV) providing the currently achievable resolution values smaller than 1nm. Nevertheless, in a conventional SEM a difference in resolution between the two modes arises because the secondary (typically $d \sim 10\text{nm}$) and reflected (typically $d \sim 100\text{nm}$) electrons originate from different depths in the specimen (figure 7).

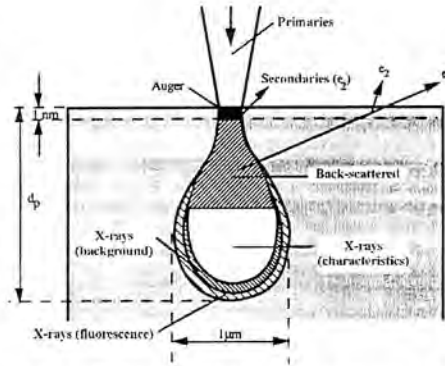


Figure 6: Different types of particles generated in a SEM apparatus. After Reading [1].

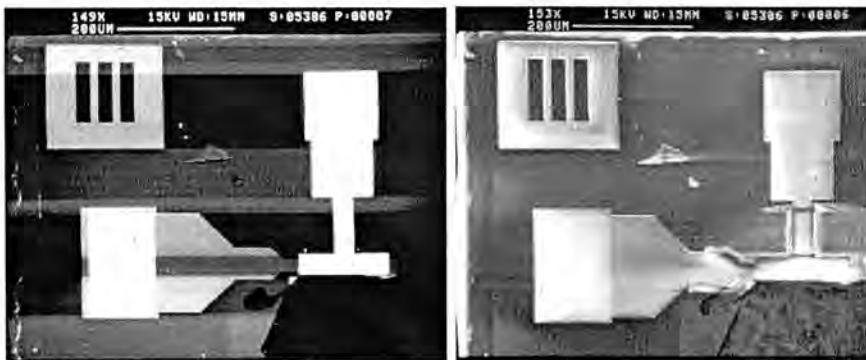


Figure 7: SEM images formed with back-scattered electrons (left) and secondary electrons (right).

2.1.3 Transmission electron microscopy

In what concerns the transmission electron microscope (TEM), the electrons focussed by a set of condenser lenses collide with the sample, the heterogeneity of which disperses them selectively. Those less dispersed are the ones that one takes advantage to form the image that fundamentally corresponds, therefore, to the structure absence. This image is magnified successively by means of diverse electromagnetic lenses and, finally, it is visualised, projecting it on a fluorescent screen, on an electron sensitive film, or on a CCD detector connected to a TV screen. From a practical point of view it is an apparatus that, of a conveniently prepared sample, allows to obtain images of its fine structure magnified some how many thousands of times or even to the atomic level, with a definition not obtained by any other instrument. Here the beam energies are usually between 40 and 200keV in conventional microscopies and between 200keV and 3MeV in high voltage instruments.

The basic scheme of a transmission electron microscope consists in (see figure 8) the illumination system, the objective lens/stage, and the imaging system. The illumination system comprises the gun and the condenser lenses (generally two) and its role is to take the electrons from the source and transfer them to the specimen. The illumination system can be operated in two principal modes: parallel beam for TEM imaging and diffraction, and convergent beam used for scanning (STEM) imaging, microanalysis, and micro or nanodiffraction. The objective lens/stage is the heart of the TEM. This is where all the beam-specimen interactions take place and where the bright-field, dark-field and selected area diffraction patterns that are the fundamental TEM operations are created. The quality of the image formed by the objective lens controls the resolution of the image that is afterwards viewed and recorded. The reason for this stage to be the most important is not only because the objective lens forms the image, but rather because the specimen must be placed so close to the centre of this short-focal-length lens, that it is impossible to make a perfect lens. The specimen is inserted through a specimen holder that can be of a great variety of types, depending on the capability of the microscope and the experiment to be done. Thus, these holders can be divided in side-entry and top-entry holders, being the former the most standard and which allows more configurations, as temperature holders, one or two axes tilting holders, straining holders, etc. Finally, the imaging system uses several lenses to magnify the image or the diffraction pattern produced by the objective lens and to focus these on the viewing screen. These lenses are referred as intermediate and diffraction lenses and the final lens as the projector lens.

When the electron microscope is properly operated, TEM is the only microscopical technique that combines the high resolution and high contrast required for the investigation of sub-micron structures, with the possibility of imaging defects inside the material. Additionally, in the last years, improved

specimen preparation techniques have been developed, which allow to obtain the

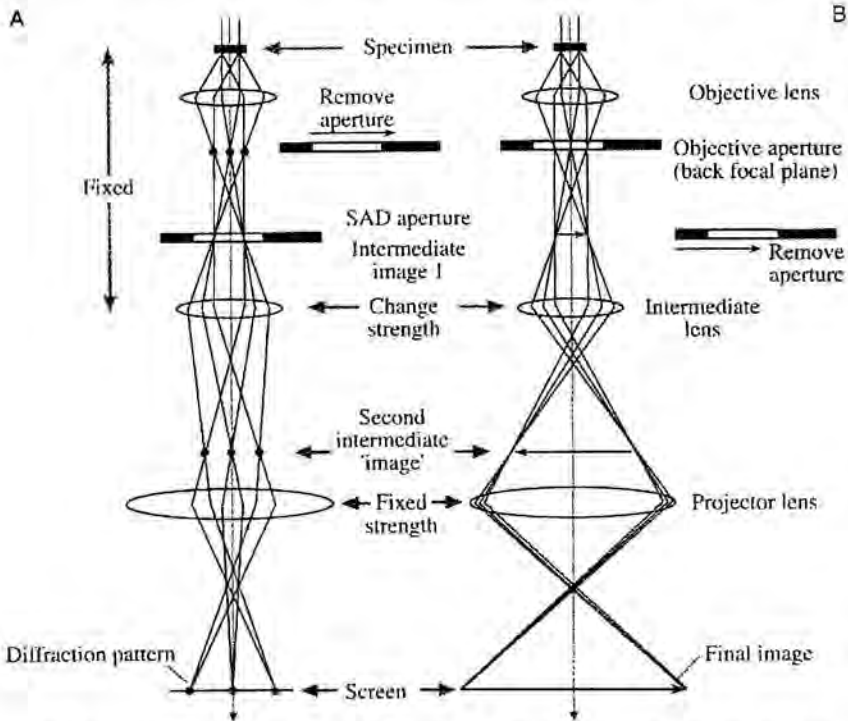


Figure 8: Schematic picture of a TEM. A) Diffraction mode. B) Imaging mode. After Reading [3].

required TEM information within a day. As it is a destructive diagnosis technique (it requires the preparation of thin films transparent for the accelerated electron beam less than $2\mu\text{m}$) it is used after full characterisation by other electrical or structural techniques.

The information that the transmission electron microscope offers can be diverse and depends of the mode of operation. In occasions the information extracted using the different modes are complemented when interpreting the structure of the matter. The different forms of frequently operating modes are:

2.1.3.1 Selected Area Diffraction

Electron diffraction can reveal if the specimen is mono-crystalline, poly-crystalline or amorphous, its lattice parameter if it is crystalline, its lattice symmetry properties, orientation of the specimen or of the individual grains with respect to the

beam direction, phases present in the specimen, existence of ordered phases, defects, etc.

Basically *selected area diffraction* (SAD) consists in performing a diffraction pattern of a specified region of the sample. For this the beam can be made smaller or an aperture can be inserted above the specimen, which would only permit electrons that pass through it to hit the specimen. The second option is the usually performed one, where the aperture of selected area is not inserted at the specimen plane, because the specimen is already there, but in a plane conjugated with the specimen, i.e., in one of the image planes. Thus, the SAD aperture is inserted in the object plane of the objective lens, creating a virtual image of the specimen. A scheme of this operation mode is presented in fig. 8.

The diffraction patterns thus obtained are very easy to interpret if we think in the reciprocal space. From an amorphous specimen, where all the distances are nearby equally probable we will obtain a series of broad rings as shown in fig. 9a. From a perfectly oriented mono-crystalline specimen (perpendicular to the beam direction) (fig. 9b), we will obtain a set of spots, which correspond, to those families of planes in the real space oriented in such a manner that the Bragg law is satisfied. As there exist a direct relationship between planes in the real space and atomic positions in the corresponding reciprocal lattice, the spots observed in the SAD pattern can be interpreted also as those (h, k, l) positions resulting from the intersection of the reciprocal lattice with a plane perpendicular to the beam direction with thickness the unit lattice in the reciprocal space. If the specimen is polycrystalline and the individual grains are randomly oriented we will obtain a set of concentric fine rings formed by fine spots (fig 9c), such as if the diffraction pattern of a mono-crystalline specimen was rotated around the beam axis.

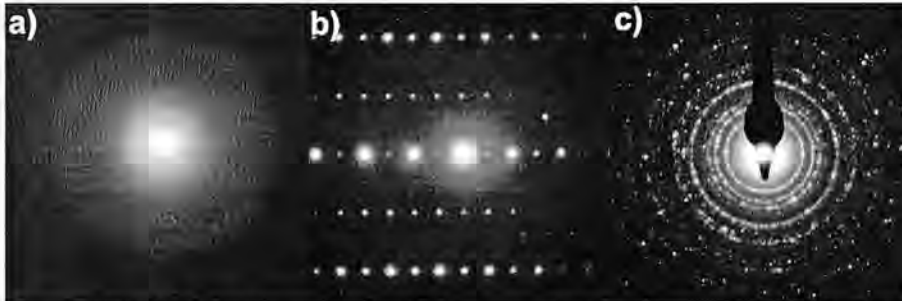


Figure 9: TED of an amorphous specimen in (a), a single-crystal taken near one zone axis in (b), and a polycrystal of small grain size in (c).

2.1.3.2 Bright field and dark-field imaging

When the SAD pattern is projected onto the viewing screen, we can use the pattern to perform the two most basic imaging operations in the TEM.

Independently of the specimen, the SAD pattern will contain a bright central spot, which contains the direct electrons (not scattered) and some scattered electrons. When we form images in TEM, we either form an image using the central spot, or we use some or all of the scattered electrons. The way we choose which electrons form the image is inserting an aperture (objective aperture) into the back focal plane of the objective lens, thus blocking out most of the diffraction pattern except that which is visible through the aperture (figure 8). If the direct beam is selected we call the resultant image a bright field (BF) image, and if we select scattered electrons of any form, we call it a dark-field (DF) image (figure 10). Typical magnifications in

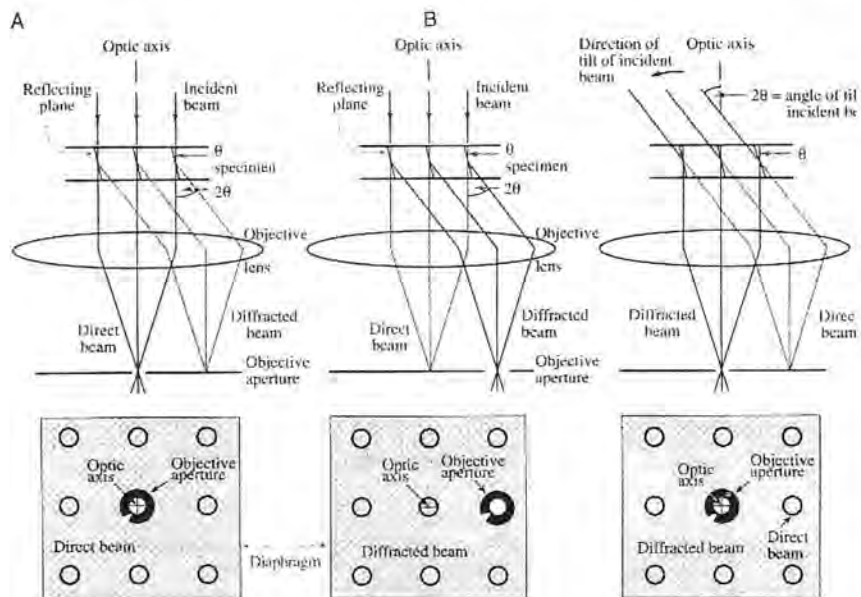


Figure 10: Bright field and dark field imaging. a) Bright field imaging by blocking out all diffracted electrons and selecting the direct beam. b) Dark field imaging by shifting the objective aperture to select diffracted electrons. c) Dark field imaging by tilting the beam to make the diffracted electrons pass through the objective aperture. After Reading [3].

these operation modes range from 25000x to 100000x, which are controlled adjusting the intermediate lenses of the microscope.

With these operation modes one can obtain very diverse information, including strain fields, type of defects, local thickness of the specimen, etc. In the following a simply information indicating how this information is obtained is done:

↻ Defects information ↻

To perform BF and DF images usually one has to adjust in the diffraction pattern the *two-beam* condition, in which only the direct and one of the reflected

beams are excited at once. Under this assumption the understanding of diffraction contrast in TEM is based on the Howie-Whelan equations, which express the variation of the direct and the diffracted beam wave amplitudes (Φ_o and Φ_g , respectively) :

$$\frac{d\Phi_g}{dz} = \frac{\pi i}{\xi_g} \Phi_o e^{-2\pi i s z} + \frac{\pi i}{\xi_o} \Phi_g \quad (9)$$

$$\frac{d\Phi_o}{dz} = \frac{\pi i}{\xi_o} \Phi_o + \frac{\pi i}{\xi_g} \Phi_g e^{-2\pi i s z} \quad (10)$$

These equations indicate that the amplitudes and, therefore, the intensities of the direct and diffracted beams are constantly changing and depend one of each other.

In the case that we have a defect (and also a phase boundary or an interface) the Howie-Whelan equations are modified to include the effects of the distortion produced by the defect as:

$$\frac{d\Phi_g}{dz} = \frac{\pi i}{\xi_g} \Phi_o e^{-2\pi i (s z + \vec{g} \cdot \vec{R})} + \frac{\pi i}{\xi_o} \Phi_g \quad (11)$$

$$\frac{d\Phi_o}{dz} = \frac{\pi i}{\xi_o} \Phi_o + \frac{\pi i}{\xi_g} \Phi_g e^{-2\pi i (s z + \vec{g} \cdot \vec{R})} \quad (12)$$

where \vec{R} is the displacement of the atom at position r (lattice distortion) and \vec{g} the diffracted beam (excited reflection). Therefore, depending on the excited reflection used for two-beam analysis and the type of defect we can have different visibility criteria, which will depend of the $\vec{g} \cdot \vec{R}$ product. Thus, it is this product which is used to completely characterise a defect. The simplest example of characterisation of an edge dislocation is presented in figure 11.

The physical understanding of why we can observe defects is given next when dealing with strain fields information.

⇒ Strain fields information ◀

When an atom is displaced from its position r a distance $\vec{R}(r)$, for example, as a consequence of the existence of a dislocation, the crystal is strained and, therefore, stressed. Thus, it is simple to see that defects produce strain, although they are not the only origin of strain in a crystal (consider for example that strain can be produced by composition inhomogeneities). To analyze how strains are observed in TEM it is typical to analyze the simple case of an edge dislocation. For this consider the scheme in fig. 12. It can be seen that the diffraction conditions have been chosen so that the specimen is slightly tilted away from the Bragg condition. In

this way, the distortion due to the dislocation bends the near-diffracting planes back into the Bragg condition and, so, it is observable.

By using the same idea it is clear how other types of dislocations, planar defects and bending contours are observed in TEM.

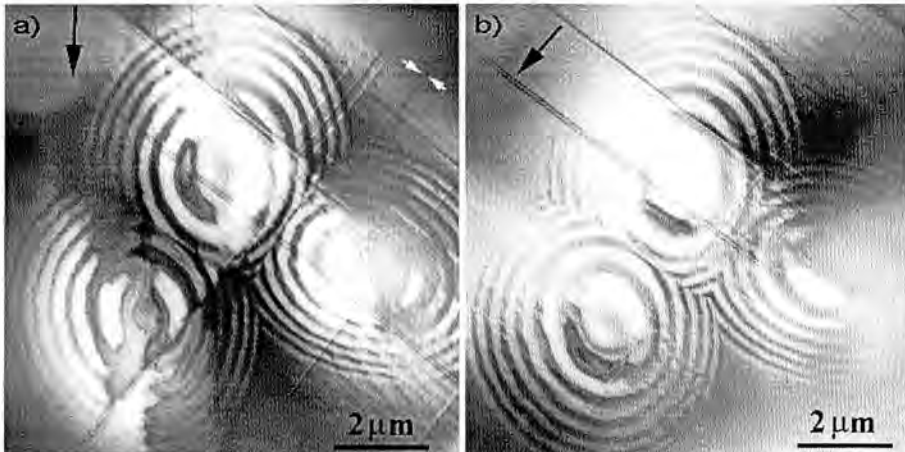


Figure 11: Example of the characterization of an edge (90°) dislocation. Dislocations are visible by using an excitation condition (black arrow) neither perpendicular nor parallel to the dislocation lines in a). In b) the use of excitation conditions parallel to the dislocation lines such as those marked in a) with white arrows, eliminate their contrast. In this case $\mathbf{g}\cdot\mathbf{R}=0$, indicating the edge character of the dislocation because \mathbf{R} is perpendicular to the dislocation line.

↻ Existence of phases, ordered phases and crystalline structures ↻

The structure of the crystal imposes certain selection rules that determine which beams are allowed. In fact these beams are related to the planes in the direct space or the points in the reciprocal space and the important feature is that some of these reciprocal points can be used under two-beam BF or DF imaging to obtain chemical information. When materials with different crystalline structures are observed one has only to select one of the spots associated with the structure desired to be revealed (figure 13). In the same manner, when ordered domains appear, these are associated with additional reflections in the SAD and

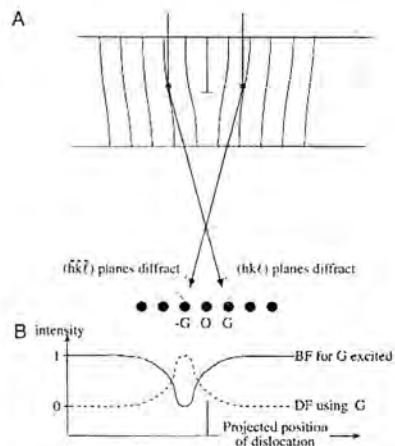


Figure 12: Scheme to understand why strains are observed in TEM. After Reading [3].

they can be used to form the image. The case in which one observes materials different but with the same structure is a little bit more complicated and chemical

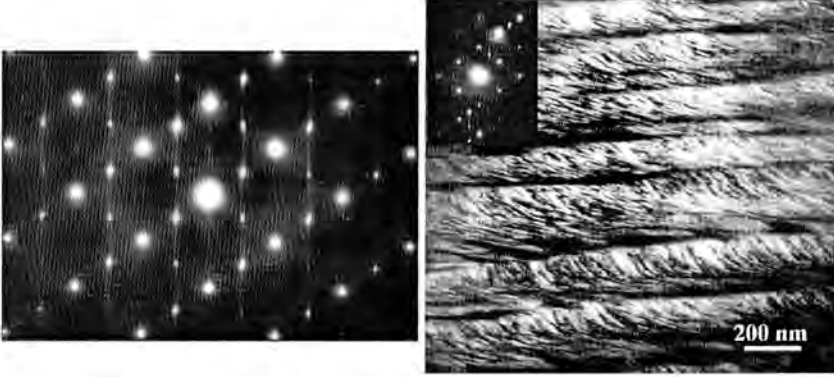


Figure 13: TED pattern (left) and dark field image (right) of a InGaP/GaAs specimen with long range order. Order makes appear additional diffraction spots in the TED pattern. By selecting a two beam condition in which one of these spots is excited (inset) and by using the diffracted beam to form the image, the ordered domains can be clearly observed.

information is obtained through the structure factor. In what continues we will discuss this with an example:

In a general case, the position of the atoms in the real lattice is given by

$$\vec{r}_i = x_i \vec{a} + y_i \vec{b} + z_i \vec{c} \quad (13)$$

and in the reciprocal lattice by

$$\vec{K} = h\vec{a}^* + k\vec{b}^* + l\vec{c}^* \quad (14)$$

So, the structure factor (equivalent of the atomic scattering amplitude for a unit-cell) is given for any crystalline lattice by

$$F_{hkl} = \sum_i f_i e^{2\pi i(hx_i + ky_i + lz_i)} \quad (15)$$

It is the expression of the structure factor for a determined crystalline lattice that will give the information needed to obtain chemical information. In the simple case of the well known ZnS structure, typical, for example, of widely used materials in micro and opto-electronics, as GaAs, the unit cell can be seen as two face centered cubic (fcc) lattices interpenetrated with one of them displaced $[\frac{1}{4}, \frac{1}{4}, \frac{1}{4}]$ of the main diagonal (fcc with a basis vector $[\frac{1}{4}, \frac{1}{4}, \frac{1}{4}]$). For the fcc structure, as the coordinates of the atoms are

$$\vec{r} = (x, y, z) = (0,0,0), (\frac{1}{2}, \frac{1}{2}, 0), (\frac{1}{2}, 0, \frac{1}{2}), (0, \frac{1}{2}, \frac{1}{2}) \quad (16)$$

then, substituting in equation (15),

$$F_{fcc} = f \{1 + e^{\pi i(h+k)} + e^{\pi i(h+l)} + e^{\pi i(k+l)}\} \quad (17)$$

and adding the basis vector $[\frac{1}{4}, \frac{1}{4}, \frac{1}{4}]$, assuming that Ga atoms are in the fcc lattice and As atoms in the displaced lattice, we have for GaAs

$$F = \{f_{Ga} + f_{As} e^{\frac{\pi}{2}i(h+k+l)}\} F_{fcc} \quad (18)$$

Analysing this expression one can see that:

- | | |
|-------------------------------|---|
| • $F = 0$ | If h, k, l are mixed even and odd |
| • $F = 4(f_{Ga} \pm if_{As})$ | If h, k, l are all odd |
| • $F = 4(f_{Ga} - f_{As})$ | If h, k, l are all even and $h + k + l = 2N$ where N is odd (e.g., the 200 reflection) |
| • $F = 4(f_{Ga} + f_{As})$ | If h, k, l are all even and $h + k + l = 2N$ where N is even (e.g., the 400 reflection) |

In the case, for example, of the ternary $Al_xGa_{1-x}As$, the atoms of Al and Ga are distributed randomly according to the value of x in one of the *fcc* sublattices. By using the 200 reflection, $GaAs$ and $Al_xGa_{1-x}As$ can be distinguished because the observed intensity is $I \propto |F|^2 = 16(f_{Ga} - f_{As})^2$ for the former and $16[xf_{Al} + (1-x)f_{Ga} - f_{As}]^2$ for the latter. As a fraction x of the Ga atoms has been replaced with the lighter Al atoms, increasing the difference $f_{III} - f_V$ in $Al_xGa_{1-x}As$, this appears lighter in the TEM. Other conditions such as $g=022$ will also reveal composition inhomogeneities although less clearly (see figure 14).

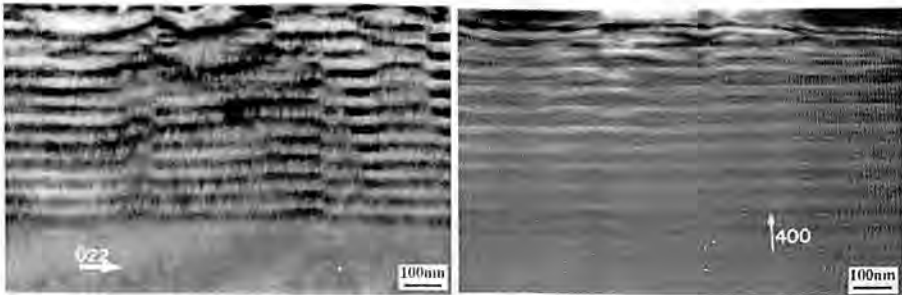


Figure 14: Bright field images of an InGaAs/GaAs multilayer on GaAs. The use of $g=022$ in the left image allows to observe composition inhomogeneities in the film as a consequence of growth. In the right figure the excitation condition $g=400$ reveals clearly the interfaces ($g \cdot R$ product)

In general it has been shown that the brightness of each material is given by the expression of its structure factor and by the orientation to the beam.

⇒ Thickness information ⇐

After solving the Howie-Whelan equation in the particular case of the two-beam assumption it can be deduced that the intensities of the two beams are related, being the intensity for the Bragg diffracted beam g (excited reflection):

$$I_g = |\Phi_g|^2 = \left(\frac{\pi t}{\xi_g} \right)^2 \left(\frac{\sin^2(\pi s_{eff} t)}{(\pi s_{eff} t)^2} \right) = 1 - I_o \quad (19)$$

where s_{eff} is the effective excitation error (separation from the exact g condition):

$$s_{eff} = \sqrt{s^2 + \frac{1}{\xi_g^2}} \quad (20)$$

and ξ_g is known as the the extinction distance (see figure 15a).

The diffracted intensity and thus the intensity of the direct beam, is periodic in the two independent quantities, the distance traveled by the diffracted beam through the specimen t , and effective excitation error s_{eff} . Therefore any difference in thickness in the specimen will produce a change in contrast in the image plane, the image appearing darker or brighter depending on the thickness of the specimen (fig. 15).

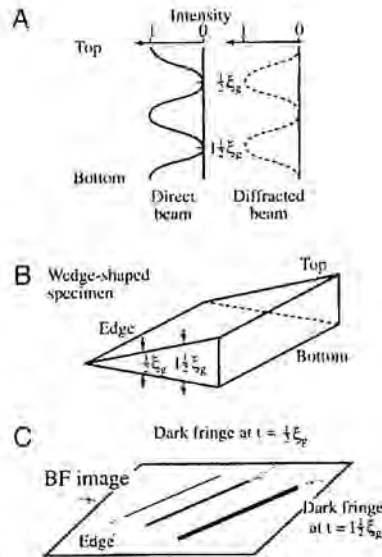


Figure 15: a) Definition of the extinction distance, ξ_g . b) Scheme of a wedge shaped specimen to show the effects of varying thickness. c) Equivalent image on a TEM under bright field imaging. After reading [3].

2.1.3.3 Mass-thickness contrast

Mass-thickness contrast is most important when observing non-crystalline materials and, in some cases, is the only observable contrast. The mechanism by which differences in mass and thickness cause contrast is shown in fig. 16 and is based on equation 7. Qualitatively, as electrons go through the specimen, they are incoherently scattered off axis by elastic nuclear interactions, i.e., Rutherford scattering. As was commented previously, the cross section for Rutherford scatter is a strong function of the atomic number Z , i.e., the mass or the density, ρ . Moreover, as the thickness of the specimen, t , increases, there will be more elastic scattering because the mean-free path remains fixed. So, one can expect high- Z regions of a specimen to scatter more electrons than low- Z regions of the same thickness. Similarly, thicker regions will scatter more electrons than thinner regions of the same average Z . So, for the case of a BF image, thicker and/or higher-mass areas will appear darker than thinner and/or lower-mass areas, and the reverse occurs for a DF image.

The TEM variables that affect the mass-thickness contrast for a given specimen are the objective aperture size and the kV used in the microscope. Using

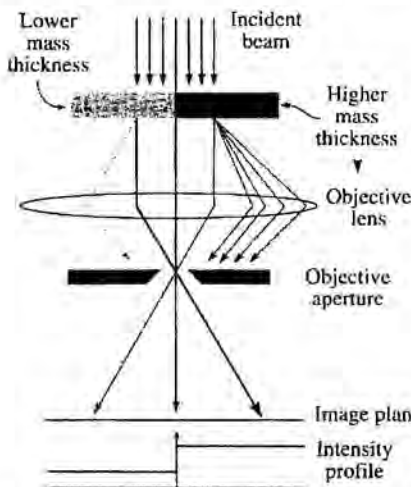


Figure 16: Mass-thickness contrast under BF imaging. After reading [3].

larger apertures more scattered electrons are allowed to contribute to the BF image. So, the contrast between scattering and non-scattering areas is lowered although the overall image intensity increases. By using lower kV, both the scattering angle and cross section increase. Hence more electrons will be scattered outside a given aperture and contrast will increase at the expense of intensity.

It has to be noted, however, that if there are small crystals of different atoms in a given foil thickness, as discussed previously, differences in their structure factor (F) from that of the matrix will cause also contrast changes, since $I \propto |F|^2$.

2.1.3.4 Phase contrast and High-resolution TEM

Contrast in TEM images can arise due to differences in the phase of the electron waves scattered through the specimen. However, phase contrast imaging is often thought to be synonymous with high-resolution TEM (HREM) because, in

general, the more beams collected to form the image, the higher resolution of the image. It is worth to note that this imaging technique constitutes the second major mode of image formation in a TEM.

HREM image formation requires that the specimen be symmetrically oriented, i.e., that in the diffraction diagram reflected beams opposite one to another have the same intensity. To form the image an objective aperture large enough to include the central beam and a number of diffracted beams is inserted and the image is formed by their interference. As a consequence, the image will appear to be strongly dependent on the lens aberrations and the defocus settings.

To understand detailedly how an image is formed in HREM one can follow the travel of electrons through the microscope:

① *The electron wave coming from the source interacts with the object.* The wavefunction of the incident electrons is multiplied with a phase factor

$$e^{i\sigma V(\vec{r})} \quad (21)$$

where $V(\vec{r})$ is the projected electrostatic potential of the object through its overall thickness, \vec{r} is a two-dimensional vector perpendicular to the incident beam and σ is a interaction constant. Taking into account the absorption by including a function $\mu(\vec{r})$, the specimen transfer function can be written as

$$f(\vec{r}) = f(x, y) = e^{-i\sigma V(x, y) - \mu(x, y)} \quad (22)$$

where, for very thin specimens (where $\mu(\vec{r})$ is negligible and $V(x, y) \ll I$),

$$f(x, y) = e^{-i\sigma V(x, y)} \approx 1 - i\sigma V(x, y) \quad (23)$$

being the specimen represented as a pure phase object (Weak-phase-object approximation or WPOA).

② *Transfer in the electron microscope.*

What the microscope does is to transform each point on the specimen $f(x, y)$ into an extended region in the final image $g(x, y)$. As each point in the image has contributions from many points in the specimen (several points in the object produce overlapping images in the image plane after being imaged by the optical system),

$$g(\vec{r}) = \int f(\vec{r}') h(\vec{r} - \vec{r}') d\vec{r}' = f(\vec{r}) \otimes h(\vec{r} - \vec{r}') \quad (24)$$

which in the more convenient representation in the reciprocal space results

$$G(\vec{u}) = H(\vec{u})F(\vec{u}) \quad (25)$$

Here $h(\vec{r})$ is known as the point-spread function and is a weighting term describing how much each point in the specimen contributes to each point in the image, i.e.,

how a point spreads into a disk. Since $h(\mathbf{r})$ tells how information in real space is transferred from the specimen to the image, $H(\mathbf{u})$ tells how information (or contrast) in the reciprocal space is transferred to the image. $H(\mathbf{u})$ is known as the contrast transfer function (CTF) and is in this function where all the microscope settings and characteristics are included. The factors contributing to $H(\mathbf{u})$ include the apertures $A(\mathbf{u})$, the aberrations of the lens $B(\mathbf{u})$, and the attenuation of the wave $E(\mathbf{u})$,

$$H(\vec{u}) = A(\vec{u})E(\vec{u})B(\vec{u}) \quad (26)$$

As $E(\mathbf{u})$ includes the effects of incoherence, it will be treated more conveniently in point 3, i.e., we are treating now with a coherent beam.

The aperture function $A(\mathbf{u})$ says that the objective diaphragm cuts off all values of \mathbf{u} (spatial frequencies) higher than some selected value governed by the radius of the aperture. It has to be taken into account that high spatial frequencies correspond to small distances and, thus, in HREM we are looking for high spatial frequencies.

$B(\mathbf{u})$ includes the spherical aberration and defocusing conditions of the objective lens, introducing an additional phase shift $\chi(\mathbf{u})$ into every diffracted beam at the back focal plane of the objective lens,

$$B(\vec{u}) = e^{-i\chi(\vec{u})} \quad (27)$$

$$\chi(\vec{u}) = \frac{\lambda}{2\pi} (C_s \lambda^4 u^4 - 2\Delta f \lambda^2 u^2) \quad (28)$$

where Δf is the total value of defocusing errors. In the real space,

$$\begin{aligned} g(x, y) &= [1 - i\sigma V(x, y)] \otimes h(x, y) \\ &= 1 + \sigma V(x, y) \otimes \sin \Phi(x, y) - i\sigma V(x, y) \otimes \cos \Phi(x, y) \end{aligned} \quad (29)$$

where $\Phi(x, y)$ is the phase of $h(x, y)$. The intensity will be given by

$$I = gg^* = |g|^2 \approx 1 + 2\sigma V(x, y) \otimes \sin \Phi(x, y) \quad (30)$$

So, in the WPOA, only the imaginary part of $B(\mathbf{u})$ contributes to the intensity and a new simplified transfer function $T(\mathbf{u})$ easier to interpret results:

$$T(\vec{u}) = A(\vec{u})E(\vec{u})2\sin \chi(\vec{u}) \quad (31)$$

This expression indicates that when $T(\mathbf{u})$ is negative, positive phase contrast results, meaning that atoms would appear dark against a bright background. When $T(\mathbf{u})$ is positive, negative phase contrast results, meaning that atoms would appear bright

against a dark background. When $T(\mathbf{u})=0$, there is no detail image for this value of \mathbf{u} .

The plot of $T(\mathbf{u})$ versus \mathbf{u} (figure 17) illustrates the general behaviour of this function, which has complex dependencies on C_s (the spherical aberration coefficient), λ (the acceleration voltage), Δf (the defocus value), and \mathbf{u} (the spatial frequency). The desired form of $T(\mathbf{u})$ should be a constant value as \mathbf{u} increases and ideally with value -1. However, $T(\mathbf{u})$ is 0 at $\mathbf{u}=0$ (what is not a problem because $\mathbf{u}=0$ corresponds to very large distances in the real space) then becomes negative and $T(\mathbf{u})=0$ another time at a certain value $\mathbf{u}=\mathbf{u}_1$. Beyond this point the sign of $T(\mathbf{u})$ changes and oscillations occur. Thus, \mathbf{u}_1 defines a limit at which the images can be directly interpreted. For $\mathbf{u} > \mathbf{u}_1$, there is not a clear relationship between the object and the image because not all the frequencies are equally transmitted. As has been shown, the position of this limit and the shape of the transfer function are determined by the microscope characteristics and settings (defocus).

As it is evident, nothing can be done with the microscope characteristics in order to obtain the ideal transfer function. However, one can optimise the defocus conditions by searching the flattest transfer function in a wide range, i.e., $d\chi/d\mathbf{u}=0$. By resolving this derivative one arrives to

$$\Delta f_{sch} = -\sqrt{\frac{4}{3}} C_s \lambda \quad (32)$$

which is known as the *Scherzer defocus* for which the transference is between the -70 and -100%. The point \mathbf{u} at which the transfer function crosses the axis is

$$u_{sch} = 1.51 C_s^{\frac{1}{4}} \lambda^{-\frac{3}{4}} \quad (33)$$

and the resolution at the Scherzer defocus:

$$r_{sch} = \frac{1}{u_{sch}} = 0.66 C_s^{\frac{1}{4}} \lambda^{\frac{3}{4}} \quad (34)$$

These are important parameters that a microscopist must know about the microscope he is using.

③ *Effects of the illumination system: spread of focus and beam convergence.*

The above presented transfer function suffers some damping produced by the spread of focus and the beam convergence. Other effects due to the vibration of the specimen or its drift can also be introduced as enveloping damping functions in the transfer function.

The spread of focus is related to the temporal incoherence of the beam, while the beam convergence, with the spatial incoherence. Both effects are included in the $E(\mathbf{u})$ enveloping function.

Fluctuations of the focus due to voltage and lens current fluctuation cause chromatic aberration, which produces a damping factor (envelope function) for the transfer function given by

$$E_c(u) = e^{-\frac{1}{2}(\pi\lambda\delta)^2 u^4} \quad (35)$$

where the defocus spread δ is related to the instabilities in the high-voltage supply (and so in the thermal energy spread ΔE of the incident electron beam) and the objective-lens current:

$$\delta = C_c \left[\frac{(\Delta V)^2 + (\Delta E)^2}{V^2} + 4 \left(\frac{\Delta I}{I} \right)^2 \right]^{1/2} \quad (36)$$

with C_c the chromatic aberration coefficient.

The effect of the beam convergence results also in an envelope function for the transfer function. If one imagines that the source has a Gaussian distribution, the enveloping function is given by

$$E_s(u) = e^{-\left[\left(\frac{\pi\alpha}{\lambda} \right)^2 \left(\frac{\partial \chi(u)}{\partial u} \right)^2 \right]} = e^{-\left[\left(\frac{\pi\alpha}{\lambda} \right)^2 (C_s \lambda^3 u^3 + \Delta f \lambda u)^2 \right]} \quad (37)$$

where α is the semiangle characterising the Gaussian distribution.

Both enveloping functions and the others not considered here contribute decreasing the information limit (when the transference is below the 10%) and, thus, the ultimate instrumental resolution of the microscope.

⇒ Interpretation of HREM images ◁

Usually it is difficult to interpret the obtained image in a straightforward way. This is mainly due to:

- ① Only a planar projection of the atomic columns is obtained in the image
- ② The information retrieval can not be obtained directly for certain defocus conditions

For this reason image calculation and matching has to be carried out when quantitative analysis is required. Simulating images becomes a problem of computing the electron wavefields at the three microscope planes. Currently, the best way to produce simulated images is to divide the overall calculation into three parts:

- 1) Model the specimen structure to find its potential in the direction of the incident beam. For this the multislice method is commonly applied. With this approach the specimen is sectioned into many slices, which are normal to the incident beam.

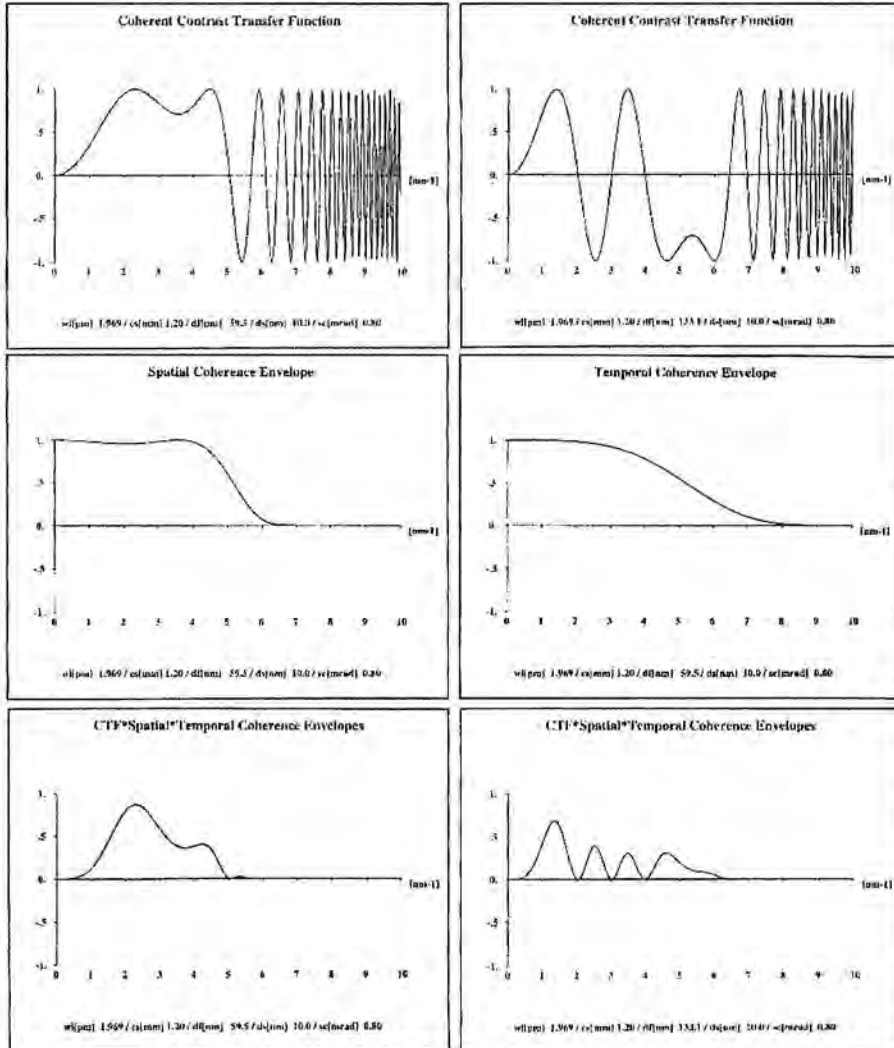


Figure 17: Transfer function for two defocussing conditions (up left: 1st maximum or Scherzer; up right: 4th maximum). In the middle Spatial coherence envelope (left) and Temporal coherence envelope (right). In the lower part they are presented the intensity (square of the Total transfer function) for the 1st (left) and 4th (right) maximum.

2) Produce the exit-surface wavefield by considering the interaction of the incident electron wave on the specimen potential. Although some different methods exist to make this calculation, basically all are based in projecting each slice onto a plane in the slice, obtaining a projected potential and then calculate the amplitudes

and the phases of the beams generated when the incident beam interacts with the projection plane. Then the beams are propagated down the microscope in free space until the next plane of projection is encountered and the calculation is performed again.

3) Compute the image-plane wavefield by imposing the effects of the objective lens on the specimen exit surface wave.

2.1.4 Electron dispersive x-ray analysis and electron energy loss spectroscopy

As commented earlier, inelastic scattering produces the loss of an appreciable amount of energy, which may be transferred to internal degrees of freedom in the atom or specimen in several ways. This transfer may cause excitation or ionization of the bound electrons, excitation of free electrons or lattice vibrations and possibly heating or radiation damage of the specimen. Measurement of these energy losses can give information of a chemical nature, and the combination of imaging and spectrometry in a TEM or a SEM gives a very powerful tool to material scientists.

In a TEM we have basically two forms of analyse the composition of a specimen:

2.1.4.1 Energy dispersive x-ray spectroscopy (EDS)

The EDS, developed in the late 1960s, was available as an option of many instruments, such as TEMs and even more widespread on other electron beam instruments, such as SEMs, by the mid-1970s. Taking advantage of the fact that when an electron ionises an atom, the emitted characteristic X-ray energy is unique to the ionised atom, the EDS produces spectra, which are plots of X-ray counts versus X-ray energy. Basically the EDS system consists in a detector, the processing electronics and a Multi-channel analyser (MCA) display, all controlled by a computer. The detector generates a charge pulse proportional to the X-ray energy. This pulse is converted to a voltage. Then the signal is amplified, isolated from other pulses, further amplified, and identified electronically as resulting from an X-ray of specific energy. Finally, a digitised signal is stored in a channel assigned to that energy in the MCA.

The most important part of the EDS, the detector, is a reverse-biased p-i-n diode cooled to the N₂ liquid temperature. Usually Si(Li) semiconductor detectors or the more efficient for high energy X-rays and robust intrinsic Ge (IG) detectors are used. When the X-rays interact with the semiconductor detector, create electron-hole pairs, which are separated by the internal reverse bias of the p-n junction. In order to avoid contamination to enter in the microscope different windows can be used. Be windows lead to detect elements below Na ($Z=11$), impeding the analysis of elements such as B, C, N, and O, which are very important in materials science. For this, ultrathin window detectors with windows made of polymer, diamond, boron nitride or silicon nitride are also used. These windows are able to transmit lighter elements, as B. Unfortunately they need its own vacuum system.

Although quantitative information can be obtained, usually one analyses qualitatively the spectra. To basically understand a EDS spectrum the only one has to know is that the difference in the two shell energies equals the energy of the

characteristic X-ray, know the nomenclature used, and be helped of a chart of characteristics X-rays. Thus if we fill a K-shell hole from the L shell we get a K_{α} X-ray, but if we fill it from the M shell we get a K_{β} X-ray. If the hole is in the L shell and we fill it from the M shell we get an L_{α} X-ray, and if we fill it from the N shell we get an L_{β} X-ray. The notation is in fact more complex because we differentiate the α X-rays in terms of α_1 and α_2 , depending from which sub-shell of the outer shell the electron falls to fill the hole. The α_1 X-ray is from the outermost sub-shell, the α_2 from the next innermost. However, for X-ray detection in electron microscopy we can not usually discriminate between the X-rays from different sub-shells, except at the highest X-ray energies. So, K, L, and M and α and β are about all it is needed to remember.

A typical EDS spectrum is shown in figure 18.

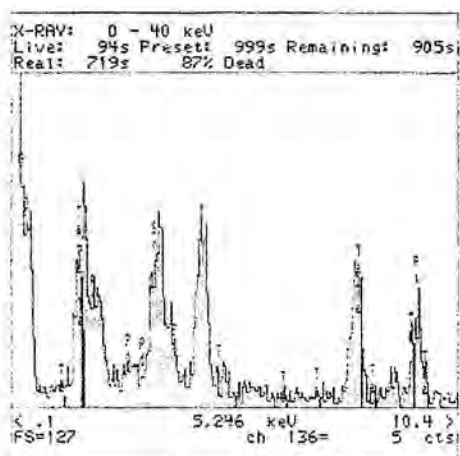


Figure 18: EDS spectrum of an specimen containing Sn, Pt, and Ti. Typical parameters like the acquisition time, dead time, etc, are visible on top.

2.1.4.2 Electron energy-loss spectroscopy (EELS)

Electron energy-loss spectroscopy is the analysis of the energy distribution of electrons that have interacted inelastically with the specimen and passed through it. In order to examine the spectrum of electron energies a magnetic prism spectrometer is generally used, which is a simple device but very sensitive, being able to resolve 0.6eV even for high energies of the incident beam. The magnetic prism (a spectrometer and a lens magnetically isolated) disperses electrons according with their energy. Afterwards, these are acquired and processed. For this two possibilities exist: In serial collection (SEELS), the spectrometer system uses a

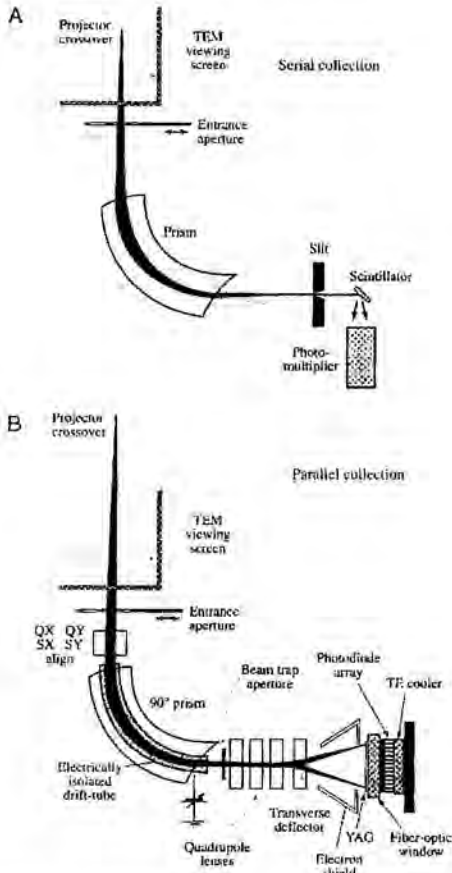


Figure 19: Scheme of a SEELS and a PEELS apparatus. After reading [3].

set of coils to scan the spectrum across a slit in the dispersion plane. Behind the slit there is a photomultiplier and a YAG scintillator. By means of SEELS one channel is detected at a time, the detector is easy to optimize and simple to operate. In parallel collection (PEELS), the electrons are collected in a YAG scintillator coupled via fiber optics to a semiconductor photodiode array located in the dispersion plane of the spectrometer. PEELS detects the whole spectrum at one time, but the diode array is hard to optimize, exhibits more artifacts and has more complex electron optics. An scheme of both modes of operation (apparatus) is presented in figure 19.

Contrarily to EDS, EELS leads to detect light elements and a lot of additional information than merely elemental information. This includes the electronic structure of the specimen atoms, which, in turns, reveals details of the nature of these atoms, their bonding and nearest-neighbour

distributions, and their dielectric response.

The EELS spectrum can be described in a general way by three regions:

① The zero-loss peak, which consists primarily of elastic forward-scattered electrons, but also contains electrons that have suffered minor (unresolvable) energy losses. This peak defines the energy resolution (at best $\sim 0.3\text{eV}$) and is essential for the calibration of the spectrum. This peak is so intense that can damage the scintillator and is not used to extract useful data.

② The low-loss regions up to an energy loss of $\sim 50\text{eV}$, that contains electrons which have interacted with the weakly bound outer-shell electrons of the atoms in the specimen, thus containing information about the electronic properties

of the specimen. The electrons collected in this region of the spectrum have set up plasmon oscillations or generated inter- or intra-band transitions. The use of low-loss spectrum for phase identification is only possible through a 'fingerprinting' process by which the low-loss spectra of known specimens are stored for later comparison with the real one.

③ Electrons in the high-loss regions that have interacted with the more tightly bound inner-shell or core electrons. Therefore they contain information characteristic of the atoms in the specimen. Just like in X-rays, where the K, L, M, etc peaks are describe in the spectrum, in EELS one obtains ionization edges from K, L, M, etc, shell electrons. However, the greater energy resolution of the EELS spectrometer means that it is much easier to detect differences in spectra that arise from the presence of different states in the shell. Thus one can differentiate edges due to the ejection of an electron from a determined orbital in a shell. Moreover, the edge details (shape) can give more information than a characteristic X-ray.

Figure 20 shows a typical EELS spectrum.

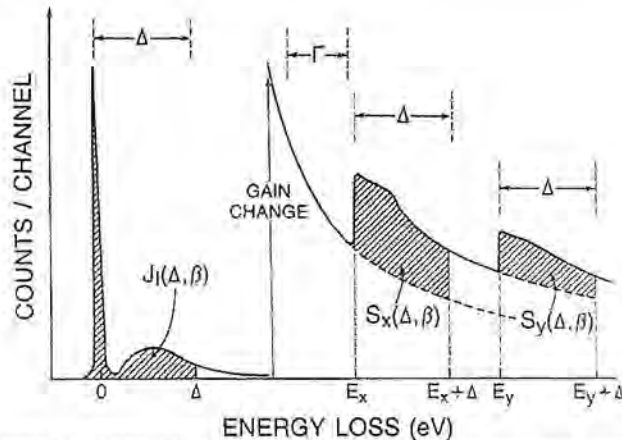


Figure 20: Typical EELS spectrum showing the zero loss peak very intense at left, and the low and high-loss regions. As the scan is done in an interval Δ of energies, and the spectrum is very intense near the zero, a gain change has to be done in the areas of interest. The areas marked in dark as S_x , and S_y , reveal information of the material. However, note that the background has to be corrected.

2.2 X-ray diffraction

One of the phenomena of interaction of X-rays with crystalline matter is its diffraction, produced by the reticular planes that form the atoms of the crystal. A crystal diffracts an X-ray beam passing through it to produce beams at specific angles depending on the X-ray wavelength, the crystal orientation, and the structure of the crystal.

In the macroscopic version of X-ray diffraction, a certain wavelength of radiation will constructively interfere when partially reflected between surfaces (i.e., the atomic planes) that produce a path difference equal to an integral number of wavelengths. This condition is described by the Bragg law (figure 21):

$$2d \sin \theta = n\lambda \quad (38)$$

where n is an integer, λ is the wavelength of the radiation, d is the spacing between surfaces, and θ is the angle between the radiation and the surfaces. This relation demonstrates that interference effects are observable only when radiation interacts with physical dimensions that are approximately the same size as the wavelength of the radiation.

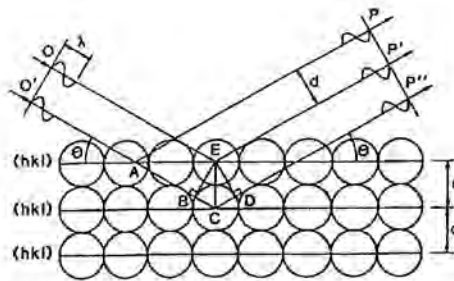


Figure 21: Bragg law.

Since the distances between atoms or ions is on the order of 10^{-10} m (1\AA), diffraction methods require radiation in the X-ray region of the electromagnetic spectrum, or beams of electrons (as has been discussed in the section dedicated to electron microscopy) or neutrons with similar wavelength.

So, through X-ray spectra one can identify and analyse any crystalline matter. The degree of crystallinity or order will conditionate the quality of the obtained result. In order to do this, a diffractometer is needed.

Basically an X-ray diffractometer consists in an X-ray generator, a goniometer and sample holder, and an X-ray detector, such as photographic film or a movable proportional counter. The most usually employed instrument to generate X-rays are X-ray tubes, which generate X-rays by bombarding a metal target with high-energy (10-100keV) electrons that knock out core electrons. The procedure is the same as described in 2.1.1.2. An electron in an outer shell fills the hole in the inner shell and emits an X-ray photon. Two common targets are Mo and Cu, which have strong K_{α} X-ray emission at 0.71073 and 1.5418\AA , respectively. Apart from the main line, others accompanying lines appear, which have to be eliminated in

order to facilitate the interpretation of the spectra. These are suppressed partially by using crystal monochromators.

2.2.1 Methods for acquiring an X-ray powder diffraction pattern

The most interesting X-ray diffraction techniques for this work are those related to the analysis of polycrystalline materials and mainly of powders. In this case the powder provides all the possible orientations of the small crystals giving rise to a large number of diffraction cones, each one corresponding to a family of planes satisfying the Bragg's law. For large grains, rings are discontinuous and formed by small spots. As the size of the grains diminishes, the spots are closer and for an optimum size a continuous ring is obtained, which is transferred into a peak when working with graphic registers or lines in a photographic register. For lower grain sizes the clarity of rings is lost again and wide peaks or bands appear. When the crystals are not randomly but preferentially oriented, the intensity of the different rings and along each ring is not uniform. It is clear the similitude with electron diffraction.

Experimental acquisition of powder patterns can be done by using powder cameras or powder diffractometers. The simplest instrument is a *powder camera* and

many factors can contribute to the decision to select a camera technique rather than a powder diffractometer. These include the lack of adequate sample quantity, the desire of maximum resolution and the lower initial cost. Of the various camera types the Debye-Scherrer camera is the most usually used, probably because is the simplest and easiest to use. The component parts of a typical Debye-Scherrer camera include a light-tight camera body and cover, which hold the sample mount and film, a main beam stop, and an incident beam collimator (fig. 22). A mount is provided, which permits the

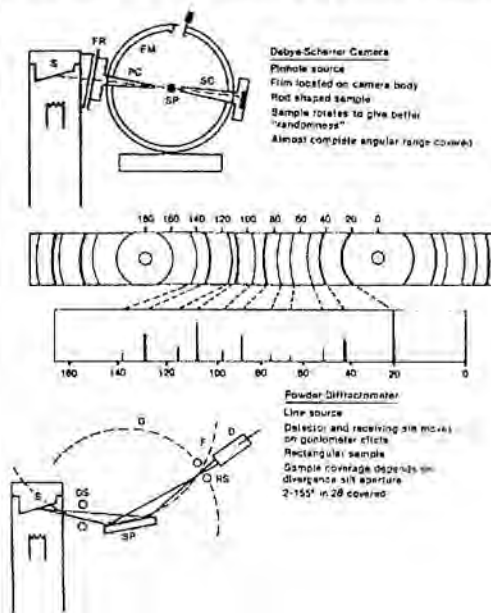


Figure 22: Debye-Scherrer camera. After reading [23].

camera body to rest on a track for stability during exposure. A filter is selected to remove most of the unwanted K_{β} component from the incident beam while passing unchanged most of the K_{α} . During operation, the incident-beam collimator selects a narrow pencil of X-rays that passes through the sample in the camera centre before striking the beam stop on the opposite end of the camera. The collimator normally selects a beam about 0.5mm diameter, and the camera is generally mounted on the point or spot focus of the X-ray tube to obtain the maximum beam intensity at the sample. The sample itself can be packed in a glass capillary or, if very small, mounted on the tip of a glass rod or other rigid material using rubber cement or other permanent adhesive. The sample is placed at the camera centre and aligned to the main beam. The intensities of the diffracted beams are proportional to the crystalline sample volume irradiated by the beam. Thus exposure times have to be increased as the sample size decreases. In the Debye-Scherrer powder camera the whole diffraction pattern is recorded simultaneously. Two factors which contribute to the low resolution of the Debye-Scherrer camera types are first, the incident-beam divergence due to a collimator which is typically designed to yield the narrowest beam with usable intensity, and second, the size of the capillary. Debye-Scherrer data are generally of significantly poorer quality than diffractometer data, mainly because the shapes of the lines (or peaks) are affected by both the absorption of the specimen and the physical size of the specimen.

In general, the major problems involved with the use of powder cameras are relatively long exposure times, the need to work with dark room facilities, and difficulties in obtaining statistically precise count data.

In *powder diffractometers* a photon detector replaces the photographic film (or some annular detector) used in cameras. Early designs were non-focusing systems that utilised X-ray tube spot foci and required relatively long data collection times and gave rather poor resolution. Actually parafocusing optics geometry is used, employing the majority of commercially available powder diffractometers the Bragg-Brentano parafocusing arrangement. A given instrument may provide a horizontal or vertical $\theta/2\theta$ configuration, or a vertical θ/θ configuration (figure 23). The basic arrangement is shown in figure 24. A divergent beam of radiation coming from the line of focus L of the X-ray tube passes through the parallel plate collimators (Soller slits) G and a divergence slit assembly B and irradiates the flat surface of a specimen C . All the rays diffracted by suitably oriented crystallites in the specimen at an angle 2θ converge to a line at the receiving slit D . Either behind or before the receiving slit may be placed a second set of parallel plate collimators E and a scatter slit F . A diffracted-beam monochromator may be placed behind the receiving slit at the position of the scatter slit. The axes of the line focus and of the receiving slit are at equal distances from the axis of the goniometer. The X-rays are detected by a radiation detector T , usually a scintillation counter or a sealed gas proportional counter. The receiving slit assembly and the detector are coupled together and move around the circle H about axis P in order to scan a range of 2θ

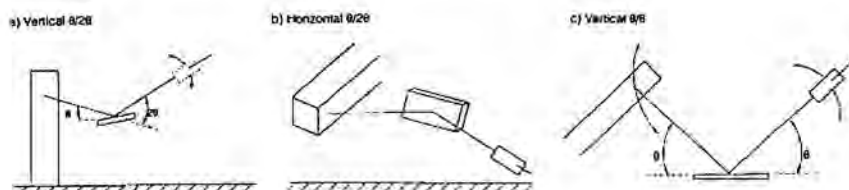


Figure 23: Configurations in a Bragg-Brentano powder diffractometer. After reading [23].

(Bragg) angles. For $\theta/2\theta$ scans, the goniometer rotates the specimen about the same axis as the detector but at half the rotational speed. The surface of the specimen thus remains tangential to the focusing circle K . In addition to being a device that accurately sets the angles θ and 2θ , the goniometer also acts as a support for all of the various slits and other

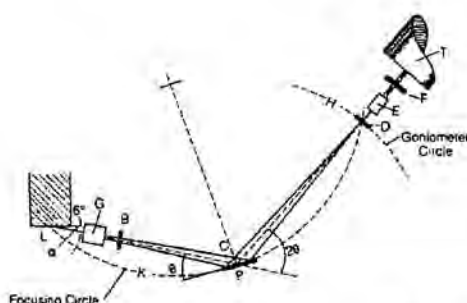


Figure 24: Bragg-Brentano parafocusing geometry. After reading [23].

components which make up the diffractometer. The purpose of parallel-plate collimators is to limit the axial divergence of the beam and hence partially control the shape of the diffracted line profile. It follows that the center of the specimen surface must be on the axis of the goniometer and this axis must be also parallel to the axis of the line focus, divergence slit, and receiving slit.

2.2.2 Analysis of the spectrum

Perhaps the most routine use of diffraction data is for phase identification. Each crystalline powder gives a unique diffraction diagram, which is the basis for a qualitative analysis by X-ray diffraction. Identification is practically always accompanied by the systematic comparison of the obtained spectrum with a standard one (a pattern), taken from any *X-ray powder data file* catalogues, published by the American Society for Testing and Materials (*JCPDS*).

The diffraction profiles of a mixture of crystalline specimens consist in spectra of each of the individual crystalline substances present, superposed. Nowadays, the superposition of lines does not impossibilitates the identification. When one wants to identify the obtained diffraction profile, the values of interplanar distances d corresponding to the major intensities are extracted and compared with the interplanar spacings of the different possible patterns of the *X-ray powder data*

file index, looking also for a match in the intensities magnitudes. To facilitate the search the index is divided usually in organic and inorganic substances and a restricted search for the existence of determined elements of the periodic table can be done.

Quantitative analysis of diffraction profiles can be diverse. In general, two main aspects are of interest: the quantitative identification of phases and the measure of grain size in polycrystalline specimens.

2.2.2.1 Quantitative analysis of crystalline phases

The diffraction diagram of a mixture of crystalline substances consists of an overlapping of the different spectra corresponding to each of the substances. Each component contributes to the total diagram with an intensity proportional to the present quantity in the mixture. This principle will be used to discuss how to calculate the quantity of different phases in a mixture, rather than other more complex procedures such as profile fitting or Rietveld analysis of the powder diffraction pattern.

The quantitative analysis by X-ray diffraction consists in the determination of the present quantity from measurements of the diffracted intensities. As intensity is not generally a lineal function of composition, a comparative analysis of the unknown sample with known patterns is needed. One of the most usual methods consists in mixing the sample with a known substance in a fixed ratio, used as reference. For this analysis the most intense lines are used, if they do not overlap with others.

All methods for quantitative analysis are based on the basic equation that relates the X-ray diffracted intensities with the absorption properties of crystalline mixtures of powder:

$$I_{ij} = \frac{K_{ij} X_j}{\rho_j [X_j (\mu_j - \mu_\mu) + \mu_\mu]} \quad (39)$$

where I_{ij} is the intensity of a line i of the compound j ; X_j is the compound j concentration, and ρ_j its density. μ_j and μ_μ are the absorption coefficients of the j component and of the matrix, and K_{ij} is a constant that depends of the characteristics of the instrument, of the wavelength and of the structure of the j component. If this equation is corrected from the background radiation:

$$I_{ij} = \frac{K_{ij} X_j}{\rho_j \mu_\tau} \quad (40)$$

where μ_τ is the total maximum absorption coefficient of the sample, including the j component.

If only one component exists, the above equation can be applied directly and X can be determined directly from the measured intensities I_{ij} , K_{ij} and μ_r being known. Nowadays, if more than one component exists the ratio intensity/concentration is not linear, and the analysis is more tedious. The methods based in absolute measures of intensity to determine directly μ_r have to be performed for systems with two or more components.

Actually, the methods that use an internal standard, are easier and more widely used. For mixtures of several components, the ratio of intensities of two of them will be:

$$\frac{I_{ij}}{I_{kl}} = \frac{K_{ij}\rho_l X_j}{K_{kl}\rho_j X_l} \quad (41)$$

being ρ_l the density of the component l , and X_l the fraction in weight present in the mixture. In this case the component l is used as internal standard for the compound j .

2.2.2.2 Grain size evaluation in polycrystalline samples

The determination of the size of the crystals in a powder can be carried out thanks to measurements that must be made on the profile of the diffraction peaks. One of the functions that best describes the powder diffraction profiles is the Voigt function. This consist in a convolution product of a Lorentzian and Gaussian function and allows to

- (1) Model size (Lorentzian component) and strain (Gaussian component) line-broadening contributions simultaneously
- (2) Separate instrumental and specimen contributions to the diffracted line profile. Instrumental broadening is due to causes such as slit widths, sample size, penetration in the sample, imperfect focusing, etc.

For simplicity, instead of a Voigt function one usually uses a pseudo-Voigt function. This approximates the Lorentzian/Gaussian convolution product by using the simple addition of the two functions using a mixing parameter, η , which varies the function from Lorentzian to Gaussian for $\eta=1$ to $\eta=0$, respectively:

$$I_{i,k} = \frac{2\sqrt{\ln 2}}{H_k} \exp\left(\frac{-4 \ln 2}{H_k^2} (2\theta_i - 2\theta_k)^2\right) \quad \text{Gaussian (G)} \quad (42)$$

$$I_{i,k} = \frac{\sqrt{4}}{\pi H_k} \left(1 + \frac{4(\sqrt{2}-1)}{H_k^2} (2\theta_i - 2\theta_k)^2\right)^{-1} \quad \text{Lorentzian (L)} \quad (43)$$

$$I_{i,k} = \eta L_{i,k} + (1 - \eta) G_{i,k} \quad \text{Pseudo-Voigt} \quad (44)$$

For one peak analysis the procedure consist in evaluate the integral widths β_G and β_L (for Gaussian and Lorantzian contributions) and the shape factor

$$\Phi = \left(\frac{\sqrt{\pi}}{2\sqrt{\ln 2}} + \left[\frac{\pi}{2} - \frac{\sqrt{\pi}}{2\sqrt{\ln 2}} \right] \eta \right)^{-1} \quad (45)$$

Therefore, if the observed profile is $O(x)$, from which one obtains I_o , A_o , $\beta_o = A_o/I_o$, $2\theta_o$, and Φ_o , and the instrumental profile is $I(x)$ from one obtains I_i , A_i , $\beta_i = A_i/I_i$, $2\theta_i$ and Φ_i , for both profiles, β_G and β_L are evaluated using the next empirical formulas:

$$\beta_L / \beta = a_0 + a_1 \Phi + a_2 \Phi^2 \quad (46)$$

$$\beta_G / \beta = b_0 + b_{1/2} \sqrt{\Phi - \frac{2}{\pi}} + b_1 \Phi + b_2 \Phi^2 \quad (47)$$

with $a_0=2.0207$, $a_1=-0.4803$, $a_2=-1.7746$, $b_0=0.6420$, $b_{1/2}=1.4187$, $b_1=-2.2043$, and $b_2=1.8706$.

Thus, for the pure profile (without the instrumental broadening):

$$\beta_{pl} = \beta_{ol} + \beta_{il} \quad (48)$$

$$\beta_{pG}^2 = \beta_{oG}^2 + \beta_{iG}^2 \quad (49)$$

The grain size is given by

$$D = \frac{\lambda}{\beta_{pl} \cos \theta} \quad (50)$$

and the micro-strain by

$$e = \frac{\beta_{pG}}{4 \tan \theta} \quad (51)$$

In practice, however, if one can neglect the micro-strain effects, which in addition sometimes give rise to mistakes and incongruencies in the evaluation of grain size, the above formulation reduces to the well-known Scherrer formula (eq. 52). Scherrer showed that the average dimension of the crystals that compose a crystalline powder is related with the profile of the peak by means of the equation:

$$D = \frac{K\lambda}{\beta \cos \theta} \quad (52)$$

where K is a proporcionality constant approximately similar to the unit, β the FWHM of the peak in radians (theoretically corrected from the instrumental

broadening), D the size of the crystal in the direction perpendicular to the reflecting planes and λ the wavelength of the X-rays used. This is the most usual and simple equation that allows to evaluate grain size.

2.3 X-ray photoelectron spectroscopy

X-ray photoelectron spectroscopy (XPS), sometimes also called Electron spectroscopy for chemical analysis (ESCA), is the quantitative surface analysis technique most sensitive to the chemical composition. By means of XPS, one can obtain information on the chemical structure, being possible the quantification for most of materials. However, some damage is induced on the sample.

Surface analysis by XPS involves irradiating a solid in vacuum with monoenergetic soft X-rays (Mg K_{α} at 1253.6 eV or Al K_{α} at 1486.6 eV are usually used) and analyzing the energy of the emitted electrons. It is obvious that only those electrons arriving to the detector without having interacted inelastically give useful information, contributing to the spectral peaks. Because the mean free path of electrons in solids is very small, the detected electrons originate from only the top few atomic layers (1-5nm), making XPS a unique surface-sensitive technique for chemical analysis. The spectrum is obtained as a plot of the number of detected electrons per energy interval versus their kinetic energy, which is given by the known photon energy ($h\nu$) minus the characteristic binding energy of the atomic orbital from which the electron originates (ψ), corrected by the spectrometer work function (ϕ_s):

$$K = h\nu - \psi - \phi_s \quad (53)$$

The binding energy may be regarded as the energy difference between the initial and final states after the photoelectron has left the atom. Variations in the elemental binding energies (chemical shifts) arise from differences in the chemical potential and polarizability of compounds. These chemical shifts can be used to identify the chemical state of the materials being analysed, because each element has a unique set of binding energies. Thus, XPS can be used to identify and determine the concentration of the elements in the surface, being possible to obtain quantitative data from peak heights or peak areas, and identification of chemical states from exact measurement of peak positions and separations. The spectrum from a mixture of elements is approximately the sum of the peaks of the individual constituents.

2.3.1 The XPS spectrometer

A typical XPS instrument (see scheme in figure 25), consist of:

① Three sample irradiation subsystems: The X-ray subsystem, which irradiates the sample surface and excites photoelectrons characteristics for the chemical structure of the surface; the ion gun subsystem for bombarding the surface of the sample and; the charge neutralizer subsystem or low energy electron beam used to neutralize the surface charge of insulators.

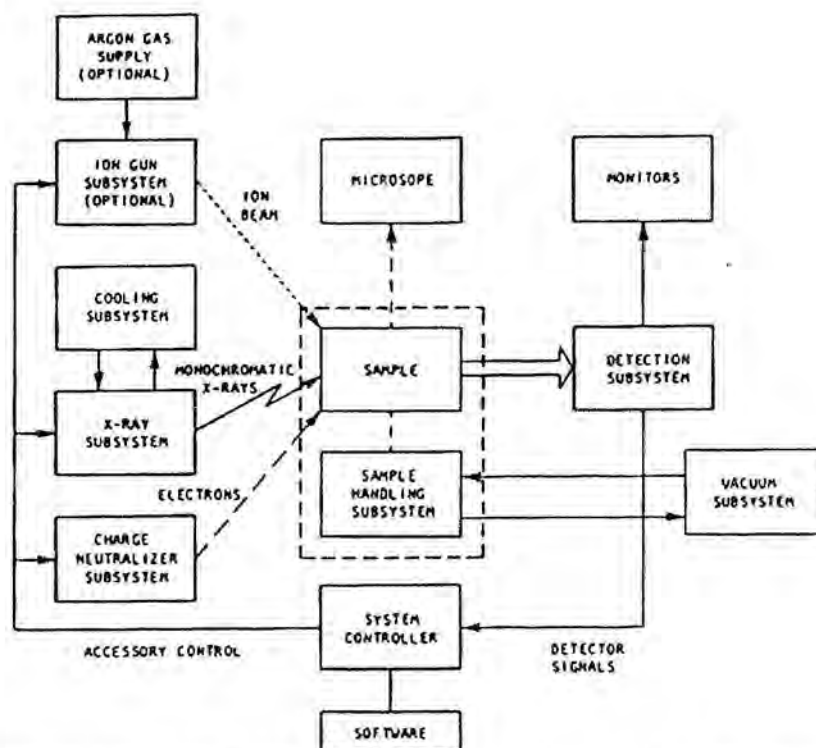


Figure 25: Scheme of the components of a XPS equipment. After reading [33].

② A detection subsystem (lenses, analyser and detector) in which an electron lens captures the released electrons, which are retarded to an average energy (pass energy) and re-focused on the entrance slit of a hemispherical analyser. This analyser spatially disperses electrons of different energies and images them on the exit slit. This dispersion is then imaged by a position sensitive detector. By selecting an appropriate pass energy for the analyser, spectral regions of different eV are dispersed on the detector. As larger pass energies are used, a higher spectrometer sensitivity is obtained at the expense of energy resolution. The detector images the exit plane of the analyser, producing an output signal for each electron detected, i.e., a digitised signal that represents the position of each single event along the energy dimension of the detector. The digitised signal is fed to a buffer in the detector electronics unit.

③ A system controller that periodically transfers the data from the buffer to the computer memory. This computer then processes the data in accordance with the used software.

④ A preparation chamber assembly (high vacuum) equipped with a gate valve that isolates it from the analyser chamber so that the preparation chamber can

be opened to the atmosphere. A transfer control located immediately below the chamber is used to transfer the sample from the preparation chamber to the analyzer chamber.

⑤ An analyser chamber assembly (ultra high vacuum) which includes the irradiation sources, a manipulator to position the sample and, a microscope.

2.3.2 The XPS spectrum

Generally in an XPS primary spectrum peaks appear due to photoemission from core levels, from valence levels, and peaks due to Auger emission.

The XPS core level spectrum is a direct picture of the electron structure of the atoms present in the analysed sample and, hence, the most important peaks of the spectrum. Except for the *s* levels, each peak corresponding to a certain electronic level presents a doublet structure, which arises through the LS spin-orbit coupling. The magnitude of the doublet energy separation is proportional to the expectation value $\langle 1/r^3 \rangle$ for a particular orbital. Therefore, this energy separation is expected to increase as the atomic number *Z* increases for constant *n* and *l* quantum numbers. On the other hand, the relative intensities for the doublet peaks are given by the ratio of their corresponding degeneracies ($2j+1$). For the *p*, *d*, and *f* doublets the intensity ratios are 1:2, 2:3, and 3:4, respectively. The intensity of the photoelectron peaks are determined by their sensitive factors. These are equal to the photoelectric cross-section for the source line, modulated by an empirical function, corresponding to the transmission characteristics of the analyser. The photoelectron peak width (ΔE), defined as the full width at half maximum, is the result of the contributions of the natural width of the core level (ΔE_n), the width of the exciting X-ray line (ΔE_p), and the analyser resolution (ΔE_a), assuming for all of them a pure Gaussian shape:

$$\Delta E = (\Delta E_n^2 + \Delta E_p^2 + \Delta E_a^2)^{1/2} \quad (54)$$

The core level notation in XPS arises from the *j-j* coupling vector summation of the orbital angular and spin momenta to produce the total electronic angular momentum. In the *j-j* coupling, the total angular momentum quantum number for a single electron (*j*) is calculated by summing the single electronic spin (*s*) and angular (*l*) momentum quantum numbers. The total angular momentum quantum number for this atom (*J*) is given by the summation over all electrons in the atom ($J = \sum j$). In this way, the *j-j* coupling gives rise to a notation based on the principal quantum number and the electronic quantum numbers *l* and *j* mentioned above. In this nomenclature, the electronic energy level is described first by the principal quantum number with *n*=1, 2, 3, ..., then states with angular momentum *l*=0, 1, 2, ...(*n*-1) (known as *s* (*l*=0), *p* (*l*=1), *d* (*l*=2) and *f* (*l*=3)), and finally the coupled *j* used as suffix (*j*=1/2, 3/2, 5/2, ...).

The low binding energy levels (0-20eV) are referred as valence levels and consist of many closely spaced levels forming a band structure in the XPS spectrum.

These levels arise from bonding orbitals in the solid. The XPS spectrum for this region reflects the initially filled density of states. The main application of the XPS valence band spectra is the study of the electronic structure of materials.

Finally, in addition to photoelectrons emitted in the photoelectric process, Auger electrons may be emitted because of relaxation of the excited ions remaining after photoemission. In the Auger process, an outer electron falls into the inner orbital vacancy, and a second electron is simultaneously emitted, carrying out the excess energy. The Auger electron possesses kinetic energy equal to the difference between the energy of the initial ion and the doubly charged final ion, and is independent of the mode of the initial ionisation. The Auger peaks are always forming series of peaks of group of lines in very complicated patterns. In XPS there are mainly four series, which can be observed. These are the KLL, LMM, MNN and NOO series, identified by the initial and final double vacancies in the Auger transition. For instance, the LMM series correspond to the following transition: formation of an initial hole in the L shell as a consequence of irradiation, filling of the hole by an M-electron and finally emission of an electron from the M shell as well. The latter is the photoelectron contributing to a peak of the series in the XPS spectra.

2.4 Optical spectroscopic techniques

The energy of a molecule or ion consists in four components that for a first approximation can be treated separately: the translational energy, the rotational energy, the vibrational energy, and the electronic energy. When the molecule is placed in an electromagnetic field, a transfer of energy from the field to the molecule will occur only when the difference in energy between two quantified states $\Delta E = E'' - E'$ equals $h\nu$, being h the Planck's constant and ν the frequency of light[†]. Because rotational levels are relatively close to each other, transitions between these levels occur at low frequencies, appearing pure rotational spectra between 1cm^{-1} and 10^2cm^{-1} (microwave and far-infrared). The separation of vibrational energy levels is greater, and the transitions occur at higher frequencies, being the pure vibrational spectra observed in the range between 10^2cm^{-1} and 10^4cm^{-1} (infrared). Finally, electronic energy levels are usually far apart, and electronic spectra are observed in the range between 10^4cm^{-1} and 10^6cm^{-1} (ultraviolet and visible regions). Separation of energy levels is schematically shown in figure 26.

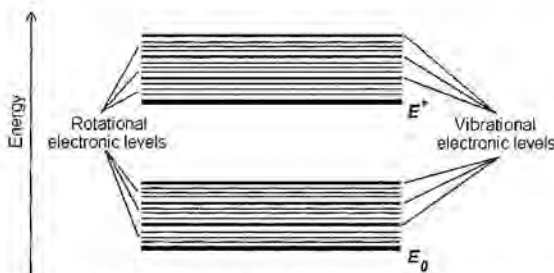


Figure 26: Energy distribution of electronic, rotational and vibrational levels in a molecule.

In what respect to the vibrational spectra, when a molecule has n atoms there are $3n-6$ independent vibrations ($3n$ degrees of freedom minus the three coordinates related to translational and rotational movement); for linear molecules $3n-5$. These so-called normal vibrations can be observed by different techniques, but specially by infrared (IR) and Raman scattering (RS). Actually, both rotation and vibration of molecules are involved in the absorption of infrared radiation, but since molecular rotation is not usually resolved in most infrared and Raman spectra, we will ignore this additional consideration. The electronic spectrum can be analysed by optical absorption (OA).

[†] The frequency, ν , is converted to the wave number, $\bar{\nu}$, or the wavelength, λ , through the relation $\nu = c\bar{\nu} = c/\lambda$, where c is the velocity of light. In spectroscopy ν and $\bar{\nu}$ are more convenient since they are proportional to the energy of radiation. The units conventionally used are cm^{-1} and cm^{-1} respectively. It is worth to note that the word wavenumbers and frequency are commonly used indistinguishably.

2.4.1 Infrared spectroscopy

Infrared spectroscopy is a very useful technique for characterisation of materials, not providing only information about the composition and the structure of molecules, but also morphological information. The advantages of infrared spectroscopy include wide applicability, nondestructiveness, measurement under ambient atmosphere, and the capability of providing detailed structural information. Besides these intrinsic advantages (of the known as *dispersive infrared spectroscopy*), the more recent *infrared spectroscopy by Fourier Transform (FTIR)* has additional merits such as:

- Higher sensitivity
- Higher precision (improved frequency resolution and reproducibility)
- Quickness of measurement
- Extensive data processing capability (as FTIR is a computer based technique, it allows storage of spectra and facilities for processing spectra).

In the following the fundamentals to understand the principles of infrared spectroscopy and a brief description of the main components of an infrared spectrometer will be done.

2.4.1.1 Description of infrared absorption

IR spectra originate in transitions between two vibrational levels of a molecule in the electronic ground state and are usually observed as *absorption spectra* in the infrared region. The range of wavelength through which an infrared spectrum is taken is presented in figure 27. For a molecule to present infrared absorption bands it is needed that it has a permanent dipole moment. Thus, molecules that do not have a permanent dipole moment do not absorb in the infrared. When a molecule with at least one permanent dipole vibrates, this permanent dipole also vibrates and can interact with the oscillating electric field of incident infrared radiation. In order for this normal mode of vibration of the molecule to be infrared active, that is, to give rise to an observable infrared band, there must be a change in the dipole moment of the molecule during the course of the vibration.

To derive the relationship between vibrational energy and molecular structure, it is necessary to solve the Schrödinger equation for vibrational-rotational interactions. Since solution of this equation is not needed to basically understand the idea of the technique, one can simply use the relationship that is derived for a harmonic oscillator. So, a molecule can therefore be thought of a series of balls of

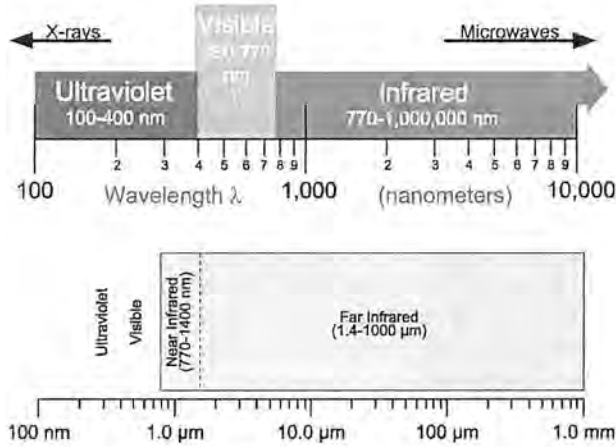


Figure 27: In the upper part it is shown the optical portion of the electromagnetic spectrum. In the lower part it is shown the two regions of measurement in infrared spectroscopy, i.e., near and far infrared.

different masses joined by springs of different degrees of elasticity in such a way that a chemical bond of the molecule can both stretch and bend. In this way, the vibration of two nuclei in a diatomic molecule is reduced to the motion of a single particle of *reduced mass* μ , such that $1/\mu = 1/m_1 + 1/m_2$, whose displacement Q from its equilibrium position is equal to the change of the internuclear distance. As commented above, the eigenvalues and eigenfunctions are found by solving the Schrödinger wave equation with a parabolic potential function as if the system was a harmonic oscillator with force constant K :

$$\frac{d^2\psi}{dq^2} + \frac{8\pi^2\mu}{h^2} \left(E - \frac{1}{2}Kq^2 \right) \psi = 0 \quad (55)$$

So, the eigenvalues are:

$$E_\nu = h\nu \left(\nu + \frac{1}{2} \right) \quad (56)$$

with the frequency of vibration:

$$\omega = \sqrt{\frac{K}{\mu}}, \quad (57)$$

being ν the vibrational quantum number, with possible values 0, 1, 2, 3, ... The corresponding eigenfunctions are:

$$\psi_v = \frac{(\alpha/\pi)^{1/4}}{\sqrt{2^v v!}} e^{-\alpha q^2/2} H_v(\sqrt{\alpha}q), \quad (58)$$

where $\alpha = 2\pi\sqrt{\mu K}/h$, and $H_v(\sqrt{\alpha}q)$ is a Hermite polynomial of the v^{th} degree.

If the vibrational frequency of the molecule, as determined by the force constant and reduced mass, equals the frequency of the electromagnetic radiation, then absorption can take place. As the frequency of the electric field of the infrared radiation approaches the frequency of the oscillating bond dipole and the two oscillate at the same frequency and phase, the chemical bond can absorb the infrared photon and increase its vibrational quantum number by +1, or what is the same, increase its vibrational state to a higher level.

As a first approximation, the larger the strength of the bond, the higher the frequency of the fundamental vibration. In the same way, the higher the masses of the atoms attached to the bond, the lower the wavenumber of the fundamental vibration. It can be ruled also that it takes more energy to stretch a bond than to bend a bond and, hence, bands due to stretching occur at higher wavenumbers than bending vibrations (also termed deformations). In the same manner, an asymmetric stretch always occurs at a slightly higher wavenumber than its associated symmetric stretch. The intensity of a band depends upon many groups of a particular type exist, the magnitude of the dipole moment within the functional group, how much the dipole moment changes within the molecule when it vibrates and related to this, the symmetry of the molecule. As a general guide, the greater the number of groups of a particular type and more polar the bond, the more intense the band.

The infrared spectrum can be divided into two regions; one called the *functional group region* and the other the *fingerprint region*. The functional group region is generally considered to range from 4000 to 1500 cm^{-1} and all frequencies below 1500 cm^{-1} are considered characteristic of the fingerprint region. The fingerprint region involves molecular vibrations, usually bending motions, that are characteristic of the entire molecule or large fragments of the molecule. Thus these are used for identification. The functional group region tends to include motions, generally stretching vibrations, which are more localised and characteristic of the typical functional groups, found in organic molecules. While these bands are not very useful in confirming identity, they do provide some very useful information about the nature of the components that make up the molecule. Table I indicates very generally a description of the vibrations of the functional group. In figure 28 they are shown the region of infrared absorption for common functional groups.

Wavenumber	Stretch type
3000 cm^{-1}	<i>single</i> bond stretch eg. C-H, O-H, and N-H
2000-2500 cm^{-1}	<i>triple</i> bond stretch eg. acetylenes, carbenes and nitriles
1500-2000 cm^{-1}	<i>double</i> bond stretch eg. carbonyls (C=O) or alkenes (C=C)
Fingerprint region	various coupled stretch and deformation bands

Table I: Common functional groups.

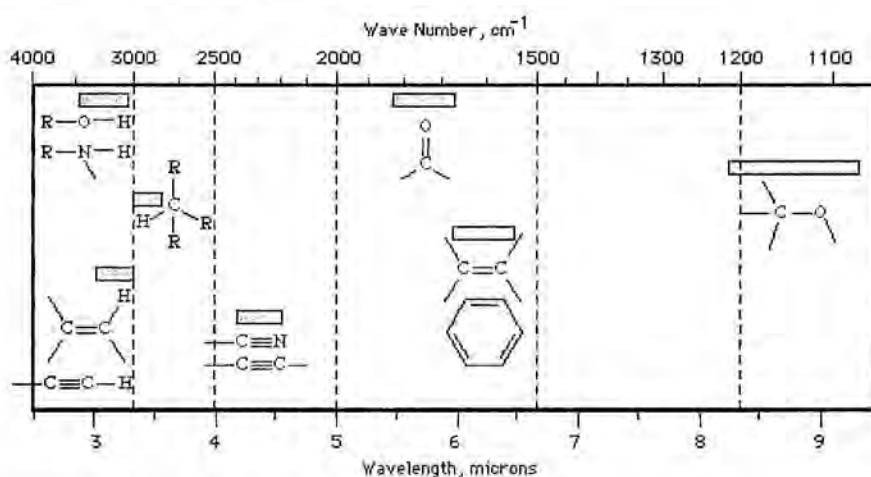


Figure 28: Infrared absorption of common functional groups.

2.4.1.2 Instrumentation for infrared spectroscopy

Basically an infrared spectrometer is composed by the source, the monochromator and the receptor. The ideal infrared source (a 1500-2000K electrically heated solid) would be one that would give a continuous and high radiant energy output over the entire infrared region. The two sources in most common use are the Nernst Glower (heated up to 2200 K) and the Globar (heated to about 1500 K with spectral output comparable with the Nernst glower, except at short wavelengths -less than 5 mm- where its output becomes larger). In general, in all infrared sources the radiant energy, which depends upon the temperature of the source, is low in the far infrared, and to obtain sufficient energy the slit width of the source has to be opened considerably with a corresponding decrease in resolution. One might compensate for this low emissivity in the far infrared by raising the

temperature of the radiator. However, raising temperature has just as bad an effect as increasing the slit width and it reduces the life of the source.

Between the source and the detector there must be some kind of device to analyse the radiation so that an intensity can be evaluated for each wavelength resolution element. There are two basic types, namely, monochromators, used in dispersive instruments, and interferometers used in Fourier Transform instruments. In a monochromator, a prism or a diffraction grating is used, separating the components of polychromatic radiation. For spectroscopic work a prism must be transparent to the particular wavelength region of interest and the dispersion of the prism must be as large as possible. These two requirements are not entirely unrelated. As the ultimate resolving power of a prism is equal to the product of the length of the prism base, L , and the dispersion, $dn/d\lambda$, the resolution can be increased by increasing the size of the prism, by using N prisms in series. However, most of infrared spectrometers have instead a Littrow arrangement in which radiation passes through the prism two or more times.

The function of a grating, like that of a prism, is to provide monochromatic radiation from radiation composed of many wavelengths. A diffraction grating consists of a number of equally spaced slits, which diffract light by interference. The theoretical resolving power of a grating may be expressed as mN , where m is the order of the spectrum and N is the number of grooves or rulings on the grating. There are basically two types of diffraction gratings, the transmission and the reflectance types.

Additionally, most infrared instruments have filters, which pass infrared radiation within a particular wavelength range. Appropriate filters can reduce stray radiation in a prism spectrometer and remove the undesired higher orders obtained with a grating spectrometer.

The final part of the spectrometer is the detector. The infrared detector is a device that measures the infrared energy of the source that has passed through the spectrometer. Their basic function is to change radiation energy into electrical energy, which can be generated to process a spectrum. Infrared detectors can be conveniently divided into two general groups, selective and nonselective. Selective detectors include those whose response is markedly dependent upon the wavelength of incident radiation, being photographic plates, photocells, photoconductive cells, and infrared phosphors categorised in this group. The second group includes detectors whose response is directly proportional to incident energy and relatively independent of wavelength, i.e., these detectors measure the heating effects of radiation and respond equally well to all wavelengths. These detectors are better suited for spectroscopic work, and among the more common types are thermocouples, bolometers, pyroelectric detectors and the pneumatic cell.

For a basic description of the sources, monochromators, filters and detectors commented, one can see for example the book of Colthup et al. [34] and references therein.

In the case of FTIR spectroscopy the spectra are recorded in the time domain followed by computer transformation into the frequency domain, rather than directly in the frequency domain, as is done by dispersive IR spectrometers. However, in spite such procedure seems more complicated, they have been outlined above the advantages to be gained with FTIR. Recording a trace in the time domain in principle could be possible by allowing radiation to fall on a detector and recording its response over time. In practice, however, no detector can respond quickly enough and interference has to be used to modulate the IR signal at a detectable frequency. This is done by means of the well known Michelson interferometer, which is used to produce a new signal (interferogram) of a much lower frequency which contains the same information as the original IR signal.

In the Michelson interferometer (figure 29) radiation leaves the source and is split. Half is reflected to a stationary mirror and then back to the splitter. This radiation has travelled a fixed distance. The other half of the radiation from the source passes through the splitter and is reflected back by a movable mirror. Therefore, the path length of this beam is variable. The two reflected beams recombine at the splitter, and they interfere. If the

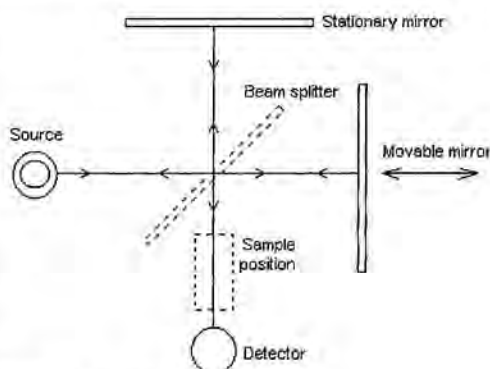


Figure 29: Michelson interferometer.

movable mirror moves away from the beam splitter at a constant speed, radiation reaching the detector goes through a steady sequence of maxima and minima as the interference alternates between constructive and destructive phases. Because all wavelengths emitted by the source are present, the interferogram is extremely complicated. The moving mirror must travel smoothly; a frictionless bearing is used with electromagnetic drive. The position of the mirror is measured by a laser shining on a corner of the mirror. A simple sine wave interference pattern is produced. Each peak indicates mirror travel of one half the wavelength of the laser. The accuracy of this measurement system means that the IR frequency scale is accurate and precise. In the FT-IR instrument, the sample is placed between the output of the interferometer and the detector. The sample absorbs radiation of particular wavelengths. Therefore, the interferogram contains the spectrum of the source minus the spectrum of the sample. An interferogram of a reference (sample cell and solvent) is needed to obtain the spectrum of the sample. After an interferogram has been collected, a computer performs a Fast Fourier Transform, which results in a

frequency domain trace (i.e intensity vs. wavenumber) that is what one needs and knows.

The detector used in an FT-IR instrument must respond quickly because intensity changes are rapid (the moving mirror moves quickly). So, pyroelectric detectors or liquid nitrogen cooled photon detectors must be used, while thermal detectors are too slow. To achieve a good signal to noise ratio, many interferograms are obtained and then averaged. This can be done in less time than it would take a dispersive instrument to record one scan.

2.4.2 Raman spectroscopy

Like infrared spectroscopy, Raman is an invaluable technique for characterisation of materials. In the field of semiconductor characterisation the use of Raman microscopes is now widespread because it offers a non-destructive and quantitative microanalysis of structures and electronic properties. However, due mainly to the higher resolution with respect to FTIR spectroscopy and the versatility and simplicity in terms of sample handling, Raman, and specially micro-Raman spectroscopy has actually an increasing use versus other similar spectroscopic techniques. In particular, in addition to the well known application of identification of compounds, a large number of reported works rule for example on the characterisation of concentration and mobility of free carriers, characterisation of strain and crystal quality, determination of local crystal orientation, etc. It is worth to comment that while infrared and Raman spectra analyse basically the same vibrational behaviour of the molecule they are not exact duplicates since the selection rules and relative band intensities differ in many cases.

As for infrared spectroscopy, a brief description of the Raman effect and some insights on the required instrumentation will be given in the following.

2.4.2.1 Description of the Raman effect

Raman spectra originate in the electronic polarisation caused by ultraviolet or visible light. The mechanism by which the incident radiation interacts with the molecular vibrational energy levels has its origins in the general phenomenon of light scattering, in which the electromagnetic radiation interacts with a pulsating deformable (polarisable) electron cloud, being this interaction modulated by the molecular vibrations.

If a molecule is irradiated by monochromatic light of frequency ν having electric field strength E ,

$$E = E_0 \cos(2\pi\nu t) \quad (59)$$

because of the electronic polarisation induced in the molecule by this incident light, it presents an induced dipole moment \vec{p} :

$$\vec{p} = \alpha \vec{E}^\dagger \quad (60)$$

where α is the *polarizability tensor*, so that in matrix form the above expression can be written as:

$$\begin{bmatrix} p_x \\ p_y \\ p_z \end{bmatrix} = \begin{bmatrix} \alpha_{xx} & \alpha_{xy} & \alpha_{xz} \\ \alpha_{yx} & \alpha_{yy} & \alpha_{yz} \\ \alpha_{zx} & \alpha_{zy} & \alpha_{zz} \end{bmatrix} \begin{bmatrix} E_x \\ E_y \\ E_z \end{bmatrix} \quad (61)$$

In normal Raman scattering the polarizability tensor is symmetric ($\alpha_{xy} = \alpha_{yx} = \alpha_{zy}$). In molecules α is not constant since certain vibrations and rotations can cause α to vary. If the scattering body has its normal modes of vibration Q described by

$$Q_k = Q_k^o \cos(2\pi\nu_k t) \quad (62)$$

these oscillations can affect the polarizability,

$$\alpha = \alpha_o + \left(\frac{\partial \alpha}{\partial Q_k^o} \right) Q_k + \dots \quad (63)$$

Thus,

$$\vec{p} = \alpha \vec{E} = \alpha_o \vec{E} + \left(\frac{\partial \alpha}{\partial Q_k^o} \right) Q_k \vec{E} + \dots \quad (64)$$

$$p = \alpha_o E_o \cos(2\pi\nu t) + E_o Q_k^o \left(\frac{\partial \alpha}{\partial Q_k^o} \right) \cos(2\pi\nu t) \cos(2\pi\nu_k t) \quad (65)$$

$$p = \alpha_o E_o \cos(2\pi\nu t) + \frac{1}{2} E_o Q_k^o \left(\frac{\partial \alpha}{\partial Q_k^o} \right) [\cos\{2\pi(\nu + \nu_k)t\} + \cos\{2\pi(\nu - \nu_k)t\}] \quad (66)$$

The first term of the above equation is elastic scattering, known as Rayleigh scattering; the second term, of frequency $\nu + \nu_k$, is anti-Stokes Raman scattering; and the third term, of frequency $\nu - \nu_k$, is Stokes Raman scattering. From the above classical description it is deduced that as the variation of the polarizability will be smaller than the polarizability itself, Raman scattering should be less intense than Rayleigh scattering, as it is the case. Concretely, Raman scattering is a factor 10^{-3} to 10^{-4} weaker than Rayleigh scattering, being needed a strong exciting source to

[†] Actually $\vec{p} = \alpha \vec{E} + \frac{1}{2} \beta \vec{E}^2 + \dots$, where $\beta \ll \alpha$ is called the hyperpolarizability and becomes important when E is large, being observed the hyper-Raman ($2\nu \pm \nu_k$) spectra.

observe the Raman scattering. The linear dependency of Raman scattering with the incident beam intensity and sample concentration is also deduced.

Since Raman lines represent frequency differences from the incident frequency, they are also called Raman shifts and are designated as $\Delta\nu$ in cm^{-1} . For the Stokes lines $\Delta\nu(\text{cm}^{-1}) = 10^8/\lambda_E - 10^8/\lambda_R$, being λ_E the wavelength in angstroms of the exciting line and λ_R the wavelength in angstroms of the Raman line.

The equivalent energy diagram for the Raman process is schematised in figure 30. As there are no energy levels at the excited conditions, the excited state for the molecule after the interaction with light is not real. As a result we describe these states as virtual.

As represented in the scheme of figure 31, the scattering at $\nu_0 + \nu_k$ starts for the vibrationally excited state but that at $\nu_0 - \nu_k$ starts at the ground state. The population of any excited level k is always less than that of the ground state, as described by the Boltzmann distribution,

$$\frac{N_k}{N_0} = e^{-\Delta E/kT} \tag{67}$$

As a result, the $\nu_0 + \nu_k$ (anti-Stokes line) are weaker than the red shifted spectrum where they appear at $\nu_0 - \nu_k$ (Stokes lines). The ratio of the intensities of equivalent pairs of lines $I_{\text{anti-Stokes}}/I_{\text{Stokes}}$ falls as the vibrational frequency increases and decreases with temperature.

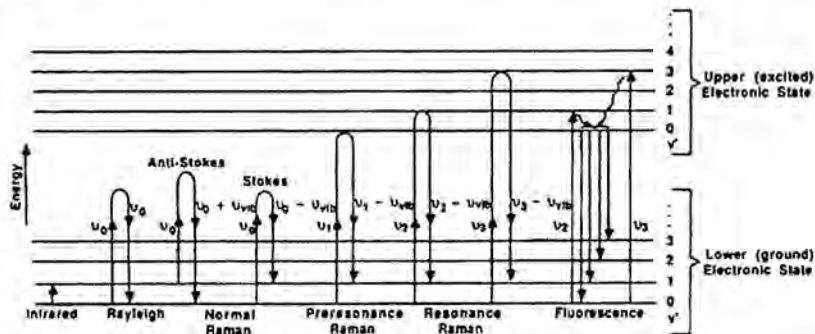


Figure 30: Schematic representation of the Raman process.

In addition to the normal Raman scattering described, other effects can be observed in a Raman experiment. these consist in *preresonance*, *resonance* and *fluorescence*. When the frequency of the exciting line approaches the frequencies of electronic transitions, the spectrum changes dramatically, showing an enhancement of intensity of certain vibrational modes. In this case the generation of the electron-hole couple is not virtual. If the exciting line is close to but not inside an electronic absorption band, the process is called preresonance Raman scattering, and if the exciting line coincides with that of an electronic transition resonance Raman occurs. On the other hand, if the photon is absorbed and then emitted during the process, it

is called resonance fluorescence. As resonance Raman improves the signal of certain vibrational modes, it is actually a field of current development with high possibilities.

2.4.2.2 Instrumentation for micro-Raman spectroscopy

Basically two types of Raman equipment can be described: Macro and micro-Raman. The former has the advantage of higher illumination region over the sample, being ideal for liquids and powder samples, and the disadvantage of the difficulty in focusing the specimen. The equipment used for both methods is basically the same, only a conventional optical microscope being added for micro-Raman spectroscopy.

A typical current Raman spectrometer incorporates (figure 31):

① The illumination source composed of an Ar^+ ion laser emitting lines between 458 and 529 nm, sometimes coupled to a dye laser or a solid state Titanium:sapphire laser providing tunable radiation between 600 nm and 900 nm.

② A macrosample chamber and a classical optical microscope for microanalysis.

③ A dispersive system composed of a double monochromator and a spectrograph. The two monochromators can be used either in subtractive mode to provide a wide field to the spectrograph or in additive mode when higher resolution is required. The double monochromator has one or two slit(s) in between the first and second stage monochromators.

④ The detection system, which includes a multichannel detector (a linear diode array) and a photomultiplier connected to a single photon counter.

The optical multichannel detector with a double monochromator requires a wide intermediate slit width. This causes an increase in the stray light and makes it difficult to measure spectra in the low-frequency region. To overcome this difficulty in the use of the optical multichannel detector, some spectrometers are equipped with a triple monochromator (a subtractive double monochromator as a filter plus a monochromator). Quadruple monochromators (a subtractive double monochromator plus an additive double monochromator) are now available in the case that high resolution is needed at the low-frequency region.

Although three different types of sample illumination methods have been proposed for the measurement of local points and Raman mapping, being point illumination, line illumination and global illumination, the first is the most commonly employed. With point illumination the laser light is focussed on a sample surface by an objective lens and the scattered light is collected by the same objective. The spot size in the focal plane is diffraction limited, being the minimal diameter given by equation (1). Although higher spatial resolution is obtained with this illumination method, heating or degradation of the samples by high density of laser powers can occur. Using a 100x objective with $NA=0.95$, the spot size in the

sample is about $0.6\mu\text{m}$ for $\lambda=457.9\text{ nm}$. This results in a very high power density in the specimen of the order of several MW/cm^2 .

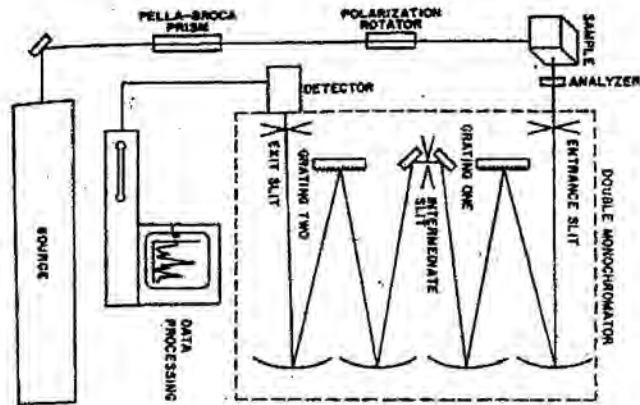


Figure 31: Scheme of a single-channel spectrometer with double monochromator.

2.4.3 Infrared and Raman allowed vibrations:

As commented before, although infrared and Raman measure the same vibrational spectrum, the obtained result is different, due to the selection rules that apply in each case. To determine the activity of a vibration in infrared and Raman spectra, the selection rule must be applied to each normal vibration mode. According to quantum mechanics, the vibration is Raman active if one of these six components of the polarizability changes during the vibration. Similarly, it is infrared active if one of the three components of the dipole moment (μ_x, μ_y, μ_z) changes during the vibration. However, changes in dipole moment or polarizability are not obvious from inspection of the normal modes of vibration when treating with non simple molecules and one has to appeal to group theory, which gives a clear-cut solution to this problem.

Therefore, the selection rule for the IR spectrum for a normal vibration whose normal coordinate is Q_n is determined by the integral:

$$[\mu]_{\nu'\nu''} = \int \psi_{\nu'}(Q_n) \mu \psi_{\nu''}(Q_n) dQ_n \quad (68)$$

where μ is the dipole moment in the electronic ground state, ψ is the vibrational eigenfunction and ν' and ν'' are the vibrational quantum numbers before and after the transition, respectively. The vibration is infrared inactive if this integral is zero,

i.e., all the three components (for μ_x , μ_y , and μ_z) are 0). If any of the three components does not vanish the vibration is infrared active.

Similarly, the selection rule for the Raman spectrum is determined by the integral:

$$[\alpha]_{\nu'\nu''} = \int \psi_{\nu'}(Q_a) \alpha \psi_{\nu''}(Q_a) dQ_a \quad (69)$$

or what is the same, by the six components in which can be resolved for the six components of the polarizability.

However, it is possible decide whether the integrals are zero or nonzero from a consideration of symmetry, because the vibrations of interest are the fundamentals in which transitions occur from $\nu'=0$ to $\nu''=1$, and $\psi_0(Q_a)$ is invariant under any symmetry operation, whereas the symmetry of $\psi_1(Q_a)$ is the same as that of Q_a . Therefore, the normal vibration associated with Q_a becomes infrared active when at least one of the components of the dipole moments belong to the same symmetry species as Q_a , and similar conclusions are obtained for the Raman spectrum.

2.5 Notes on specimen preparation techniques

➤ Sample preparation for Scanning Electron Microscopy ◀

The preparation of samples for the observation in SEM is in most of the cases none. The sample is simply dusted with an adhesive tape to a metallic support, which is placed inside the camera of the microscope. In some cases, however, due to the low conductivity of the material to be observed, it is necessary the coverage of the surface to study with some monolayers of Carbon or Gold to ensure conductivity and increase resolution, avoiding charging of the specimen.

➤ Sample preparation for Transmission Electron Microscopy ◀

There are numerous methods for preparing electron transparent specimens for observation in a transmission electron microscope. However, we will centre in those performed usually in our laboratory in the case of (1) films and (2) powders.

① Preparation of cross-section and planar specimens of films:

The cross-section preparation technique, schematically represented in figure 32, can be summarised as:

- a) Sawing of the wafer in order to have stripes of rectangular size.
- b) Glueing of two stripes face to face or if few material is disposable, one stripe together with a stripe of a material of similar hardness.
- c) Mechanical pre-thinning (grinding and polishing) of the sample for both sides until the specimen has a thickness of approximately $20\mu\text{m}$ if (d) is not performed or $100\mu\text{m}$ if (d) is performed.
- d) Optional dimpling of the flat parallel specimen in order to thin the central part, while still having relatively thick borders allowing to handle the specimen easily using tweezers.
- e) One side or two sides ion milling until perforation using moderate voltage and current settings in order to reduce the damage introduced in the specimen. However, sometimes is preferable the use of harder conditions in order to reduce the operational time of the ion milling.

In the case of planar specimens the preparation method is very similar. It is schematically shown in figure 33 and the steps are:

- a) Cutting a disc from the wafer using an ultrasonic cutter, a mechanical punch or something like this.
- b) Flat grinding of the backside of the disc until obtaining a disc of approximately $100\mu\text{m}$ thick.

- c) Dimpling of the disc from the same side in a concave polisher until the central region is about $20\mu\text{m}$ thick.
- d) Ion milling from the dimpled side. For this, in order to avoid contamination with the sputtered material it is convenient to cover the face of interest with a thin glass.

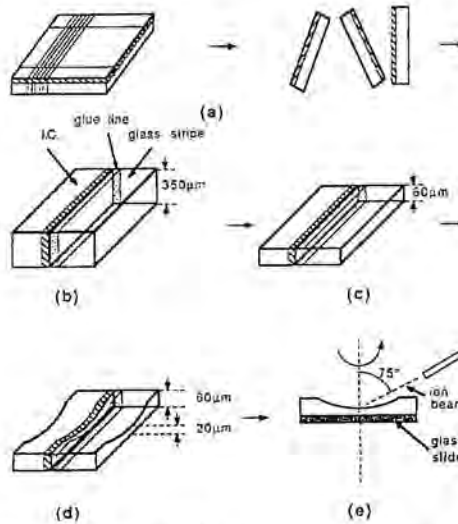


Figure 32: Preparation for cross-section observation. a) Cutting of stripes. b) Glueing face to face. c) Polishing. d) Ion milling.

② Preparation of powders for observation in TEM

The preparation of powder samples for TEM examination is enough documented. In general, the preparation of powder samples is with difference much easier than film preparation when the size of the grains in the powder are small enough. In this case the procedure is as follows:

- a) Mixing of approximately 1 part of powder with 100-500 parts of an inert liquid like ethanol.
- b) Ultrasonic stirring of the liquid containing the particles.
- c) Depositing of a drop of liquid on a holey carbon film on a ~ 100 -200 mesh grid and let evaporate in a dry environment.

However, not always the powder contains grains of sufficient small grain size or the powder results extremely agglomerated after being dissolved in a liquid because of electrostatic forces. In this case rather than the dispersion technique is better to mix the powders with some ductile material like Al and then ball mill with for example steel balls in order to obtain an agglomerate of the mixture. After

cutting it in discs, ion milling can be performed to obtain the transparent specimen for observation or, if preferred ultramicrotomy can be done. However, this method has serious problems. Between them one can include the difficulty in finding a material suitable for the mixture, i.e., that when cutting or ion milling is performed the agglomerate maintains its consistency, and the introduction of structural changes during the ball milling step.

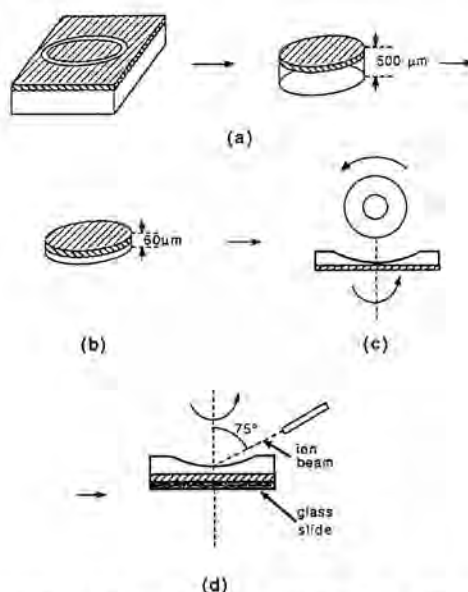


Figure 33: Preparation for planar-view observation. The procedure consists in cutting of discs (a), planar and concave polishing from the substrate (b and c), and ion milling from the substrate (d).

➤ Sample preparation for X-ray Diffraction ◀

In the case of films as well as in the case of powders, some cautions have to be taken into account when observing a sample by XRD. In general, unfilled holders, beams that do not strike on the sample because the samples are too thin, rough surfaces or with curvature, and sample-height displacement errors, produce spurious diffraction peaks, increase the background or produce diffraction peaks from the holder.

In the case of films, no preparation method is required, although it does not mean that mounting of the sample be a easy task, because of the commented factors. Usually, layer samples are mounted over a solid plate coated with a viscous material such as vaseline or silicon grease, or simply using plastiline. In the case of

powders, these are usually disposed recovering the cylindrical hole of a plastic holder about 1-2mm height and 2-5cm of diameter (for reflexion analysis) or filling a quartz capillary of 100-500 μ m diameter (for transmission analysis). However, in the case of powders some additional considerations have to be observed, specially when the grain size of the powder is large. In this case, it is needed to do a grinding of the powder in order to reduce grain size \sim 2-10 μ m, because coarser grains involve problems related to particle statistics, preferred orientation, microabsorption, and extinction. The grinding is made in hand mortars and pestles made of agate, mullite, or corundum. Rarely it is necessary to appeal to automatic grinding machines due to the hardness of the material.

⇒ *Sample preparation for X-ray Photoelectron Spectroscopy* ◀

In majority of XPS applications, sample preparation and mounting are not critical. Typically, the sample is mechanically attached to the specimen mount, and analysis is begun with the sample in the as-received condition. Additional sample preparation is discouraged in many cases because any preparation might modify the surface composition. However, in the analysis of bulk material, sometimes, due to contamination it is convenient to sputter the first layers of the region of interest directly in the XPS apparatus, which will improve specially the quantification.

In the case of powder samples, there are a number of methods that can be used to mount powders for analysis. Perhaps the most widely used method is dusting the powder onto a polymer-based adhesive tape with a camel-hair brush. The powder must be dusted across the surface carefully and lightly, with no wiping strokes

⇒ *Sample preparation for Infrared Spectroscopy* ◀

As for the others techniques, there are a large quantity of methods for preparing samples to be observed by infrared spectroscopy. However, only a brief comment on the most important will be given here.

Generally, no preparation is needed in the case of films that do not absorb completely in the infrared region. If the film is not transparent at all for the infrared radiation sometimes is better to observe it by reflection that by transmission, before to appeal to any type of grinding of the film or something like this.

Measurement of the transmission infrared of liquids poses no great problem from the sampling viewpoint. These materials may be squeezed between polished plates of sodium chloride, potassium bromide, or another suitably transparent material until absorption bands of measurably intensity are obtained. Alternatively, if information of a quantitative or semi-quantitative nature is required, the sample is made up in solution, at 5 or 10% concentration, in a solvent such as cyclohexane,

carbon tetrachloride, chloroform or carbon disulphide and examined in a sealed cell.

Powders being examined by infrared spectroscopy, in transmission, are generally prepared by mulling in liquid paraffin (Nujol), or by grinding with potassium bromide (KBr) powder, being the latter then pressed into a disk. The first method, however, has the inconvenient that most mulling agents contain bands in the spectrum, which may mask bands in the sample spectrum. KBr does not contain bands in the mid-IR region of the spectrum although contains bands in the far-IR region. For this region the same procedure is applied with a CsI powder for the analysis in the far-IR. It could be said that a KBr pellet is a dilute suspension of a solid in a solid. It is usually obtained by first grinding the sample in anhydrous KBr at a ratio of approximately 1 part sample to 100 parts KBr. Although it is best to weigh the sample (1mg) in the KBr (100mg), with some experience it is possible to use your judgement in assigning proportions of sample to KBr. The mixture is then ground up, most of times manually with an agate pestle, until the sample is well dispersed. The ground up sample mixture is then placed in a die assembly, being the powder located between two steel cylinders. Afterwards the steel sandwich is placed in a hydraulic press and subjected to pressures of 4-5atm for about 20 seconds. Once time the die has been dismantled, the KBr disk is ready to be transferred to the spectrometer disk holder for observation. However, it has to be checked that the disk is translucent and that the sample is homogeneously distributed in the disk, because the spectrum quality is affected by the quality of the disk.

➤ Sample preparation for Raman spectroscopy ◉

By means of Raman spectroscopy one can get a spectra in a routine manner with almost no sample. In addition, in any case one needs to prepare the sample for observation. In the case of solids, only leaving them in a typical glass microscope slide is enough. For liquids, them can be placed in a small glass bottle or capillary that can be sealed if necessary.

2.6 Equipment used in this work for the structural characterisation

For transmission electron microscopy:

Philips CM30-SuperTwin

Electron gun: LaB₆

Acceleration voltage: 15-300kV

Magnification: 53-700000x

Eucentric side entry goniometer with 25° double tilt specimen holder

Line resolution: 0.14nm

C_s=1.2mm

C_c=1.2mm

Scherzer defocus= -56nm

EDS analysis LINK LZ-5 with Si(Li) detector and window less.

Philips CM200 FEG

Electron gun: Schottky Field Emitter

Acceleration voltage: 20-200kV

Magnification: 25-1000000x

Eucentric side entry goniometer with 45° double tilt specimen holder

Line resolution: 0.10nm

C_s=1.2mm

C_c=1.2mm

Scherzer defocus= -67nm

EDS analysis EDAX 9100 Si(Li) detector with S-UTW window

Gatan 766 DigiPEELS spectrometer, mounted on axis

For scanning electron microscopy:

Jeol JSM 840

Resolution: 3nm (LaB₆); 4nm (W)

Magnification: 10-600000x

Acceleration voltage: 400-40000V

Detectors: Backscattered, secondaries and transmitted

EDS: LINK AN10000 (Si(Li) detector and Be window)

Resolution: 156 eV

Hitachi S-120

Resolution: 4.5nm

Magnification: 20-200000x

Acceleration voltage: 500-25000V

Detectors: Backscattered, secondaries

EDS: LINK (Si(Li) detector and Be window)

For X-ray diffraction:

X-Ray powder diffractometer INEL

X-ray generator: ENRAF NONIUS FR 590

120° sensible detector CPS 120

Quartz Primary monochromator

Cu tube

Debye-Scherrer geometry

X-ray powder diffractometer SIEMENS D-500

X-ray generator: Kristalloflex 710H

Scintillator detector

Graphite Secondary monochromator

Cu tube

Low temperature chamber TTK-HC (-193<T<250°C)

High temperature chamber HTK 10 AP PAAR (T<1600°C)

Bragg-Brentano parafocussing geometry

X-Ray single-crystal diffractometer Philips MRD

Cu or Mo tube

Flat Graphite secondary monochromator

Proportional detector

Bragg-Brentano parafocussing geometry

For X-ray photoelectron spectroscopy:

Perkin-Elmer PHI 5500

Radiation: AlK α (1486.6eV), MgK α (1253.6 eV)

FWHM (Ag 3d_{5/2}): 1-1.5eV

C binding energy: 248.8eV

For infrared spectroscopy:

FTIR Bomem DA3

Working range: 10 a 25000 cm^{-1}

Resolution limit: 0.02 cm^{-1}

Detectors: DTGS, MCT (wr), MCT (nr), InSb, Si, bolòmetre

Beam Splitters: KBr, CaF_2 , quartz, mylar

Source: glowbar, quartz, Hg

FTIR Bomem MB-120

Working range: 350 a 5000 cm^{-1}

Resolution limit: 1 cm^{-1}

Detectors: DTGS

Beam Splitters: KBr

Source: glowbar

For Raman spectroscopy:

Jobin Yvon T64000

Source: Ar^+ laser Coherent INNOVA 300

Olympus metallographic optical microscope BH2 (10x, 50x, 100x)
triple monochromator (1800 g/mm)

Bidimensional CCD detector cooled with N_2

2.7 Further readings

On electron microscopy:

General:

- [1] P.J. Grundy, and G.A. Jones, *Electron Microscopy in the Study of Materials*, ed. B.R. Coles, Edward Arnold, London (1976).
- [2] J.C.H. Spence, *Experimental High-resolution Electron Microscopy*, ed. C.E.H. Bawn, H. Frölich, P.B. Hirsch, and N.F. Mott, Clarendon Press, Oxford (1981).
- [3] D.B. Williams, and C.B. Carter, *Transmission Electron Microscopy: a Textbook for Materials Science*, Plenum Press, New York and London (1996).
- [4] T. Geipel, and M. Hohenstein, Analytical description of image contrast in HRTEM and applications, *Ultramicroscopy* **45**, 167-183 (1992).
- [5] M. Sarikaya, Evolution of resolution in microscopy, *Ultramicroscopy* **47**, 1-14 (1992).
- [6] M. Sarikaya, and J.M. Howe, Resolution in conventional transmission electron microscopy, *Ultramicroscopy* **47**, 145-161 (1992).
- [7] D.Van Dyck, and A.F. de Jong, Ultimate resolution and information in electron microscopy: general principles, *Ultramicroscopy* **47**, 266-281 (1992).
- [8] M.A. O'Keefe, 'Resolution' in high-resolution electron microscopy, *Ultramicroscopy* **47**, 282-297 (1992).
- [9] P.J. Wilbrandt, A simple concept for better alignment and simplified operation of a transmission electron microscope, *Ultramicroscopy* **52**, 193-204 (1993).
- [10] H. Rose, Correction of aberrations, a promising means for improving the spatial and energy resolution of energy-filtering electron microscopes, *Ultramicroscopy* **56**, 11-25 (1994).
- [11] M.A. O'Keefe, and R. Kilaas, *Users guide to NCEMSS: a program for simulation of HRTEM images*, Berkeley (1994).
- [12] P.A. Stadelmann, EMS – A software package for electron diffraction analysis and HREM image simulation in materials science, *Ultramicroscopy* **21**, 131-146 (1987).

Specimen preparation (films and powders):

- [13] A. Romano, J. Vanhellefont, H. Bender, and J.R. Moranté, A fast preparation technique for high-quality plan view and cross-section TEM

- specimens of semiconducting materials, *Ultramicroscopy* **31**, 183-192 (1989).
- [14] A. Romano-Rodríguez, TEM Techniques for the Development of ULSI Technology, *Thesis*, Barcelona (1991).
- [15] S.B. Rice, and M.J. Treacy, The art of the possible: an overview of catalyst specimen preparation techniques for TEM studies, *Mat. Res. Soc. Symp. Proc.* **115**, 15-26 (1988).
- [16] P.S. Sklad, The preparation of TEM specimens from hazardous or difficult materials, *Mat. Res. Soc. Symp. Proc.* **115**, 39-50 (1988).
- [17] E.M. Ekmejian, and J.B. Bulko, Preparation techniques for structural characterization of powdered and composite materials, *Mat. Res. Soc. Symp. Proc.* **115**, 87-92 (1988).
- [18] E.A. Kamenetzky, M. Wall, R. Castro, and L.E. Tanner, The preparation of mechanically alloyed powders for TEM examination, *Mat. Res. Soc. Symp. Proc.* **115**, 167-172 (1988).
- [19] T. F. Kelly, M. R. Libera, and J.B. Vander, Preparation of thin-foil TEM specimens from sub-millimeter particulate, *Mat. Res. Soc. Symp. Proc.* **115**, 205-210 (1988).
- [20] J.Y. Huang, Y.K. Wu, and H.Q. Ye, A novel technique for specimen preparation of metal or ceramic powders for TEM or HREM observations, *Mat. Lett.* **21**, 167-170 (1994).

On X-ray diffraction:

- [21] H.P. Klug, L.E. Alexander, *X-ray diffraction procedures*, John Wiley and Sons Inc., New York, 1954.
- [22] R.C. Reynolds, JR., Principles of Powder Diffraction, in *Reviews in Mineralogy vol. 20: Modern Powder Diffraction*, ed. D.L. Bish, and J.E. Post, The Mineralogical Society of America, Washington, D.C., pp 1-17 (1989).
- [23] R. Jenkins, Instrumentation, in *Reviews in Mineralogy vol. 20: Modern Powder Diffraction*, ed. D.L. Bish, and J.E. Post, The Mineralogical Society of America, Washington, D.C., pp 19-43 (1989).
- [24] D.L. Bish, and R.C. Reynolds, Jr., Sample Preparation for X-ray Diffraction, in *Reviews in Mineralogy vol. 20: Modern Powder Diffraction*, ed. D.L. Bish, and J.E. Post, The Mineralogical Society of America, Washington, D.C., pp 73-97 (1989).
- [25] R.L. Snyder, and D.L. Bish, Quantitative Analysis, in *Reviews in Mineralogy vol. 20: Modern Powder Diffraction*, ed. D.L. Bish, and J.E. Post, The Mineralogical Society of America, Washington, D.C., pp 101-142 (1989).

- [26] B.E. Warren, *X-ray Diffraction*, Dover publications, Inc., New York (1990).
- [27] F. H. Chung, Quantitative Interpretation of X-ray Diffraction Patterns of Mixtures. II. Adiabatic Principle of X-ray Diffraction Analysis of Mixtures, *J. Appl. Cryst.* **7**, 526-531 (1974).
- [28] F. Plana, La difracció de raigs X com a eina de caracterització de materials ceràmics, *Bull. Soc. Cat. Cièn.* vol. XIII, 449-461 (1992).
- [29] S. Galí, El anàlisi de perfil en difracció de polvo: utilidad y limitaciones, *Boletín de la Sociedad Castellonense de Cultura* **LXV**(IV), 627-641 (1989).

On X-ray photoelectron spectroscopy:

- [30] J.F. Moulder, W. F. Stickle, P.E. Sobol, K.D. Bomben, *Handbook of X-ray Photoelectron Spectroscopy*, ed. J. Chastain, Perkin-Elmer Corp., Minnesota (1979).
- [31] D. Briggs, and M.P. Seah, *Practical Surface Analysis vol. 1: Auger and X-ray Photoelectron Spectroscopy*, John Wiley and Sons, Chichester (1990).
- [32] F. Salvat, R. Mayol, and J. Parellada, Anàlisi quantitativa amb espectroscòpies d'electrons, *Bull. Soc. Cat. Cièn.* vol XIII, 463-475 (1992).
- [33] J.Ll. Alay, *Removal and ion-beam induced growth of thin oxides on Si and Al_xGa_{1-x}As studied by X-ray photoelectron spectroscopy*, Thesis, Leuven (1993).

On infrared and Raman scattering:

- [34] N.B. Colthup, L.H. Daly, and S.E. Wiberly, *Introduction to Infrared and Raman Spectroscopy*, Academic Press Inc., New York and London, 1st ed. 1964 and 3rd ed. 1990.
- [35] K. Nakamoto, *Infrared and Raman Spectra of Inorganic and Coordination Compounds*, John Wiley and Sons, New York (1986).
- [36] S. Nakashima, and M. Hangyo, Characterization of Semiconductor Materials by Raman Microprobe, *IEEE Journal of Quantum Electronics* **25**(5), 965-975 (1989).
- [37] J.R. Ferraro, and K. Krishnan, *Practical Fourier Transform Infrared Spectroscopy: Industrial and Laboratory Chemical Analysis*, Academic Press Inc., San Diego (1990).
- [38] J. G. Grasselli, and B.J. Bulkin, *Analytical Raman Spectroscopy*, John Wiley and Sons Inc., New York (1991).

- [39] T. Jawhari, Applications of Micro-Raman Spectroscopy, in *Handbook of advanced materials testing*, Ed. By N.P. Cheremisinoff, Marcel Dekker, New York, 105-144 (1995).

CHAPTER 3

ON THE INVESTIGATION OF FUNDAMENTAL
PROPERTIES OF SnO₂ NANOPARTICLES AND
IMPROVEMENT OF STABILITY AND
SELECTIVITY OF SOL-GEL FABRICATED SnO₂
THICK FILM GAS SENSORS

It has been outlined the importance of the control of the microstructure of the sensing material in the sensing capabilities of semiconductor gas sensors. Before the control of microstructure, it is obvious, that one needs to know how it evolves as a function of the controlling parameters. In this respect, an important quantity of work has been performed in our laboratory during more than five years. The main objective of *Chapter 3* is to gather all of this information and, to provide, somehow, what could be called 'nanoparticles engineering' for gas sensing. The investigated processes in this work are calcination, introduction of the additives Pt and Pd, and the grinding of the SnO₂. Particularly, the work is focussed in obtaining maximum sensitivities to NO₂ and CO, two of the most interesting gases to be analysed.

In the first part of the *Chapter* the sol-gel method to fabricate nanoparticles and the different ways to obtain the sensor are explained. The rest of the *Chapter* relates the optimisation of the sensor characteristics and comprises three different parts. In the first one, after reviewing the most important properties of tin dioxide, the structural characteristics of SnO₂ nanoparticles as a function of the calcination temperature at which they are treated are investigated in detail. So, this concrete part of the *Chapter* concerns the influence of calcination temperature on the structural properties of SnO₂ nanoparticles fabricated by sol-gel. Extrapolation of the results to SnO₂ nanoparticles fabricated using similar wet chemical methods can be done. The analysis of such nanoparticles has been performed by several techniques, including FTIR and Raman spectroscopies, TEM, and XRD. During this part, particular methodologies for nanoparticles of these techniques, not explained in *Chapter 2*, will be applied and/or developed. Special relevance is given to the Raman spectrum of nanometric SnO₂ particles, which is explained in the complete range of interest for the first time.

After this initial study the calcination temperatures which are more adequate to fabricate the sensors are selected and a new parameter is introduced in the second part of the analysis: the introduction of noble metals as catalytic materials. Structural and electrical characterisations are correlated to deduce the better performance in the case of application to the detection of NO₂ or CO.

The final part concerns the improvement of the sensor characteristics by adding a new step in the fabrication of the powders. This consists in grinding the particles before, after or before and after the calcination. In this last part, the structural and electrical characteristics are correlated again to assure the better response. To our knowledge this technological step is introduced for the first time to improve sensor characteristics.

3.1 Sol-gel fabrication of thick film gas sensors

The fabrication of a thick film gas sensor generally includes two steps. The first is the preparation of a powder of the selected material, in principle composed by grains as small as possible and with a fine size distribution. The second is the fabrication of a paste using this material and its deposition onto an adequate substrate.

Powder synthesis and processing have a large influence on the final properties of ceramic materials. Therefore selection of the appropriate processing route determines to a large extent the results that can be attained in the end product. In this respect, synthesis of compounds through wet chemical methods has become an invaluable step in reaching improved material properties. Typically these methods start from a liquid solution of the cations. For transformation into the precursor powder, different routes can be followed, such as co-precipitation, freeze drying, spray drying, and sol-gel methods, all of them having their specific advantages and problems.

In *co-precipitation* different compounds are precipitated from the solution by a sudden change in pH through the addition of a base or acid. Problems can arise if during precipitation segregation occurs, and also the complete stoichiometric precipitation of the intended compound or phase mixtures may be a problem. In *freeze drying* a solution is frozen in droplet form as fast as possible and the water is sublimed in vacuum. Intrinsically a slow process, freeze drying still is an interesting alternative as no addition of any chemical agent is necessary and processing conditions can be very pure. *Spray drying* consists of spraying a solution or an emulsion in a heated gas flow. Initial droplet size and gas temperature determine the drying speed of the spray and thereby the possibility of partial segregation, and final powder size distribution. Finally, in the *sol-gel* processes, somehow similar to co-precipitation, the mixing level of the solution is retained in the final product. The solution is transformed in a semi-solid gel, which in turn is transformed to the precursor powder by decomposition. Sometimes, gels are obtained by adding complexing agents to the solution in order to prevent precipitation during the concentration phase and the sol to gel transition. It is worth to mention that there are other ways to prepare powders to be used to fabricate thick-film gas sensors. The only requirement for a specific route is that there exist precursors able to react under that procedure. For example, not all the reactants needed to generate SnO₂ by means of the laser pyrolysis technique are available, as this technique needs a reactant that absorbs the laser radiation [1, 2].

To form the paste with the obtained powders, these are mixed with an organic solvent. Afterwards, the most used method to fabricate the sensor consists in dipping the substrate in the mixture, or painting or printing the paste onto one side of the substrate.

In the following, SnO₂ powder synthesis by the sol-gel route and the printing and dipping methods of sensor fabrication are discussed in more detail.

3.1.1 The preparation of SnO₂ by the sol-gel route

Among many others, the main advantages of the sol-gel process include the ability to form well-defined oxides with excellent homogeneity and the possibility to selectively dope a material with extreme purity [3, 4]. The low cost is also remarkable.

The formation of a powder by the sol-gel route, in general, involves two major steps, the formation of a wet gel, and the drying of the wet gel to form an hydrated powder. The preparation of tin oxide usually starts from water-soluble Sn⁴⁺-containing salts, which yield a gelatinous precipitate of the corresponding hydroxide in alkaline or neutral media (*inorganic route*). Subsequent washing and drying and eventual heating at several hundreds of Celsius degrees produces a white powder of SnO₂. The first authors who reported the preparation of SnO₂ powders by this procedure were Goodman and Gregg [5]. In their work they observed the gel formation during the precipitation by ammonia hydroxide addition in an aqueous solution of SnCl₄. In order to allow the gel formation it has been observed that it is necessary the elimination of NH₄⁺ and Cl⁻ ions by washing in distilled water for a long period (~30 days) [6]. So, while this process works well, the reaction forms salts within the gel that need to be removed by many repetitive washings, which is a long and laborious procedure.

Other form of obtaining SnO₂ by the sol-gel route is through metal alkoxides, as for example the butylate Sn(C₄H₉O)₂ [7]. The process involves the reaction of the metal alkoxide (M-OR) with water, forming a metal hydroxide (M-OH). Alkoxide-based sol-gel chemistry avoids the formation of undesirable salt by-products, and allows a much greater degree of control over the final product. However, alkoxides are expensive, extremely sensitive to heat, moisture and light, and their preparation is time consuming.

In spite of the large quantity of work done in this field, one of the main unknowns in the sol-gel technique is how solutions change over time. It is not known exactly how reaction starts in the solution nor even exactly how the gelation process takes place. Therefore almost all laboratories try to at least follow procedures as reproducible as possible, maintaining constant pH, pressures, temperatures and times.

In principle, after the hydrolysis (the reaction through which the metal hydroxide is formed), a condensation stage takes place. The condensation reaction occurs when two metal hydroxides (M-OH + HO-M) combine to give a metal oxide species (M-O-M), with one molecule of water as by product. The known as sol is a solution of various reactants that are undergoing hydrolysis and condensation reactions. The molecular weight of the oxide species produced, continuously

increases, and it seems that as these species grow, they may begin to link together in a three-dimensional network. The gel point is defined at that point in time at which the network of linked oxide particles spans the container holding the sol. At the gel point, the mixture forms a rigid substance called an alcogel, which consists of two parts, a solid part and a liquid part. The solid part is formed by the three-dimensional network of linked oxide particles. The liquid part (the original solvent of the sol) fills the free space surrounding the solid part. As condensation reactions progress the sol will set into a rigid gel. When a sol reaches the gel point, it is often assumed that the hydrolysis and condensation reactions of the reactant are complete, but this is far from the case as the gel point simply represents the time when the polymerizing species span the container containing the sol. At this point the gel contains a significant number of unreacted alkoxide groups. In fact, hydrolysis and condensation can continue for several times the time needed for gelation and sufficient time must be given for the strengthening of the network. This can be enhanced by controlling the pH and water content of the covering solution. After aging the gel, water is still contained within its pores.

Sometimes the kinetics of the reaction makes the formation of the product impracticably slow at room temperature, often requiring several days to reach completion. For this reason, acid or base catalysts are added to the reaction. The amount and type of catalyst used play key roles in the microstructural, physical and optical properties of the final product. In other cases the opposite occurs, i.e., the reaction occurs too fast. In order to obtain nanometric SnO₂ particles the rate of the reaction has to be well controlled because on the contrary too large crystals would be obtained. In this case, lowering of the temperature of the recipient containing the sol and adding the appropriate catalyst allows the desired control.

3.1.2 Printing versus dipping

Over time, one of the most widely used techniques for the fabrication of thick-film gas sensors has been the sintering of powders. However, current tendency is directed towards the use of dip-coating and screen-printing technologies.

In the *dip-coating* sol-gel method [8-10] a metal oxide film is produced by the hydrolysis of the corresponding metal alkoxide, nitrate or chloride directly on a substrate. The procedure is very simple, consisting in dipping the substrates into the colloidal solution and then slowly withdrawn them from the bath. During pulling, the sol in the meniscus turns to a gel by releasing the solvent and sticks to the substrate in the form of a xerogel film. The thickness of the obtained film depends on the number of dippings and the speed of withdrawal [9]. To turn the xerogel into an oxide and densificate the film, further heating at temperatures ~500°C during some minutes is required. A scheme of the dip-coating apparatus is presented in figure 1.

The pulling process is one of the most important factors determining the characteristics of the film, as many exchanges occur between the liquid phase and the atmosphere through the meniscus. As a consequence drastic control of the atmosphere surrounding the sample appears to be necessary and the work has to be performed in a 'clean room' with environmental parameters kept fixed.

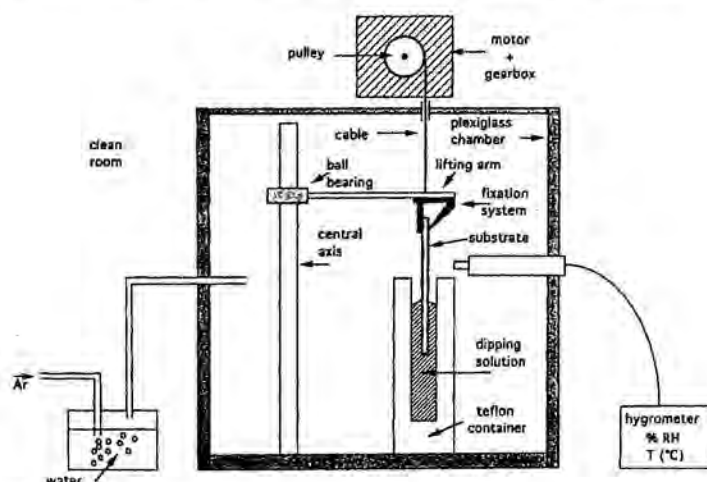


Figure 1: Scheme of the dip coating apparatus. After [10].

The advantages of the dip-coating technique include the possibility of using high-purity starting materials, easy coating of large and complex-shaped substrates (if the angles are not too sharp), the obtaining of high-quality and homogeneous films, mass production and low cost. Moreover, the addition of dopant species is made in a simply way by introducing them directly into the sol. The main disadvantage is the need of environmental control.

The *screen printing* method [11-15] consists in printing a paste containing the SnO_2 powder over the substrate. The procedure is shown in figure 2. The paste is obtained by mixing the SnO_2 sol-gel obtained powder with an organic compound that will aid the binding to the substrate and binding between grains. The size of the area to print depends on the screen-printing machine, but the practical limit for the minimum line width in screen printing is currently about $100\mu\text{m}$. As this technique is widely used for printing of electrodes, some modifications allow to overcome this limit and to print more complex shapes than rectangles. For example, with pad printing [12] the desired pattern, which is etched in a gravure plate, is first flooded with ink and then scraped clean so that ink remains only in the engraved pattern. Subsequently the pattern is picked up and transferred from the plate by a flexible silicone rubber when it is pressed against the substrate. The suitable organic binder has to be used to make the viscosity suitable for this procedure.

Like in the dip-coating process, the films have to be heated at temperatures $\sim 500^\circ\text{C}$ during several minutes in order to densificate the film and evaporate the organic components.

The advantages of screen printing are very similar to those of the dipping technique, as most of them come from the sol-gel process itself. The main inconvenient versus the dip-coating technique is the limited size and shape of the area to print (which depends on the printing machine used). However, a controlled ambient is not necessary and, a higher versatility in the sensor design and miniaturisation are possible.

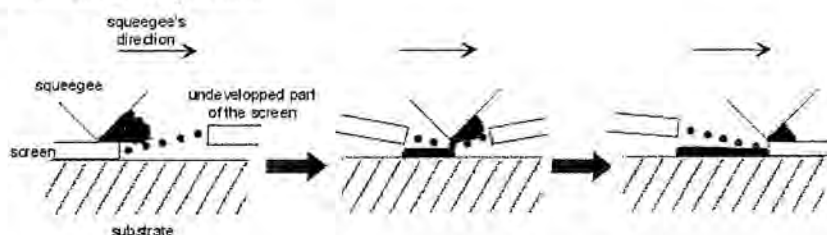


Figure 2: Scheme of the printing procedure. A droplet of the paste is deposited on the screen (a vertically mobile mesh). When squeegee passes over the mesh it pushes the mesh to the surface to be printed and the paste towards hollow of the mesh.

3.1.3 Preparation of powders and sensors for this work

3.1.3.1 Powder preparation

The SnO_2 powders used throughout this work were prepared by the inorganic sol-gel route at the University of Tübingen. One of the main reasons why no commercial powder has been employed is the ability of control of grain size through calcination treatments. To investigate fundamental properties of nanoparticles an initial grain size as low as possible is needed, which can not be attained using a commercial powder as starting material.

Pure SnO_2 was fabricated in two steps. First ultrapure water-free SnCl_4 (Merck) was mixed with water and the resulting mixture was cooled down to 0°C in a bath with ice blocks. The mixture is then added to a water-diluted solution of ammonia, also cooled. The refrigeration of both reaction partners at 0°C becomes enforced in order to reduce the reaction speed and to generate an as fine-grained as possible product. This first step gives rise to an hydrated tin oxide of approximate formula $\text{Sn}(\text{OH})_4$.

After multiple careful washing of the resulting suspension with bidistilled water, the hydrated tin oxide follows a dry process in an oven and a centrifugation of the suspension (Heraeus UT 12) at 80°C . The second production-step to the tin oxide extraction is the oxidation of the hydrated tin oxide. This is attained

maintaining the hydrated oxide some hours (between 8h and 24h) at high temperature (250 to 1000°C) into an oven (Heraeus ROK/A 6/30).

In order to obtain the product with the smallest possible grain size and to eliminate the large agglomerates formed in the powder (undesirable for printing because introduce cracks when drying the paste), some series of the tin hydrated oxide and of the SnO₂ resulting after oxidation were milled in a planetary mill (Fritsch pulverisette 5). For that the powder is mixed with a certain amount of ZrO₂ milling balls in a milling recipient which is turning at high speed (figure 3). Because of the resulting centrifugal acceleration, the ZrO₂ balls impact with strong force against the powder and this is milled. The duration of the milling process is in the range of several hours and after two hour of milling the addition of water is needed. At the end of the process the obtained powder is again dried (at 80°C in the Heraeus UT 12).

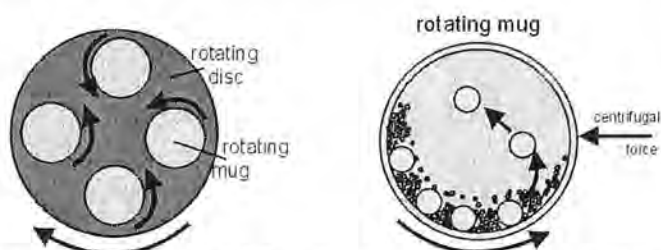


Figure 3: The grinding of the powders was performed, as an aqueous slurry, in a planetary mill with ZrO₂ balls (6 balls, diameter: 10 mm) for up to 20h. Approximately 10ml of slurry was used on 50ml mugs. The rotation speed was 200rpm.

To introduce the noble metal additives, the SnO₂ powder is impregnated with the corresponding metal chlorides (PdCl₂ or PtCl₄). In this way, the necessary amount of metal chloride was thoroughly mixed using a magnetic stirrer (IKA RCT basic) with the calculated amounts of SnO₂ powder and water (40 hours at room temperature). After that an annealing step during 1 hour at 450°C in the Heraeus ROK/A 6/30 was used to reduce the employed metal chloride to pure metal. As noble metal introduction is performed after the calcination step it is expected that the distribution of the dopant atoms will be rather limited to the surface (surface doping). After noble metal introduction powders were submitted to a thermal treatment at 450°C for 1h.

Schematisation of the process and overview of powders

The complete process, including orientative duration of each step is schematized in figure 4. Figure 5 shows schematically a full description of the samples selected to be investigated in this work. A different background has been used to describe the part of the chapter where the samples are of interest. In this

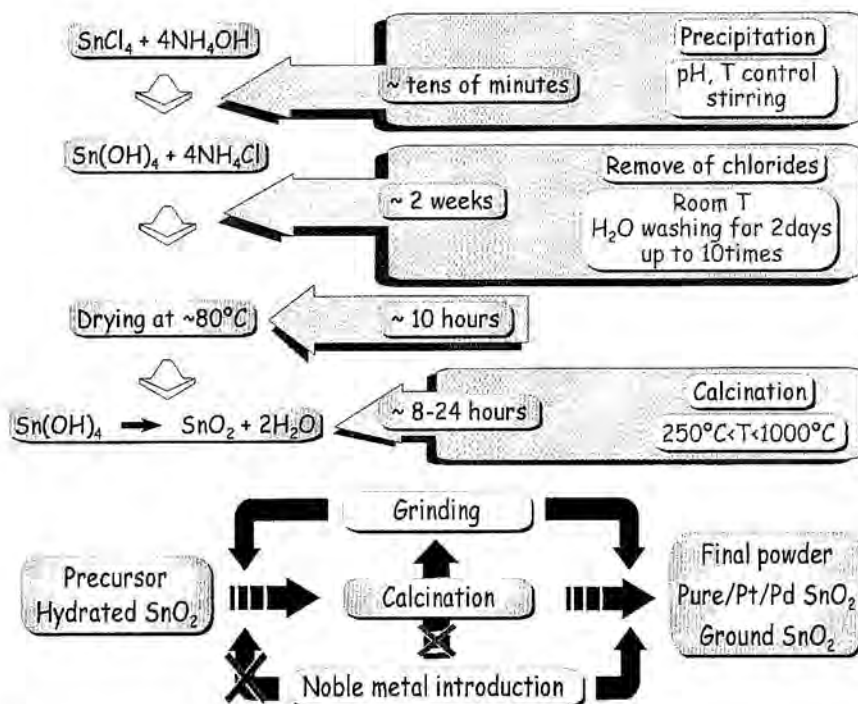


Figure 4: Complete procedure followed to fabricate SnO₂ nanoparticles by the sol-gel route. Orientative times for the duration of each step is indicated. In the up part it is shown the process to obtain the hydrated precursor. In the bottom part is shown the procedure to obtain the final powder from the precursor (with doping and grinding). Note that some possible steps are marked with a red cross because they have not been performed, although are possible.

way, green background corresponds to the set of samples used to analyse the fundamental properties of nanoparticles and general trends as a function of calcination temperature in 3.3. It is necessary to mention that all the powders presented in yellow were submitted to a short grinding step after calcination in order to improve the fabrication of a possible paste. Powders calcinated in the range 450-1000°C, marked in blue, were not ground after calcination. All the samples where noble metal were introduced do not present any special background and will be treated in part 3.4. The set of samples with a red background corresponds to a general investigation of the influence of grinding before or after calcination and calcination time, which will be presented in part 3.5. The samples used to investigate the grinding process in more detail (grinding time) are marked with an orange background and will be treated in part 3.5 also. For better clarity the set of samples treated in each part of the chapter will be presented in table form in the opportune moment.

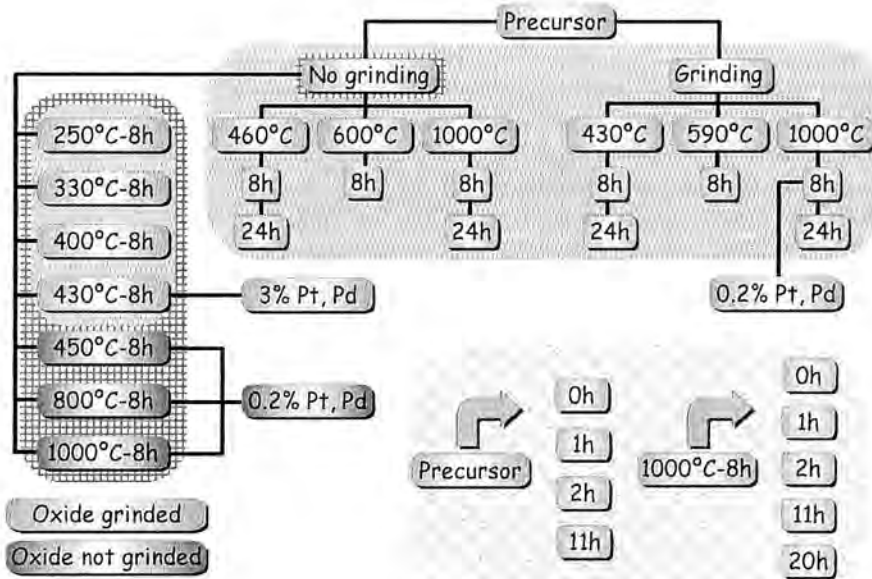


Figure 5: Scheme of all the powder samples analysed in this work grouped by: i) investigation of the calcination temperature and time, ii) investigation of the introduction of additives, and iii) investigation of the grinding process (hydrated oxide and/or calcinated oxide), in the right bottom part of the scheme.

3.1.3.2 Fabrication of the sensors

After the obtaining of the powders, these are mixed with an organic carrier in a magnetic stirrer (IKA RCT basic). For this, the organic carrier is added until the desired consistence of the paste is achieved. After mixing both components for several hours a homogeneous paste is obtained, which can be used directly in the printing machine or can be used to paint the substrates.

For the fabrication of the sensors two types of substrates were used. The first consist of an Al_2O_3 cylindrical substrate. The cylinder is crossed in its interior part by a Pt filament, acting as heater and has the electrodes (Pt or Au) on the surface. In this case the paste is painted on the substrate to obtain the sensors, which will be referred hereinafter as *cylindrical* or *Taguchi type*. An image of one of these gas sensors is presented in figure 6.

The second type were planar alumina substrates (2x2 inches, thickness 0.7 mm, purity 99,6%) with Pt electrodes on the front side and Pt heater on the back side. The electrodes have the typical shape used for conductivity sensors, namely 2 combs opposed one to the other, the so-called interdigital structure. The width of the teeth of the electrodes is 0.2 mm and the distance between the teeth is also 0.2 mm.

Each substrate contained 20 sensors, as is prescribed in order to be able to separate easily the individual sensors. Details of the printing machine and procedure can be found in the thesis of Kappler [16]. The paste was printed by using a full-automatic printing machine (EKRA microtronic II) on a rectangular area of the substrates as shown in figure 7.

In both cases, after some period at room temperature, to allow the paste to settle down, and some short period at 80°C, to perform a first drying, the sensors were next thermally pretreated in order to harden the paste and bond it to the substrate.

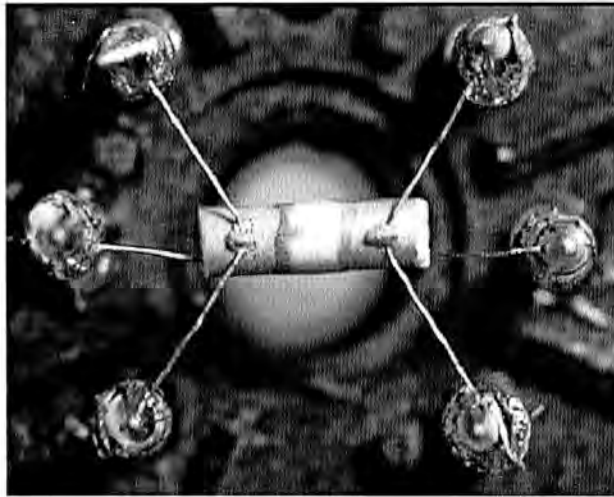


Figure 6: Image of a cylindrical (Taguchi) thick film gas sensor. In this case an asymmetric distribution of the electrodes was used (Pt and Au).

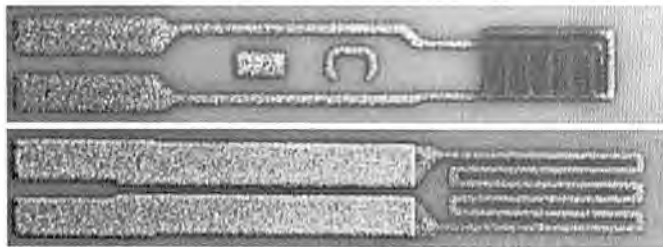


Figure 7: Planar thick film gas sensor. The upper part of this image shows the front side of the sensor on which the SnO_2 layer is printed (dark area). The Pt interdigitated electrodes are visible under the SnO_2 . The lower part of the image corresponds to the backside of the sensor, where the Pt electrodes have been printed. The sensor has such long structure to be mounted in a special socket.

3.2 Structural, vibrational and, electronic properties of SnO₂

The utility of SnO₂ to different parts of the electronics and technological world is known from decades. Without demanding nanometric particles, tin dioxide has been applied extensively to many parts in electric equipment where transparency is required, such as transparent electrodes in solar cells, transparent antistatic coatings and, transparent heating elements. In all cases, although for different reasons, the structural properties of this material and hence its control are of fundamental importance. Thus, thanks to its multiple applications, SnO₂ has been intensively investigated. Their structural, vibrational and electronic properties, when it is in single-crystalline or polycrystalline form, are known, thus, since a long time. Nevertheless, at the actual moment there is a large interest in the properties of nanometric tin dioxide for gas sensing, which change substantially from those that the material posses in single-cistalline or polycrystalline form.

In this section, the structural, vibrational and electronic properties of non-nanometric SnO₂ will be briefly reviewed. For further details one can read a more complete review found for example in the work of Z.M. Jarzebski et al. [17-19]. Afterwards, in the following sections, some characteristics of nanometric SnO₂ will be presented.

3.2.1 Crystalline structure

Tin dioxide is an anisotropic polar crystal that crystallises in the tetragonal rutile structure with point group D_{4h}^{14} and space group $P4_2/mnm$. The mineral form of this material is known as cassiterite. The unit cell contains two molecular units, i.e., six atoms, two tin and four oxygen, as illustrated in figure 8. Each tin atom is at the centre of six oxygen atoms placed approximately at the corners of a regular slightly deformed octahedron. Every oxygen atom is surrounded by three tin atoms, approximately at the corners of an equilateral triangle. The lattice parameters are $a=b=4.737\text{\AA}$ and $c=3.186\text{\AA}$. The c/a ratio is thus 0.673. The ionic radii for O²⁻ and Sn⁴⁺ are 1.40 and 0.71\AA, respectively. The metal atoms (cations) are located at positions (0,0,0) and ($\frac{1}{2}, \frac{1}{2}, \frac{1}{2}$) in the unit cell, and the oxygen atoms (anions) at $\pm(u, u, 0)$ and $\pm(\frac{1}{2}+u, \frac{1}{2}-u, \frac{1}{2})$, where the internal parameter, u , takes the value 0.307. Each cation has two anions at a distance of $\sqrt{2}ua$ (2.053\AA) and four anions at $[2(\frac{1}{2}-u)^2+(c/2a)^2]^{1/2}a$ (2.597\AA). According to the crystalline structure and lattice parameters the corresponding lattice spaces for the different planes are presented in *part A* of the *Annex*. Given the interest to other related structures such as Sn, SnO, ..., which will be treated in *Chapter 4*, their *JPDS* cards are also given in the *Annex*.

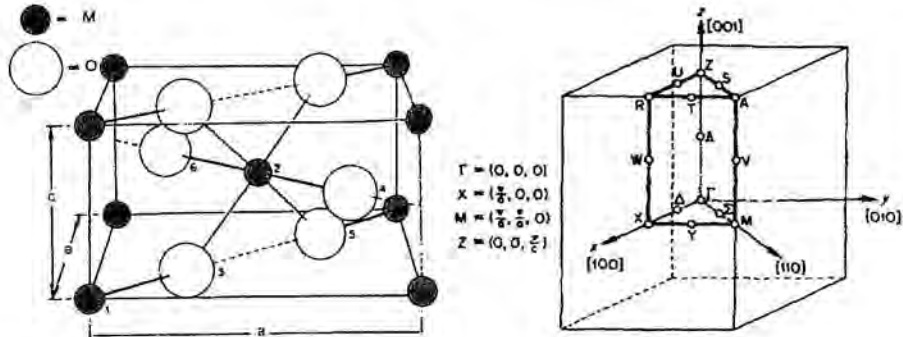


Figure 8: Direct and reciprocal cells of rutile.

3.2.2 Vibrational structure

Correspondingly with six atoms in the unit cell there exist a total of 18 branches for the vibration modes in the first Brillouin zone. The mechanical representation of the normal modes of vibration at the centre of the Brillouin zone is given by [20, 21]:

$$\Gamma = \Gamma_1^+(A_{1g}) + \Gamma_2^+(A_{2g}) + \Gamma_3^+(B_{1g}) + \Gamma_4^+(B_{2g}) + \Gamma_5^+(E_g) + 2\Gamma_1^-(A_{2u}) + 2\Gamma_4^-(B_{1u}) + 4\Gamma_5^-(E_u) \quad (1)$$

where we have used the Koster notation and, in parenthesis, the notation used commonly by the spectroscopists, which indicates the symmetry of the vibration. The last will be used thoroughly this work.

Of these 18 modes 3 are acoustical and 15 are optical modes. Of the optical modes, 2 are active in infrared (the single A_{2u} , and the triply degenerate E_u), four are Raman active (three non-degenerated modes A_{1g} , B_{1g} , B_{2g} , and a doubly degenerate E_g), and two are silent (A_{2g} , and B_{1u}). One A_{2u} and two E_u modes are acoustic. In the Raman active modes oxygen atoms vibrate, while Sn atoms are in rest (see figure 9 of figure 1 in [22]). The non-degenerated modes, A_{1g} , B_{1g} and B_{2g} , vibrate in the plane perpendicular to the c axis, while the doubly degenerated E_g mode vibrates in the direction of the c axis. The B_{1g} mode consists in a mode of rotation of the oxygen atoms around the c axis, taking part all the six oxygen atoms of the octahedra in the vibration. In the A_{2u} infrared active mode, Sn and oxygen atoms vibrate in the c axis direction, and in the E_u mode both, Sn and O atoms, vibrate in the plane perpendicular to the c axis. The silent modes correspond to vibrations of the Sn and O atoms in the direction of the c axis (B_{1u}), or in the plane perpendicular to this direction (A_{2g}).

The corresponding calculated or observed frequencies of the optic modes, according to the literature, are presented in table I. However, it has been observed that when the size of the SnO_2 crystal is reduced, the infrared spectrum is modified,

resulting from dependence of the interaction between the electromagnetic radiation and the particles on their size and shape, as well as on their state of aggregation [26-29]. From the point of view of Raman spectroscopy, experimental modification of the spectrum has also been reported, at least partially. Low frequency bands have been observed previously in SnO₂ [30]. On the other hand, several authors have reported the existence of several bands not observed in single-crystalline or polycrystalline SnO₂, which have been found to be intimately related to grain size [31-34]. However, some of these previous observations lack of sufficient justification about the origin of the abnormal spectrum. The aim of section 3.3.3 of this chapter will be to present the complete Raman spectrum of SnO₂ nanoparticles.

A _{1g}	B _{2g}	B _{1g}	A _{2g}	E _g	A _{2u}		B _{1u}	E _u		REF
					TO	LO		TO	LO	
638	782	100 [*]	398 [*]	476	477	705	140 [*] 505 [*]	244	276	[23]
								293	366	
								618	770	
					465	704		243	273	[24]
								284	368	
								605	757	
634	776	123		475						[25]

Table I: Frequencies of the different optical modes of SnO₂. Three references have been considered enough to report all of them. In the three references large crystals were examined. Superscript * indicates that the value has been calculated.

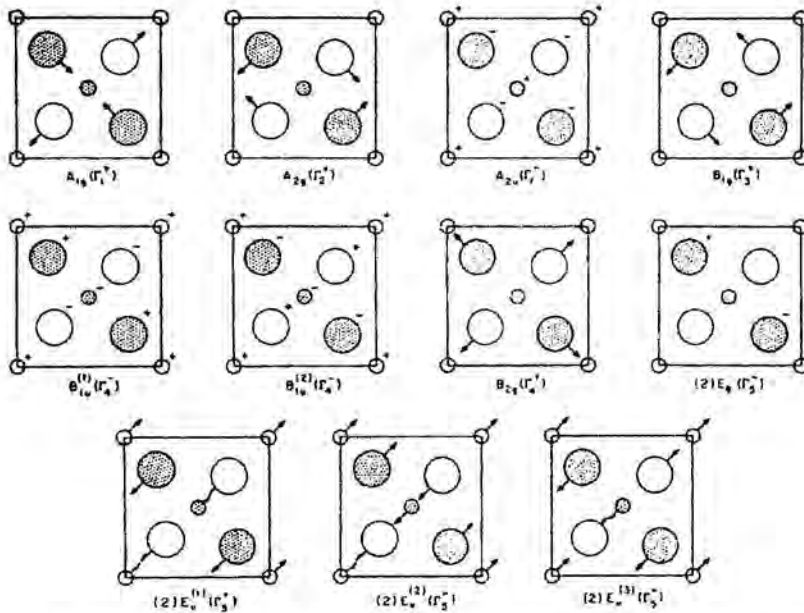


Figure 9: Vibrations in rutile. Small circles represent metallic atoms. Large circles represent oxygen atoms.

3.2.3 Electronic properties

It is generally agreed that SnO_2 in its undoped form is an n-type, wide-bandgap semiconductor. The lowest conduction band has its minimum at the Γ point in the Brillouin zone and is a 90% tin s-like state. The upper valence band consists of a set of three bands (2^+ , 3^+ and 5^+). The valence band maximum is a Γ_3^+ state. In this way, SnO_2 has a direct bandgap, with energy $E_{dir}(\Gamma_{3v}^+ - \Gamma_{1c}^+) = 3.596\text{eV}$ for E_{\perp} and 3.99eV for E_{\parallel} , measured at 4K. Figure 10 shows the band diagram for SnO_2 .

The projection of the density of states (DOS) for the 1-states of Sn and O is presented also in figure 10. According with Ph. Barbarat et al. [35] a large contribution of Sn(s)-states is found at the bottom of the valence band between -7 and -5eV . Then, from -5eV to the top of the valence band, the Sn(p)-states contribution is decreasing, as the Sn(d)-states are found to occupy the top of the valence band. A large and extended contribution of the O(p)-states is found in the valence band. Clearly, bonding between Sn and O is predominated by the p-states of the latter. Each anion in the unit cell is found to be bonded to the cations in a planar-trigonal configuration in such a way that the oxygen p orbitals contained in the four-atom plane, i.e., p_x and p_y orbitals, define the bonding plane. Consequently, the oxygen p orbitals perpendicular to the bonding plane, i.e., p_z orbitals, have a non-bonding character and are expected to form the upper valence levels [35]. The conduction band shows a predominant contribution of Sn(s) states up to 9eV . Then, for energies larger than 9eV , an equal contribution of Sn- and O-states is found in the conduction band.

Because we will not deal with the electronic structure of SnO_2 , we will not extend more in this respect. More information, mainly about the valence band, can be found in [36-38] and references therein.

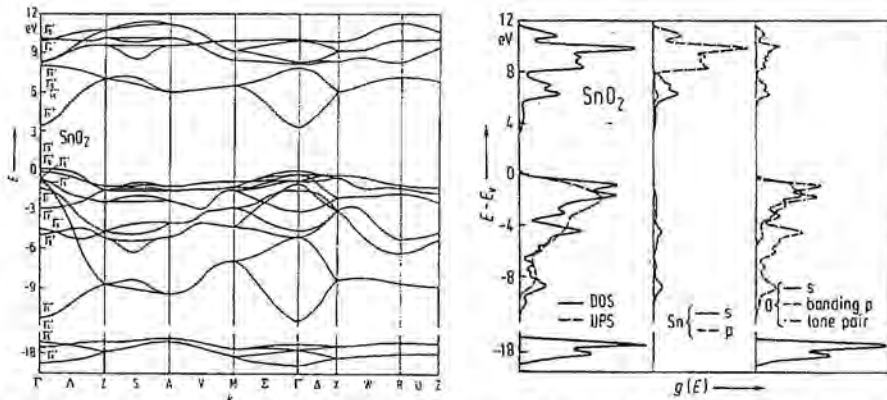


Figure 10: Band diagram of SnO_2 (left) and projection of the DOS for the 1-s states of SnO_2 , Sn and O (right). After [35].

3.2.4 Interrelating structure and gas sensing: Defects and surface structure of SnO₂

It is widely known that non-stoichiometry in SnO₂ leads at least to the appearance of two native shallow donor levels with energies at 0.03-0.034eV and 0.14-0.15eV below the conduction band edge, which seem to result from single and double ionisation of oxygen vacancies [39, 40]. Beyond the role of bulk oxygen vacancies to actuate as donor centres, the existence of other donor centres has also been suggested as a consequence of tin interstitials [40], and outlined the role played by of other defects such as the terminate place of Coherent Twin Boundaries and their steps [41]. It is clear that any type of non-punctual defect, including dislocations, twins and stacking faults, will probably actuate generating centres at the bandgap, which will modify the electronic properties of the material (at least the position of the Fermi level), an could affect the sensing capabilities in gas sensors. However, little is known about this topic at the moment.

As commented in *Chapter 1*, gas sensing is a phenomena related, to large extent, to the surface of the sensing material. In this respect it is important to make some comments about the surface properties of tin dioxide crystals. It is obvious than in a polycrystalline sample (as used in gas sensing) several facets will form the surface of the particles. However, the (110) surface is the most stable face of this semiconducting oxide (the face with lowest energy) and, therefore, the dominant orientation in polycrystalline samples. On the other hand, it has been shown that the (110) surface forms three successive ordered phases as a function of the temperature when annealing in vacuum, with 4×1 , 1×1 , and 1×2 LEED periodicities [42, 43]. These surfaces form irreversibly, being maintained when the sample is cooled to room temperature. Moreover, under oxygen atmosphere the 4×1 surface converts to a 1×1 , as a result of oxidation at high oxygen pressures [44]. These different reconstructions have been explained in terms of ordered patterns of surface oxygen vacancies. So, the defect structures for the different reconstructions is different and hence the adsorption of oxygen as well. Concretely, it has been observed that 4×1 and 1×1 surfaces are more conductive and more reactive under certain temperature conditions [44]. So, the above commented studies on surface reconstruction demonstrate that oxygen vacancies at the surface can also influence the conductivity, as bulk vacancies do. As commented by C.F. Cox and coworkers [45], oxygen vacancies or oxygen deficiencies on the (110) surface can increase the surface conductivity by more than two orders of magnitude with respect to the bulk conductivity. The same authors demonstrate that the surface vacancies existing under 1×1 reconstruction introduce also donor electronic states in the bandgap.

To conclude, something is known about the role of bulk oxygen vacancies in the electronic and thus probably sensing properties of SnO₂. However, little or practically nothing is known about the modifications of the electronic states of SnO₂

introduced by defects (mainly the structure of the core of dislocations and twin terminations). Moreover, it is clear that there exist several ways of finishing the surface through different facets, besides the (110) being the most probable, each facet could terminate in different reconstructions, which would give rise to different types of oxygen vacancies and surface conductivities. As can be clearly understood, there is a great complexity in relating the structural characteristics and sensing properties in SnO₂, but is necessary in order to understand the sensing capabilities of SnO₂ based gas sensors.

3.3 Effect of the calcination temperature on the properties of SnO₂ nanoparticles

In this part of the chapter the main characteristics of the nanoparticles as a function of calcination temperature will be discussed. Concrete information about nanoparticle characterisation will be also given. For this study we will focus on the set of samples presented in table II.

CODE	Calcination		Grinding		Metal
	T _{calcination} (°C)	t _{calcination} (h)	Before (h)	After (h)	
ART	RT	--	--	--	--
A250	250	8	--	2	--
A330	330	8	--	2	--
A400	400	8	--	2	--
A430	430	8	--	2	--
A450	450	8	--	--	--
A800	800	8	--	--	--
A1000	1000	8	--	--	--

Table II: List of samples for the analysis of the influence of calcination temperature.

3.3.1 General evolution

The typical aspect of the SnO₂ powders is presented in figure 11 and 12. Figure 13 shows the Transmission Electron Diffraction Patterns corresponding to some of the powders analysed. From the diameter of the rings, the corresponding plane spacings can be deduced. These are 0.33, 0.26, 0.23, 0.21, and 0.18nm, respectively, for the first 5 rings, and are in agreement with the spacings of [110], [101], [200], [210], and [211] planes for the tetragonal phase of SnO₂, even in the case of the as-obtained powder. As it is clear from figure 13a, the as-obtained powder consists of very small crystalline particles of approximate spherical shape with a high degree of agglomeration. However, in spite they are crystalline, a high degree of surface and internal disorder is observed also in these nanoparticles, visible through the distortion of the lattice planes in the HREM images.

In order to analyse the grain size distribution, TEM has been used, as this technique gives a direct description through simple visual inspection. Nanoparticle size evolves from ~3nm to ~100nm from the as-obtained material to that calcinated at 1000°C (figures 14 and 15). Two different growth regimes are found below and above ~400°C. Below 400°C, the rate is quite low ($\sim 8 \cdot 10^{-3}$ nm/°C), while above the grain size strongly increases ($\sim 14 \cdot 10^{-2}$ nm/°C). As calcination temperature increases, it is observed also a spreading of the size distribution (figures 14 and 15), the faceting of the particles and an increase of lattice ordering (crystalline quality). The powders annealed at temperatures below ~400°C are mainly quasi-spherical in shape, being the size and shape of the crystallites quite uniform. As commented above, calcination at higher temperatures gives rise to a strong increase of the average grain

size, which is accompanied by a large broadening of the size distribution and by the development of flat surfaces. Explanation can be given by taking into account that when the annealing temperature is large enough, the atoms at the surface are redistributed in such a manner that the total energy of the system is decreased, normally by faceting of the crystallite through the formation of planes with minimum energy at their surface.

TEM also reveals qualitative changes in the density and type of defects present in the powders with the different annealing temperatures (no quantitative measurements have been done due to the intrinsically experimental difficulty in performing these measurements on polycrystalline and disperse samples). The defects present in the smaller nanoparticles are mainly dislocations. After annealing at 450°C a large quantity of twins appear, although dislocations and other types of planar defects have also been observed (see figures 16a and 16b). Annealing at 800°C or higher, twins are still observed (figure 16c), but in a much lower density compared with those appearing in the powder annealed at 450°C. It has to be mentioned that the mechanism of twin formation at low and high temperatures could be different. While for the former, defects can appear during the reorganisation of atoms in the grain and remain during coalescence at low temperatures, in the latter it is the coalescence mechanism of the grains, which might produce the twins. It is this reason that explains why the density of defects diminishes with increasing the annealing temperature. At higher temperatures atoms continue reorganising their positions, the crystalline quality increasing through decreasing of lattice disorder, and the defects inside the grains can vanish, while other defects such as twins can develop due to the coalescence of several grains with different orientations. In the low temperature regime the natural disorder of the particles can facilitate the coalescence avoiding the appearance of planar defects. At 1000°C the density of defects in the powder is comparable with that of the annealed at 800°C.

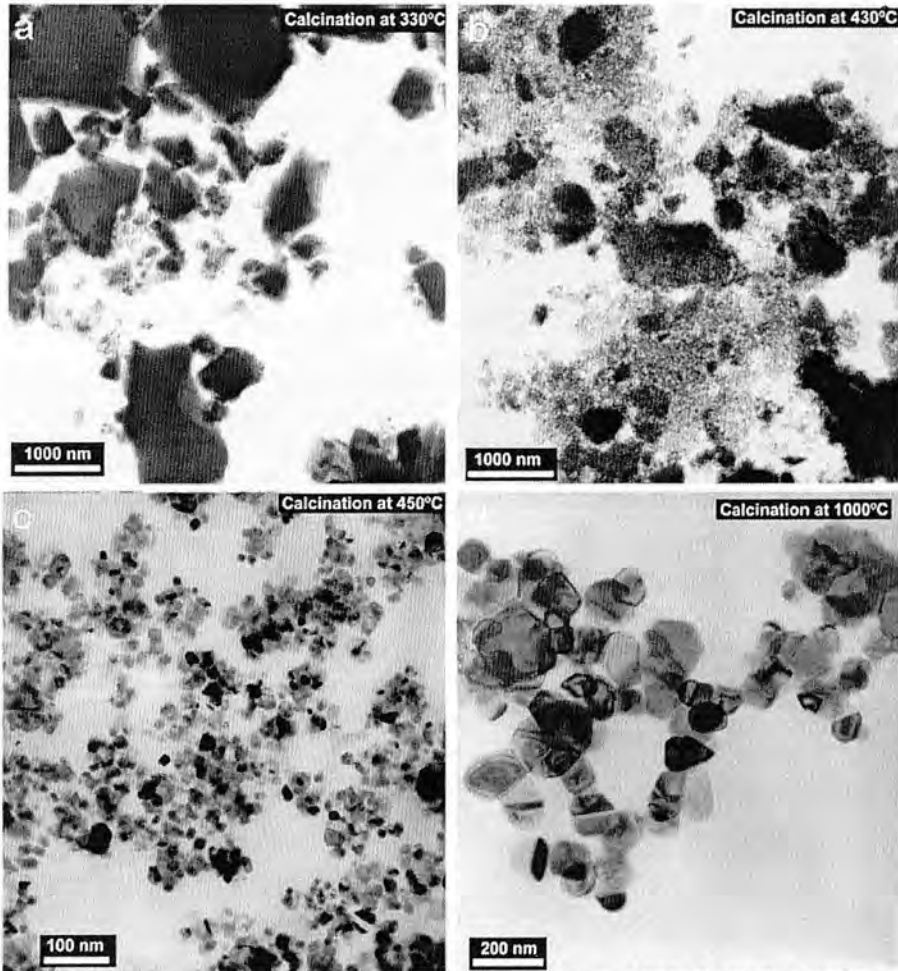


Figure 11: TEM images of the powders after calcination for 8h at: a) 330°C, b) 430°C, c) 450°C, and 1000°C. It is clear in these images the decrease of the state of agglomeration of the nanoparticles with the increase of calcination temperature.

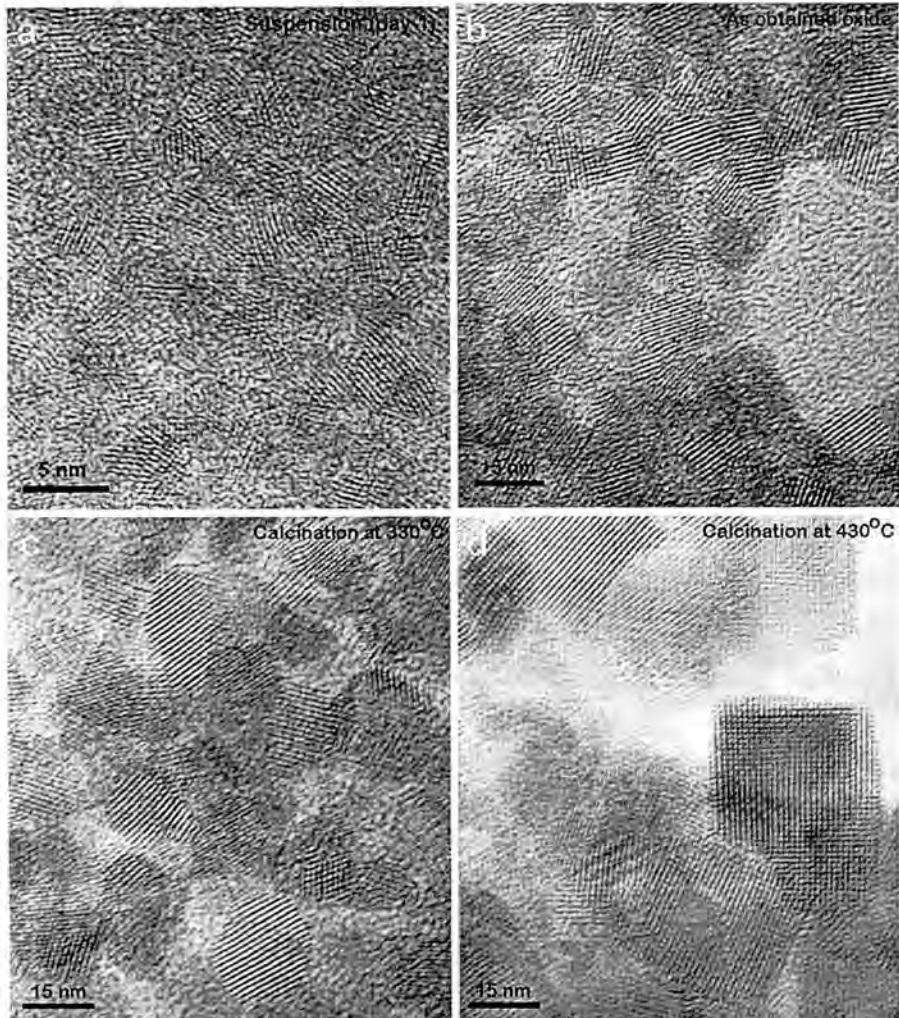


Figure 12: TEM images of some of the powders studied. Images from a) to d) correspond to HREM images of the powders showing the evolution of disorder (visible through the distortion of the crystalline lattice), faceting, and evolution of grain size. In figures e) and f), they are shown two images corresponding to the powders calcinated at 800 and 1000°C. In that images is clear the increase of grain size and faceting. Moreover, they are observed grains with apparent plate-like shape. (Continues).

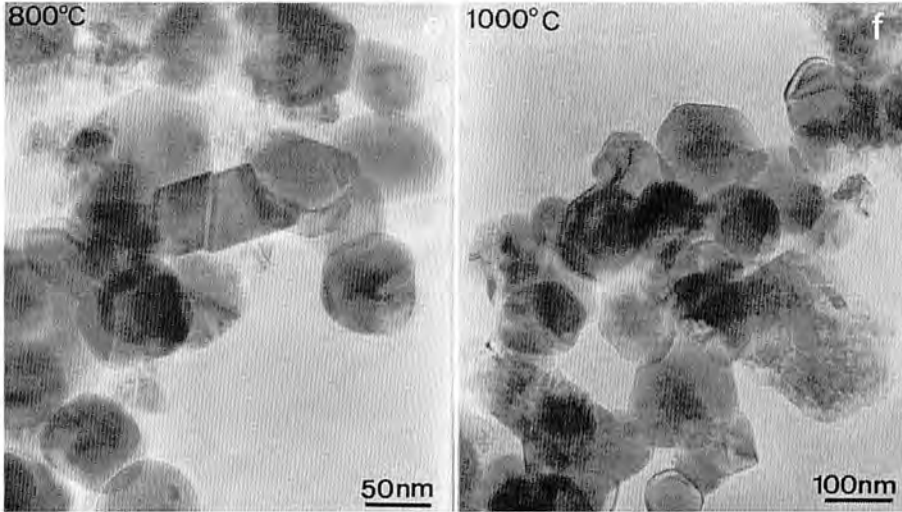


Figure 12 (cont.)

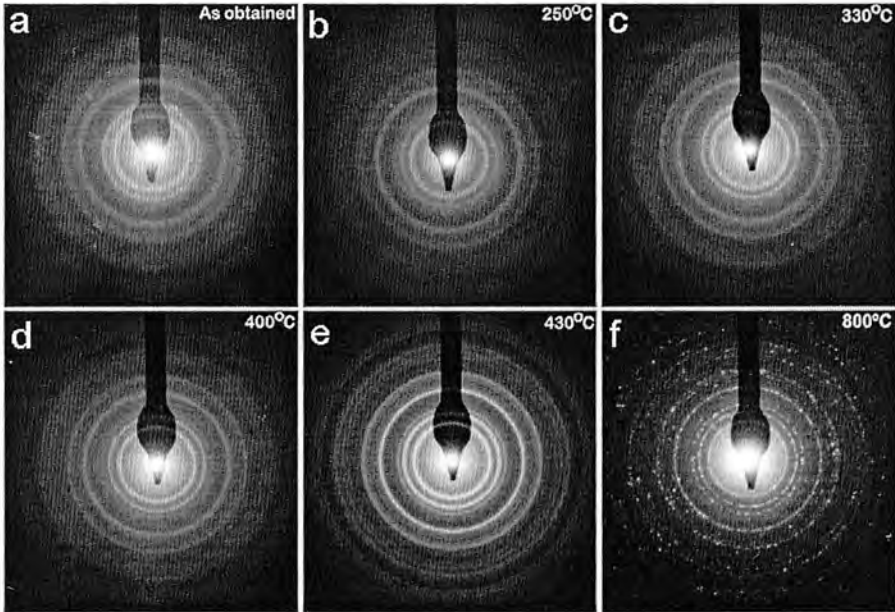


Figure 13: TED of the powders analysed. From a) to f) correspond to the uncalcinated powder, and to those calcinated for 8h at 250, 330, 400, 430, and 800°C. With the increase of calcination temperature, rings are narrow, indicating the increase of grain size. At 800°C rings are constituted by individual spots (large grain size and particles oriented randomly).

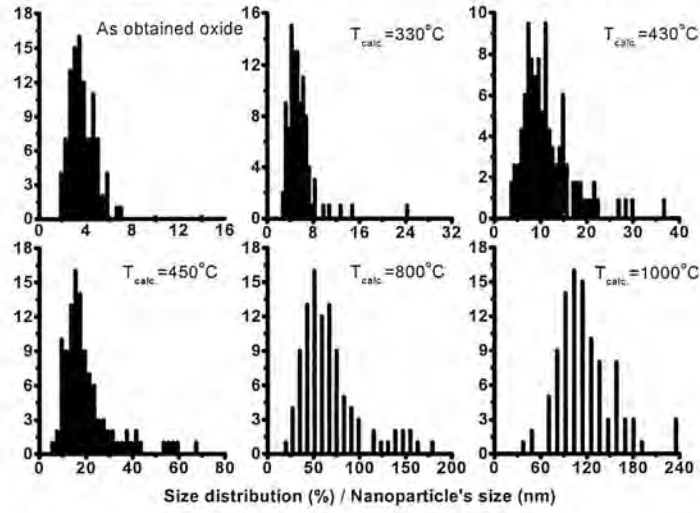


Figure 14: Size distributions. With the increase of calcination temperature, the distribution is wider and the average nanoparticle size larger. Note the shape of the histograms with the peak not centered, which is characteristic of coalescence.

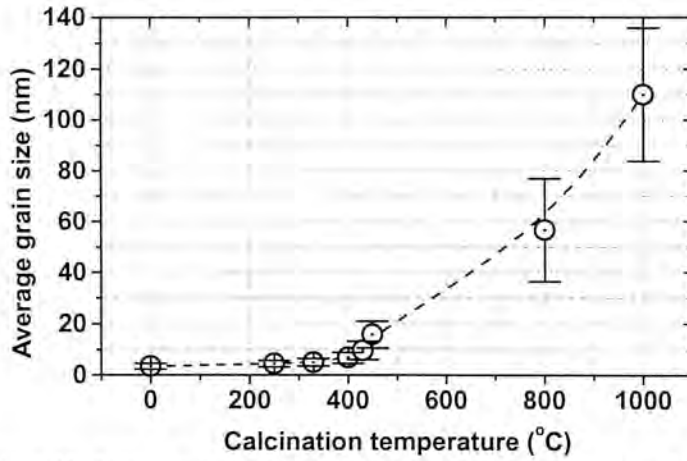


Figure 15: Average grain size as a function of calcination temperature, and size dispersion (vertical error bars).

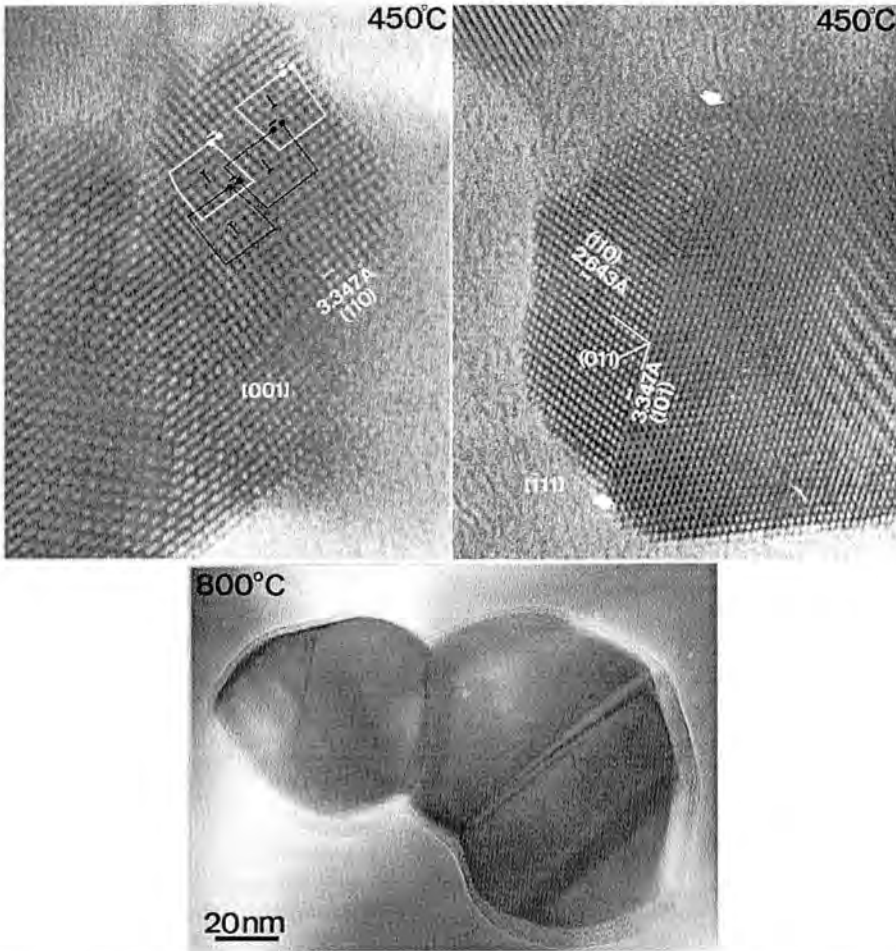


Figure 16: High resolution TEM images of the powder calcinated at 450°C for 8h (top), and TEM image of the powder calcinated at 800°C for 8h (bottom). Two dislocations (dislocation line and Burgers circuit) and a twin are characterised in these HREM images. The appearance of twins increases with calcination temperature as a consequence of coalescence (see for example the TEM image of the sample calcinated at 800°C). Nevertheless, the density of defects is qualitatively lower. Sometimes they are observed nanoparticles covered by an amorphous layer (bottom).

The XRD reflections appearing in the spectra presented in figure 17 confirm the results obtained by TEM, i.e., the SnO_2 powders are crystalline with the tetragonal rutile structure (cassiterite), even for the as-obtained hydrated oxide. The main feature of the spectra is the narrowing and intensity increasing of the XRD peaks with the increase of the calcination temperature, related mainly to grain size

increase but also to a higher crystalline quality. Confirmation of strong lattice disorder in the smaller nanoparticles and its evolution with calcination temperature is obtained through the monitoring of the lattice parameters a and c , evaluated from the shift of the peaks in the XRD spectra (figure 18). It is found again that approximately at 450°C nanoparticles consist already of a well defined and ordered lattice.

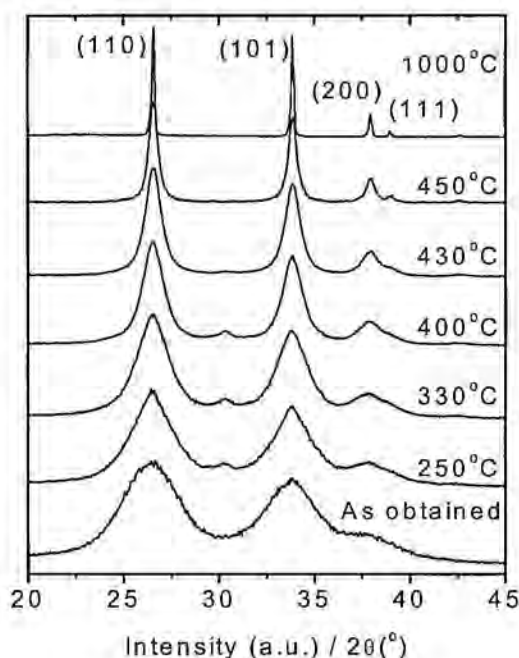


Figure 17: XRD profiles of the powders calcinated up to 1000°C. Features of the spectra are the sharpening and shift of the diffraction peaks with increasing calcination temperature.

Beyond the typical bands of SnO₂ in the region 300-700cm⁻¹, the FTIR spectra, presented in figure 19, show the presence of bands due to water and hydroxyl groups. Moreover, other features are observable because of the powder structure of the material. These are the ascent of the absorbance curves when going to higher wavenumbers, and the rapid change of the absorbance in the region between 3500 and 3750 cm⁻¹. The first is due to the dispersion of light by the agglomerates of particles or by the holes between agglomerates. The second is due to a pole in the dielectric function. This pole appears as a consequence of the observation of both TO and LO modes. Because IR measurements were done in transmission with normal incidence, only the TO modes should be observed. In the

case that the incidence was not normal or the measurements were done in reflection (where non-normal incidence is used to be able to collect the reflected light), both TO and LO modes could be observed. In our case, in spite incidence is normal, because of the dispersion of light by the material some LO modes appear in the spectra.

Because of the particular features of the vibrational spectra of SnO_2 and the large quantity of work made on this respect, the FTIR and Raman spectra require special comments, which will be given in parts 3.3.2 and 3.3.3 of this *Chapter*, respectively.

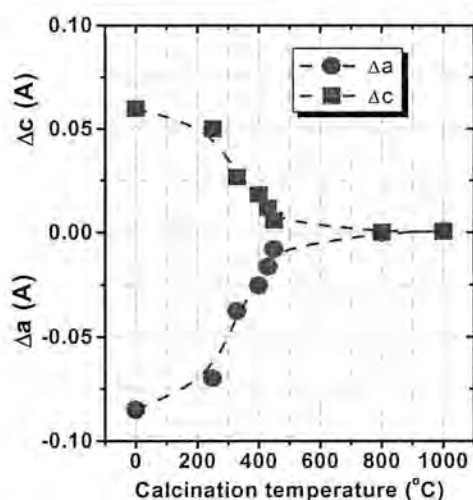


Figure 18: Variation of the lattice parameters, a , and c , as a function of the calcination temperature (nanoparticle size).

3.3.2 Particular aspects of the FTIR spectra

3.3.2.1 Influence of morphology and aggregation on the spectra

It is well known that the 4 IR active modes have expected positions for single-crystalline SnO_2 (table I) at A_{2u} at $\omega=465\text{cm}^{-1}$ and E_u at $\omega=243$, 284, and 605cm^{-1} . However, it is also accepted that the shape and state of aggregation of the particles together with the matrix in which they are embedded produce variations in the position, relative intensity and width of the IR absorption bands in microcrystalline polar solids [26-28, 46-47]. Such variations are due to polarisation charges induced at the surface of the microcrystals by their interaction with the electromagnetic field of

the incident radiation. To model it, the Theory of the Average Dielectric Constant (TADC) has been employed [26-28]. According to this theory, the absorption coefficient of small absorbing particles embedded in a matrix is given by:

$$K = \frac{\omega I(\epsilon_{av})}{C n_{av}} \quad (2)$$

where $I(\epsilon_{av})$ stands for the imaginary part of the average complex dielectric constant of the composite medium formed by the solid and the matrix and n_{av} is the real part of the average complex refractive index of the same medium. ϵ_{av} is computed as:

$$\epsilon_{av} = 1 + \frac{3(1-f)(\epsilon_m - 1) + \sum_k f_k (\tilde{\epsilon}_1^k + \tilde{\epsilon}_2^k + \tilde{\epsilon}_3^k)}{3(1-f) + \sum_k f_k (\hat{\epsilon}_1^k + \hat{\epsilon}_2^k + \hat{\epsilon}_3^k)} \quad (3)$$

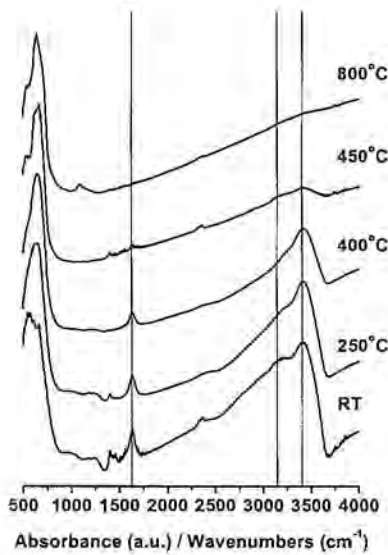


Figure 19: FTIR spectra of some of the specimens of the set of samples. Vertical lines indicate the regions of vibrations of water and hydroxyl groups.

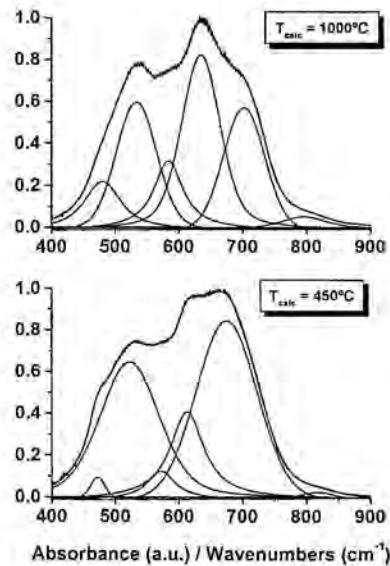


Figure 20: Fitting of the different contributions of the SnO₂ IR active modes according to the TADC. Peaks are observed at 481, 534, 584, 635, 702, and 796cm⁻¹ for calcination at 1000°C, and at 473, 523, 572, 613, and 672cm⁻¹ for the powder calcinated at 450°C.

where f is the filling factor, i.e., the fraction of the total volume occupied by the particles, which are assimilated to ellipsoids. f_k is the filling factor of the k th type of ellipsoid with $f = \sum f_k$ and

$$\tilde{\varepsilon}_i^k = (\varepsilon_i - 1) \hat{\varepsilon}_i^k \quad (4)$$

$$\hat{\varepsilon}_i^k = \frac{\varepsilon_m}{\varepsilon_m + g_i^k (\varepsilon_i - \varepsilon_m)} \quad (5)$$

where $\varepsilon_i(\omega)$ is the dielectric constant of the absorbing material, $\varepsilon_m(\omega)$ the dielectric constant of the matrix, and the subscript i runs from 1 to 3, the principal axes of the dielectric tensor of the solid, which are assumed to be coincident with the three principal axes of the ellipsoid. g_i are the shape or depolarisation factors, having values between 0 and 1 and such that $g_1 + g_2 + g_3 = 1$, where the subscripts refer to each principal axis. Therefore, f accounts for the agglomeration of the particles, while g accounts for their shape. For uniaxial crystals $g_1 = g_2 = g_\perp$ and $g_3 = g_\parallel$. When $g_\parallel \rightarrow 0$ represents long prolates (elongated ellipsoids or cigars) and $g_\parallel \rightarrow 0.5$ represents flat oblates (plate-like shape or pancakes). A value of 0.333 corresponds to spherical particles. On the IR spectra the main effect of the filling factor is to change the total intensity of the infrared bands, while the shape factor affects the peak positions.

In this way, the deconvolution of the absorbance spectra of the powders (figure 20) leads to interpret different shapes of the particles according to the results obtained by TEM and figure 21. The FTIR spectra of the powders annealed at 800° and 1000°C are practically identical. For these powders, as already was seen by TEM in the powder annealed at 1000°C, some particles are plate-like, which is confirmed by the presence of bands corresponding to the mode A_{2u} at 635cm⁻¹ and E_u at 702cm⁻¹. As also expected, quasi-spherical particles are evident through the presence of the mode A_{2u} at around 584cm⁻¹ and slightly elongated ellipsoids are accounted through the same mode A_{2u} at 534cm⁻¹. So, these bands are not associated to different modes of the SnO₂ but to the same mode consequence of different morphologies of the particles. As could be expected from the TEM results, for the powder annealed at 450°C the deconvolution of the spectrum not shows the existence of the plate-like morphologies observed in the powder annealed at 1000°C. This spectrum could be interpreted as a sum of contributions for quasi-spherical particles (slightly elongated and plate-like) at 523, 572 and 613cm⁻¹ for mode A_{2u} and at 675cm⁻¹ for mode E_u , which are positions displaced from the mode A_{2u} found approximately at 473cm⁻¹ and mode E_u at 613cm⁻¹.

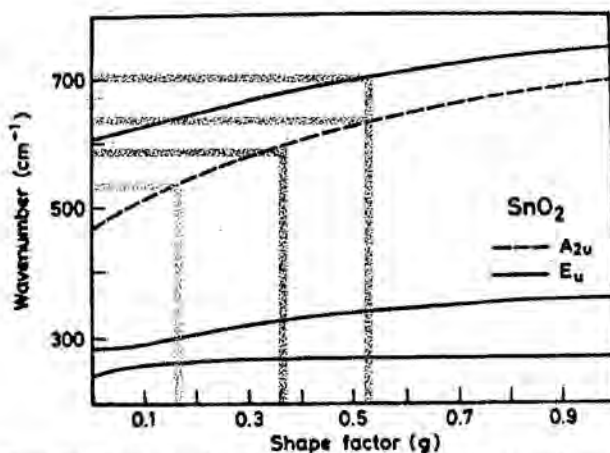


Figure 21: Evolution of the SnO_2 vibrational modes with shape factor, g . After [27]. Color lines correspond to the powder calcinated at 1000°C . Red (right): plate-like; Blue (middle): spherical; Green (left): elongated ellipsoids.

These results are interesting from the fact that the FTIR spectra can account for the shape and state of aggregation of the particles through the TADC. However, their relevance to structural characterisation of nanoparticles for gas sensing finalises at this point, as the same results can be extracted by TEM, which is a more secure method and which will be used extensively through this work. Specialists in IR spectroscopy could use this model to, knowing the shape and filling factors from TEM, calculate real dielectric functions.

3.3.2.2 Water desorption

The FTIR spectra of the nanoparticles show, beyond the typical features of SnO_2 commented in the previous section, hydroxyl as well as water absorption bands. They are easily identified as a very broad band from *ca.* 3700cm^{-1} to *ca.* 1700cm^{-1} (centered at 3200cm^{-1}) corresponding to the unsymmetrical hydroxyl stretching vibration of molecular water physisorbed at the surface of the nanoparticles, and the band at *ca.* 1630cm^{-1} corresponding to the bending vibrational mode, also of water molecules physisorbed on the nanoparticle surface. The bands observed in the range $850\text{-}1550\text{cm}^{-1}$ are identified as hydroxyl deformation modes of different types of surface hydroxyl groups, and the band superposed to that of the unsymmetrical hydroxyl stretching vibration of molecular water at *ca.* 3440cm^{-1} corresponds to the vibration of isolated surface hydroxyl groups. The very small bands at $\sim 2420\text{cm}^{-1}$ correspond to CO vibrations.

The evolution of water in the powders as a function of calcination temperature is important because the quantity of water and hydroxyl groups influences the quality of the nanoparticles, and hence, the stability of the sensor. Internal water and surface hydroxyl groups can produce large changes in the sensor response when the sensor is operated as a consequence of their evaporation. On the other hand, the existence of surface hydroxyl groups can affect also the sensing properties of the nanoparticles, as molecules other than the expected gas ones occupy the surface. Moreover, as commented in *Chapter 1*, hydroxyl groups can bond, forming water, and desorb at certain temperatures.

In this respect, it is interesting to observe the evolution of the water content in the powders, for example, through the band at $\sim 1630\text{cm}^{-1}$. As can be observed in figure 22, water content is maintained for calcinations up to 330°C for 8h. For larger temperatures, it decreases steeply and disappears for calcination performed at temperatures higher than 450°C during 8h.

Table III shows the percentage of water loss found in this work, separated into those corresponding to the isolated OH groups and of those OH of molecular water. It is also presented the ratio of O/Sn extracted from XPS spectra. For comparison we also show the phenomena occurring according to the thermogravimetric and infrared studies of SnO_2 gels prepared by Harrison et al. [48], and the estimated formula of the compound according to the work of Giesecke et al. [6].

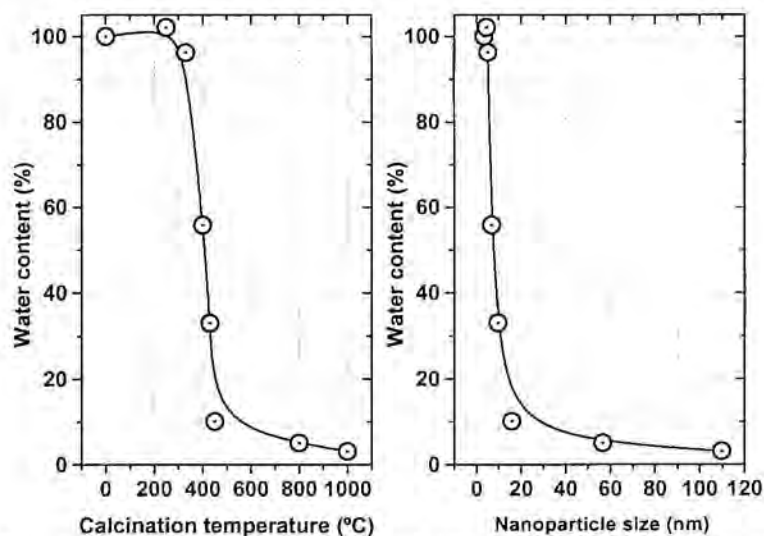


Figure 22: Evolution of water content as a function of calcination temperature and nanoparticle size.

Finally, it is worth to remember that the regions below and above 430-450°C are characterised by different growth rates, as well as by a substantial difference in water and isolated hydroxyl groups contents. It is reasonable to think that they are the surface OH which hinder grain growth, because atoms from neighbouring particles can not migrate to incorporate from one grain to the other. The disappearing of these groups is accompanied by the strong faceting of the grains and by a change in the growth mode, probably determined by coalescence.

T	Ref [48]	Ref [6]	Lost _{OH}	Lost _{water}	O/Sn _{XPS}
RT					
100-150°C	Physisorbed water is released	Sn ₂ O ₃ (OH) ₂ ·H ₂ O			
150°C	Condensation of surface hydroxyl groups				
250°C		Sn ₂ O ₃ (OH) ₂	7%	44%	1.24
330°C	Formation of strained Sn-O-Sn bridges at the surface	Sn ₄ O ₉ H ₃	15%	55%	1.36
400°C			40%	74%	1.28
430°C	Almost all hydroxyl groups on the SnO ₂ surface desorbed		55%	81%	1.31
450°C		Sn ₃ O ₁₆ H ₂	67%	90%	1.97
800-1000°C		SnO ₂	>90%	>97%	1.95-2.16

Table III: Percentage of water and OH groups lost at each temperature of the total, extracted from the FTIR spectra. It is also shown the ratio Sn/O extracted by XPS and approximate formulation and processes taking place taken from the literature.

3.3.3 The complete Raman spectra of nanometric SnO₂ particles

The complete Raman spectrum of SnO₂ nanoparticles obtained by sol-gel is presented and analysed in this part of the chapter. Beyond the normal modes observed by Raman spectroscopy in the rutile structure, two different regions have been found to present Raman activity for very small nanoparticles. The Raman bands appearing in the low frequency region have been attributed to acoustic modes related to the vibration of the individual nanoparticles as a whole. The high frequency region results active as a consequence of activation by disorder. The analysis of both regions, as well as the modification of the normal modes of SnO₂ will be analysed in detail as a function of the size of the nanoparticles. Therefore we will study: i) the modification of the normal vibration modes active in Raman when the spectra is obtained from nanocrystals of SnO₂ ('classical modes'), ii) the disorder activated surface modes in the region around 475-775cm⁻¹, and iii) the appearance of the acoustic modes in the low frequency region of the spectra.

Figure 23 shows the complete Raman spectrum of the powders of table II. For clearer inspection the spectra have been divided in two regions. Powders composed of nanoparticles with size smaller than ~7nm present bands in the low frequency region (figure 23 left). For the larger particles (T_{calcination}=1000°C), the Raman spectra has contributions only in the high-frequency region, being observed the 'classical' modes of SnO₂. However, with decreasing nanoparticle size below ~16nm, other contributions are visible also in the high-frequency zone (figure 23

right). To show them, a typical fitting of all the contributions in this regions is presented in figure 24 for the powder calcinated at 400°C. As a summary, nanoparticle size, together with the frequencies of the different bands appearing in the spectra are presented in table IV.

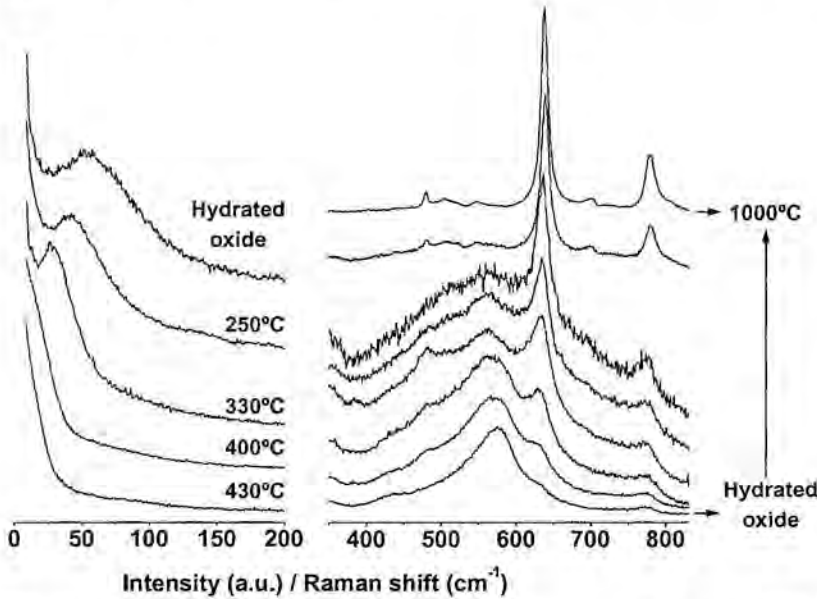


Figure 23: Raman spectra of the powders calcinated up to 1000°C for 8h. The spectra have been divided in the low frequency region (left) and the high frequency region (right). The spectra in the high frequency region correspond from bottom to top to the uncalcinated powder, and the powders calcinated at 250, 330, 400, 430, 450, 800, and 1000°C for 8h. Additional features were not observed out of these regions.

Therefore, it can be observed that the Raman spectrum depends in a large extent of the temperature at which the initial obtained oxide was calcinated, i.e., of the size of the nanoparticles. The general features of the spectra consist in:

1) The mode A_{1g} shifts to lower wavenumbers as nanoparticle size decreases. At the same time the modes B_{2g} and E_g approach to A_{1g} , i.e., shift to lower and higher wavenumbers, respectively. However, the variation of the mode E_g is very small. The shift is accompanied by a broadening of the band. Mode B_{1g} is fairly observed in the smaller nanoparticles and difficult to fit, as a consequence of its very low intensity with respect to the other modes ($0.001 \cdot I(A_{1g})$) [25] and the existence of the low frequency bands.

2) The presence of several bands in the region between 475 and 775 cm^{-1} (named S1, S2 and S3 in figure 24). The intensity of these bands as well as their position depends also of the nanoparticle size. The tendency of bands S1 and S2 is

always to decrease in intensity and position with the increase of nanoparticle size. No evidence of shift has been found in the case of band S3.

3) The appearance of low frequency bands, which position and intensity depend of the size of the nanoparticles. These bands shift to higher wavenumbers and are less intense and broader with decreasing the average nanoparticle size. For particles larger than $\sim 7\text{nm}$ these bands are not observed under simple visual inspection.

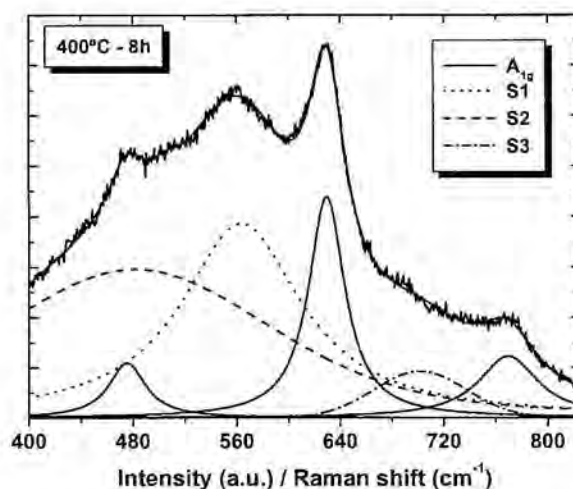


Figure 24: Fitting of the bands appearing in the high frequency region of the Raman spectrum of a SnO_2 powder of very small grain size.

T (°C)	L (nm)	A_{1g}	B_{2g}	E_g	S1	S2	S3 (A_{2u})	A_S/A_{A1g}	LFRB
1000	109.8	637.9	779.2	479.2	--	--	--	--	
800	56.6	637.9	778.9	479.5	--	--	--	--	
450	15.8	635.2	774.2	479.7	568.9	493.2	696.3	1.32	
430	9.6	634.3	774.1	479.6	568.0	501.2	706.9	4.07	16.4
400	6.7	633.9	776.2	479.6	568.1	485.9	705.8	5.82	21.7
330	5.0	633.1	772.9	--	572.0	503.7	691.7	10.02	33.4
250	4.5	631.6	767.7	--	573.3	518.0	--	14.79	44.5
RT	3.5	631.5	--	--	575.8	541.7	--	47.17	58.3

Table IV: Raman shift of the most important bands observed in the spectrum of SnO_2 nanoparticles. Modes A_{1g} , B_{2g} and E_g correspond to the 'classical' vibration modes, while bands S1, S2, and S3 appear as a consequence of disorder activation. LFRB refers to the bands appearing in the low-frequency region of the spectrum. A_S/A_{A1g} corresponds to the sum of the areas of bands S1 and S2 with respect to the area of the band corresponding to the A_{1g} mode. The values given for nanoparticle size result from a high statistics (in some cases more than 500 measurements) and the use of imaging processing software.

In the following the different characteristics of the Raman spectra are explained in detail as a function of grain size and disorder.

3.3.3.1 Classical modes of SnO_2

In an infinite perfect crystal, it is well known that as a consequence of the momentum conservation rule between phonons and incident light, only the phonons near the centre of the Brillouin zone ($q_0 \approx 0$) contribute in the scattering of the incident radiation. As the size of the crystal is reduced, the vibration is limited to the size of the crystal, which gives rise to the breakdown of the phonon momentum selection rule $q_0 \approx 0$, allowing phonons with $q \neq 0$ to contribute to the Raman spectrum [49, 50]. According to the phonon dispersion curves [25], this implies that modes A_{1g} and B_{2g} shift to lower wavenumbers as grain nanoparticle size decreases, while mode E_g shifts to higher wavenumbers, which is precisely the behaviour observed for the nanoparticles of this work. According also with table IV, the B_{2g} mode is the one that varies more quickly. Mode A_{1g} shifts slowly, and mode E_g practically is immobile until a strong confinement is considered.

In the spatial correlation model (also known as phonon confinement model), the localisation of the phonons is described by a weighting function $W(r, L)$ for the phonon amplitude, where L is the size of the nanocrystals, and hence, the vibrational wave function in a nanocrystal can then be approximated by

$$\Psi(\vec{q}_0, \vec{r}) = W(\vec{r}, L)\Phi(\vec{q}_0, \vec{r}) \quad (6)$$

The first-order Raman spectrum of a nanocrystal, $I(\omega)$, is so given by

$$I(\omega) = \int_{BZ} \frac{|C(\vec{q})|^2}{[\omega - \omega(\vec{q})]^2 + (\Gamma_0/2)^2} d\vec{q} \quad (7)$$

where $\omega(\vec{q})$ is the phonon dispersion curve of the infinite crystal, Γ_0 is the natural linewidth, and $C(\vec{q})$ are the Fourier coefficients of the vibrational weighting function expanded in a Fourier integral, which will determine the line shape of the Raman bands,

$$W(\vec{r}, L) = \int C(\vec{q}) e^{i\vec{q}\vec{r}} d\vec{q} \quad (8)$$

$$C(\vec{q}) = \frac{1}{(2\pi)^3} \int W(\vec{r}, L) e^{-i\vec{q}\vec{r}} d\vec{r} \quad (9)$$

In most cases a Gaussian is used as the weighting function to characterise the Raman spectra of nanoparticles [51-55]. In this case [55],

$$W(r, L) = e^{-r^2/L^2} \quad (10)$$

and,

$$\left|C(\vec{q})\right|^2 = \frac{L^6}{16(2\pi)^2 \alpha^3} e^{-q^2 L^2 / 2\alpha} \quad (11)$$

with $\alpha=8\pi^2$.

As below 400-450°C nanoparticles of this work present quasi-spherical shape, it seems to be a good assumption to use this weighting function.

The integral over the entire Brillouin zone can be approximated by an unidimensional integral over a spherical Brillouin zone:

$$I(\omega) \approx \int_0^1 \frac{e^{(qL/4\pi)^2} 4\pi q^2}{[\omega - \omega(q)]^2 + \left(\Gamma_0/2\right)^2} dq \quad (12)$$

where the $4\pi q^2$ term arises from passing to spherical coordinates and integrate over the radius. Hence, the wave vector q and the correlation length L are expressed in units of $2\pi/\langle a \rangle$ and $\langle a \rangle$, respectively, with $\langle a \rangle = (2a+c/3) = 0.422\text{nm}$ being an average lattice constant for SnO_2 . As no data has been reported for Γ_0 , it has been estimated about 11.5cm^{-1} by fitting of the A_{1g} band in the Raman spectrum of the powder calcinated at 1000°C , which is the nearest to a single SnO_2 crystal. For the fitting, it has not been taken into account a convolution of bands due to the size distribution, which should not influence the spectrum due to the large grain size.

For the phonon dispersion curve of the A_{1g} mode we have used a five-degree polynomial fitting of the curve in reference [25]:

$$\omega(q) = A + B_1(q\pi) + B_2(q\pi)^2 + B_3(q\pi)^3 + B_4(q\pi)^4 + B_5(q\pi)^5 \quad (13)$$

with $A=638.22\text{cm}^{-1}$, $B_1=-2.81\text{cm}^{-1}$, $B_2=6.52\text{cm}^{-2}$, $B_3=-7.25\text{cm}^{-3}$, $B_4=0.27\text{cm}^{-4}$, and $B_5=0.21\text{cm}^{-5}$.

In this way, it is plotted in figure 25 the calculated Raman spectra using the spatial correlation model, for nanoparticles of sizes between 10 and 110nm. For particles of size lower than ~10nm there is too much contribution of the limit of the Brillouin zone and calculation gives an exaggerated asymmetrical curve.

In order to allow an easy comparison of theoretical predictions and experimental data, we have plotted the Raman shift and FWHM as a function of nanoparticle size in figures 26a and 26b, respectively. It is observed that for particles larger than 10-15nm there is agreement between model and experiments. However, for smaller sizes, experimental points separate from the calculated ones. Considering that as nanoparticle size decreases, there is an increasing contribution

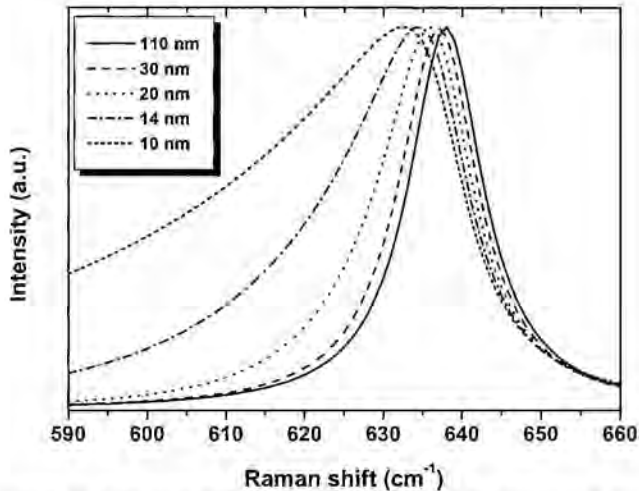


Figure 25: Calculated Raman spectra for the A_{1g} mode according to the Spatial Correlation Model.

not only of the particles with averaged grain size, but of all the size distribution, this result is completely reasonable (In the case of large particles, which present a higher volume for Raman scattering there is no contribution of the size distribution). Other factors that can contribute to the disagreement are the existence of defects, which would reduce the correlation length, L , and the existence of disordered regions contributing partially to the 'classical' modes. In any case, the application of the spatial correlation model is demonstrated for SnO_2 , which can be easily applied to estimate nanoparticle size, by using, for example, figure 26. However, it has to be considered that figure 26 gives larger sizes than those extracted by TEM in the case of particles with size smaller than $\sim 10\text{nm}$.

3.3.3.2 Modes activated by disorder in SnO_2 nanoparticles

It has been commented that in addition to the 'classical' bands, others are visible in the high-frequency region. As can be observed in table IV, the most important of these bands appear at $568\text{-}576\text{cm}^{-1}$ (S1), $486\text{-}542\text{cm}^{-1}$ (S2), and $691\text{-}707\text{cm}^{-1}$ (S3). Of them, S1 and S2 are always the most intense. The shift of the S3 band is attributed more to the difficulty in performing the fitting in that region than to a real shift. In principle, as has been previously reported, this band can be attributed to a disorder activation of the A_{2u} IR active and Raman forbidden mode [34]. The evolution of the bands S1 and S2 with decreasing nanoparticle size (calcination temperature) indicates that they arise as a consequence of reducing particle dimensions or as a consequence of the conversion from amorphous to

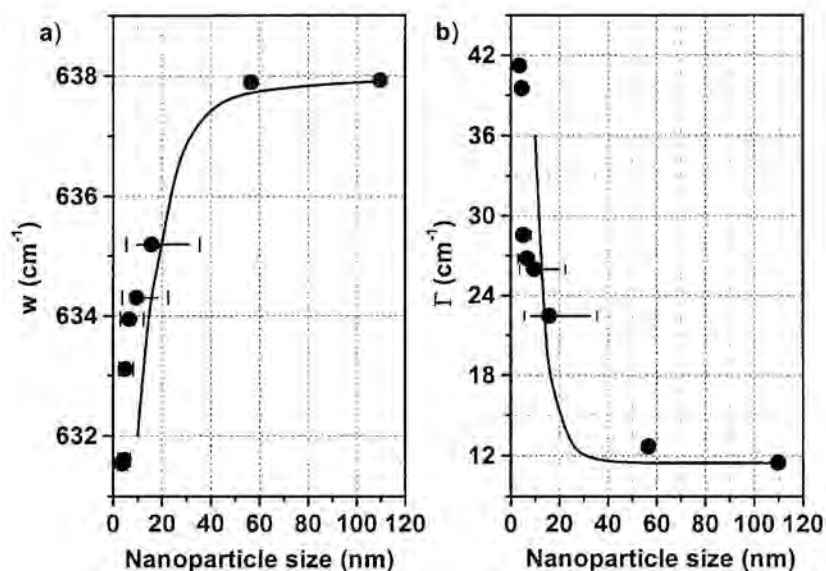


Figure 26: Calculated (lines) and experimental (points) values of the Raman shift and FWHM as a function of nanoparticle size. Horizontal error bars, shown for powders calcinated at 450°C or lower, indicate the dispersion of sizes extracted from the histograms. The position of the points correspond to the average grain size.

crystalline material. However, as nanoparticles are crystalline in the complete range of sizes analysed in this work, the appearance of these bands as due to amorphous material is excluded. Other factors such as phonon-plasmon coupling can be also rejected as it is well known that when SnO_2 nanoparticles have very small sizes, the grain is formed in a large extent by a depletion region when exposed to an atmosphere containing oxygen. So, one can not expect an increase of the contribution of the bands S1 and S2 with decreasing nanoparticle size if their origin is the phonon-plasmon coupling.

On the other hand, in a disordered crystal, crystal imperfections modify the symmetry of the crystal, preventing atoms to vibrate in phase and preventing their displacements to be correlated. The changes in the local symmetry of the crystal make some of the components of the polarizability tensor change even for usually forbidden modes of vibration, i.e., due to the loss in long-range order all phonons are optically allowed and the Raman spectrum should resemble the phonon density-of-states. In an intermediate case, a shift of the 'classical' modes accompanied by a broadening, and the appearance of some of the forbidden modes of SnO_2 should be observed. This is what occurs with modes A_{1g} , B_{2g} , E_g , and A_{2u} . However, bands S1 and S2 do not fit with any of the Raman forbidden modes of SnO_2 , and the appearance of a new mode as a consequence of coupling between modes would not

explain the high contribution of these bands observed in the spectrum of the smaller nanoparticles. On the other hand, it is well known that nanometer-sized crystalline materials are composed by a crystalline component forming the nucleus of the crystallite and an interfacial component corresponding to all atoms situated in the grain boundaries between particles or at their surfaces. The last, usually comprises several atomic layers in which atoms do not have exactly the positions that would correspond according to the crystalline structure of the material, but are slightly displaced. Thus, it is possible that bands S1 and S2 arise from this surface region, which as an approximation, can be considered of constant thickness. To check this hypothesis figure 27 represents the ratio of the summed area of bands S1 and S2 to the area of the band of the A_{lg} mode. By assuming that each nanocrystal is made of a crystalline core of radius r , surrounded by a shell, which is a disordered layer of thickness $(r-d)$, the ratio of the volumes corresponding to the scattering by each component is directly related to the ratio of the areas of the Raman bands:

$$\frac{A_{S1+S2}}{A_{A_{lg}}} \propto \frac{V_{Shell}}{V_{Core}} = K \left[\left(\frac{r}{(r-d)} \right)^3 - 1 \right] \quad (14)$$

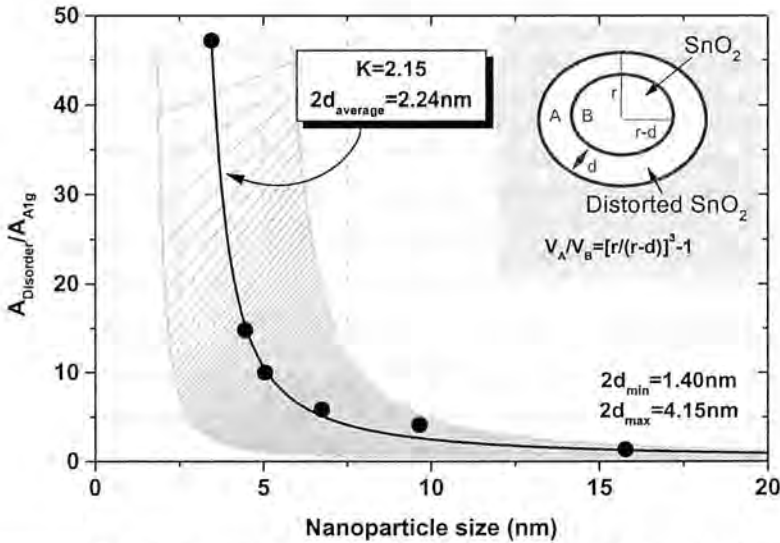


Figure 27: Ratio of the summed area of bands S1 and S2 with respect to the area of the band of the A_{lg} mode as a function of nanoparticle size. The dashed area corresponds to the minimum and maximum grain sizes relevant in the TEM histograms. According to the fitting indicated in the figure, the thickness of the disordered surface region is ~ 1.1 nm.

As observed in figure 27, when reducing nanoparticle size the volume composed by interface and surface material increases with respect to the volume occupied by core material. In this way, one can evaluate an average thickness of the shell, $d \approx 1.1 \text{ nm}$, i.e., approximately 2-3 unit cells of SnO_2 , which is in agreement with the usual thickness found for surface layers [56, 57]. For example, it has been shown that in the concrete case of single crystals of SnO_2 , which is an extreme case, surface reconstruction in the (110) surface involves up to three monolayers of atoms and the presence of oxygen vacancies [43]. This gives rise to a non-stoichiometric SnO_x at the surface, which is plausible to think to be the responsible of producing bands S1 and S2. The reason why this bands are observed in SnO_2 and not in other nanocrystalline semiconductors can be the high reactivity of the SnO_2 surface with the gases in the ambient, as when the surface of the nanoparticles is exposed to H_2S , surface phonon bands are considerably reduced [58]. The same experiments [58] suggest that there is not a direct relationship between Sn-OH bonds, where OH come from water and hydroxyl isolated groups present at the surface of the nanoparticles, as the Raman bands S1 and S2 are recovered after purging of the H_2S gas. The high Raman activity of these bands for very small crystals, which results then from disordered SnO_x and probably from the interaction of surface material with adsorbed oxygen, can be explained according with the works of Hama and Matsubara [59] and Hayashi and Yamamoto [60], which suggest that the Raman enhancement of the shell contribution is caused by the larger vibrational amplitudes and much higher electric field in the shell than in the core.

The calculated value of d corresponds to an average of the thickness of the surface region for all the particles forming the size distribution, assuming that this thickness is similar for all the samples. In principle, although not exact, it seems a better approximation than consider the existence of only one monolayer of atoms in the surface of the nanoparticles [31, 34], especially for the smaller ones.

It is also worth to comment that by taking into account the size distribution and the decrease of the nanoparticles diameter by $2d$, better agreement is obtained for some points in figure 26. However, some other mechanisms have to be considered for particles smaller than 8nm. The existence of surface stresses as a consequence of the bonding of the shell atoms to the core atoms and the presence of adsorbed species at the surface of the nanoparticles could be taken into account for a more exact approximation to this problem. In fact, it has been commented in section 3.3.2.2 the existence of water as well as isolated hydroxyl groups at the surface of the nanoparticles, which both would not be observed under TEM inspection but should have effects on the Raman spectra.

3.3.3.3 Low frequency modes of SnO_2 nanoparticles

The last feature of the Raman spectrum of nanometric SnO_2 are the low-frequency bands observed for particle sizes smaller than 7nm. After correcting for

the Bose-Einstein occupation factor (as the investigation is done in the low-frequency region, the analysis has been performed on the reduced Raman intensity, $I_r = I/[n(\omega) + 1]$, where $n(\omega)$ is the Bose-Einstein occupation factor and I is the observed Raman intensity) and the background and Rayleigh line correction, the resulting spectra gives bands at c.a. 58, 44, 33, 22, and 16 cm^{-1} for particles of 3.5, 4.5, 5.0, 6.7, and 9.6nm respectively. These bands shift to higher frequencies and are less intense and broader with decreasing the average nanoparticle size. Except for the last powder (9.6nm), other very less intense band can be found as a shoulder on the previous band at frequencies around 96, 62, 49, and 38 cm^{-1} . The experimental difficulties in the analysis of these bands mandates to focus the discussion on the principal ones.

Low-frequency bands have been reported already in the case, for example, of Ag particles embedded in SiO_2 thin films [61], CdSe nanocrystals in glasses [62], CdS microcrystals [63, 64], $\text{MgCr}_2\text{O}_4\text{-MgAl}_2\text{O}_4$ crystals in glass [65], and nanosized TiO_2 [66]. In the case of SnO_2 , in spite of the publications related to SnO_2 and Raman spectroscopy, these bands have not been usually reported [31-34].

It seems to be quite clear that low-frequency bands arise as a consequence of the acoustical vibration of the nanoparticle as a whole. To analyse these vibrations it is typical to assume an elastic body of perfectly spherical shape, homogeneous and isotropic. In this way the acoustical vibrations are characterised by the longitudinal and transverse sound velocities, v_l and v_t , respectively. According to the classical theory of Lamb [67] and its extension by Tamura et al. [68], this body has two types of vibrational modes, spheroidal and torsional. The energy associated to these modes is only few cm^{-1} and its effects can be measured in the Low-Frequency region of the Raman spectra. Lamb's theory begins with the equation of motion of a three-dimensional elastic body:

$$\rho \frac{\partial^2 \vec{D}}{\partial t^2} = (\lambda + \mu) \vec{\nabla} (\vec{\nabla} \cdot \vec{D}) + \mu \vec{\nabla}^2 \vec{D} \quad (15)$$

where \vec{D} is the displacement vector, the two parameters λ and μ are Lamé's constants, and ρ is the mass density. This equation is solved by introducing a scalar potential Φ_s and a vector potential $\vec{A} = (r\Psi_t, 0, 0)$, expressed in spherical coordinates. The displacement vector \vec{D} can now be written as $\vec{D} = \vec{\nabla} \Phi_s + \vec{\nabla} \times \vec{\nabla} \times \vec{A}$, obtaining the above mentioned spheroidal and torsional modes. Φ_s is solution of the Helmholtz wave equation and both Φ_s and Ψ_t are proportional to the spherical harmonic $Y_{lm}(\theta, \phi)$.

The spheroidal mode is a vibration with dilatation and its eigenvalue equation in the case of 'stress-free' boundary conditions at the surface of the nanoparticle is given by

$$\begin{aligned}
& 2 \left[\eta^2 + (l-1)(l+2) \left[\frac{\eta j_{l+1}(\eta)}{j_l(\eta)} - (l+1) \right] \right] \left[\frac{\xi j_{l+1}(\xi)}{j_l(\xi)} - \frac{\eta^4}{2} + (l-1)(2l+1)\eta^2 \right] \\
& + \left\{ \eta^2 - 2l(l-1)(l+2) \right\} \frac{\eta j_{l+1}(\eta)}{j_l(\eta)} = 0 \quad \text{for } l \geq 0
\end{aligned} \tag{16}$$

which can be simplified for the particular case $l=0$, to

$$\frac{\tan(\xi)}{\xi} = \frac{1}{1 - \eta^2/4} \tag{17}$$

where $\eta = \omega L / v_t$ and $\xi = \omega L / v_l = \eta v_t / v_l$ are dimensionless eigenvalues, and $j_l(\eta) = \sqrt{\pi / 2\eta} J_{l+1/2}(\eta)$ is the spherical Bessel function of first kind. ω is the angular frequency characterised by the angular momentum quantum number l , and L is the diameter of the nanocrystal. The spheroidal mode is derived from the scalar and vector potentials and its eigenvalues depend on the material through the ratio v_l / v_t . Conversely, the torsional mode is a vibration without dilatation and does not depend on the material because it is derived only from the vector potential.

When the particles are embedded in a matrix the assumption of a 'stress-free' boundary condition can not be justified and a 'rigid' boundary condition has to be introduced, which takes into account the matrix effects and, thus the no displacement at the particle surface. Recently, Saviot et al. [62] considered this last boundary condition and reported for the spheroidal mode:

$$\tan(\xi) = \xi \quad \text{for } l = 0 \tag{18}$$

$$\xi j'_l(\xi) [\eta j'_l(\eta) + j_l(\eta)] - l(l+1) j_l(\xi) j_l(\eta) = 0 \quad \text{for } l \geq 1 \tag{19}$$

For any of the two boundary conditions the parity of \vec{D} for the spheroidal mode is equal to that of the scalar functions Φ_S and Ψ_V , which, at its time, is the same as that of $Y_{lm}(\theta, \phi)$ and, thus, of l . Consequently, only the spheroidal modes for even l are Raman-active modes [63].

In the case of SnO_2 the numerical solving of the previous equations using the average sound velocities of bulk SnO_2 [23], $v_l = 6.53 \cdot 10^5 \text{ cms}^{-1}$ and $v_t = 3.12 \cdot 10^5 \text{ cms}^{-1}$, allows to estimate the frequencies of the Raman lines according to $\omega = S_l v_l / Lc$ for $l=0$ and $\omega = S_t v_t / Lc$ for $l=2$ [65], where c is the vacuum light velocity. The values obtained for S_l and S_t for the 'rigid' and 'stress-free' boundary conditions are presented in table V, where the different values of n arise from the different order of roots of equations 12 to 15. To check to which of these conditions has to be applied the size dependence of the low-frequency bands positions on the inverse of the average diameter of the nanocrystals is presented in figure 28. Lines represent the theoretical dependences for the 'rigid' and 'stress-free'

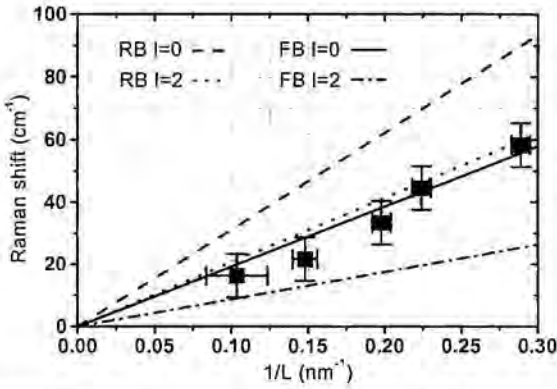


Figure 28: Experimental and calculated Raman shift for the different boundary conditions, as a function of the inverse of nanoparticle size.

boundary condition of the surface modes with $l=0$ and $l=2$. It can be seen that the curves with $l=0$ for the 'stress-free' boundary condition, and $l=2$ for the 'rigid' boundary condition approximate well to the experimental results, i.e., $l=0$ for the 'stress-free' boundary condition, and $l=2$ for the 'rigid' boundary condition.

	'rigid'		'stress-free'	
$l=0$	$S_f=1.430$	$n=1$	$S_f=0.887$	$n=1$
	$S_f=2.459$	$n=2$	$S_f=1.952$	$n=2$
	$S_f=3.471$	$n=3$	$S_f=2.969$	$n=3$
$l=2$	$S_f=1.987$	$n=1$	$S_f=0.844$	$n=1$
	$S_f=2.586$	$n=2$	$S_f=1.638$	$n=2$
	$S_f=3.432$	$n=3$	$S_f=2.760$	$n=3$

Table V: Values of S_f and S_r for the rigid and stress-free boundary conditions of the spheroidal modes for $n=1, 2, 3$. Values have been calculated using *MatLab*.

Experimental discrimination of the 'stress-free' boundary condition could be explained by the fact that only the Raman scattering of the spheroidal mode with $l=0$ is expected to be perfectly polarised and that of all other modes, partially depolarised, because only the spheroidal mode with $l=0$ is perfectly symmetric. In this way, spheroidal modes with $l=0$ are expected to be observed in parallel polarisations only, whereas the $l=2$ ellipsoidal mode should be observed both for parallel and perpendicular polarisations [63]. Because no changes in the shape of the spectra were detected by using HH or HV polarisations, the experimental data would be coherent with the 'rigid' boundary condition and $l=2$. This result would confirm the high agglomeration of the nanoparticles observed by TEM, which act as a powder matrix. According to the results presented in part 3.3.3.2, it could seem that a 'rigid' boundary condition could not be valid. However, the vibrations of the material of the shell of the nanoparticle do not imply that the sphere can not vibrate as a whole being partially fixed at the surface by neighbouring particles [68]. However, it has to be considered that the spheroidal mode with $l=0$ is perfectly polarised only if the nanocrystals are perfectly spherical, which is not the case, as real nanocrystals of 4-7 nm can not be perfect spheres.

Grain size distribution determination by Low-frequency-Raman spectroscopy

Once the correct boundary condition is identified the deconvolution of the theoretical curve with the Raman spectra can be performed in order to have a simple, fast, and non-destructive measurement of the nanoparticle size distribution. In the particular case of SnO_2 , the impossibility to determine the correct boundary condition is not very important, as curves for 'stress-free' boundary and $l=0$ and 'rigid' boundary and $l=2$ are practically identical. This makes that their indetermination do not vary appreciably the extracted grain size distribution. By using an averaged curve, we present in figure 29 the comparison of the grain size distribution obtained by TEM with those obtained with the described process in the case of the as obtained powder and those calcinated at 250 and 330°C.

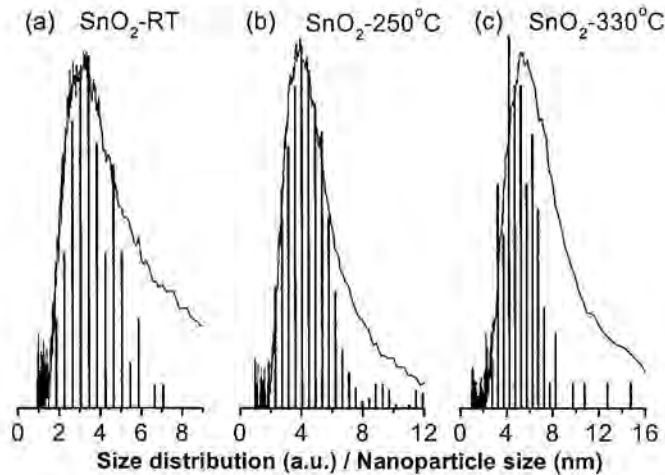


Figure 29: Comparison of the size distribution obtained by TEM (histograms) and LFR (curves).

The agreement is excellent in the sense that the nanoparticle size distribution obtained by Raman spectroscopy is an envelope of that obtained by TEM, especially for the smaller nanoparticles. The nanoparticle size thus obtained according by LFR are 3.5, 4.4, 5.6, 8.8 and 11.4 nm for the as obtained SnO_2 and the powders calcinated at 250, 330, 400, and 430°C respectively. For the larger nanoparticles, the peak position shifts to lower frequencies, approaching to the laser line and the spectrum is more influenced by the Rayleigh contribution, which strongly increases the uncertainty of the results. Furthermore, as already indicated, faceting and deagglomeration occurs for the samples calcinated at 400 and 430°C and, thus, their shape and boundary conditions are different. Nevertheless, the

results presented in this work show that Raman spectroscopy can account for the monitoring of the nanoparticle size and distribution for nanoparticles in the range of sizes considered more interesting for gas sensing by some authors. Higher calcination temperatures give rise to coalescence mechanisms and the strong increase of the nanoparticles size, thus producing the appearance of the Raman peak positions at frequencies too low to be used.

3.3.4 Comparison of grain size obtained by different techniques

In this chapter we have presented several methods to evaluate grain size. TEM, the direct method, gives accurate estimation of the whole size distribution if enough statistics are used. However, this technique implies the preparation of the sample, which is not a major problem in the case of powders, but is destructive in the case of sensors. XRD gives without much complications the average grain size, and the whole distribution could be obtained with more or less complicated procedures. The experimental preparation requires correction for instrumental broadening (obtained for example with a sample 50% Si, 50% boemite in a previous measurement) and mounting the powders in a powder holder or in a capillar. After measurement, the average crystallite size can be estimated by fitting for example the [110] reflection with pseudo-Voigt functions or averaging multiple fittings of different reflections. Finally, we have presented in this work three methods to analyse grain size by Raman spectroscopy, which is a non-destructive technique which requires no sample preparation.

In order to compare the different techniques and their reliability we present the average grain size extracted by TEM, XRD and Raman spectroscopy in table VI.

T _{Calc.} (°C)	L _{TEM}	L _{XRD}	L _{Raman} (SCM)	L _{Raman} (LFR)
RT	3.4	2.5	8.7	3.5
250	4.4	3.4	9.3	4.4
330	5.0	4.3	11.6	5.6
400	6.7	6.3	13.5	8.8
430	9.2	9.1	14.2	11.4
450	15.7	16.5	16.7	--
800	56.6	52.9	62.5	--
1000	109.8	69.7	110	--

Table VI: Grain size extracted by TEM, XRD, and Raman. The XRD value has been averaged from the value calculated with the [110] and [101] reflections using $K=0.9$. The Raman value according to the Spatial Correlation Model has been calculated by averaging those values extracted from ω and $\Delta\omega$ of figure 26.

As it is clear, the results show only a slight agreement between the different techniques. There is no doubt that TEM gives the most accurate result and the complete size distribution. XRD would be only used to estimate grain size for an initial analysis or to see the tendency of grain size when varying some parameters of

fabrication. The same occurs for the spatial correlation model, which only agrees with TEM for large nanoparticles. Finally, Low-Frequency Raman spectroscopy gives a good description of the average grain size and size distribution in the case of very small nanoparticles, which are indeed the preferred in gas sensing. It has to be considered that the existence of defects and strain is directly reflected in the Raman spectra through variations in the FWHM and shift respectively. XRD also presents influence of these effects. For large nanoparticle sizes the accurate determination of the experimental broadening has also large effects on grain size estimation by XRD.

3.4 The addition of noble metals

According with section 3.3, in order to have a starting material for sensor fabrication of good crystalline quality, and hence good stability, it is necessary that powders are calcinated at temperatures higher than 450°C. For lower calcination temperatures, water as well as isolated OH desorption and ordering of the crystalline lattice of SnO₂ can make the sensor response to drift with time. It is also important for the discussion of this section to remark that powders calcinated at 450°C or above do not present the existence of necks connecting grains, at least in an appreciable manner. Thus, changes in conductivity will arise mainly as a consequence of Schottky barrier controlled conduction or tunneling through grain boundary barriers. Indeed, in spite of the high degree of agglomeration of powders resulting of lower calcination temperatures, no physical connection through necks was observed.

In the present part, the main objective will be to improve selectivity by introducing catalytic materials (Pt and Pd) on the SnO₂ nanoparticles. This implies to search for the better sensitivities to selected gases and lower sensitivities to others. For this, we will use sensors fabricated with powders calcinated at temperatures $\geq 450^\circ\text{C}$. The investigation will comprise two parts. In the first one we will analyse the electrical behaviour of sensors without catalytic additives and with Pt or Pd to search for the better sensitivity to CO and NO₂. As the general aim of this work is not to perform a detailed electrical characterisation we will use the electrical results to the exposed purpose only. Afterwards, in the second part, we will search how these noble metals distribute on the SnO₂ nanoparticles and we will try to correlate electrical and structural behaviour.

Table VII shows the set of powders used for the analysis. Sensors were fabricated from each powder in the table, as well as from the corresponding pure powders. For powders calcinated at 450-1000°C two types of sensors were fabricated, with Taguchi and planar geometries.

CODE	Calcination		Grinding		Metal
	T _{calcination} (°C)	t _{calcination} (h)	Before (h)	After (h)	
A430Pt/Pd	430	8	--	2	3% w. Pt, Pd
A450Pt/Pd	450	8	--	--	0.2% w. Pt, Pd
A800Pt/Pd	800	8	--	--	0.2% w. Pt, Pd
A1000Pt/Pd	1000	8	--	--	0.2% w. Pt, Pd

Table VII: 'Doped' samples.

3.4.1 Influence of noble metal additives and calcination on the sensor response

Figure 30 presents the sensor resistance in synthetic air (base resistance), resistance under exposure to 100ppm of CO, and resistance under exposure to 2ppm of NO₂, for the Taguchi type sensors of table VII with Pt electrodes. The values of sensor resistance to the presented concentration of gases were extracted from measurements like that presented in figure 31. The measurements consist in exposing the selected sensor to pulses of CO of varying concentration allowing the sensor to reach a stationary response during each pulse. Afterwards CO pulses are suppressed and the procedure is repeated for NO₂. The humidity conditions were set to 50% r.h. and the measurement temperature was varied between 170 and 420°C by applying a voltage to the heater electrodes between 2.5 and 3.75V, respectively.

Similarly, figure 32 presents the sensor signal to the same gases and concentrations 100ppm CO and 2ppm NO₂. For these graphs sensor signal has been defined as usual, i.e., R_{air}/R_{gas} for reducing gases like CO, and R_{gas}/R_{air} for oxidising gases like NO₂. From the trend of the curves, it is clear that in the case of NO₂, the temperature of maximum sensitivity is below the measured range for all sensors, except for the one corresponding to calcination at 1000°C and 0.2% wt. Pd doped. The temperature of maximum sensitivity to CO is always within the measured range. In the case of sensitivity to CO the general trend is to decrease the temperature of maximum sensitivity with the introduction of the noble metals.

3.4.1.1 Sensor resistance

As can be seen in figure 30, for the three calcination temperatures and dopings, the general effect of exposing to CO or NO₂ is the one expected according to what has been exposed in *Chapter 1*. Resistances are lower under an atmosphere containing CO, and higher under an atmosphere containing NO₂. In the case of exposure to air, resistance increases when going from 170 to ~300°C, reaches a maximum and drops for higher temperatures of measurement. This behaviour is typically explained by the change of the species ionosorbed at the surface of the SnO₂ grains, as was commented in *Chapter 1*.

For simplicity it is plotted in figure 33 the sensor resistance in air measured at 170°C (the lowest temperature available) for the sensors calcinated at the three temperatures. The next conclusions can be drawn:

- The increase of resistance with increasing calcination temperature (nanoparticle size)
- The lower resistance for the pure material and increasing resistance with Pt and Pd addition

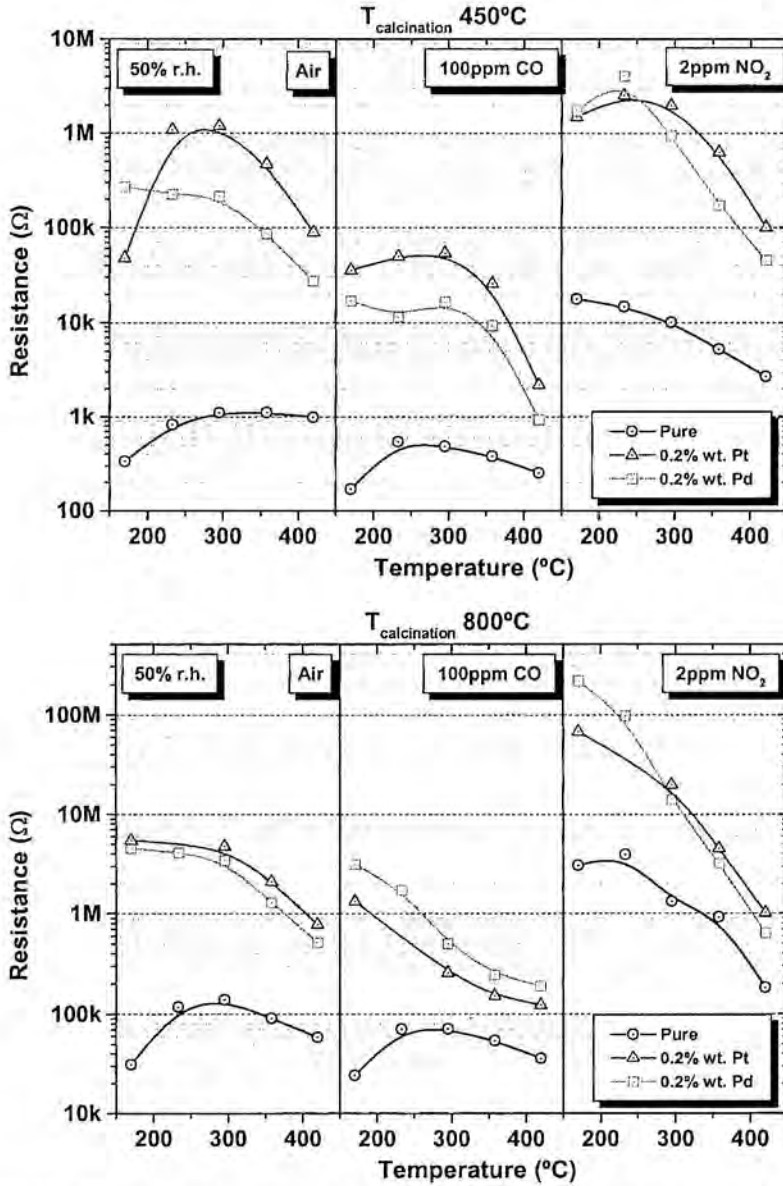


Figure 30: Resistance in air, 100ppm CO and 2ppm NO₂ for the sensors prepared with powders calcinated at 450, 800, and 1000°C for 8h, pure, and with 0.2% Pt or Pd.

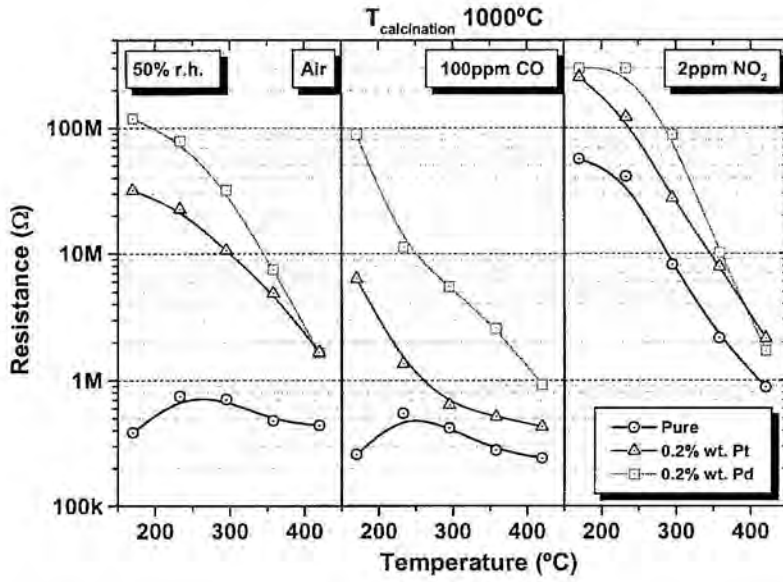


Figure 30 (cont.): Resistance in air, 100ppm CO and 2ppm NO_2 for the sensors prepared with powders calcinated at 450, 800, and 1000°C for 8h, pure, and with 0.2% Pt or Pd.

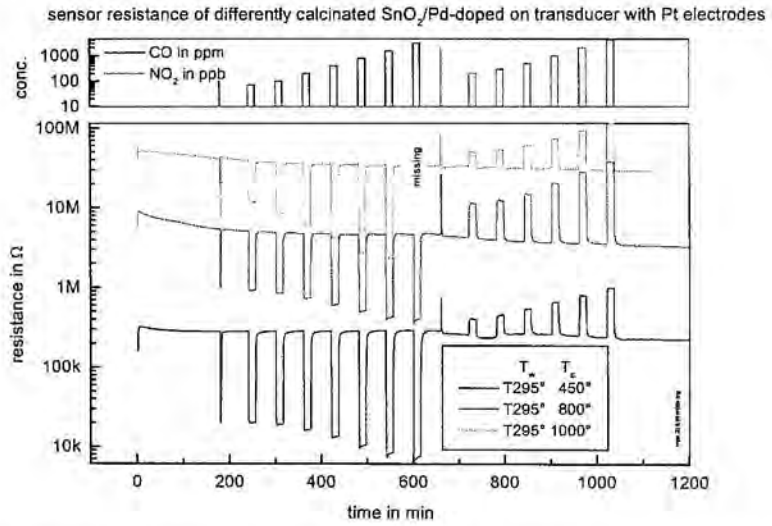


Figure 31: Raw signal showing the resistance of a 0.2% wt. Pd doped sensor calcinated at 450, 800, and 1000°C to varying concentration of CO and NO_2 , over time.

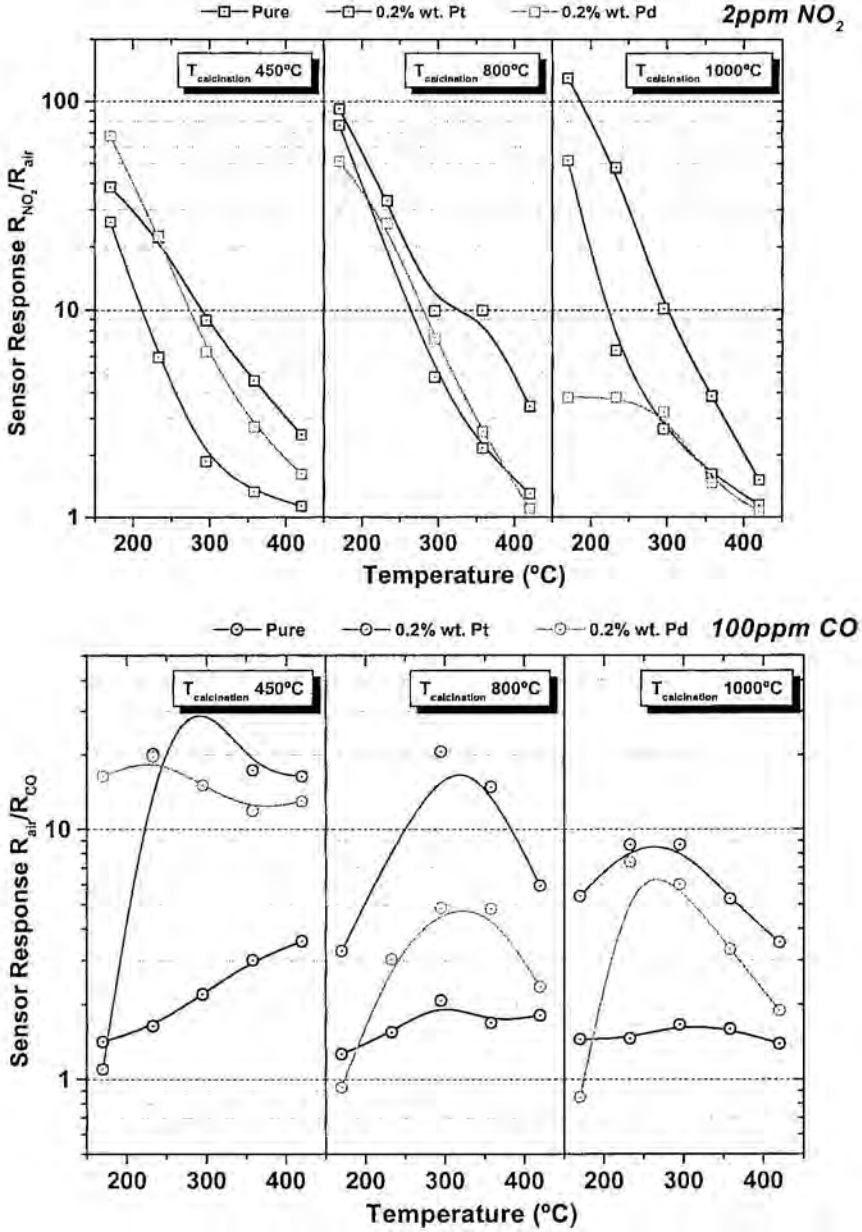


Figure 32: Sensitivity plots for the same sensors of figure 30. Introduction of noble metal additives changes the temperature of maximum sensitivity and the maximum sensitivity.

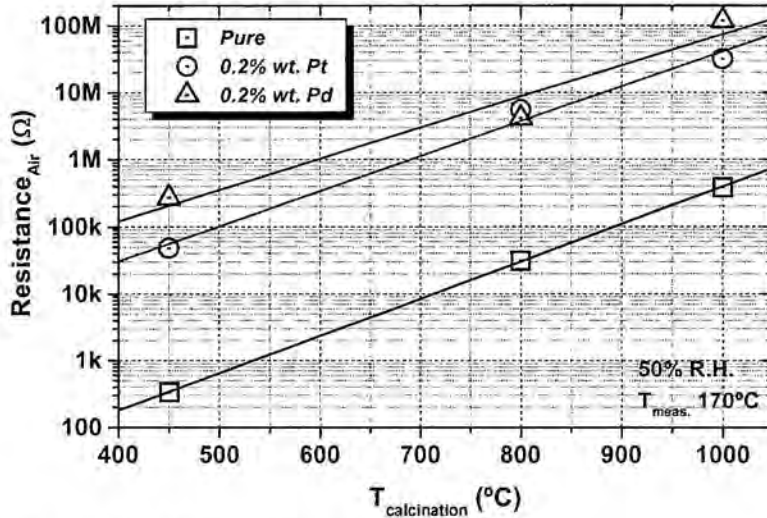


Figure 33: Review of sensor resistance in air measured at 170°C.

Moreover, resistance in air apparently has a power law behaviour with calcination temperature (at this temperature of measurement). However, this result can not lead to a general conclusion with only three points. As the curves are parallel, it could be inferred that the same mechanism takes place, independently of the introduction of additives.

Effects of calcination temperature (nanoparticle size)

To explain the above results let us consider a simplified model of the sensor, assuming that it is formed by parallel chains of grains between the electrodes (figure 34). The resistance will have the contribution of the contact with the electrodes, the resistance of the interior of the grains and the resistance corresponding to the grain boundaries. In oxygen rich ambient, one can consider the resistance of the grain boundaries, R_{gb} , to be dominant against the bulk resistance, R_g , of the grain. Thus, the total resistance of the sensor can easily be deduced to be function of the number of grains between the electrodes and, hence, inverse function of the grain size, d ,

$$R_{\text{Sensor}} \sim \frac{R_{gb}}{d} \quad (20)$$

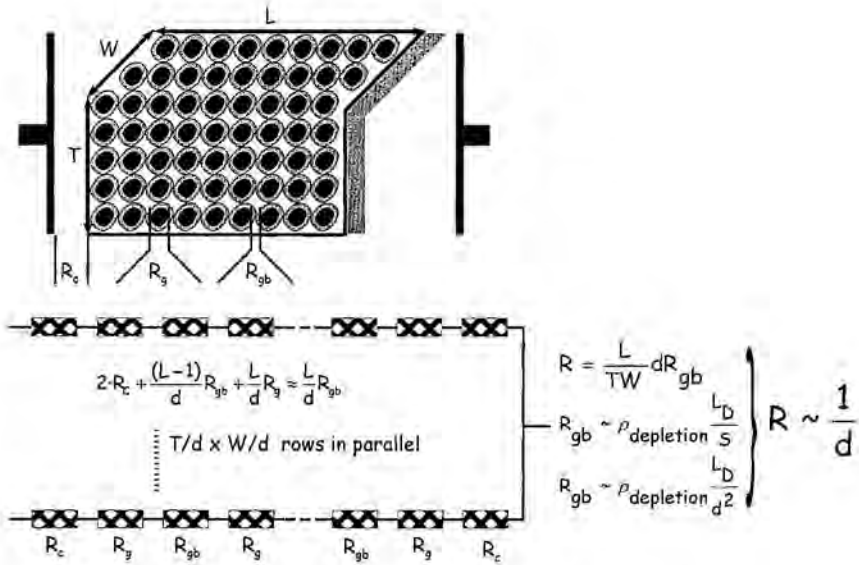


Figure 34: Simple scheme of a thick film sensor. R_c is the contact resistance with the electrodes, R_g the bulk resistance of each grain, and R_{gb} the grain boundary resistance, which is dominant.

In this way, by inspection of figure 33, it is obvious that the grain size variation due to the calcination process can not explain the resistance change. So, it should be attributed to the grain boundary resistance modification. Intuitively one can observe that R_{gb} includes mainly two factors, namely, i) the barrier height, V_s , that carriers see when travelling from grain to grain, and ii) the carrier concentration n_b , which can be related to the flux of carriers able to cross the barrier. Thus, R_{gb} can be written as [69, 70]:

$$R_{gb} \propto \frac{e^{qV_s/kT}}{n_b} \tag{21}$$

$$R_{gb} = R_o e^{(E_c - E_F)_{bulk}/kT} e^{qV_s/kT} \tag{22}$$

The above expression indicates that resistance variations can be produced mainly by two factors. These are:

- i) the modification of the density of free electrons (movement of the Fermi level), which in pure tin dioxide traduces in the modification of the density of bulk oxygen vacancies, and
- ii) the modification of the barrier height through the change of the charge state of the interfaces of the grains.

In the case of resistance increase this would imply decrease of the Fermi level towards the valence band (decrease of bulk oxygen vacancies), and/or increase/decrease of the number or density of existing interface acceptor/donor centres below/above de Fermi level (see figure 35). The movement of the Fermi level could change, in addition, the state of charge at the interfaces.

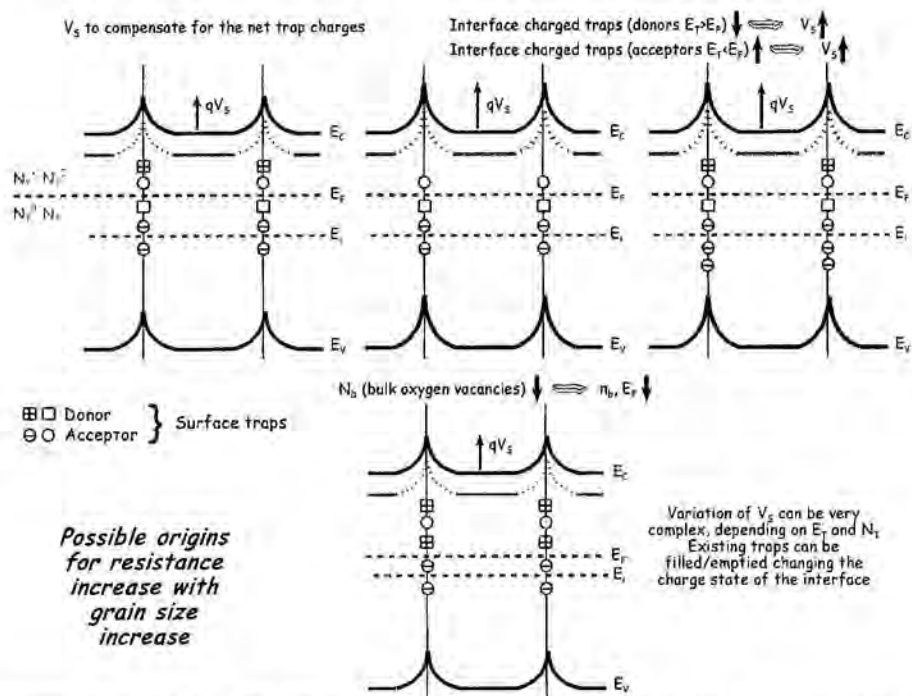


Figure 35: It is schematised how resistance can vary by modification of the density/population of interface centres (top), or by the modification of the density of free carriers (or oxygen vacancies) in the bulk of SnO_2 (bottom). In the first case, resistance can increase by reducing the population/density of donors with energetic position $E_T > E_F$, or by increasing the population/density of acceptors with energetic position $E_T < E_F$. It has to be taken into account that a change of the concentration of interface centres, as well as a change of the change in the concentration of free carriers in the bulk, is associated with the corresponding movement of the Fermi level, giving rise to a complex evolution (in general).

According with section 3.3, the increase of calcination temperature makes nanoparticles to grow more for the same calcination time. At the same time nanoparticle size becomes spreader and an increasing faceting of the surfaces occurs. As a consequence of faceting it is expected a better reconstruction of the surfaces. So, in principle, there is no reason to increase the number or density of existing interface acceptor levels with the increase of calcination temperature, at least that these centres would be associated with dangling bonds of a reconstructed surface. In the same way, it is usually expected the decrease of the number of

surface donor centres as a consequence of surface reconstruction. As we previously commented in *Chapter 1*, precisely it is well known that one of the reasons for choosing SnO₂ as oxide in conductance sensors is the negligible concentration of electronic band-gap states at their geometrically ideal surfaces [71], and that as nanoparticle size decreases such ideal surfaces no longer exist. According with [72, 73], oxygen vacancies on certain surfaces do not act as donor centres, and only when the temperature (of measurement) is high enough (~700K), surface oxygen vacancies on these surfaces migrate to the bulk, where become bulk vacancies and thus contribute to increase the conductivity of the material [45]. These surfaces correspond to stable surfaces of SnO₂ (like (110)), which develop more as faceting increases. It is directly a clear indication of decrease of the density of donor centres with increasing calcination temperature of the powders, as oxygen vacancies at these surfaces are excluded as origin for the resistance increase, because they give rise to interface electrically inactive traps. For a more detailed analysis the existence of different types of surface reconstruction should be taken into account in addition, as the electrical activity of the surface depends on the reconstruction.

On the other hand, bulk stabilisation would give rise to the reduction of bulk oxygen vacancies also, making difficult to assure which of these mechanisms dominate. To try to solve this uncertainty one can calculate the variation of the concentration of electrons or of the barrier height needed to produce the observed resistance change, according with equation 21. For this rapid calculation we assume that all donors are ionised and that the total density for the more perfect powder (1000°C) is $N_D \sim 10^{16} \text{cm}^{-3}$. The obtained variations maintaining the remaining parameters constant are presented in table VIII. From that table, it can be observed that concentration of bulk electrons has to change one and three orders of magnitude when going from 1000°C to 800°C and 450°C, respectively. This is why we choose $N_D \sim 10^{16} \text{cm}^{-3}$, rather than the usual values reported of $10^{18} - 10^{19} \text{cm}^{-3}$, for which the conclusion would be obvious. Nevertheless, for the same transition, only a small change of the barrier height of 0.064 and 0.18 eV is needed to explain the observed resistance change. It is likely that the change of barrier height is the responsible of the observed results because the interior of the bulk is well formed even at 450°C (section 3.3).

Effects of noble metal introduction

When introducing noble metals the observed results can be explained similarly. On one hand decreasing of the concentration of free electrons in the bulk is possible through bulk doping by the noble metal, which introduces an acceptor level. The higher resistance for Pd with respect to Pt could be explained by the higher density of the trap created by Pd or by the lower position in the band gap of the trap created by Pd with respect to the position of the Pt trap. On the other hand, the existence of the noble metal or its corresponding oxide at the surface of the

semiconductor can form a Schottky barrier, as it is schematised in figure 8 of Chapter 1. The height of such Schottky barrier would depend on the state of oxidation of the metal and thus on gas adsorption. The corresponding variation of the concentration of conduction electrons assuming a constant barrier height and of the variation of the barrier height assuming a constant concentration of conduction electrons is presented in table VIII. As in the case of calcination temperature one can see that it is easiest to explain the observed results through a modification of the barrier height. This would imply that noble metals are mainly distributed at the surface of the SnO₂ particles.

It is obvious that although both, volume doping and surface distribution of noble metals, could give rise to the observed results, a change on the free electron concentration is associated with bulk properties of the material, and hence, could not explain why noble metal introduction changes, for example, the temperature of maximum sensitivity of the sensors (figure 32).

$T_{\text{calcination}} (^{\circ}\text{C})$	450	800	1000	1000 (Pt)	1000 (Pd)
$R(\Omega) \sim \frac{1}{N_D} e^{q\psi_s/kT}$	~300	~30K	~400K	~30M	~100M
$R_{T_2}/R_{T_1} \sim N_{T_1}/N_{T_2}$ $N_{T_2} \sim N_{T_1}R_{T_1}/R_{T_2} \text{ (cm}^{-3}\text{)}$	$1 \cdot 10^{19}$	$1 \cdot 10^{17}$	$1 \cdot 10^{16}$	$7.5 \cdot 10^{17}$	$2.5 \cdot 10^{18}$
$(V_{T_2} - V_{T_1}) \sim \frac{kT}{q} \ln \left\{ \frac{R_{T_2}}{R_{T_1}} \right\} \text{ (eV)}$	-0.18	-0.064	—	0.108	0.138

Table VIII: Modelling of resistance changes with calcination temperature and noble metal introduction. T_1 in the table corresponds to calcination at 1000°C. The values of resistance correspond to measurements at 170°C.

3.4.1.2 Sensor response

Figure 36 summarises the results of sensor sensitivity to 100ppm CO and 2ppm NO₂ for Taguchi-type gas sensors, operating at a temperature around 230°C under 50% r.h. conditions. The use of this temperature ensures a fast response to NO₂ ($t_{90} \leq 5$ min). Similarly, the same figure shows the response to 5ppm CO and 500ppb NO₂ for planar-type gas sensors, operating at the same temperature and humidity conditions. As can be observed, the general tendency of sensitivity with noble metal introduction and calcination treatments, although is not the same, is similar in the limit cases (maximum and minimum sensitivities to CO and NO₂).

It can be seen that undoped material, calcinated at 1000°C, presents both, the best sensitivity to NO₂ and the lowest cross sensitivity to CO. It seems that the use of catalytic metals (Pt and Pd) enhances the sensitivity to reducing gases (CO) at these working temperatures, as they fix more oxygen at the surface of the nanoparticles, which will imply that noble metals distribute at the surface of the

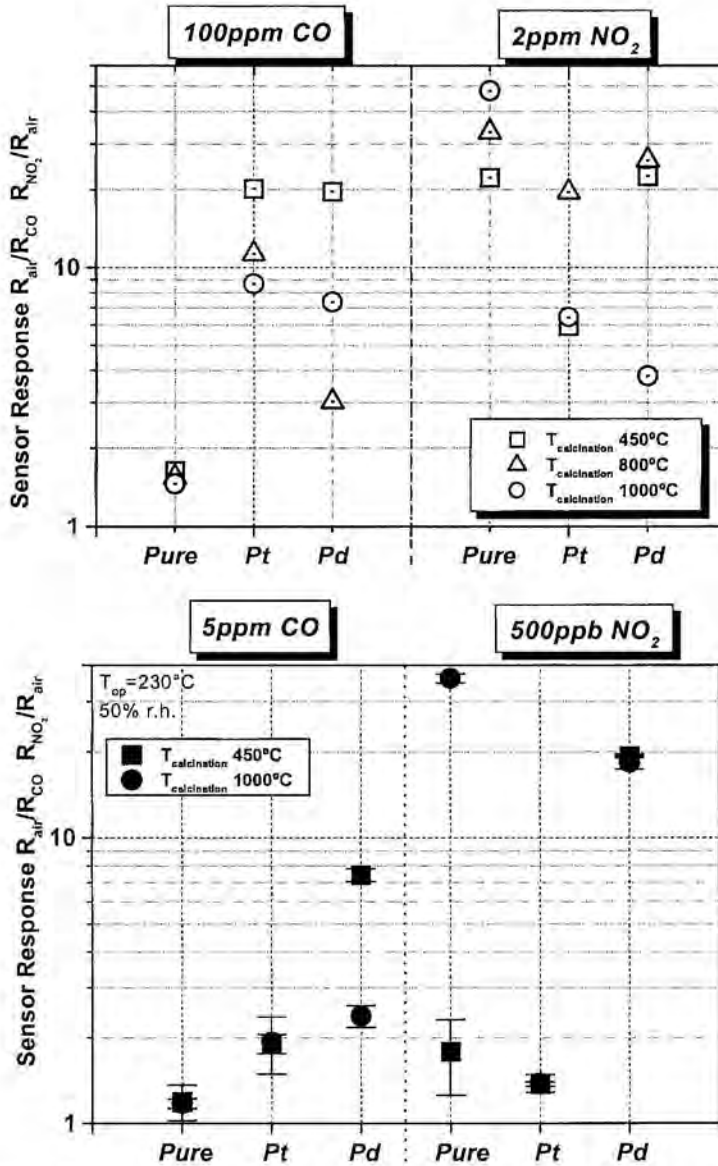


Figure 36: Summary of the sensor response to CO and NO₂ of Taguchi (top) and planar (bottom) thick film gas sensors measured at ~230°C.

nanoparticles. So, the pure material respond less to CO, while the high electronic affinity of NO₂ allows a reaction without the "help" of additional sensitizers. On one hand, the high resistivity of the material calcinated at 1000°C points out the

existence of a high grain boundary barrier associated with a high density and energy distribution of available surface states for molecules absorption. At this respect, it is well known that for SnO₂ the last oxygen anion layer, bridging oxygens, is very reactive and interacts with the NO₂ molecules, which form surface nitrates, whose decomposition starts above 100-150°C [74]. On the contrary, the presence of catalytic metal additives enhances the absorption of oxygen species, changing completely the surface reaction scenario. Thus, for detection of CO, it is better to introduce Pt or Pd, and to calcinate the powder at 450°C.

Based on the obtained results, it is clear that in spite of the higher grain size and grain size dispersion, shown in figure 15, when high sensitivity to NO₂ with low cross sensitivity to CO are looked for, nanoparticles should be calcined at 1000°C and undoped. As the crystalline quality of the grains improves and faceting increases, the surface defect distribution available for gas absorption changes also. Therefore, it could be expected that the higher reactivity to NO₂ will be promoted by the better crystalline quality and faceting of the grains calcined at 1000°C. The opposite occurs for CO.

3.4.1.3 Sensor stability

To investigate the stability properties of this type of sensors, a long-term characterisation was performed. The sensor signals to 1ppm NO₂ were measured for more than 3 months. The sensor showed an excellent stability as the fluctuation in resistance under exposure to 1ppm NO₂ over three months is less than 5% (figure 37). The larger fluctuation of the base resistance can be related to the change of the synthetic air cylinders and their different residual contamination (up to 1ppm CO, 0.5ppm H₂ and 0.1ppm NO_x). It is believed that for the high calcination temperature sensors, the whole loss of water and of hydroxyl groups, together with the better crystalline quality and the increase of faceting, are responsible for the stability in comparison with material prepared at lower temperature (<450°C), for which their structural characteristics change with temperature and/or time.

3.4.2 Distribution of noble metal additives

From the electrical results it seems evident that Pt and Pd are distributed over the surface of the SnO₂ particles. Structural characterisation could give the support needed for such assumption. In order to clarify this point powders calcinated at 450, 800, and 1000°C in pure form or doped with 0.2 or 3% wt. of Pt or Pd have been investigated by TEM, XPS, XRD and Raman spectroscopy. No appreciable differences in the XRD spectra were observed with the introduction neither of Pt nor Pd. However some results were obtained from TEM, Raman and XPS. which are explained in the following.

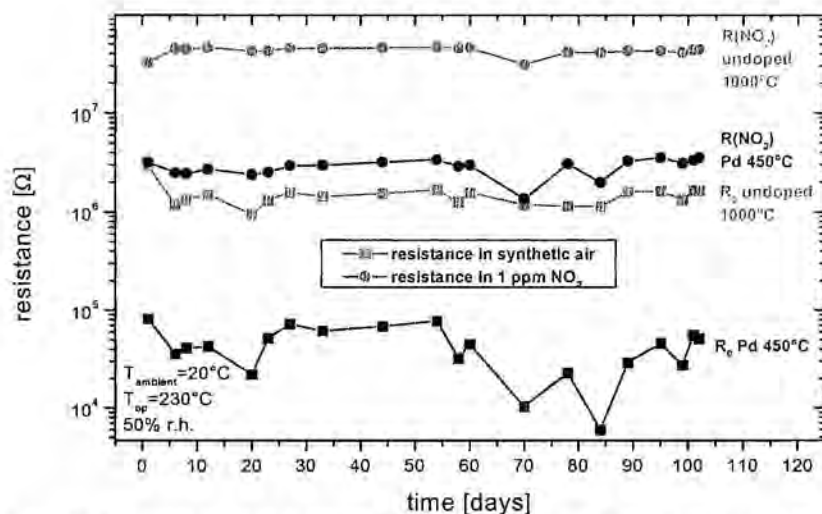


Figure 37: Resistance variation of two sensors during ca. 100 days. The stability of these sensors is clearly good and higher in the case of the sensor fabricated with the powders calcinated at 1000°C.

3.4.2.1 Transmission electron microscopy

In principle it is expected that noble metal clusters form at the surface of the nanoparticles, according to the impregnation method employed to introduce the noble metal additives. To try to observe such clusters intensive TEM work was done. According to *Chapter 2*, part 2.1.3.3, Pt and Pd should present a darker contrast than SnO_2 under conventional bright field conditions. Nevertheless noble metal precipitates were never observed with this technique. Such result, which a priori could result in contradiction with the electrical characterisation, is not surprising when considering the low quantity of noble metal introduction.

Under TEM imaging some sporadic regions in the Pd containing powders presented very smaller particles (2-4 nm) which could not be attributed directly to the formation of noble metal clusters (figure 38). The combined use of HREM with high-resolution EDS or EELS, however, demonstrated that such smaller particles were in effect metallic Pd clusters with very low oxygen content as can be observed in the EDS spectrum presented in figure 39. By assuming that the only Pd introduced in the powder comes from regions such as that presented in figures 38 or 39 and that it is distributed uniformly over the surface of the whole image, it has been estimated a coverage of less than ~ 0.1 monolayers in the powders calcinated at 430°C with 3% wt. Pd (the thickness of a monolayer was assumed to be half the lattice parameter of Pd).

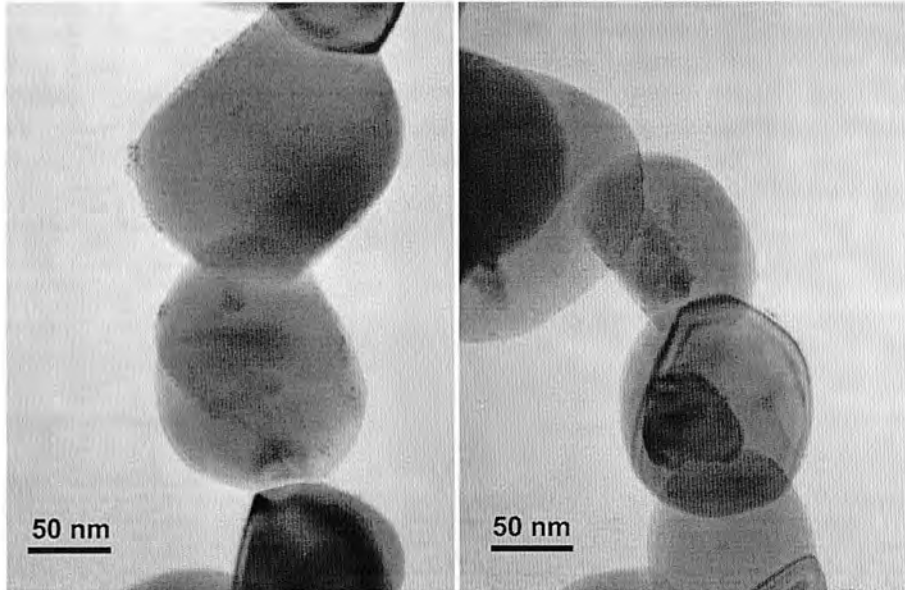


Figure 38: TEM images of the 0.2% wt. Pd doped sample calcinated at 1000°C for 8h. Some sporadic and very small particles are visible at the surface of the SnO₂ grains (larger).

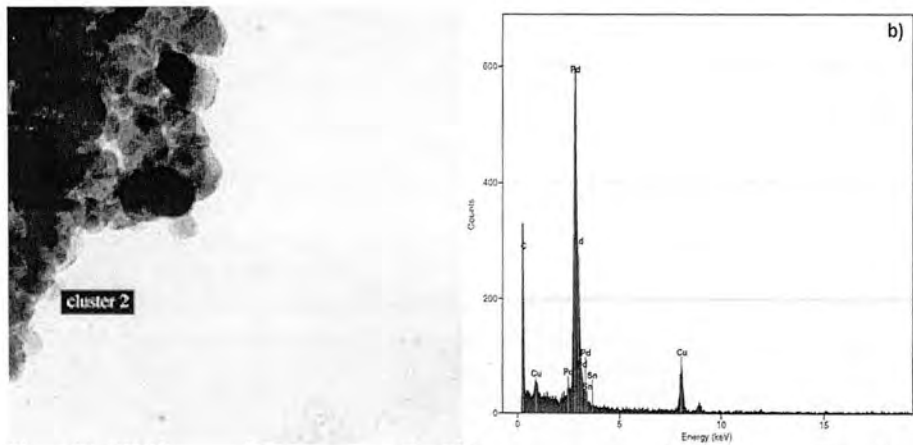


Figure 39: TEM image and EDS spectrum. The EDS spectrum corresponds to the very small particles present in the background of the TEM image. The nature of these particles is clearly Pd.

In the case of Pt introduction, we never observed similar regions.

3.4.2.2 Raman spectroscopy

By simply comparison of the Raman spectra of the pure and doped powders it can be concluded without doubt that if Pt and Pd are in metallic form, they do not cover the surface of the SnO_2 particles, since a metallic coverage would scatter a large amount of the incident laser light. Indeed it can be said that Pt and Pd are even not forming metallic clusters because no appreciable reduction of the intensity of the 'classical' modes of the cassiterite was observed when taking the spectra under identical conditions. The existence of oxidised Pt/Pd could explain why the dark contrast expected for Pt and Pd was not observed by TEM.

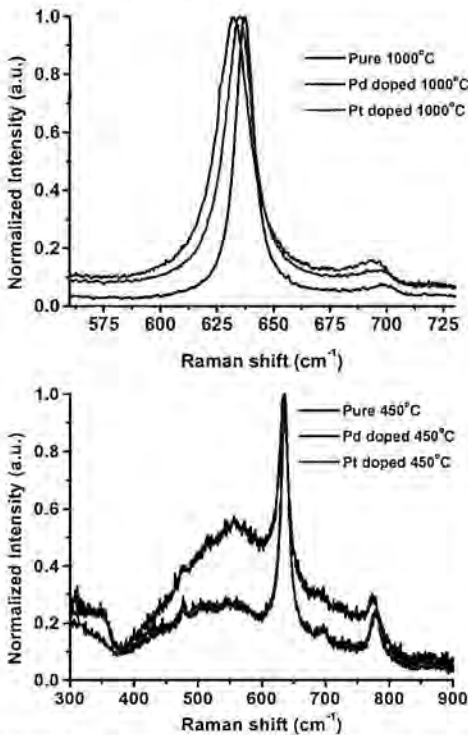


Figure 40: Raman spectra of the pure and doped powders calcinated at 1000°C (top) and 450°C (bottom).

The general aspect of the Raman spectrum of the Pt/Pd doped powders calcinated at 800 and 1000°C is very similar of the pure SnO_2 . Nevertheless, some small differences can be found by inspection of the 'classical' modes of cassiterite. As it is presented in figure 40 for the A_{1g} mode, Pt introduction produces the shift of this mode to lower wavenumbers. This shift is even larger in the case of Pd. Moreover, this shift is larger in the case of the powders calcinated at 1000°C. The FWHM of the A_{1g} mode changes accordingly with the corresponding Raman shift. The Raman spectrum of the oxides of PtO and of PdO₂ has not been reported in the literature, at least to our knowledge. On the other hand, the Raman spectrum of PdO presents its most intense and practically the unique visible band at 651cm^{-1} [75]. This makes the possibility of the shift of the

A_{1g} mode of the cassiterite resulting as a superposition of this mode and the band of PdO to be refused. Without being completely clarified it seems that the shift of the

Raman spectrum could be attributed to the presence of stress in the powder introduced by Pt/Pd or to distortion of the surface produced by the additives.

The most important changes on the whole Raman spectrum are observed on the powder calcinated at 450°C. As can be observed in figure 40 the bands attributed to disorder in part 3.3.3.2 are modified in an important way with the introduction of noble metals. According to the conclusions drawn about such bands, a modification of the surface of the SnO₂ particles could have occurred. This change can be due to three factors: i) a change of nanoparticle size as a consequence of noble metal addition, ii) the decrease of surface disorder as a consequence of the additional thermal treatment at which the doped powders were submitted and, iii) the presence of Pt/Pd on the surface of the SnO₂ particles.

In order to eliminate the first possibility grain size was measured by TEM. As can be seen in figure 41 no important modification of the size distribution was revealed, average nanoparticle size being always $\sim 15.8 \pm 0.4$ nm. Therefore grain size was to not vary after the noble metal introduction, i.e., after the thermal treatment, because impregnation is performed at room temperature. So, the modification of the surface disorder activated Raman bands, has to be explained, mainly by the increase of lattice order at the surface, or by the decrease of the Raman efficiency of such bands by the presence of Pt/Pd or of the corresponding oxides on the surface of the particles.

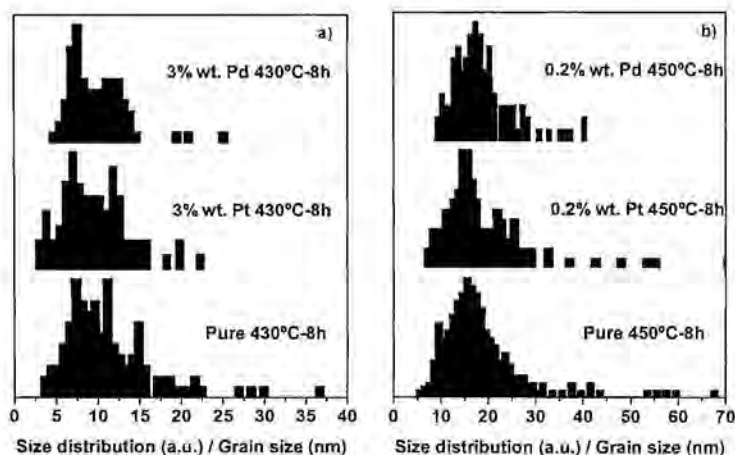


Figure 41: Histograms of the 'doped' powders calcinated at 450°C and 1000°C, compared with those of the pure samples.

Whatever be the origin of the modification of such bands, it is clear that the obtained spectra are a clear indication of the origin of such bands as disorder activation on the surface of the SnO₂. The independence of grain size on metal addition can be understood by the fact that metallic impregnation was performed

after the calcination process and because grain growth mechanisms are controlled by time constants large enough to do not influence in the post-calcination thermal treatment.

3.4.2.2 X-ray photoelectron spectroscopy

In spite it has been concluded from Raman experiments that Pt/Pd are localised mainly at the surface of the particles and that are mainly oxidised, one can not determine their state of oxidation. To solve this question XPS was used.

The state of oxidation can be inferred from the position of the Pd3d and Pt4f bands in the XPS spectra (not shown). XPS analysis shows the presence of +2 and +4 metallic oxide states (Pt^{+2} and Pt^{+4} for Pt, and Pd^{+2} and Pd^{+4} for Pd). It is worth to mention that according to the electron microscopy data, the concentration of the metallic state is beyond the XPS detection limits, i.e., does not correspond to the small particles observed by TEM. Likely, this low tax of metallic fixation can be attributed to the use of a chlorine solution, because the remaining Cl has to be taken out of the SnO_2 , and in this process the metal is also dragged.

After Argon ion sputtering of the first atomic layers of the nanoparticles, the +4 metallic oxide concentration decreases, while the +2 metal oxide component remains almost unchanged in comparison to Sn. Hence, metal atoms fixed at the surface and surrounded by absorbed oxygen atoms are the origin of the +4 chemical state of the introduced metal. In the same way, the +2 metal oxide component corresponds to metal atoms in the inside of the SnO_2 , i.e., Pt and Pd atoms are surrounded by Sn and O atoms.

The Valence band analysis of the different powders shows the existence of a high density of surface states related to the noble metal presence. As can be seen in figure 42, these states are revealed at the top of the valence band, below the Fermi level position. The presence of surface states is more clearly observed in the case of Pd introduction. However, in both cases (Pt and Pd) the density of states is more important as calcination temperature (\sim inverse of effective surface area) or as the percentage of introduced material increase.

As XPS measurements are performed up to a few Å of the surface, the modification of the electronic state distribution corresponds to the surface of the nanoparticles. This supposes an induced change in the band bending energy. These changes can be followed through the binding energy of the Sn against that of the oxygen, as summarised in figure 43. In this figure the samples calcinated in the range 450-1000°C, pure and 0.2%wt. Pt or Pd introduction, are plotted. By comparison, for example, with the resistance variation presented in figure 33, it is observed that agreement between band bending caused by calcination and noble metal introduction and resistance variation is not exactly found. The discrepancy can arise because the comparison is not direct due to the existence of the electrodes, which take part in the measurement of resistance.

In view of these results it seems straightforward to interpret the sensitivity curves of these sensors: the availability of electronic surface states as well as their occupancy factor varies the interaction condition between the gas molecules to be detected and the surface of the nanoparticles.

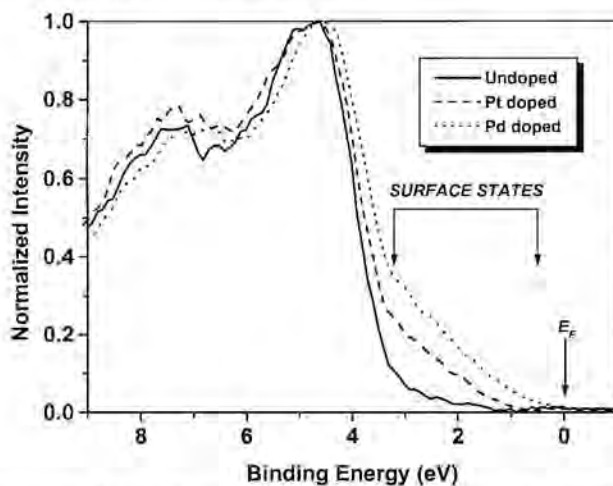


Figure 42: Valence band spectra of the powders calculated at 800°C, pure and with 0.2% wt. of Pt and Pd.

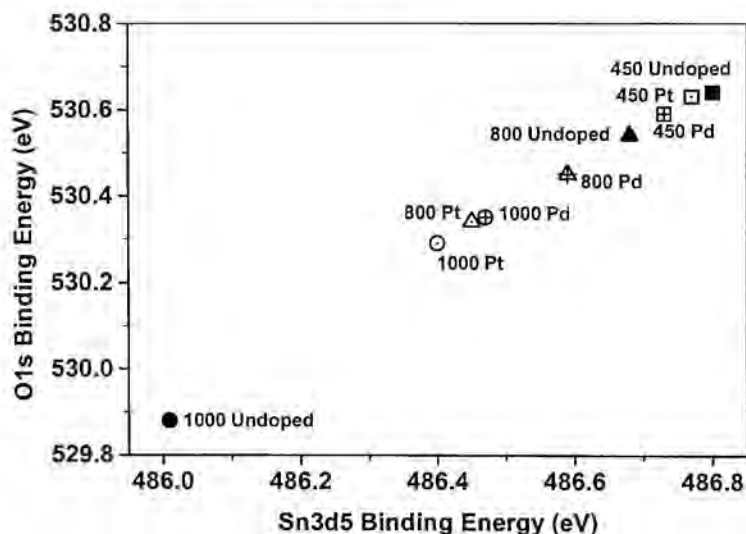


Figure 43: Modification of the O(1s) bending energy against Sn(3d) bending energy, pointing out the bending energy variations.

3.5 Improvement of the sensor characteristics by means of grinding treatments

Inspection of a powder formed by nanoparticles shows that it is composed by agglomerates (figure 11) of different sizes. The origin of such agglomerates is the electrostatic force between the surfaces of neighbouring grains. The size of the agglomerates depends on the size of the nanoparticles composing the powder in such a way that the smaller the grains are, the larger agglomerates are obtained (figure 11). It has been previously commented that for the fabrication of the paste to paint or print the sensors, powders are mixed with an organic binder. The problem is that a good mixture can not be obtained when large agglomerates are present. In such case large agglomerates are poorly bound, resulting in adhesion problems and possibility of breaking of the layer during the tempering step. To avoid this problem usually a grinding of the powder is needed before the fabrication of the paste in order to improve the effectiveness of the organic binder. This is the origin of the grinding of the powders after calcination performed in almost all the samples presented up to now.

Although it is clear that grinding after calcination is needed to fabricate the sensors, comparison of the size of calcinated powders ground or not ground after calcination gives rise to a decrease of nanoparticle size with grinding. For such comparison one can see the value of the powder calcinated at 1000°C in table IV (section 3.3.3) and the value of the powders calcinated at 1000°C, on which a grinding after calcination has been performed, in table IX presented below. Reduction in grain size promoted by grinding treatments have been previously reported also [76-78]. Therefore a first idea is to use the same procedure to decrease the grain size of the powder before calcination in order to have a starting material with minimum size. The advantage of reducing particle dimensions, as has been outlined previously, is an increased sensitivity. Likewise, an increase in the effective active surface is produced.

The adjustment of the grain size is normally carried out by variation of the calcination temperature. But a change in the calcination temperature affects also bulk and surface properties of the individual grains. Without, in principle, changing bulk properties, grinding could produce the same control.

Table IX and figure 44 show particle size and size dispersion in powders which have been treated under different thermal treatments (temperature and time) and grinding steps. To make these curves the histograms, extracted by TEM, were fitted with a gaussian function. Thus, average nanoparticle size was extracted from the peak value and size dispersion from the FWHM.

The following important results are inferred:

- Increase of the calcination time from 8h to 24h produces a large average grain size but lower size dispersion.
- Grinding before calcination makes the final grain size after calcination to decrease. This is only observed for calcination temperatures higher than 600°C.

The decrease of the size dispersion with increase of average size implies that the coalescence process is easier to the smaller particles, which convert in larger ones. The larger particles need more energy to perform coalescence, as results from their faceting [79]. Faceted surfaces imply a more stable surface and the existence of less adjacent surfaces. As a consequence these effects are better observed for larger sizes ($T_{\text{calc.}}=600\text{-}1000^{\circ}\text{C}$).

CODE	Calcination		Grinding		L(nm)	ΔL (nm)
	$T_{\text{calcination}} (^{\circ}\text{C})$	$t_{\text{calcination}} (\text{h})$	Before (h)	After (h)		
ART	RT	--	--	--	3.46	1.13
A250	250	8	--	2	4.46	1.26
A330	330	8	--	2	5.05	1.41
A400	400	8	--	2	6.75	2.12
A430	430	8	--	2	9.24	3.1
B430	430	8	2	2	9.0	3.09
D430	430	24	2	2	11.77	2.93
A460	460	8	--	2	10.15	2.7
C460	460	24	--	2	10.94	3.04
B590	590	8	2	2	22.61	10.09
A600	600	8	--	2	22.65	11.16
A1000	1000	8	--	2	91.81	42.54
C1000	1000	24	--	2	106.02	35.83
B1000	1000	8	2	2	51.67	24.42
D1000	1000	24	2	2	60.98	20.24

Table IX: Powder samples for the initial analysis of the grinding process. It is presented the average nanoparticle size (L), and size dispersion (ΔL).

For low calcination temperatures ($T_{\text{calc.}} < 600^{\circ}\text{C}$) grinding before or after calcination does not have a significant influence on the final particle size. On the other hand, grinding before (table IX and figure 44) or after (comment above) calcination is effective in reducing nanoparticle size at high calcination temperatures. This obtained result took to carry out a study more meticulous. It is the aim of this last part of the chapter to describe such analyses.

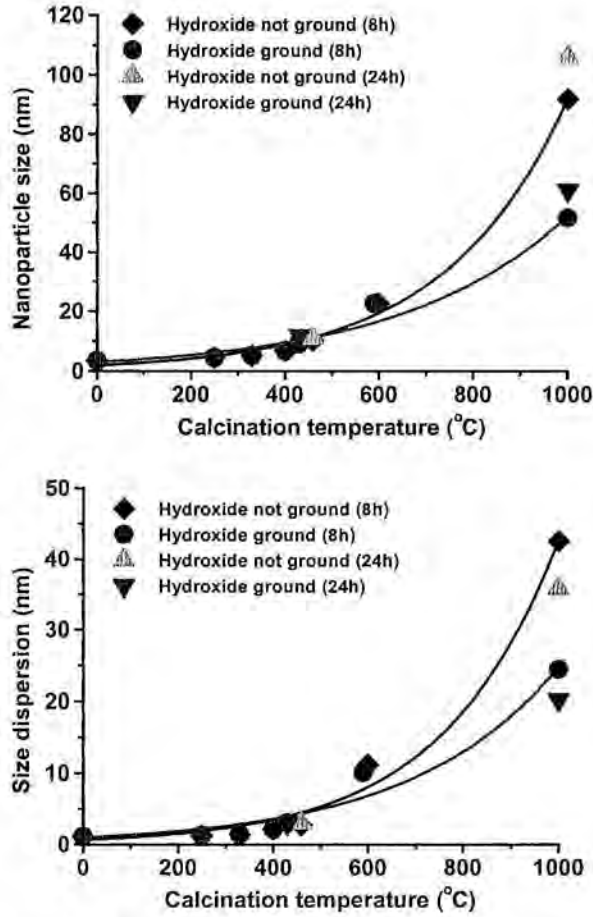


Figure 44: Average grain size and size dispersion of powders submitted to different thermal treatments and grinding steps.

As a consequence of grinding some of the powders resulted contaminated by ZrO_2 . The degree of contamination is not directly related to the grinding time or if the grinding is performed before or after calcination. Indeed, adding water to the planetary mill at certain moments of the process can substantially reduce contamination. Nevertheless, when contamination occurs, the Raman spectra of SnO_2 results modified in a large manner by the presence of photoluminescence bands. As can be seen in figure 45, these bands make difficult an accurate analysis of the modes of cassiterite. However, as their origin is photoluminescence, the bands

can be shifted enough by using the appropriate wavelength, such as it is demonstrated in figure 45. At $\lambda=514.5\text{nm}$ the effects of ZrO_2 can be minimised by making the appropriate baseline subtraction. However it is better to use $\lambda=457.9\text{nm}$, where the contribution of ZrO_2 is really a background.

Therefore, with the appropriate wavelength the Raman spectrum does not result altered by the presence of small quantities of ZrO_2 . An important presence of ZrO_2 gives rise to the appearance of the Raman spectrum of this material, which unfortunately presents bands (mainly at 476, 616 and 638cm^{-1} [80]) superimposed with the edges of some Raman modes of SnO_2 . The samples analysed in sections 3.3 and 3.4 presented very low concentration of ZrO_2 and the Raman spectra were recorded in a proper way to avoid photoluminescence effects ($\lambda=457.9\text{nm}$).

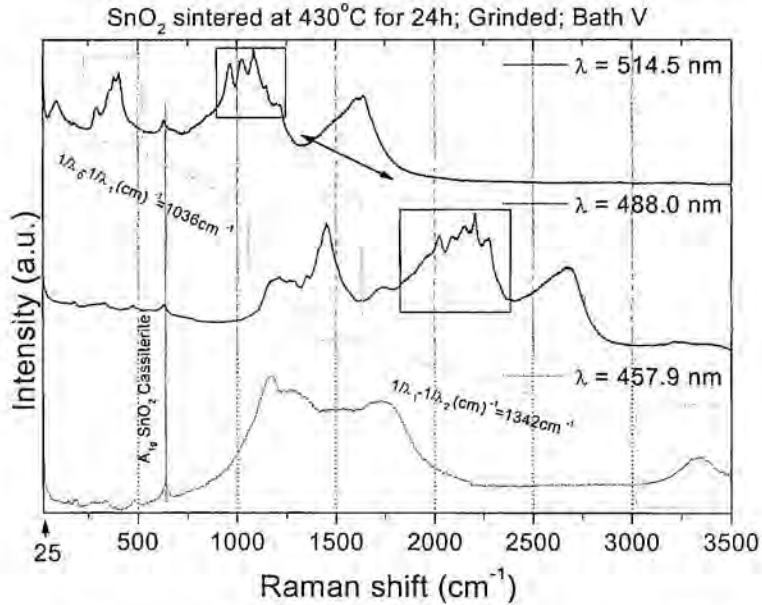


Figure 45: Demonstration of the existence of photoluminescence bands in SnO_2 (as a consequence of the presence of ZrO_2). Raman bands remain fixed while changing the excitation wavelength because they are relative to such energy. However, photoluminescence bands are energy independent and hence shift by changing the wavelength, as is indicated in this figure.

3.5.1 Microstructure changes induced by grinding treatments

In order to investigate powders and sensors with different grain sizes but obtained using identical calcination temperature, different grinding treatments have been applied to the powders. The complete set of powders used for that purpose is

presented in table X. A dark background and white letters in the same table indicate that sensors have been fabricated using these powders.

The grinding of powders has been performed either before or after calcination at 1000°C. The reason for choosing this temperature was three-fold:

- i) better stability of sensors fabricated with powders calcinated at 1000°C,
- ii) better sensor response to NO₂ and low cross sensitivity to CO of the pure SnO₂ calcinated at 1000°C, and
- iii) the most important differences observed in figure 44 for this calcination temperature.

In both types of grinding, powders were ground for 1, 2 or 11h. For grinding after calcination a fourth point was added by grinding up to 20h. A combined grinding for 2h before and after calcination has also been applied.

CODE	Calcination		Grinding		Metal	Zr (%)
	T _{calcination} (°C)	t _{calcination} (h)	Before (h)	After (h)		
G ₀	RT	--	--	--	--	--
G ₁	RT	--	1	--	--	--
G ₂	RT	--	2	--	--	--
G ₁₁	RT	--	11	--	--	--
G _{0,0}	1000	8	--	--	--	--
G _{1,0}	1000	8	1	--	--	--
G _{2,0} /A	1000	8	2	--	--	--
G _{11,0}	1000	8	11	--	--	--
G _{0,1}	1000	8	--	1	--	0.38
G _{0,2} /B	1000	8	--	2	--	0.54
G _{0,11}	1000	8	--	11	--	0.95
G _{0,20}	1000	8	--	20	--	1.6
G _{2,2} /C	1000	8	2	2	--	0.85

Table X: Set of samples for the detailed investigation of grinding.

3.5.1.1 Overview of the influence of grinding

As shown in figure 46, the reduction of grain size after 2 or 11h of grinding of the calcinated oxide is of ~6 or ~9%, respectively. Moreover, it seems that grinding of the calcinated oxide for much longer than 11h will not be too much efficient in reducing nanoparticle size, as a saturation seems to be reached. If the hydrated oxide is ground for 2 or 11h before calcination, the reduction in the final grain size is of ~14% or ~28%, respectively. It is observed again that grain size stabilises after some period of grinding, not too much being gained for grindings longer than 11h. Moreover, from the point of view of grain size, it is observed that grinding of the hydrated oxide is more effective than grinding of the oxide after calcination. When grinding is performed for 2h both before and after calcination, a reduction of nanoparticle size ~25% is obtained. As a mixed grinding before and after calcination produces lower grains sizes than the sum of them independently,

this indicates that the effects of grinding on grain size also depends of the initial sizes.

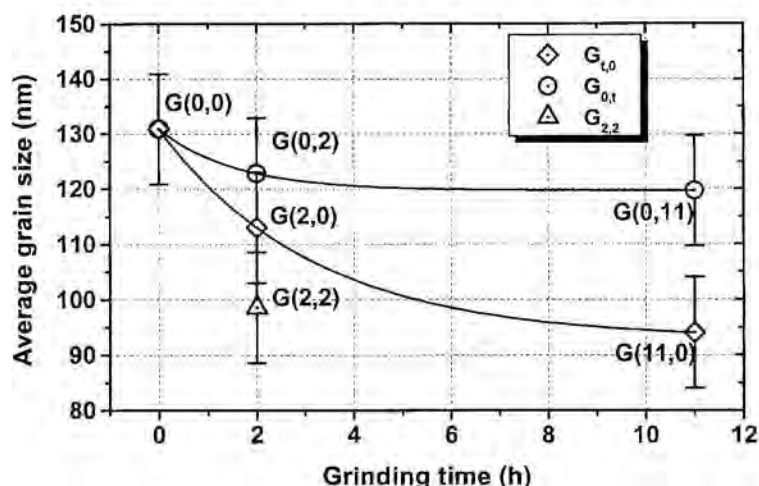


Figure 46: Evolution of the grain size as a function of grinding time. Vertical bars represent the size dispersion with respect to the mean value. Grain size was obtained by TEM.

3.5.1.2 Origin of particle size reduction by grinding after calcination

The comparison of the histograms of the grain size distributions of the powder not ground ($G_{0,0}$) and that ground for 11h after calcination ($G_{0,11}$), presented in figure 47, shows that grinding after calcination gives rise to a shift and spreading of the size distribution to lower particle sizes. From the shape of the histogram of the ground sample it seems clear that in this case the reduction of grain size due to grinding occurs because of breaking of the larger grains. The histogram of powder $G_{0,20}$ also goes in the same direction. Detailed observation of the TEM images (figure 48) shows that the larger grains present signals of impacts at their surface, which results deteriorated, together with the appearance of very small grains as a consequence of fracture. In general these very small nanoparticles remain stuck to the surface of the larger grains.

With the grinding treatment performed it is observed that only the larger particles are appreciably affected by grinding after calcination. This explains why particles calcinated at lower temperatures are not influenced by this treatment.

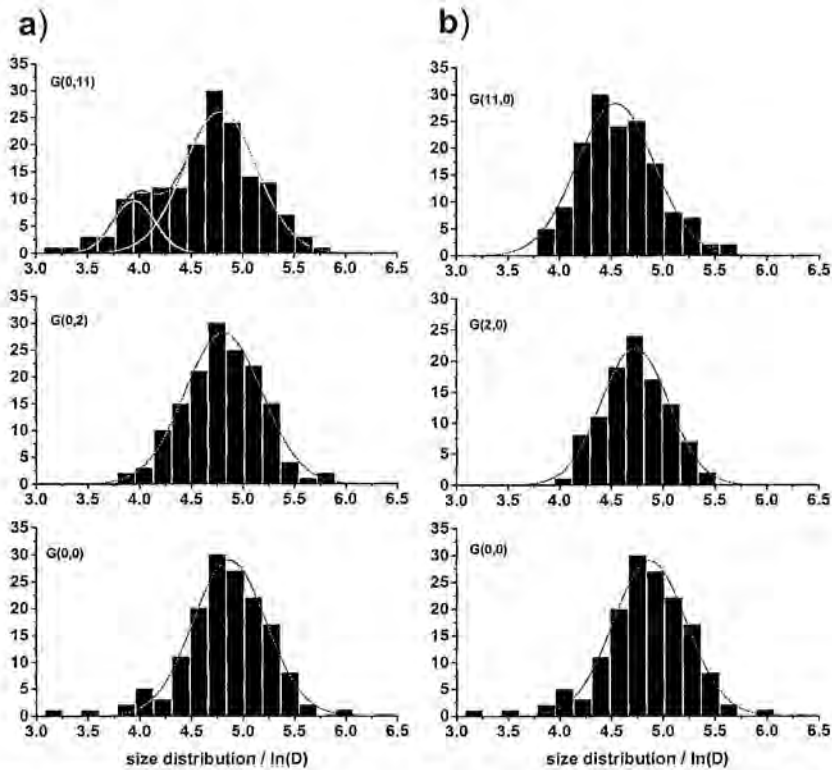


Figure 47: Nanoparticle size distributions extracted by TEM of the unground oxides and of the oxides ground up to 11h before or after calcination.

3.5.1.3 Origin of particle size reduction by grinding before calcination

The comparison of the histogram of the unground powder ($G_{0,0}$) with the powder ground for 11h before calcination ($G_{11,0}$), also presented in figure 47, shows a narrowing of the histogram and a lowering of the average size in the case of the ground powder. However, the unique difference between the unground and the ground powder showed by the TEM images (figure 48) is a higher degree of agglomeration in the case of the ground powder.

In order to understand the modification of the size distribution, the analysis of the corresponding starting hydrated oxides was done. It was observed that no important differences in initial nanoparticle size are found in the starting hydrated oxide before and after grinding (previous to the calcination). However, from the TEM images of figure 49 it is clear that this procedure affects mainly the morphology of the hydrated oxide agglomerates. Similar modification of the hydrated oxide has been previously reported in the case of the $\text{Al}_2\text{O}_3\text{-ZrO}_2$ system,

although in that case it was obtained by modification of the Al-Zr alkoxides by organic acids [81], and not by using grinding treatments. After grinding, the SnO₂ agglomerates appear much more dense and with spherical shape. The higher compactness of the hydrated oxide after grinding can arise because the poor strength of the particles at the beginning and the 'low' effectiveness of the grinding process for small particles. Moreover, the large quantity of water and hydroxyl groups in the hydrated oxide can favour the agglomeration.

When calcinating, inhibition of grain growth is due to the compactness obtained:

i) The compactness of the agglomerates hinders the evaporation of water and hydroxyl groups and, as was observed in section 3.3, grain growth occurs slowly until water and hydroxyl groups have not been released in a large extent. This was interpreted in terms of the difficulty of the migrations of atoms from grain to grain, in order to effectuate grain coalescence or any other type of mechanism for grain growth.

ii) The compactness obtained makes the contour conditions around each grain to change for the calcination process. While in an unground hydrated oxide particle movement in an agglomerate or between agglomerates due to coalescence is easy, in a ground hydrated oxide only the particles on the agglomerate are able to merge. This makes both types of oxides to grow the same for low calcination temperatures. If calcination temperature is higher (1000°C), the particles in a highly compacted agglomerate have grown all that they can grow and, the coalescence mechanism is delayed with respect to what should occur in a less compact agglomerate. In fact, the effects of agglomeration on sintering have been extensively reported in the literature [82-85], indicating that highly agglomerated precursors inhibit the sinterability of the powder, thus hindering the formation of large grains. The different intermediate size distribution of the particles would also affect further grain growth [86-89].

3.5.2 Influence of grinding on the electrical characteristics of sensors

Two factors can influence sensor characteristics with the use of grinding. One and the more evident is grain size reduction. The other, less evident, is the modification of the surface of the particles. The influence of grinding procedures on the characteristics of the base resistance and sensitivity to CO and NO₂ have been analysed. For this, planar sensors with Pt electrodes from unground powder G_{0,0} (sensor A), from powder which has been ground after calcination for 2h G_{0,2} (sensor B) and from powder which has been ground before and after calcination for 2h G_{2,2} (sensor C) were prepared and tested.

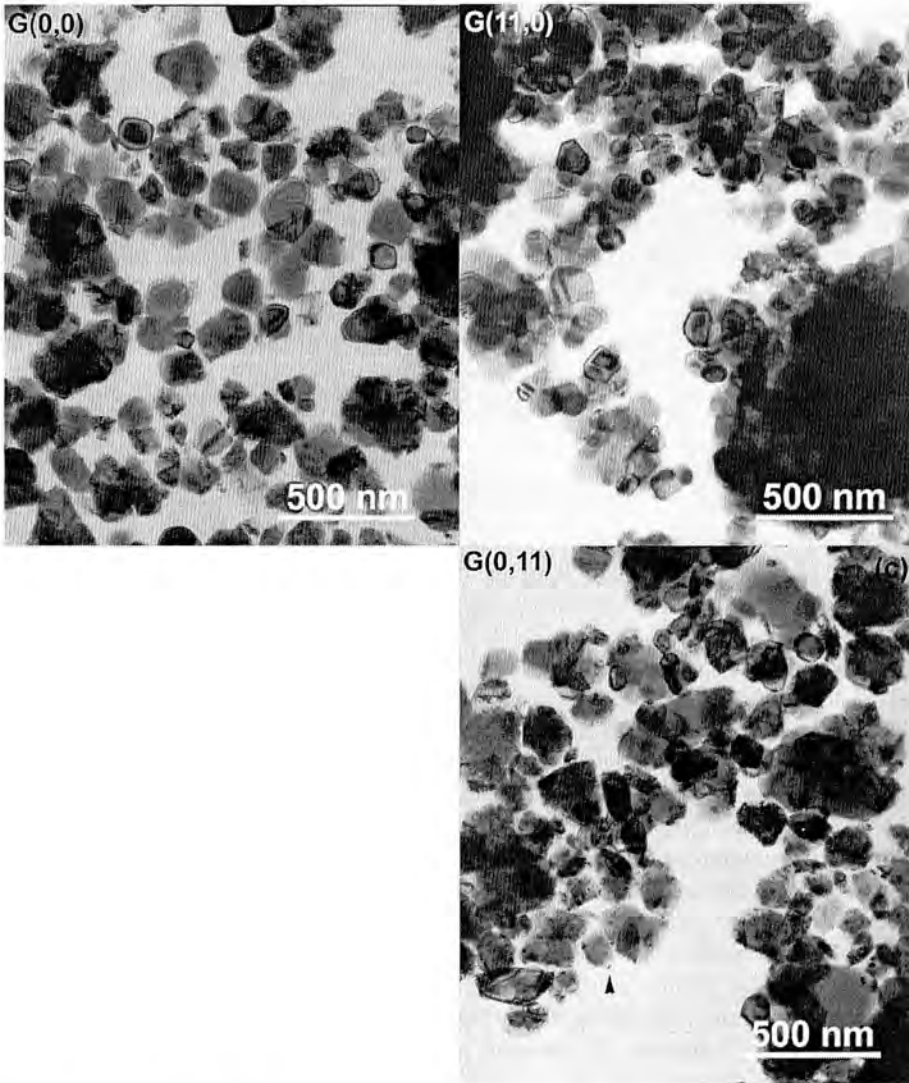


Figure 48: TEM images of the unground powder calcined at 1000°C (a), of the powder ground for 11h before calcination at 1000°C (b), and of the powder ground for 11h after calcination at 1000°C (c). The black arrow in (c) shows a very small particle stuck to the surface of a larger one.

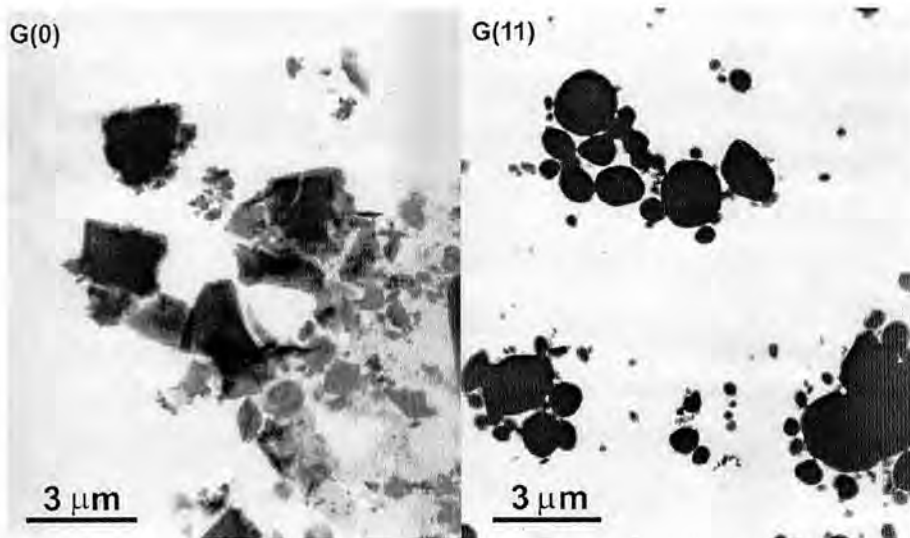


Figure 49: TEM images of the hydrated oxides, before (a) and after (b) grinding. It is clear the severe influence of grinding on the agglomeration of the nanoparticles.

3.5.2.1 Influence of grinding on the sensor resistance

Figure 50a shows the resistance in air of the measured sensors. The resulting strong dependence of the resistance in air on the grinding is striking. It seems that by changing the grinding procedure a tailoring of the base resistance is possible. Concretely, by means of the grinding procedures used in this work, a variation of almost three orders of magnitude in the resistance value has been obtained.

Such modification of resistance could result from changes in the grain size and surface state density and energy distribution. However, the variation of grain size (figure 46) can not explain the resistance variation observed. Accordingly with part 3.4.1.1 and equation 20, the total resistance of the sensor is deduced to be inversely proportional to the grain size, d . It is then obvious that the grain size variation due to the grinding process can not explain the resistance change. So, it should be attributed to the grain boundary resistance modification (equations 21 and 22). If we take into account that the applied thermal treatment is the same for all the sensors, we can assume that the intrinsic doping must be the same for all of them. Therefore, the resistance values must be associated uniquely to the bending potential,

$$R_{gb} \propto R_o' e^{qV_s/kT} \quad (23)$$

and it is directly related to the surface state concentration, N_{ss} , by considering an ideal Schottky barrier (*Chapter 1*),

$$N_{ss}^2 = \left(\frac{2\epsilon\epsilon_o n_{bulk}}{q} \right) V_s \quad (24)$$

where $\epsilon\epsilon_o$ is the permittivity of SnO_2 , and n_{bulk} is the electron concentration in the bulk of the grain.

Taking sensor A as reference, it is necessary to consider a band bending variation at 250°C as about 114meV for sensor B and 270meV for sensor C. At this point, it is worth to note that relatively small variations of the surface states density (an increase in a factor of 1.5 for example) are enough to justify these band bending variations and, hence, resistance changes of more than two orders of magnitude. As is shown in figure 51, the position of the O(1s) peak versus the Sn(3d) deduced from XPS measurements, using the Carbon peak position as reference, allows to see that the grinding process shifts the peak position, pointing out the variation of the band bending. The trend is in agreement with the above band bending values deduced from the electrical measurements, although quantitative values are difficult to extract.

Moreover, as can be observed in table X, the quantity of Zr introduced by the grinding treatment can not account for the resistance variation observed, as do not exist correlation between the degree of contamination and resistance.

3.5.2.2 Influence of grinding on sensor response

Likewise, the sensor signals are influenced also by grinding. Such as it is shown in figure 50b, grinding of the precursor improves the sensitivity to NO_2 , whereas grinding after calcination reduces the sensitivity to CO. In the case of CO, at the low range of sensor operation temperatures used in this work sensitivity is quite low, such as can be expected for undoped materials.

It is worth noting that the sensitivity plots of sensors B and C to NO_2 are parallel, whereas that of sensor A behaves different. So, from the point of view of sensitivity, sensors B and C appear to be equivalent and, the sensing mechanisms to which they respond seem to be the same. Sensor A is different from the other two, and for this sensor the mechanisms to which it responds should not be exactly the same because the corresponding surface state distribution and density are probably different, making the NO_2 absorption to take place in a different way.

When analysing sensitivity to CO, we find again a similar behaviour for sensors B and C and different in the case of sensor A. Again, resistance and

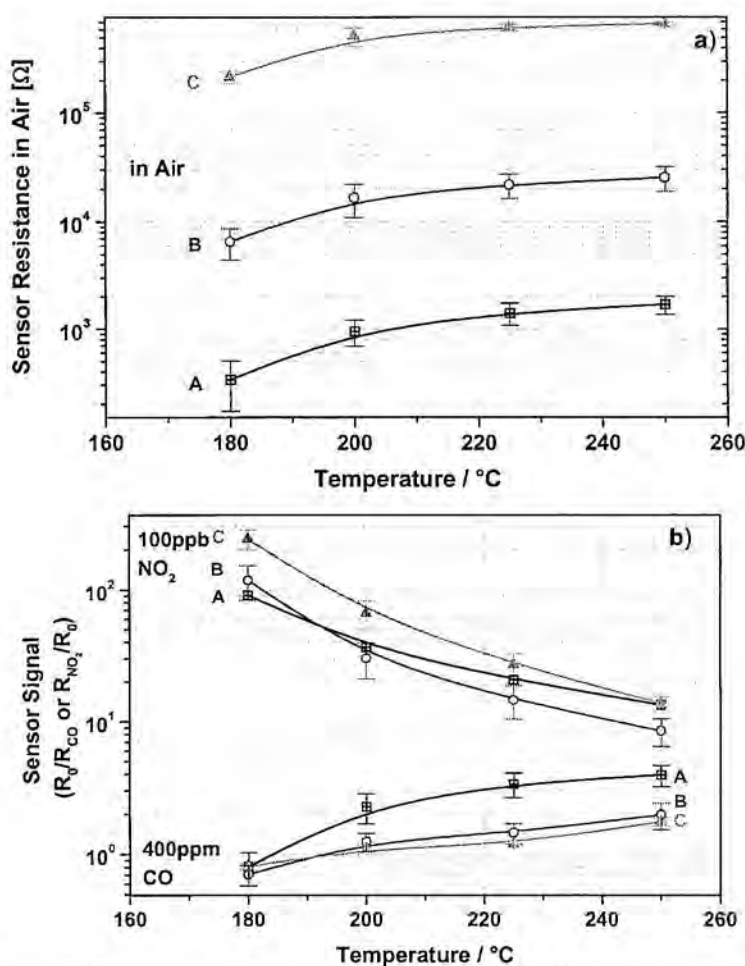


Figure 50: Resistance in air in (a) and sensor signal in (b) to 400ppm CO and 100ppb NO_2 of the sensors fabricated using unground powders calcined at 1000°C (A), powders ground for 2h after calcination at 1000°C (B), and powders ground for 2h before and after calcination at 1000°C (C).

sensitivity plots suggest that the surface state of the nanoparticles is more similar if the material is ground after calcination (sensors B and C), than if the material is not ground (sensor A).

According to these results, we can consider the hypothesis that sensors B and C present similar energy distributions of surface states although different density, whereas sensor A has different distribution and density. In this way, the absorption of gas molecules is different in concentration and/or type for each one of

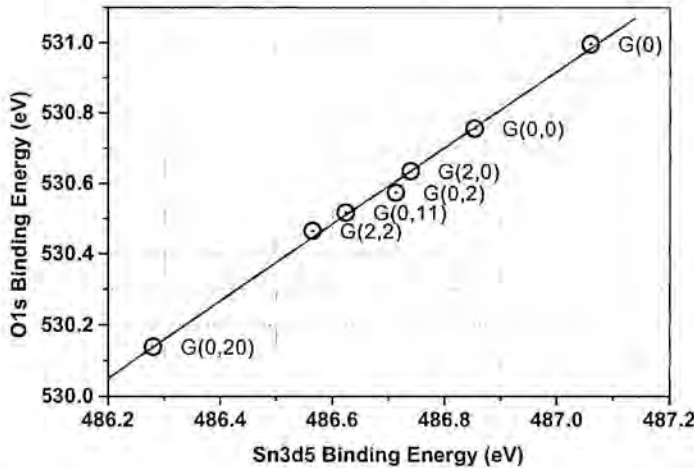


Figure 51: Position of the O(1s) peak versus the Sn(3d) deduced from XPS measurements and referenced to the Carbon peak position. An indication of band bending induced by grinding is inferred from shift of the peak positions.

these sensors, contributing to the different base resistances observed. It is plausible to think that grinding enhances the formation of certain surface sites, mainly at the bridging oxygen layer, which can locate negative adsorbed molecules. Moreover, it could also modify the electron affinity of the dipole layer and the negative adsorbed charge. The negative charge modification can contribute to increase the grain boundary barrier height, which determines the resistance value. The surface sites created would correspond to acceptor states. The observed enhancement of NO_2 sensitivity might be explained by the generation of acceptor states, which are below the sites for oxygen adsorption and above the sites for NO_2 adsorption. Therefore, it decreases the number of oxygen species adsorbed in relation to the adsorbed NO_2 species. As bending increases, surface Fermi level position is lower, near to Valence Band maximum.

At these states, the interaction with CO molecules, in the low temperature range, is more difficult without the help of the catalytic metal clusters. It is possible to think that although the unground sensor presents also adsorbed oxygen, the sites are not the same and their fixation is weaker than for the ground sensors. The reduction of sensitivity to CO after grinding can be explained again by a trapping of electrons in the acceptor surface states generated by grinding, because in this way, a more reduced number of adsorbed oxygen species needed for the CO reaction would be available. As a consequence of this last characteristic we can expect a higher reactivity with the CO molecules in the low temperature range, such as it is shown in figure 50.

So, grinding before and after calcination ($G_{2,2}$) produces smaller grain sizes than if the powder is only ground after calcination ($G_{0,2}$), but it seems also to produce a higher density of surface states than if the powder is ground only after calcination. It should be observed that when the powders are ground before calcination and annealed, during the calcination step a recovery of the produced surface damage takes place, as could be deduced from the XPS results shown in figure 51. If after the calcination, step the sample is ground again, its final characteristics become influenced by the initial conditions ($G_{2,2} \neq G_{0,2}$). A higher density of surface states seems to be formed according to both resistance and XPS data.

It can be summarised that grinding modifies the structural characteristics of the material determining the processes involved in the sensing mechanisms. So, grinding after calcination leads to establish in a controlled way the state of the surface of the nanoparticles, i.e., somehow the conditions to compare sensors.

3.6 CONCLUSIONS

In this *Chapter* we have analysed the fundamental properties of SnO₂ nanoparticles obtained by sol-gel. The investigation has included analysis of the calcination of as-obtained powders, the introduction by impregnation of low quantities of the metal additives Pt and Pd, and the grinding of SnO₂. The main conclusions are:

XRD spectra and electron diffraction patterns of the different SnO₂ powders indicate that their crystalline structure is cassiterite even for the as obtained hydrated oxide. For low calcination temperatures, nanoparticles are characterised by a quasi-spherical shape, a strong distortion of the crystalline structure and a high degree of agglomeration. Likewise the FTIR spectra of these nanoparticles show water content as well as hydroxyl absorption bands. Both, content of OH groups and lattice distortion progressively disappear with the increase of calcination temperature, having disappeared around 450°C. Nanoparticles calcinated at temperatures higher than 450°C are of good crystalline quality, deagglomerated and faceted. As a consequence of faceting a change in their surface states is also expected. From the transition temperature at which changes occur very fast (430-450°C), the strong grain size increase becomes determined by coalescence.

Through the analysis of nanoparticles ranging in size between 3-100 nm we have been able to completely describe the Raman spectrum of nanometric SnO₂. It has been found that disorder and nanoparticle size have a strong influence on the vibrational properties of this material, i.e., in the Raman as well as in the infrared spectrum. By decreasing nanoparticle size the bands associated to the 'classical' modes of SnO₂ shift according to the phonon dispersion curves and broaden. Their dependency with nanoparticle size has been shown to be quite well described by the spatial correlation model, at least for particles larger than 8-10nm.

Associated to the decrease of grain size mainly two bands arise in the spectrum. These bands arise from a surface layer composed of non-stoichiometric SnO_x with different symmetries than SnO₂, and the influence of surface hydroxyl groups. The thickness of this layer has been calculated to be c.a. 1.1nm, i.e., more or less 2-3 unit cells.

In the low-frequency region the Raman spectrum presents bands which have been related to the spherical vibration of the nanoparticles as a whole. Without being completely clarified if these vibration arise by considering displacement of atoms or not at the particle surface, low-frequency Raman has been shown to be very effective in giving the whole size distribution of very small nanoparticles. Therefore, both the application of the spatial correlation model and low-frequency Raman scattering can be applied to give a quite accurate estimation of nanoparticle

size in a non-destructive way, for what we have given the necessary theoretical background, and which could be used directly in sensors.

For application in gas sensing, it has to be considered that, although it has been proposed that small crystals seem to be the best for improve the gas sensor response, other effects such as those provided for the highest density of defects found in the smallest crystals should be taken into account because of, for example, the modifications that they could promote on the transport properties of the semiconductor. Moreover, the presence of water and hydroxyl groups will produce, in the smaller nanoparticles, drifts in the sensor response and lower sensitivities than the expected.

According to electrical and structural analysis it seems evident that noble metals appear at the surface of the tin oxide particles. Moreover, it has been shown that they do not appear as metallic but in their oxidised forms. The small quantity of both metals introduced could initially support such idea. Apart that Pt and Pd can also be in the interior of the grains, the surface analysis has shown that these metal introduce levels near the valence band edge, which perfectly can account for the resistance measurements of the sensors. On the set of experiments performed, the role played in sensitivity should correspond to the electronic sensitisation mechanism rather than to spill-over. Nevertheless, the presence of reducing gases and the low loading performed, could change Pt and Pd to metallic forms due to the low quantity of material introduced and, thus change the sensitivity mechanism. However, more experiments not included in this work, are needed to evaluate that problem.

By systematic variation of the sensor preparation we obtained that undoped SnO₂ calcinated at 1000°C shows a very good sensitivity to NO₂, with a low cross sensitivity to CO, together with a high long term stability, as a consequence of its well defined structural characteristics. On the other hand, good sensitivity to CO is obtained by introducing Pt or Pd and calcinating at 450°C.

The grinding of powders before or after calcination has been shown a tool to control nanoparticle size and surface state. Although important changes were only observed for particles calcinated at 1000°C, modifications of the grinding procedure could allow grain size control for smaller particles. Particle size reduction due to grinding after calcination occurs via breaking of the larger particles. On the other hand, reduction of grain size when performing grinding before calcination results from a change in the scenario of coalescence. In this last case, the influence of the different surface state density could also play some role on the sintering process.

It has been shown that the grinding procedure of the precursor and/or of the oxide has a strong effect on the resistance in air, thus allowing the tailoring of the base resistance according to the application. Additionally, effects on the sensor response have also been observed. In particular, grinding produces acceptor surface

states and, as a consequence, it improves the cross sensitivity of NO_2 with respect to CO and, besides, it increases the resistance value of the sensor.

These results prove that a controlled modification of the sensing properties of SnO_2 nanoparticles is possible by an adequate control of the technological process, and contribute to define fundamental aspects of nanoparticle engineering for gas sensor design.

3.7 REFERENCES

- [1] F. Curcio, M. Musci, M. Notaro, and G. Quattroni, Laser induced synthesis of ultrafine TiO₂ powders, *Ceramics Today*, Ed. P. Vincenzini, Elsevier Science Publishers B.V., pp. 2569-2578 (1991).
- [2] F. Curcio, M. Musci, N. Notaro, and G. de Michele, Synthesis of ultrafine TiO₂ powders by a CW CO₂ laser, *Appl. Surf. Sci.* **46**, 225-229 (1990).
- [3] B.L. Bischoff, and M.A. Anderson, Peptization process in the sol-gel preparation of porous anatase (TiO₂), *Chem. Mater.* **7**, 1772-1778 (1995).
- [4] S.S. Park, J.D. Mackenzie, Sol-gel derived tin oxide thin films, *Thin Solid Films* **258**, 268-273 (1995).
- [5] J.F. Goodman, and S.J. Gregg, The production of active solids by thermal decomposition, Part XI. The heat treatment of precipitated stannic oxide, *J. Chem. Soc.* **237**, 1162-1167 (1960).
- [6] W. Giesekke, H.S. Gutowsky, P. Kirkov, and H.A. Laitinen, A proton magnetic resonance and electron diffraction study of the thermal decomposition of Tin(IV) hydroxides, *Inorg. Chem.* **6**, 1294-1297 (1967).
- [7] J.C. Giuntini, W. Granier, J.V. Zanchetta, and A. Taha, Sol-gel preparation and transport properties of a tin oxide, *J. Mater. Sci- Lett.* **9**, 1383-1388 (1990).
- [8] B. Orel, U. Lavrencic-Stangar, Z. Crnjak-Orel, P. Bukovec, and M. Kosec, Structural and FTIR spectroscopic studies of gel-xerogel-oxide transitions of SnO₂ and SnO₂:Sb powders and dip-coated films prepared via inorganic sol-gel route, *J. Non-Cryst. Solids* **167**, 272-288 (1994).
- [9] S.C. Ray, M.K. Karanjai, and D. DasGupta, Tin oxide based transparent semiconducting films deposited by the dip-coating technique, *Surf. and Coat. technol.* **102**, 73-80 (1998).
- [10] J.P. Chatelon, C. Terrier, E. Bernstein, R. Berjoan, and J.A. Roger, Morphology of SnO₂ thin films obtained by the sol-gel technique, *Thin Solid Films* **247**, 162-168 (1994).
- [11] F. M enil, C. Lucat, and H. Deb eda, The thick-film route to selective gas sensors, *Sensors and Actuators B* **24-25**, 415-420 (1995).
- [12] V. Golovanov, J.L. Solis, V. Lantto, and S. Lepp avuori, Different thick-film methods in printing of one-electrode semiconductor gas sensors, *Sensors and Actuators B* **34**, 401-406 (1996).
- [13] G. Martinelli, and M.C. Carotta, Thick-film gas sensors, *Sensors and Actuators B* **23**, 157-161 (1995).
- [14] M. Honor e, S. Lenaerts, J. Desmet, G. Huyberegts, and J. Roggen, Synthesis and characterization of tin dioxide powders for the realization of thick-film gas sensors, *Sensors and Actuators B* **18-19**, 621-624 (1994).

- [15] M. Bauer, N. Bárzan, K. Ingrisch, A. Zeppenfeld, I. Denk, B. Schuman, U. Weimar, and W. Göpel, Influence of measuring voltage, geometry and electrodes on the characteristics of thick film SnO₂ gas sensors, *Proc of the 11th European Microelectronic Conference, Venice, Italy, May 14-16 (1997)*.
- [16] J. Kappler, Herstellung von Halbleitersensoren durch Sol-Gel Technologie auf Dickschichtbasis, *Diplomarbeit der Fakultät für Physik der Eberhard-Karls-Universität Tübingen, 1997*.
- [17] Z.M. Jarzebski, and J.P. Marton, Physical properties of SnO₂ materials. I. Preparation and defect structure, *J. Electrochem. Soc.* **123**(7), 199C-205C (1976).
- [18] Z.M. Jarzebski, and J.P. Marton, Physical properties of SnO₂ materials. II. Electrical properties, *J. Electrochem. Soc.* **123**(9), 299C-310C (1976).
- [19] Z.M. Jarzebski, and J.P. Marton, Physical properties of SnO₂ materials. III. Optical properties, *J. Electrochem. Soc.* **123**(10), 333C-346C (1976).
- [20] R.S. Katiyar, Dynamics of the rutile structure: I. Space group representations and the normal mode analysis, *J. Phys. C* **3**, 1087-1096 (1970).
- [21] J.G. Traylor, H.G. Smith, R.M. Nicklow, and M.K. Wilkinson, Lattice dynamics of rutile, *Phys. Rev. B* **3**(10), 3457-3472 (1971).
- [22] P. Merle, J. Pascual, J. Camassel, and H. Mathieu, Uniaxial-stress dependence of the first-order Raman spectrum of rutile: I. experiments, *Phys. Rev. B* **21**(4), 1617-1626 (1980).
- [23] R.S. Katiyar, P. Dawson, M.M. Hargreave, and G.R. Wilkinson, Dynamics of the rutile structure: III. Lattice dynamics, infrared and Raman spectra of SnO₂, *J. Phys. C* **4**, 2421-2431 (1971).
- [24] R. Summitt, Infrared absorption in single-crystal stannic oxide: Optical lattice-vibration modes, *J. Appl. Phys.* **39**(8), 3762-3767 (1968).
- [25] P.S. Peercy, and B. Morosin, Pressure and temperature dependences of the Raman-active phonons in SnO₂, *Phys. Rev. B* **7**(6), 2779-2786 (1973).
- [26] M. Ocaña, V. Fornés, J.V. García Ramos, and C.J. Serna, Factors affecting the infrared and Raman spectra of rutile powders, *J. Sol. State Chem.* **75**, 364-372 (1988).
- [27] M. Ocaña, and C.J. Serna, Variations of the infrared powder spectra of TiO₂ and SnO₂ (rutile) with polarization, *Spectrochimica Acta* **47A**(6), 765-774 (1991).
- [28] M. Ocaña, C.J. Serna, and E. Matijevic, Preparation and characterization of uniform nanocrystalline prismatic SnO₂ particles, *Mater. Lett.* **12**, 32-36 (1991).
- [29] A. Diéguez, A. Romano-Rodríguez, J.R. Morante, U. Weimar, M. Schweizer-Berberich, and W. Göpel, Morphological analysis of

- nanocrystalline SnO₂ for gas sensor applications, *Sensors and Actuators B* **31**, 1-8 (1996).
- [30] A. Diéguez, A. Romano-Rodríguez, J.R. Morante, N. Bárzan, U. Weimar, and W. Göpel, Nondestructive assessment of the grain size distribution of SnO₂ nanoparticles by low-frequency Raman spectroscopy, *Appl. Phys. Lett.* **71**(14), 1957-1959 (1997).
- [31] J. Zuo, C. Xu, X. Liu, Ch. Wang, Ch. Wang, Y. Hu, and Y. Qian, Study of the Raman spectrum of nanometer SnO₂, *J. Appl. Phys.* **75**(3), 1835-1836 (1994).
- [32] C. Xie, L. Zhang, and Ch. Mo, Characterization of Raman spectra in nano-SnO₂ solids, *Phys. Stat. Sol. A* **141**, K59-K61 (1994).
- [33] K.N. Yu, Y. Xiong, Y. Liu, and C. Xiong, Microstructural change of nano-SnO₂ grain assemblages with the annealing temperature, *Phys. Rev. B* **55**(4), 2666-2671 (1997).
- [34] L. Abello, B. Bochu, A. Gaskov, S. Koudryavtseva, G. Lucazeau, and M. Roumyantseva, Structural characterization of nanocrystalline SnO₂ by X-ray and Raman spectroscopy, *J. Solid State Chem.* **135**, 75-85 (1998).
- [35] Ph. Barbarat, S.F. Matar, and G. Le Blevenec, First-principles investigations of the electronic, optical and chemical bonding properties of SnO₂, *J. Mater. Chem.* **7**(12), 2547-2550 (1997).
- [36] J.M. Themlin, M. Chtaïb, L. Henrard, Ph. Lambin, J. Darville, and J.M. Gilles, Characterization of tin oxides by x-ray-photoemission spectroscopy, *Phys. Rev. B* **46**(4), 2460-2466 (1992).
- [37] P. De Padova, M. Fanfoni, R. Larciprete, M. Mangiantini, S. Priori, and P. Perfetti, A synchrotron radiation photoemission study of the oxidation of tin, *Surf. Sci* **313**, 379-391 (1994).
- [38] L. Kövér, G. Moretti, Zs. Kovács, R. Sanjinés, I. Cserny, G. Margaritondo, J. Pálkás, and H. Adachi, High resolution photoemission and Auger parameter studies of electronic structure of tin oxides, *J. Vac. Sci. Technol. A* **13**(3), 1382-1388 (1995).
- [39] S. Samson, and C.G. Fonstad, Defect structure and electronic donor levels in stannic oxide crystals, *J. Appl. Phys.* **44**, 4618-4621 (1973).
- [40] C.G. Fonstad and R.H. Rediker, Electrical properties of high-quality stannic oxide crystals, *J. Appl. Phys.* **42**, 2911-2918 (1971).
- [41] J.G. Zheng, X. Pan, M. Schweizer, F. Zhou, U. Weimar W. Göpel, and M. Rühle, Growth twins in nanocrystalline SnO₂ thin films by high-resolution transmission electron microscopy, *J. Appl. Phys.* **79**(10), 7688-7694 (1996).
- [42] E. de Fresart, J. Darville, and J.M. Gilles, Surface properties of tin dioxide single crystals, *Surf. Sci.* **126**, 518-522 (1983).

- [43] F.H. Jones, R. Dixon, J.S. Foord, R.G. Egdell, and J.B. Pethica, The surface structure of $\text{SnO}_2(110)(4 \times 1)$ revealed by scanning tunneling microscopy, *Surf. Sci.* **376**, 367-373 (1997).
- [44] J.W. Erickson, and S. Semancik, Surface conductivity changes in $\text{SnO}_2(110)$: effects of oxygen, *Surf. Sci. Lett.* **187**, L658-L668 (1987).
- [45] D.F. Cox, T.B. Fryberger, and S. Semancik, Oxygen vacancies and defect electronic states on the $\text{SnO}_2(110)-1 \times 1$ surface, *Phys. Rev. B* **38**(3), 2072-2083 (1988).
- [46] J. Monecke, Collective excitations in microcrystal aggregates and composites, *Phys. Stat. Sol. B* **155**, 437-444 (1989).
- [47] P. Clippe, R. Evrard, and A.A. Lucas, Aggregation effect on the infrared absorption spectrum of small ionic crystals, *Phys. Rev. B* **14**(4), 1715-1721 (1976).
- [48] P.G. Harrison, and A. Guest, Tin oxide surfaces, *J. Chem. Soc.* **83**(11), 3383-3397 (1987).
- [49] H. Richter, Z.P. Wang, and L. Ley, The one phonon spectrum in microcrystalline silicon, *Solid State Commun.* **39**, 625-629 (1981).
- [50] I.H. Campbell, and P.M. Fauchet, The effects of microcrystal size and shape on the one phonon Raman spectra of crystalline semiconductors, *Solid State Commun.* **58**(10), 739-741 (1986).
- [51] J.W. Ager III, D.K. Veirs, and G.M. Rosenblatt, Spatially resolved Raman studies of diamond films grown by chemical vapor deposition, *Phys. Rev. B* **43**(8), 6491-6499 (1991).
- [52] M. Yoshikawa, Y. Mori, H. Obata, M. Maegawa, G. Katagiri, H. Isida, and A. Ishitani, Raman scattering from nanometer-sized diamond, *Appl. Phys. Lett.* **67**(5), 694-696 (1995).
- [53] D. Bersani, P.P. Lottici, and X.Z. Ding, Phonon confinement effects in the Raman scattering by TiO_2 nanocrystals, *Appl. Phys. Lett.* **72**(1), 73-75 (1998).
- [54] T. Werninghaus, J. Hahn, F. Richter, and D.R.T. Zahn, Raman spectroscopy investigation of size effects in cubic boron nitride, *Appl. Phys. Lett.* **70**(8), 958-960 (1997).
- [55] J. Zi, K. Zhang, and X. Xie, Comparison of models for Raman spectra of Si nanocrystals, *Phys. Rev. B* **55**(15), 92623-92666 (1997).
- [56] X. Zhu, R. Birringer, U. Herr, and H. Gleiter, X-ray diffraction of the structure of nanometer-sized crystalline materials, *Phys. Rev. B* **35**(17), 9085-9090 (1987).
- [57] W. Romanowski, Equilibrium forms of very small metallic crystals, *Surf. Sci.* **18**, 373-388 (1969).

- [58] T. Pagnier, M. Boulova, A. Galerie, A. Gaskov, and G. Lucazeau, In situ coupled Raman and impedance measurements of the reactivity of nanocrystalline SnO₂ versus H₂S, *J. Sol. State Chem.* **143**, 86-94 (1999).
- [59] T. Hama, and T. Matsubara, Self-consistent Einstein model and theory of anharmonic surface vibration, *Prog. Theor. Phys.* **59**(5), 1407-1417 (1978).
- [60] S. Hayashi, and K. Yamamoto, Amorphous-like Raman spectra of semiconductor microcrystals, *Superlattices and Microstructures* **2**, 581-585 (1986).
- [61] M. Fujii, T. Nagareda, S. Hayashi, K. Yamamoto, Low-frequency Raman scattering from small silver particles embedded in SiO₂ thin films, *Phys. Rev. B* **44**(12), 6243-6248 (1991).
- [62] L. Saviot, B. Champagnon, E. Duval, I.A. Kudriavtsev, A.I. Ekimov, Size dependence of acoustic and optical vibrational modes of SdSe nanocrystals in glasses, *J. Non-Cryst. Sol.* **197**, 238-246 (1996).
- [63] A. Tanaka, S. Onari, and T. Arai, Low-frequency Raman scattering from CdS microcrystals embedded in a germanium dioxide glass matrix, *Phys. Rev. B* **47**(3), 1237-1243 (1993).
- [64] L. Saviot, B. Champagnon, E. Duval, and A.I. Ekimov, Resonant low-frequency Raman scattering in CdS-doped glasses, *J. Cryst. Growth* **184**, 370-373 (1998).
- [65] E. Duval, A. Boukenter, B. Champagnon, Vibration eigenmodes and size of microcrystallites in glass: Observation by very-low-frequency Raman scattering, *Phys. Rev. Lett.* **56**(19), 2052-2055 (1986).
- [66] M. Gotic, M. Ivanda, A. Sekulić, S. Music, S. Popovic, A. Turkovic, K. Furic, Microstructure of nanosized TiO₂ obtained by sol-gel synthesis, *Mater. Lett.* **28**, 225-229 (1996).
- [67] H. Lamb, On the vibrations of an elastic sphere, *Proc. London Math. Soc.* **13**, 189-212 (1882).
- [68] A. Tamura, K. Higeta, T. Ichinokawa, Lattice vibrations and specific heat of a small particle, *J. Phys. C* **15**, 4975-4991 (1982).
- [69] V. Lantto, and P. Romppainen, Electrical studies on the reactions of CO with different oxygen species on SnO₂ surfaces, *Surf. Sci.* **192**, 243-264 (1987).
- [70] K.D. Schierbaum, , U. Weimar, W. Göpel, and R. Kowalkowski, Conductance, work function and catalytic activity of SnO₂-based gas sensors, *Sensors and Actuators B* **3**, 205-214 (1991).
- [71] W. Göpel, Chemisorption and charge transfer at semiconductor surfaces: implications to design gas sensors, *Prog. Surf. Sci.* **20**, 9-103 (1985).

- [72] E. de Fresart, J. Darville, and J.M. Gilles, Influence of the surface reconstruction on the work function and surface conductance of (110) SnO_2 , *Appl. Surf. Sci.* **11-12**, 637-651 (1982).
- [73] D. Kohl, The role of noble metals in the chemistry of solid.state gas sensors, *Sensors and Actuators B* **1**, 158-165 (1990).
- [74] G. Ghiotii, and F. Prinetto, FT-IR study of the nature and stability of NO_x surface species on ZrO_2 , VO_x/ZrO_2 and $\text{MoO}_x/\text{ZrO}_2$ catalysts, *Research on Chemical Intermediates* **25**(2), 131-156 (1999).
- [75] S.C. Su, J.N. Carstens, and A.T. Bell, A study of the dynamics of Pd oxidation and PdO reduction by H_2 and CH_4 , *J. of Catalysis* **176**, 125-135 (1998).
- [76] T.D. Shen, C.C. Koch, T.L. McCormick, R.J. Nemanich, J.Y. Huang, and J.G. Huang, The structure and property characteristics of amorphous/nanocrystalline silicon produced by ball milling, *J. Mater. Res.* **10**(1), 139-148 (1995).
- [77] J.Z. Jiang, R. Lin, S. Morup, K. Nielsen, F.W. Poulsen, F.J. Berry, and R. Clasen, Mechanical alloying of an immiscible $\alpha\text{-Fe}_2\text{O}_3\text{-SnO}_2$ ceramic, *Phys. Rev. B* **55**(1), 11-14 (1997).
- [78] T.D. Shen, I. Shmagin, R.M. Kolbas, Y. Fahmy, L. Bergman, R.J. Nemanich, M.T. McClure, Z. Sitar, and M.X. Quan, Photoluminescence from mechanically milled Si and SiO_2 powders, *Phys. Rev. B* **55**(12), 7615-7623 (1997).
- [79] M.J. Bannister, Shape sensitivity of initial sintering equations, *J. American Ceramic Soc.* **51**(10), 548-553 (1968).
- [80] L. Fangxin, Y. Jinlong, and Z. Tianpeng, Raman and Fourier-transform infrared photoacoustic spectra of granular ZrO_2 , *Phys. Rev. B* **55**(14), 8847-8851 (1997).
- [81] S. Dick, C. Suhr, J.L. Rehspringer, and M. Daire, Particular-shaped powders obtained by modification of Aluminium and Zirconium Alkoxides, *Materials Science and Engineering A* **109**, 227-231 (1989).
- [82] W.H. Rhodes, Agglomerate and particle size effects on sintering Ytria-stabilised Zirconia, *Journal of the American Ceramic Society* **64**(1), 19-22 (1981).
- [83] F.W. Dynys, and J.W. Halloran, Influence of aggregates on sintering, *Journal of the American Ceramic Society* **67**(9), 596-601 (1984).
- [84] R.L. Coble, Sintering crystalline solids. I. Intermediate and final state diffusion models, *J. Appl. Phys.* **32**(5), 787-799 (1961).
- [85] F.F. Lange, Sinterability of agglomerated powders, *J. American Ceramic Soc.* **67**(2), 83-89 (1984).
- [86] R.L. Coble, Effects of particle-size distribution in initial-stage sintering, *J. American Ceramic Soc.* **56**(9), 461-466 (1973).

- [87] R.M. German, Sintering densification for powder mixtures of varying distribution widths, *Acta Metall. Mater.* **40**(9), 2085-2089 (1992).
- [88] J.S. Chappell, T.A. Ring, and J.D. Birchall, Particle size distribution effects on sintering rates, *J. Appl. Phys.* **60**(1), 383-391 (1986).
- [89] E.A. Barringer, and H.K. Bowen, Formation, packing, and sintering of monodisperse TiO₂ powders, *Comm. of the American Ceramic Soc.* C199-C201 (1982).

CHAPTER 4

IMPROVEMENT OF THE STABILITY OF
HIGHLY POROUS SnO₂ THIN FILM GAS
SENSORS

Chapter 4 is devoted to thin film gas sensors, especially to their stability. The separation between the category of thin or thick film, in general, is made straightforward by classifying the film according to its thickness. However, it is sometimes preferred to classify thin and thick films according to the procedure of fabrication, i.e., when no powder precursor is used we are dealing with thin films, where the film is obtained directly through a deposition process. Therefore, sensors fabricated using r.f. sputtering, r.f. reactive sputtering, r.f. magnetron sputtering, thermal evaporation, chemical vapor deposition (metal-organic, plasma-assisted, ...), electron gun evaporation, ion-beam assisted deposition, reothaxial growth and thermal oxidation, ... correspond to the thin film group, as these are techniques usually related to thin film fabrication. In particular, the work presented in *Chapter 4* is dedicated to SnO₂ thin films fabricated by the *Ion Beam Assisted Deposition of SnO₂* (IBAD), and the *Rheotaxial Growth and Thermal Oxidation of tin* (RGTO).

Chapter 4 begins with a brief introduction about the origin of the use of thin films for sensor fabrication. After introducing the main technologies of fabrication, the results obtained for the IBAD and RGTO methods are presented. In both methods the structural characterisation allows to detect possible sources for sensor drift.

The IBAD method (section 4.2) gives rise to very densely packed layers, which according to *Chapter 1*, should be categorised as field effect sensors rather than conductometric. In the case of RGTO, to which the more important part of the work is devoted, it is worth to comment that, although this is the name originally given to the technique, after several manufacturers fabricated these films, other names can be found in the literature. The most important characteristic of all of these sensors is their highly porous surface morphology, corresponding to a high surface area, and probably the most appropriate name should be '*highly porous thin film gas sensors*', as introduced in the title of the chapter. So, under this category one should remind that sensors such as those fabricated for example by *Motorola* and *Microsens* based on the thermal oxidation of tin or of non-stoichiometric SnO_x, requiring further oxidation, should be included, and the conclusions of this chapter should be extrapolated directly to these sensors as well.

After introducing the RGTO methodology, the rest of the chapter deals about the characterisation of these types of films and the problems appearing as a consequence of the method of fabrication, mainly the oxidation of tin. In this way, after the analysis of the deposition of tin in section 4.3, its oxidation to produce tin dioxide films is investigated in detail in section 4.4 and the conclusions to obtain stable films are used in section 4.5, when the multilayer RGTO method is presented and studied.

4.1 Introduction

4.1.1 Justification of the use of thin film gas sensors

During years several reasons have given rise to the appearance of thin film gas sensors. Among them one can include the improvement of the sensor sensitivity [1-3], the decrease of response time [4, 5], and the lower power consumption with respect to other types of solid state gas sensors. However, probably the most important and real reason to be highlighted is the technological impetus to utilise silicon microfabrication techniques in sensor production to:

- Reduce device size
- Enhance production efficiency and cost reduction by fabricating a large number of sensors on a single substrate
- Increase reproducibility in comparison with discrete devices
- Integrate multisensor gas-detection systems
- Integrate devices with signal processing capability

The last two points probably require additional explanations. As has been commented in *Chapter 1*, semiconductor gas sensors usually present high sensitivity, but respond in a similar manner to several gases. This produces a serious problem of selectivity when more than one gas is present in the ambient to analyse. In order to improve selectivity and, at the same time, the sensing capability to different gases, a large quantity of works have been focussed during the past few years to the use of several sensors (an array of sensors) as an entire sensing unity and recently on their integration on a IC. For this, a great variety of options exist, which have to be controlled by the adequate circuitry:

- Using sensors made of the same sensing material
 - working at different temperatures [6, 7]
 - impregnated with different catalytic materials [8]
 - using sensing layers of different thickness
 - using different electrode configuration or electrode material composition
 - using several types of catalytic filters [9, 10]
 - ...

- Using sensors made with different materials [11, 12] or even different types of sensors [8]

It is evident that this list is not closed at all, as it is relatively easy to think in new combinations.

Moreover, sometimes, when the scientific research is not the only purpose of the investigation, the data acquisition, signal-conditioning, processing functions, output interfacing, and autocalibrating electronics should be accommodated in the same IC. The integration of the sensor or of several sensors in one unique chip,

together with the signal processing electronics, gives rise to the obtaining of the broadly called *smart sensors*. Although the smart sensor concept is an attractive idea, because the design of the microfabricated parts must be done in a monolithic way, every detail of the sensor has to be designed at the same time. When one part of the sensor design is changed, the complete set of masks and probably significant parts of the process have to be changed. This implies an important cost that may make sensor production not feasible when it is not produced in large scale. Therefore, to be realistic and contrarily to what occurs with mechanical sensors manufacture, it seems that the actual tendency in the case of chemical sensing is to use hybrid technology rather than fabricate a complete microsystem [13], being currently complete integration a matter of purely scientific interest.

4.1.2 Low power consumption miniaturised gas sensors

The obtaining of miniaturised gas sensor elements with reduced power consumption is directed actually by most R&D groups [14-22] to prepare the active layers on silicon micromachined structures, such as the schematically presented in figure 1. It has to be mentioned that, for example, with the classical Taguchi gas sensor high power consumption (400-1100 mW) is needed only to heat the sintered tin oxide. However, with the use of micromachined structures power consumption can be as small as typically 100mW. Moreover, the low thermal inertia of these sensors implies new possibilities of operation, because thermal response can be in the order of microseconds.

In low power consumption miniaturised gas sensors, or if preferred, low thermal inertia gas sensors, to provide a thermally well-insulated, low heat capacity support for the thin film, it is deposited on the top of a suspended dielectric (commonly Si₃N₄, SiO₂, or SiN_xO_y) membrane[†]. By using this scheme, it is possible to reduce considerably power consumption, as less power dissipation is needed to heat the structure under the sensing layer (the membrane), than the entire substrate. Due to the short heating time of the membrane a rapidly pulsed mode of sensing is possible.

Despite the advantages of these types of sensors, depending on the way of how these sensors are made, some problems have to be solved, mainly the thermal budget which is applied to the entire wafer during each process. In this way, the different processing steps of the wafer are constrained by the lowest maximum temperature of tolerance of any other device or layer on the wafer. For example, if

[†] Widely used materials in silicon technology capable for being used as membrane materials are silicon, silicon dioxide, silicon nitride, or oxinitrures. Silicon is usually excluded because has a significantly higher thermal conductivity. Si₃N₄ is more effective from the point of view of electrochemical etch stop, but large stresses are generated. Thus, an intermediate solution is being adopted by using a mixed compound between SiO₂ and Si₃N₄, i.e., SiN_xO_y. In the same way, polysilicon is the only material used commonly in IC fabrication and, for this, highly doped polysilicon is used as heater material. Pt can also be used.

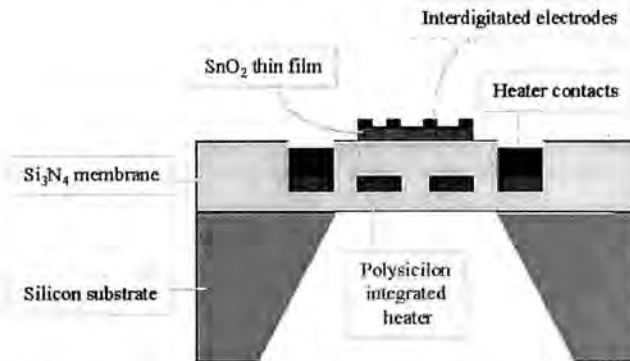


Figure 1: Scheme of a Silicon micromachined gas sensor structure.

the SnO_2 layer is grown from the thermal oxidation of tin, a high-temperature oxidation process is necessary, which could prevent the microsensors fabrication from being compatible with general VLSI processes. Nevertheless, this problem can be overcome by using some micromachining techniques, through which, it is possible to create small structures on silicon wafers thermally isolated from the rest of the wafer. In this way, the works, for example, of R.E. Cavicchi et al. [17], and L.Y. Sheng et al [21, 22], show the use of micro-hotplates, fabricated using CMOS-compatible processes, for temperature control during sputter deposition and MOCVD deposition of SnO_2 thin films. By their method, it is allowed only different portions of the chip to be heated to high temperatures individually.

In this fabrication, one of the most critical decisions is if the sensing layer is deposited (or grown) before or after the etching of the wafer from the backside to form the membrane. Thus, to avoid the damage of the membrane, some people propose depositing the Sn thin film and oxidise it just before the back-side of the silicon substrate is removed [16]. In other cases [22], however, it is preferred the depositing of the SnO_2 layer at the end of the fabrication process to avoid any chemical or physical damage to the gas-sensitive film. Nevertheless, in this last case it would be difficult to obtain stoichiometric SnO_2 , unless a later thermal treatment is applied.

4.1.3 Importance of the stability of gas sensors

Once the gas sensor parameters (sensor type, material, ...) have been selected, its combination with a pattern recognition algorithm is usually considered a well suited tool for the identification and quantification of unknown chemicals in an ambient where only a few of known compounds could be emitted, and this is true for hybrid systems as well as for monolithically integrated sensors. As described in

part 4.1.1 of this *Chapter*, and in *Chapter 1*, the gas sensor system can include one or several semiconductor gas sensors whose sensitivity and selectivity are modified by altering the operating temperature of the individual sensors or by adding different catalytic metals to the active material, between others. On the other hand, the signal processing can involve sophisticated statistical techniques or artificial neural networks [23]. However, in spite of the high degree of improvement of the algorithms used, the properties of each particular sensor may vary in different ways as a function of time, making the predictions of the recognition algorithm wrong and, thus, hindering the correct gas identification. According with H.E. Endres et al. [24], short-term drift of the sensor is correlated with a relaxation process in the material after heating up, whereas the long-term drift is correlated with the material degradation after certain preageing period. The time domains in which these drifts occur are ~0.1-30h for the former and > 100h for the last.

Quite recently, some works have been directed to the modellisation of the drift of the sensor in order to introduce time dependent corrections in the sensor response. It is shown, for example, in the work of H.E. Endres et al [24], how sensor rise time and the baseline drift appearing in the semiconductor gas sensors that they analyse can be modellised with a double-exponential curve shape for each one. These are introduced afterwards as an analytical preprocessing step in the artificial neural network signal processing. However, despite the success of applying such correction algorithms for the sensor instabilities, it is seriously doubted that these procedures allow correcting sensor drift in most sensors without complete or at least advanced knowledge of its origin. Therefore, even though it is commonly accepted that stability is associated to material properties, there exist few works related to the relationship between the structural characteristics of the material and short and long-term drifts. Nevertheless, as stated above, it is extremely important not only to increase the knowledge of material characteristics and stability, but also to establish the conditions of fabrication of the sensor, which will improve its stability for the largest possible period of time and which will diminish parameter dispersion. So, the improvement of the sensor stability through material control is of fundamental importance and for this reason a wide part of this *Chapter* is dedicated to this purpose.

4.1.4 Usual methods for SnO₂ thin film gas sensor fabrication

Up to date, SnO₂ polycrystalline thin films are fabricated basically by sputtering (including d.c. sputtering, r.f. sputtering, r.f. reactive sputtering and r.f. magnetron sputtering), thermal decomposition or evaporation, electron beam evaporation, different chemical vapor deposition methods (thermal CVD, plasma-activated CVD, photon-activated CVD, ...), and spray pyrolysis. All of the commented methods can be categorized more generally under *chemical* or *physical deposition methods*.

4.1.4.1 Chemical methods

Chemical methods are based upon the decomposition of a selected precursor material to form the desired film. The two most important techniques into this group are chemical vapor and spray deposition.

Vapour deposition consist in vaporise the precursor of the film material, which is allowed to condense onto a substrate atom by atom. *Chemical vapour deposition* is a simple and inexpensive process in terms of equipment cost, the dopants can be introduced easily whenever desired, and the reactants, which are in the vapor phase, are in highly pure form. A typical experimental set-up for CVD is shown in figure 2. Basically it consists of a long resistance-heated furnace capable of giving temperatures up to 1000°C and bubblers and tubes for carrying the reactants into the reaction chamber. When dopants are required, more bubblers (one for each reactant) are introduced, together with the corresponding flow controllers for the carrier gas, which controls the partial pressure of each source. By using CVD, SnO_2 is typically obtained from $\text{SnCl}_2 \cdot 2\text{H}_2\text{O}$, $\text{SnCl}_4 \cdot 5\text{H}_2\text{O}$, tetramethyltin (TMT = $\text{Sn}(\text{C}_2\text{H}_5)_4$), and SnSO_4 , between others. Dopants are introduced from the corresponding chlorides (ex. SbCl_2 , and SbCl_5 to introduce Sb). In the case of photochemical vapor deposition a usual precursor is tin(II) acetate $\text{Sn}(\text{CH}_3\text{COO})_2$, the process taking place under UV irradiation for example with a mercury lamp. A typical carrier gas is N_2 . Chemical baths usually are at 250-400°C. The vapor zone temperature is usually in the range 700-1000°C.

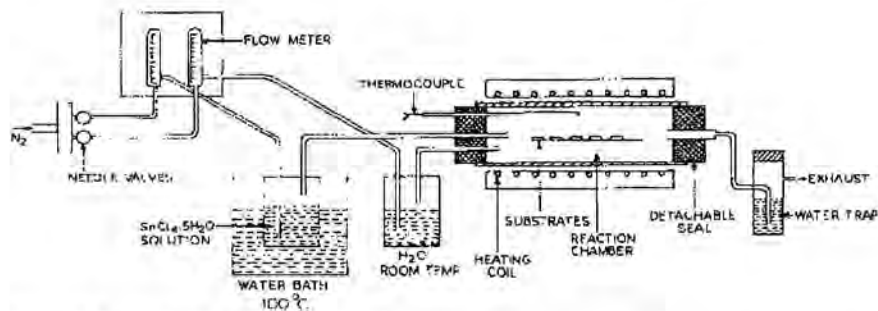


Figure 2: Typical CVD equipment. After [39].

The *spray deposition* method is particularly attractive because of its simplicity. It is fast, inexpensive and vacuumless, and is suitable for mass production. The spray deposition technique is basically a chemical deposition technique in which fine droplets of the desired material solution are sprayed onto a heated substrate. In essence, the process consists in two stages, i.e., droplet drying and precursor decomposition. Depending if they take place before or after the

droplet reaches the substrate, spray pyrolysis can be understood, respectively, as a chemical vapour deposition, with gaseous species reaching out and reacting at the surface, or as a hydrothermal growth, being the film surface eventually covered by a thin liquid layer. What happens depends on the specific heat of the solution, the amount of liquid reaching the film per time unit, and the substrate temperature. Liquid spraying usually produces droplets of different sizes, which are subjected to the action of gravitational forces, thermophoretic forces (which depend of the air and aerosol thermal conductivities, the air viscosity, air density, and air-hot plate thermal gradient) and Stokes forces (which depends of the droplet and air speed). This makes spray pyrolysis a poor reproducible deposition process if strict control is not applied.

Typical spray equipment is shown in figure 3. The atomiser, which is the main part, consists in a nozzle mounted in a glass flask. Filtered compressed air is used as the carrier gas and the flow is controlled by a flow meter. The furnace is an electrically heated stainless steel cylinder, with an aperture a certain distance below the upper surface for inserting a thermocouple. Spray pyrolysis is made usually by spraying an alcoholic (ex. C₂H₅OH) solution of SnCl₄·5H₂O onto a hot substrate in an open air atmosphere. In this case a poor conductive film is obtained and usually F is added from NH₄F (ex. C₂H₅OH + NH₄F) in order to obtain a more conductive film. Other typical precursors for spray pyrolysis are tetra-*n*-butyltin (TBT) diluted in ethanol, and di-*n*-butyltin acetate (DBTDA). The temperature of the substrate is kept between 300 and 600°C. As the substrate is cooled during spraying, the spraying is done intermitently in order to kept the substrate temperature as constant as possible.

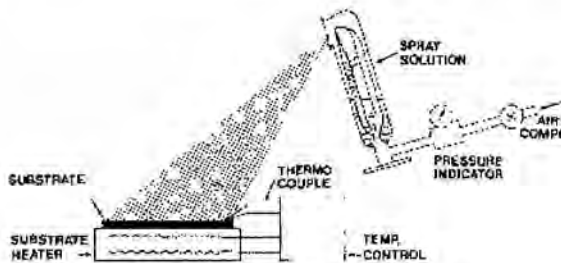


Figure 3: Spray pyrolysis equipment. After [59]

For CVD as well as for spray pyrolysis, chloride-based precursors give rise to SnO₂ films with electrical resistivities in the range 10^{-3} - $5 \cdot 10^{-4}$ Ωcm. On the contrary, organometallic tin-based precursors yield films with low electrical conductivity. Moreover, the film texture depends on the precursor used for deposition, and precursors also influence the growth rate and the appearance of certain preferential orientations.

4.1.4.2 Physical methods

Physical methods include thermal evaporation, electron gun evaporation and sputtering techniques.

For *thermal evaporation* Sn is used as starting material. In this case the metal can be evaporated by suspending it in the coil of a coiled filament made of a material with high melting temperature such as tungsten, which is heated to the required temperature (figure 4a). To obtain SnO_2 oxygen is introduced in the evaporation chamber in order to react with the Sn atoms and form SnO_2 (*reactive thermal evaporation*). The disadvantages of this method are the possible contamination from the heater and the limited film thickness due to the small quantity of Sn that can be suspended in the filament. In order to allow for higher charges other method consists in locate the Sn in a crucible that is heated by r.f. induction (figure 4b). In this case contamination is possible from the crucible but higher deposition rates are possible.

A typical *electron beam evaporation* source is shown schematically in figure 4c. A thermoionic filament supplies the electrons, which are accelerated by an electric field to strike the surface of the Sn or SnO_2 charge to be evaporated.

In the case of Sn evaporation, oxygen is introduced in the chamber as for thermal evaporation. To prevent impurities from the filament reaching the charge a magnetic field bends the e-beam path, thus screening the impurities. In more general cases, it is possible also to use multiple sources in the same chamber in order to form alloy films. In this case it is possible to obtain high deposition rates ($\sim 0.5 \mu\text{m}/\text{min}$) depending on the source-to-substrate distance. The disadvantage of the process is the generation of X-rays by the e-beam, which can penetrate the surface layers of the devices, causing damage such as the creation of oxide-trapped charges, which might change the device characteristics.

The most important form of obtaining SnO_2 by physical deposition methods is sputtering. *Sputtering* is usually done from a target of Sn or SnO_2 of at least 99.99% purity and deposition rates on the order of $\sim 1 \mu\text{m}/\text{min}$ can be obtained, depending also on the source-to-substrate distance. The process involves the acceleration of ions, usually Ar^+ , created for example by a plasma discharge r.f. generator, through a potential gradient and, the bombardment by these ions of a

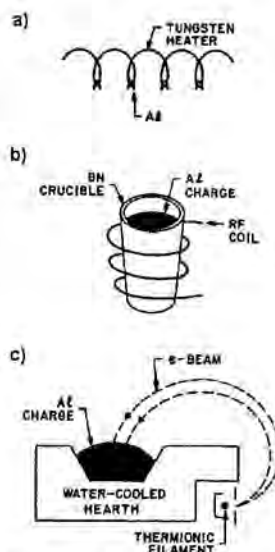


Figure 4: a) Thermal evaporation. b) Thermal evaporation in a crucible heated by r.f. induction. c) Electron beam evaporation.

target or cathode. Through momentum transfer, atoms near the surface of the target material become volatile and are transported as a vapour to the substrate, where the film grows by deposition. The target can be mounted face down in the top plate of the sputtering chamber, as well as face up in the bottom part of the chamber, and is usually cooled during sputtering. To ensure uniform thickness of the film, the substrates are placed in a rotary arm of the system or distributed in a planetary system, approximately 5-10cm away from the target. To avoid possible contamination, the substrates are covered before the start of the deposition by a shutter and the target is cleaned by a pre-sputtering process. Therefore, the only possible source of contamination can be oil of the vacuum pumps.

When the target is an isolating or semi-isolating material, the bombardment with ions produces the charging of the target and of the deposited film. This makes necessary the use of *r.f. sputtering*. The complete scheme is constituted by the generator, the cathode, the plasma, the anode, and the conduction threads to the generator. If at the surface of the cathode there is an isolating material (the material to be deposited), a capacitor is formed, through which dc current can not flow. However, this is avoided when a rf current is applied, because there is the electrical continuity needed to do the sputtering. Unfortunately the rf sputtering system is much more complex than the dc sputtering system because impedances have to be matched. Nevertheless, more uniform films and higher deposition rates can be obtained.

In *reactive sputtering* a certain percentage of the sputtering ions are not inert in order to react with the sputtered material (a chemical reaction is produced). This is the case for example of the sputtering of Sn with a mixture of argon and oxygen ions in order to obtain SnO₂.

Sometimes a conical magnetron is used for sputter deposition. In this case, electrons originating at the cathode are confined by the fields from the permanent magnets and are collected by the anode. A large fraction of the sputtered material (neutral atoms) from the target cathode is ejected forward and deposited on a substrate that need not be an electrode of the system. With the magnetron sputtering a plasma is created near the target in such a way that the sputtered material (ions) is more confined than with normal sputtering. The magnetron operates at voltages an order of magnitude below the e-beam source voltage and thus generates less penetrating radiation.

To finalise this section, table I shows a summary of most of the papers concerning the fabrication of SnO₂ polycrystalline thin films during the last years, being a crude representation of the percentage of use of each technique. When it was available from the reference, the precursor material to obtain the film is presented, as well as the gases detected in each case. Some of the referred papers are included because they contain interesting information not about the application to gas sensing, but about the structural characterisation of the material. It can be seen that

most SnO₂ thin films are fabricated by any type of sputtering (as corresponds to the best purity of the obtained material), followed by CVD methods and spray pyrolysis, which are used in a similar proportion. It is important to remark the importance that during the past few years has acquired the RGTO method.

4.1.5 Today's modifications for improvement of thin films

Chemical methods usually give rise to a contaminated layer (p.e., a typical contaminant is Cl as chlorides are used as precursor materials for the reactions). Therefore, although more infrastructures are needed for physical deposition methods (vacuum pumps, r.f. generators, ...), these are more widely used because of the higher purity of the resulting SnO₂. However, it is well known that the sputtering of Sn or SnO₂, as well as the thermal evaporation of Sn or the electron beam evaporation of SnO₂ produce non-stoichiometric thin films, the obtained material being tin rich. This yields to instability problems such as drifts in the sensor response and sensor degradation. As a consequence some attempts to improve these techniques have emerged. Basically these include the Ion Beam Assisted Deposition (IBAD) and the Reoaxial Growth and Thermal Oxidation (RGTO) techniques. The description of the IBAD and RGTO techniques is the aim of the next sections of this *Chapter*.

Technique		Doping/Catalyst	Gas measured	Reference
Chemical vapor deposition (MOCVD, PECVD, ...)	Origin			
	DBTD	Pt	Oxygen	[25]
	SnCl ₂	Cu, Pt, Sb	CO	[26]
	Sn(CH ₃ COO) ₂	Pd	CO	[27]
	DBTD		CO, CH ₄	[28]
	DBTD		CH ₄	[29], [30]
	DBTD		ethanol	[132], [31]
	SnCl ₂	Sb, Pd	NO _x	[32]
	TMT	Pd	H ₂ S, SO ₂	[33]
			CO, iso-C ₄ H ₁₀ , ethanol, H ₂	[34]
	SnCl ₄	Sb, Ga	CO, CH ₄	[35]
	SnCl ₄			[36]
	SnCl ₄ , SnCl ₂			[37]
	SnCl ₂		H ₂	[38]
	SnCl ₄			[39]
	SnCl ₄	Sb		[40]
	SnCl ₂			[83]
	TMT			[41]
	Sn(CH ₃ COO) ₂			[42]
	DBTDA		H ₂ , CH ₄ , C ₂ H ₅ OH,	[43]
	Sn(O ^t Bu) ₄		CO	[44]
Sn(C ₂ H ₅) ₄		H ₂	[45]	
TMT			[46]	

Table I: Review of the literature on the most usual preparation techniques for thin films. (CVD)

Technique		Doping/Catalyst	Gas measured	Reference
Spray pyrolysis	Origin			
	SnCl ₄		CO, ethanol	[47]
	SnSO ₄	Pd	ethanol	[47]
	DBTD	Pd	CO, ethanol	[48]
	SnCl ₄	Sb	ethanol	[131]
	SnCl ₄	CuO	H ₂ S	[49]
	SnCl ₄	Zr, Pd	PH ₃	[50]
	SnCl ₄	In	C ₂ H ₅ OH	[51]
	SnCl ₄		H ₂	[38]
	SnCl ₄			[52]
	SnCl ₄			[83]
	SnCl ₄			[53]
	TBT			[54]
	[Sn(C ₄ H ₉) ₂](CH ₃ COO) ₂			[55]
	SnCl ₄			[56]
	SnCl ₄			[57]
	SnCl ₄	F		[58]
	SnCl ₄	F		[59]
	SnSO ₄		CO, C ₂ H ₅ OH	[60]
	SnCl ₂ , SnCl ₄	CuO	C ₂ H ₅ OH, CO	[61]
	SnCl ₄	F, Ag	H ₂	[62]
		CuO, NiO	C ₂ H ₅ OH, CO, H ₂ S, CH ₄	[63]
	SnCl ₄	Pt	CO	[64]
	DBTDA	Pd	CO, C ₂ H ₅ OH, CH ₄	[65]
	SnCl ₄	Mn ₂ O ₃	N ₂ , H ₂	[66]

Table I (cont.) (Spray pyrolysis)

Technique	Target	Doping/Catalyst	Gas measured	Reference
(r.f. sputtering, r.f. magnetron sputtering, and r.f. reactive sputtering)	Sn	Pd	H ₂	[67]
	Sn	Sb, Cu, Pt	CO	[68], [69]
	Sn		CO	[70]
	Sn		ethanol	[71]
	Sn	In	NO _x	[72]
	Sn		NO _x	[73]
	Sn	In	NO _x	[74]
	Sn		NO ₂ , CO	[75]
	Sn		NO _x	[76]
	Sn		CO, CH ₄ , ethanol	[77]
	Sn	Pt, Pd	CO, H ₂	[78]
	Sn		Oxygen	[79]
	Sn		ether	[80]
	Sn		CO, H ₂ , NO ₂ , NH ₃	[4]
	Sn		CO, ethanol	[81]
	Sn			[82], [83]
	Sn	F, Sb, Mo		[84]
	Sn	Cu, Pt	Cl ₂ , CO, H ₂	[85]
	Sn	Cu, Ni, Pd, Pt	N ₂ , H ₂ S, O ₂ , N ₂	[86]
	SnO ₂	Pd, Ga	H ₂ , ethanol	[87]
	SnO ₂	Sb, Au	H ₂	[88]
	SnO ₂	Pd, Ag	H ₂ , H ₂ S	[89]
	SnO ₂		H ₂	[90]
	SnO ₂	Li	Oxygen, alcohols	[91]
	SnO ₂		NO _x	[92]
	SnO ₂	Pt, Pd	CO	[93]
	SnO ₂	Pt, Al	CO, NO _x	[94]
	SnO ₂	Pt, Pd	CO	[95]
	SnO ₂	Pt	CO	[96]
	SnO ₂	Pt	CO, CO ₂	[97]
	SnO ₂	Pt, Ca	CO, CO ₂ , NH ₃	[98]
	SnO ₂		CO	[99]
	SnO ₂	Pt, In	CO, NO _x	[100]
SnO ₂	Pd	CO, ethanol, H ₂ S, SO ₂	[101]	
SnO ₂	SiO ₂	CH ₄	[102]	
SnO ₂	Al	NO _x	[103], [104]	
SnO ₂	In ₂ O ₃ , In, Bi	H ₂ , NO _x	[105]	
SnO ₂	In, V	NO _x	[106]	
SnO ₂	Pt, In	NO _x	[107]	
SnO ₂		H ₂ S, H ₂ , C ₂ H ₅ OH	[108]	
SnO ₂ :Pd		CH ₃ SH	[109]	
SnO ₂	Pd	CH ₃ SH	[110]	
SnO ₂	Al ₂ O ₃ , Fe ₂ O ₃	HF	[111]	
SnO ₂		CO	[112]	
SnO ₂		O ₂ , H ₂ , H ₂ S, NO	[113]	
SnO ₂	Pd	CH ₄ , H ₂	[114]	
SnO ₂		CO, H ₂	[115]	

Table I (cont.) (Sputtering)

	SnO ₂		phenylarsine	[116], [117]
	SnO ₂			[118], [119]
	BaSnO ₃		CO, NO _x	[120], [121]
			H ₂ , CO	[122]
		Pd	H ₂	[123]
			CO	[124]
			AsH ₃ , PH ₃	[125]
	SnO ₂	ZnO	C ₂ H ₅ OH	[126]
	SnO ₂		NO ₂ , NO, O ₃	[127]
	SnO ₂		NO ₂ , CO	[128]
		Ag, Au, Pd, Pt		[129]

Table I (cont.) (Sputtering)

Technique	Doping/catalyst	Gas measured	Reference
<i>Thermal evaporation/decomposition</i>			
	Pd, Pt, Au, Bi ₂ O ₃ Sb ₂ O ₃ , Cr ₂ O ₃	H ₂	[130]
		ethanol	[131], [132]
		CCl ₄	[133]
			[134]
		ethanol, H ₂ , CO	[135]
		C ₆ H ₆ , H ₂ S	[136]
			[137]
			[138]
	Pd	CO	[139]

Table I (cont.) (Thermal evaporation/decomposition)

Technique	Doping/catalyst	Gas measured	Reference
<i>Electron gun evaporation of SnO₂</i>			
	Pd	H ₂ , CO	[140]
	Pt	CO	[141]
	Pt	CO	[142]
			[143]
		CO, ethanol	[144]
		H ₂ , NH ₃	[145]
			[146]

Table I (cont.) (Electron gun evaporation)

Technique	Target	Doping/Catalyst	Gas measured	Reference
IBAD	Sn			[147]
	Sn			[148]
	Sn			[149]
	Sn	Ag, Pd, Pt	H ₂	[150]

Table I (cont.) (Ion beam assisted deposition)

Technique	Doping/Catalyst	Gas measured	Reference
Rheotaxial growth and thermal oxidation	Pd	H ₂ , NO _x	[105]
	Pd	H ₂	[42]
		H ₂	[151]
	Bi ₂ O ₃	H ₂ , CO, NO _x	[152]
	Bi ₂ O ₃	H ₂ , CO, NO _x , CH ₄	[153]
	Cd	H ₂ , CO, butane, NO _x	[154]
	Bi	H ₂ , CO, NO _x , CH ₄	[155]
	Pt	CO, H ₂ S	[156]
	Pt, Pd, Ag	CO	[157]
	Fe	CO	[158], [159]
	Pd	CO, H ₂ , C ₃ H ₈ , i-C ₄ H ₁₀	[160]
		ethanol	[161]
	Cd	NO _x	[162], [163]
	Pd	H ₂ , CO	[140]
	Pd	H ₂ , CO, C ₂ H ₅ OH, CH ₄	[164]
	Cd	NO _x	[165]
		N ₂ , O ₂ , CO	[166]
			[167]
			[168]
		H ₂	[169]
		CO, NO, NO ₂	[19]
	Au, In	CO, NO ₂	[170]
	Al, Pt, Au	CO, NO, O ₂ , CH ₄ , NO ₂	[171]

Table I (cont.) (RGTO)

4.2 The deposition assisted with ions: The IBAD technique

In recent years, it has become clear that low-energy ion beams play an important role in influencing the processing of semiconductor thin films, thereby providing additional mechanism of control. It is evident that since ions of sufficient energy striking a film physically displace atoms, film microstructure is directly affected. So, low and high-energy ion beams are used to sputter surfaces, clean and etch them, enhance dopant incorporation, modify strain, and change the growth modes of the films (changing morphology and increasing densification and compactness). Moreover, low-energy ion beams can be used to reduce thin-film deposition temperatures, suppressing dopant diffusion and preventing segregation. When depositing thin films at low temperatures, usually only amorphous material forms. Increasing either the energy or the flux of the ion beam facilitates crystallisation of the amorphous material [172] by local heating. Nevertheless, when the energy of the ion beam exceeds a certain limit, etching by the ion beam can occur, sputtering exceeding the deposition rate. The same is applied when depositing non-elemental materials, in which case the additional bombardment by the ion-assisting beam generally causes preferential sputtering of one of the species so that the resultant composition of deposited material can change [173].

IBAD (or IAD) is a *physical vapor deposition* (PVD) method through thin films are deposited by electron gun evaporation, thermal evaporation or sputtering, assisted with an ion beam bombarding the growing film. So, accelerated ions and evaporated atoms arrive simultaneously at the surface of the substrate. In general Ar^+ or Ne^+ ions are used. Nevertheless, the adhesion of films produced with oxygen IBAD results improved as a consequence of promotion of electronic processes and reactions on the bombarded surface [174]. In addition in the case of oxide deposition, oxygen ions lead to a better stoichiometry.

A typical IBAD equipment consists of a low-energy ion source, a deposition unit, and a target holder within a vacuum chamber. The equipment used to deposit the SnO_2 thin films structurally characterised in this work is schematically shown in figure 5. It consists in an electron-beam evaporation source, where the target material is SnO_2 , a Kaufman source for the oxygen ion beam, and the rotary arm for the substrates. The deposition rate of tin oxide was monitored with a quartz crystal thickness monitor. With this system the SnO_2 thin films were deposited on individual chips. In some cases, the complete process involves a second step of annealing in order to obtain a fully oxidised SnO_2 film.

In what follows some of the depositing parameters will be considered for optimisation. Concretely we will deal with:

- Deposition rate
- Substrate temperature
- Annealing temperature

The addition of noble metal catalysts was also analysed.

It can be seen that from the point of view of the IBAD process only the deposition rate is a fundamental parameter. In general, the parameters to optimise are the ion beam energy (low-energy beams reduce the sensing layer damage, while high-energy ion beams promote mixing and adhesion), the ion beam flux, and the oxygen partial pressure. The substrate temperature is not usually analysed, as IAD is usually performed at low temperature, since the activation of the substrates is achieved by the ion beam.

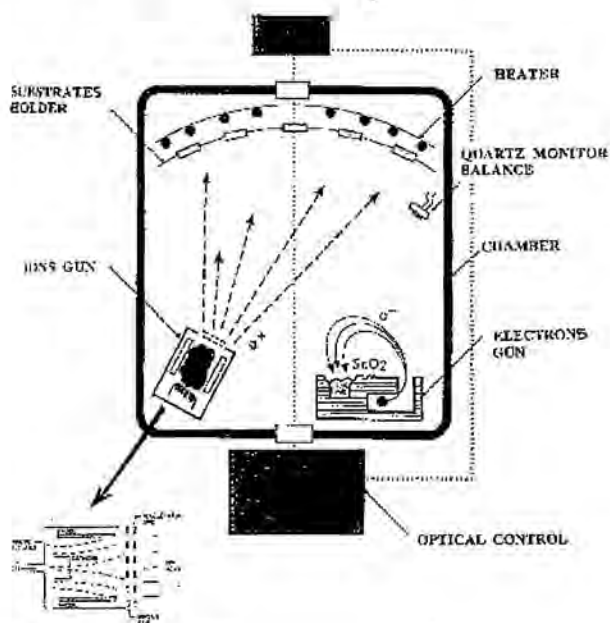


Figure 5: IBAD equipment.

4.2.1 Description of the substrates

Silicon substrates ($380\mu\text{m}$ thick) as well as thin films were prepared by SAGEM. Silicon was chosen because in these moments there is a great interest for such material, as was outlined in the introduction of this *Chapter*. Other reasons include the industrial facilities already existent at the SAGEM laboratory.

As corresponds to a thin film gas sensor, the substrate had to comprise the detection electrodes and the heater element, together with their corresponding contacts. All the electrical bondings were defined on a single side of the chip to facilitate all the further bonding operations. However some films were prepared also

without the heater, or without any of these two elements to facilitate the structural characterisation.

Electrical insulations were obtained by SiO_2 layers between the substrate, the heater level, and the detection electrodes level. These SiO_2 layers were intended also to avoid any diffusion between the chip and the sensitive film. Nevertheless, to reinforce the effectiveness of this layer, in some cases an additional Si_3N_4 layer on top of the thermally grown SiO_2 was added.

The heater consisted of a Pt resistor deposited by sputtering on an adhesion layer of TiW, and patterned by ion etching. To ensure the thermal uniformity on the maximum area, the filament width is large ($250\mu\text{m}$), the gap thin ($50\mu\text{m}$) and a larger area is designed in the corners. The thickness of $0.18\mu\text{m}$ allows a resistance of 100 Ohms. The structure heating and the temperature control are obtained by a 4-point scheme. The detection electrodes consisted of a TiW/Pt layer of $0.1\mu\text{m}$ deposited by sputtering. Different kinds of detection electrodes were designed. Type *A* corresponds to 4-point electrodes arrangement, and types *B*, *C*, and *D* to interdigitated electrodes with a finger width of $50\mu\text{m}$ and gap dimensions between the fingers of 50, 100, and $200\mu\text{m}$ respectively. The description of the heater and the different configuration of the detection electrodes is presented in figure 6. For further details on the masks used, sizes, and procedures of deposition the reader is referred to reference [175].

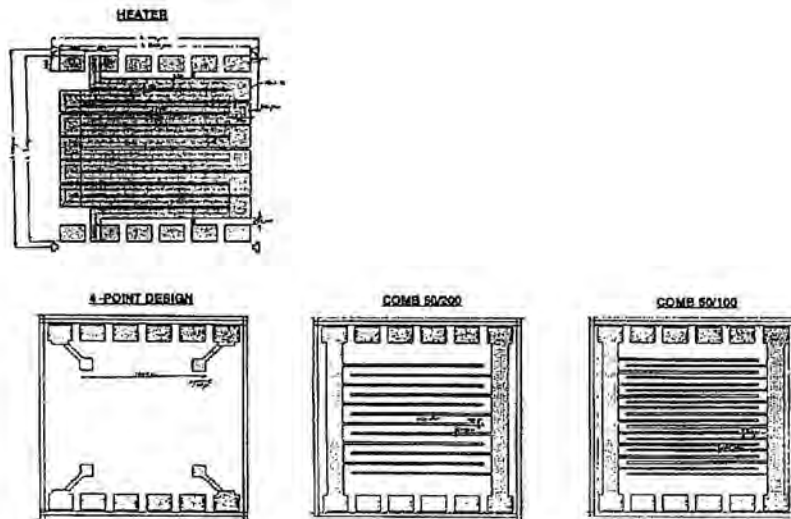


Figure 6: Heater structure (top) and different configuration of the electrodes (bottom).

The nomenclature and characteristics of the substrates used for SnO_2 IAD are presented in table II.

IBAD						
NOTATION	Substrate	Electrodes	Heater	Dimension	Substrate Cleaning	Substrate heating
Be	Si/SiO ₂ /electrode	Yes	No	4.9x4.9 mm ²	No	No
F	Si/SiO ₂	No	No	9.9x9.9 mm ²	No	No
F _H	Si/SiO ₂	No	No	9.9x9.9 mm ²	No	Yes
A	Si/SiO ₂ /Si ₃ N ₄	Yes (4 points)	Yes	4.9x4.9 mm ²	No	Yes
B	Si/SiO ₂ /Si ₃ N ₄	Yes (comb 50/50)	Yes	4.9x4.9 mm ²	No	Yes
C	Si/SiO ₂ /Si ₃ N ₄	Yes (comb 50/200)	Yes	4.9x4.9 mm ²	No	Yes
D	Si/SiO ₂ /Si ₃ N ₄	Yes (comb 50/100)	Yes	4.9x4.9 mm ²	No	Yes

Table II: Characteristics of the substrates used for SnO₂ IBAD.

4.2.2 Influence of the deposition rate and final annealing on the film characteristics

According to [175], for deposition rates below 0.4 Å/s sputtering exceeds deposition. Thus, the investigation was only performed for values of deposition rate ranging from 0.8 to 1.9 Å/s. Substrate temperature (35°C), pressure ($1.5 \cdot 10^{-4}$ mbar), beam voltage (400V) and current density (1.41 mA/cm²) were fixed. The growing conditions are presented in table III. The substrates were type Be and F for this part of the analysis, but only samples on F substrates were structurally characterized for simplicity.

The final annealing step was done in synthetic air (20% O₂ – 80% N₂) because of the more aggressive conditions observed under annealing in O₂ atmosphere only [176]. The temperature used for thermal treatments was 500°C for periods of 10 and 18h. The nomenclature of the samples investigated is presented in table IV.

IBAD						
Dep. n°	Substrate temperature	Pressure	Rate	Beam voltage	Current density	Thickness
4	35°C	$1.5 \cdot 10^{-4}$ mbar	0.8 Å	400 V	1.41 mA/cm ²	125 nm
5	35°C	$1.5 \cdot 10^{-4}$ mbar	1.0 Å	400 V	1.41 mA/cm ²	125 nm
6	35°C	$1.5 \cdot 10^{-4}$ mbar	1.3 Å	400 V	1.41 mA/cm ²	125 nm
7	35°C	$1.5 \cdot 10^{-4}$ mbar	1.9 Å	400 V	1.41 mA/cm ²	125 nm

Table III: Conditions for growing of SnO₂. The varying parameter is the deposition rate.

IBAD		
Kind of chip	Deposition n°	Annealing (synthetic air)
OBe F	4	0 1 (500°C-10h) 2 (500°C-18h)
	5	
	6	
	7	
	0 (no SnO ₂)	

Table IV: Nomenclature of the first group of samples.

4.2.2.1 Characteristics of the as-obtained films

Figure 7 shows cross-section TEM images of samples F40, F50, F60, and F70. The SADP of sample F40 is presented in figure 8. Images of figure 7 reveal the existence of an amorphous region at the SiO₂-SnO₂ interface (the growing surface), which thickness increases with the increase of the deposition rate (table V). In sample F70, which is completely amorphous, two different regions (with a different contrast) are distinguished with a detailed inspection. It is observed that the thickness of the amorphous layer follows a linear dependence with the deposition rate. Such dependence suggests the existence of a period for which the ion flux is not enough to induce crystalline material and which depends on the deposition rate. It is as if:

- i) the ion beam is not able to prepare the SiO₂ surface for proper adhesion, and
- ii) the oxygen ion beam induces a strong disorder on the deposited SnO₂ material.

A possible solution could be the increase either of the oxygen ion flux or of its energy during the first minutes of deposition [172]. However, increase of the energy of the ion beam could cause also a higher damage at the SiO₂ surface.

Sample	Deposition rate	Thickness _{amorphous}	Time
F40	0.8 Å/s	18 nm ± 7 nm	3.75 min.
F50	1.0 Å/s	27 nm ± 12 nm	4.5 min.
F60	1.3 Å/s	41 nm ± 22 nm	5.25 min.
F70	1.9 Å/s	71 nm ± 54 nm	6.22 min.

Table V: Thickness of the amorphous region observed in the interface SiO₂-SnO₂. The time needed to form such amorphous region according to the deposition rate is presented in the last column.

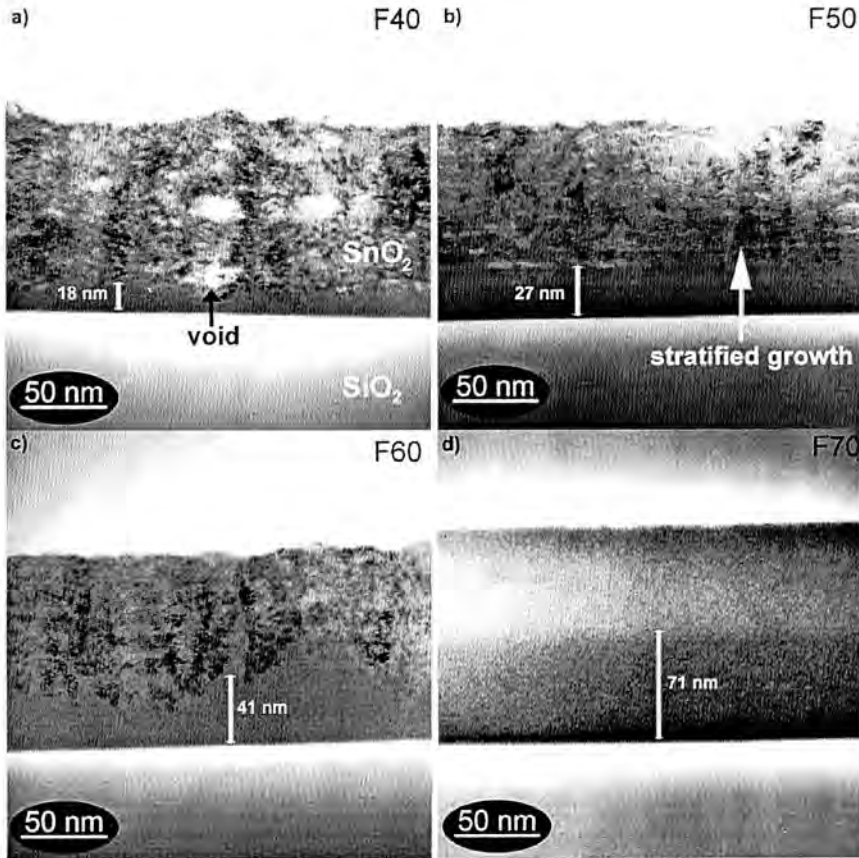


Figure 7: Cross-section TEM images of samples deposited at a deposition rate of 0.8 Å/s (a), 1.0 Å/s (b), 1.3 Å/s (c), and 1.9 Å/s (d). The amorphous region and its thickness is indicated with a white line. Other features such as the stratified growth are also marked. Note that sample F70 is completely amorphous. Nevertheless, two regions of different contrast can be observed.

The crystalline regions of the film present always the cassiterite phase of SnO₂ as it is deduced from the spacing of the rings appearing in the SADP of figure 8. From the transmitted beam in the centre of the image, the observed rings correspond to the [110], [101], [200] and [211] reflections. These crystalline regions of each sample are also characterised by a stratified growth (see figure 7). It is difficult to observe in sample F40 but very clear in samples F50 and F60. In these two last cases, the periodicity is 12 and 14 nm respectively. Calculating the thickness of the "layers" and taking into account the deposition rate, it could be possible that the origin was the rotation of the substrate during growth at ~0.5 rev/min. Other

origin could be a pulsed mode of operation of the ion beam. However, none of these hypotheses has been confirmed and, the no appearance of stratified growth in sample F70 makes difficult these hypotheses. Therefore, it is possible that the origin of the stratification be a problem of low mobility on the growing surface due to the low temperature of deposition rather than a technological problem.

Composition inhomogeneities have been also observed in the crystalline regions of the SnO_2 films. They are observed in the cross-section images of samples F40, F50 and F60, as well as in the planar view. These can correspond to gaps of material (voids), or to regions rich in oxygen (due to their lower absorption). The first option is the more probable, as there is no reason to obtain oxygen rich regions, because if these would exist, probably oxygen would react with Sn or would evaporate.

In some regions, these samples are also characterised by what seems a columnar growth. Indeed, the SADP of these samples show indications of preferential orientation, which has been confirmed by XRD to be in the $[101]$ direction [175]. If the film tends to contain voids or gaps at grain boundaries, sideways creep can result and close these spaces. Since the phenomenon depends on the orientation of the planes with respect to the direction of stress existing in the film, some grains will be affected more than others resulting in texturing [177]. Texturing could also be promoted by the angle of incidence of the oxygen ions thorough a mechanism of preferential sputtering in some directions [178].

Nanoparticle size is very difficult to estimate due to the compactness of the film. Nevertheless it is very small, its maximum value limited approximately as 6-7nm, except when an amorphous film is obtained.

4.2.2.2 Characteristics of the films after annealing

After the thermal treatment at 500°C for 10h the amorphous region as well as the stratified growth disappear (figure 9a). A densification of the film is also observed. The amorphous region appears now as a highly defective area (figure 9b), very large planar defects being the most observed. The disappearance of the

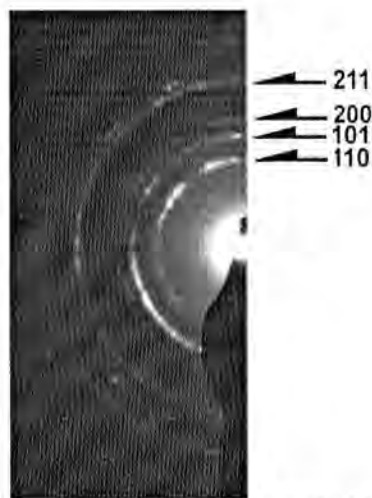


Figure 8: TED pattern of sample F40. Rings indicate that the layer is polycrystalline. However, some zones of the ring are more intense, which indicates preferential orientation.

stratification and of the amorphous region under heating suggests their origin due to a diffusion problem. Preferential orientation remains after annealing. This could be explained by the preferential orientation existing prior to annealing and by the disappearance of voids according to the mechanism commented above.

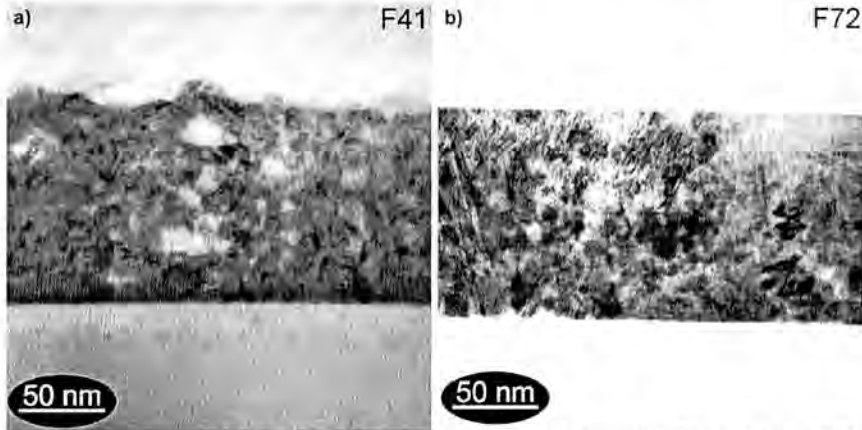


Figure 9: Cross-section TEM images of some of the annealed samples (F41 in (a), and F72 in (b)). Disappearance of the amorphous regions is evident. Instead highly defective regions are found.

The more clear case of crystallisation is obtained with sample F70. In addition, as a result of crystallisation an increase of surface roughness is also observed. In the as obtained sample the RMS value for surface roughness is $\sim 2.2\text{\AA}$ and the maximum roughness $\sim 1.2\text{nm}$, while the RMS and maximum values after 18h of annealing at 500°C are 7.9\AA and 5.5nm respectively. As it is clear from the Atomic Force Microscopy (AFM) images of figure 10, material diffusion causes, together with the crystallisation, surface roughness to increase. For the other deposition rates surface roughness is not affected by annealing (the RMS value is maintained at $\sim 2.5\text{nm}$ and the maximum value at $\sim 12\text{-}14\text{nm}$).

As should occur, the thermally treated samples present a larger grain size. However, the increase of grain size with respect to the unannealed samples is not uniform. Concretely after 18h of annealing, the grain size near the SiO₂ can reach values near 40nm , while it is below 15nm on the SnO₂ layer surface. This behaviour has been previously reported in other SnO₂ thin films and ascribed to limited diffusion of the interface [176]. Thus, according to that work, a good behaviour of the SiO₂ as stopping layer is inferred. As a consequence, the annealed films result inhomogeneous in depth.

In any case the high compactness of films after annealing make these sensors to present lower sensitivities than the obtained by other techniques.

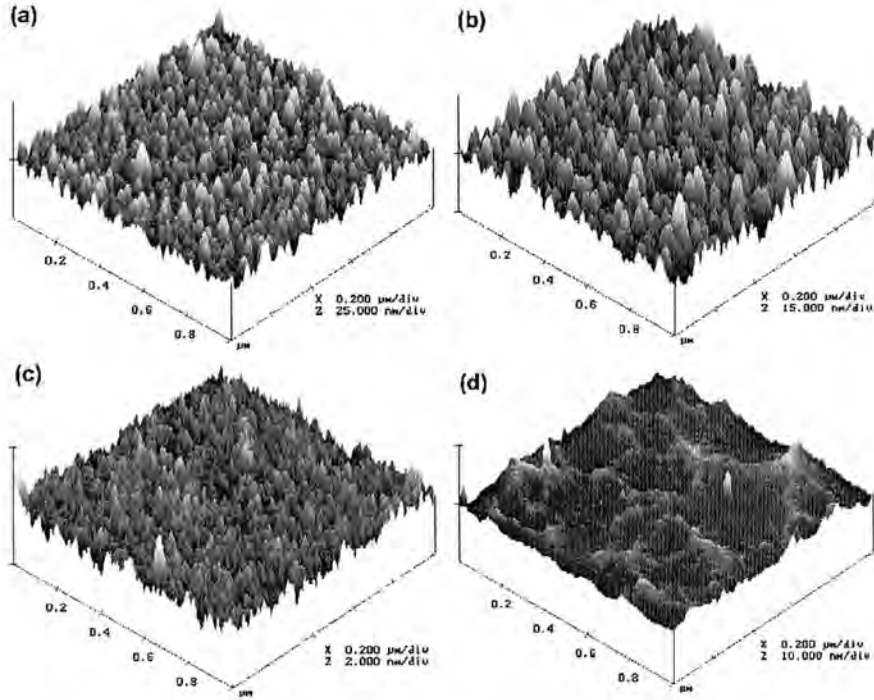


Figure 10: AFM images of samples F50 in (a), F52 in (b), F70 in (c), and F72 in (d).

4.2.3 Optimisation by substrate heating during deposition

In order to improve the quality of the SnO_2 thin films the heating of the substrate during deposition has been included as a process parameter. The group of samples analysed is presented in table VI. Because deposition rates higher than 1.3 \AA/s resulted in too much amorphous material, for this analysis only the samples corresponding to deposition rates of 0.8 and 1.0 \AA/s were investigated.

IBAD		
Kind of chip	Deposition n°	Annealing (synthetic air)
F_H	4	0
	5	1 (500°C-18h) 2 (500°C-30h)

Table VI: Characteristics of the IBAD samples.

The comparison of the cross-section images of samples F50 and F_H50 presented in figure 11 shows how the heating of the substrate benefits the quality of the SnO₂ film. On one hand, temperature increases material diffusion (oxygen), thus avoiding the formation of the amorphous layer at the SiO₂-SnO₂ interface. At the same time it hinders the appearance of a stratified growth. On the other hand, the absence of the amorphous region implies that this region not has to crystallise after further annealing, thus preventing the formation of planar defects, which surely would affect the sensing properties of the sensor.

In any case, after thermal annealing for 18h at 500°C grain size results increased but lower than 25nm and the stabilisation of the film is evident.

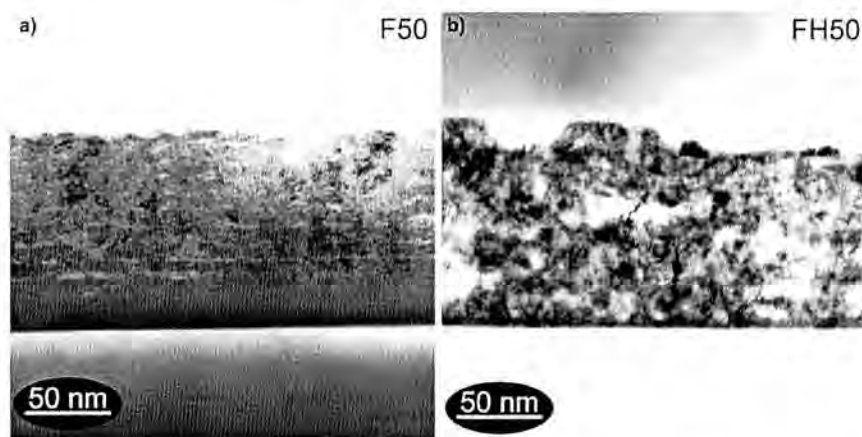


Figure 11: Comparison of a SnO₂ film deposited without heating of the substrate (a) and with simultaneous heating of the substrate (b).

4.2.4 Introduction of noble metals as catalysts

In order to analyse how catalysts are distributed on the SnO₂ surface Pt and Pd were deposited by sputtering on sensors of type *A*, *B*, *C* and *D* (see table VII).

IBAD			
Kind of chip	Deposition n°	Doping	Annealing (synthetic air)
A	5	0 (undoped)	u (no anneal.)
B		x (Platinum)	l (500°C-18h)
C		y (Palladium)	
D			

Table VII: Characteristics of the deposited samples.

From figures 12 and 13, it can be observed that Pt and Pd are deposited on the top of the SnO₂ film in a different manner. While Pt forms connected clusters

(thin polycrystalline layer), Pd forms disconnected clusters of approximately 14nm x 10nm (see detail in figure 13), probably due to the different mobility of Pt and Pd atoms at the SnO₂ surface.

After a thermal treatment for 18h at 500°C, a stabilisation of the SnO₂ film occurs, together with the increase of grain size (from c.a. 7-8nm to 10-11nm). However, HREM images of the layer are not capable of showing any evidence of noble metal diffusion. This result is confirmed by XPS profiles [183] which show that noble metal diffusion inside the film occurred only marginally, independently of if the film was annealed or not.

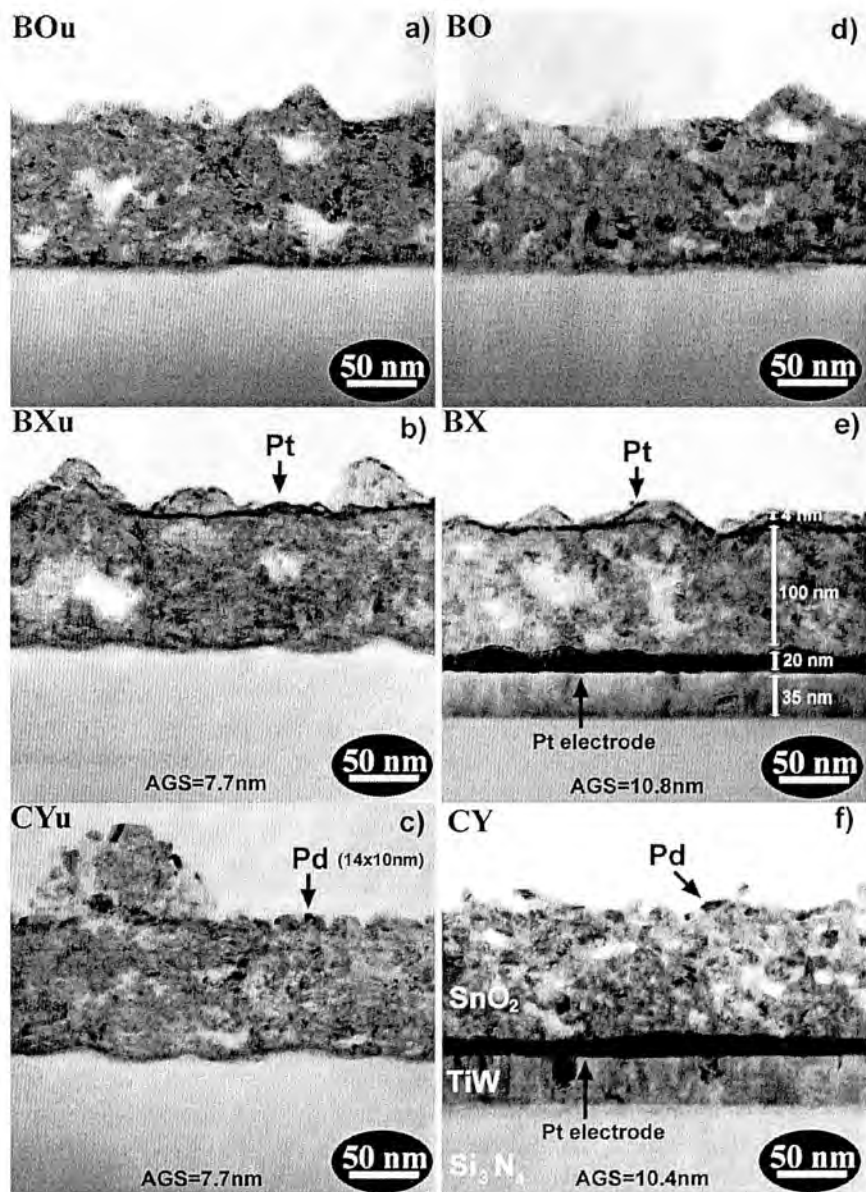


Figure 12: Cross-section TEM images of pure and 'doped' samples. Average grain size of the SnO₂ nanoparticles, is indicated in the bottom of each figure. In figures e) and f) they are also marked the different parts forming the sensor and their thickness.

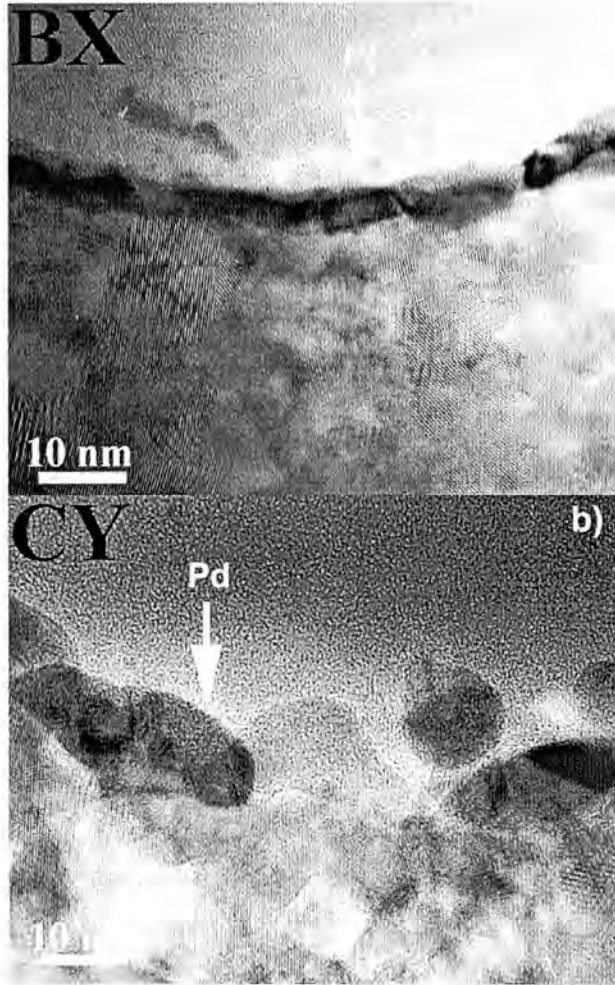


Figure 13: HREM images of sensors BX and CY. Pt distributes on the surface of SnO₂ forming a quasi-continuous film. Pd forms disconnected grains of average size approximately 14nm x 10nm.

4.3 The improvement of the sputtering technique: The RGTO technique

It has been previously commented that although the sputtering technique seems to generate the most interesting perspectives for massive industrial production using thin film procedures, the sputtering from a target of SnO₂ produces generally a non-stoichiometric SnO_x oxide, being needed an additional step to reach the correct stoichiometry. The idea of the Reothaxial Growth and Thermal Oxidation (RGTO) technique is to include this unavoidable oxidation step into the process. Thus, RGTO is a more simple procedure based on the deposition of the metal directly from its metallic target and subsequently thermally oxidize it. In this way, apart of the growing of SnO₂ thin films, the RGTO method has been successfully applied for example to grow Bi₂O₃ [153], Sn_xFe_{1-x}O_y [159], Ga₂O₃, In₂O₃, and Al₂O₃ [164], and in principle the RGTO technique can be applied to the growth of oxides of all metals that do not evaporate above the melting point and that tend to form stable oxides by means of a thermal oxidation cycle.

The original method, developed at the Brescia University consists in:

- 1) The reothaxial growth: The sputter-deposition of a metal that does not sublimate, on top of an insulating substrate, maintained at a temperature above the melting point of the metal (232°C for tin).
- 2) The thermal oxidation: The annealing of the sample under an oxygen atmosphere, synthetic air, or in normal air, at temperatures high enough to form the metal oxide. For the oxidation of tin, temperatures above 500°C are the most suitable in order to allow the oxygen diffusion into the metallic tin layer in an acceptable range of time [167]. However the technology for sensor fabrication hinders the use of temperatures higher than 650-700°C, which cause mainly problems of material diffusion inside the sensor structure.

Variants of the method consist in depositing the Sn in an oxidant atmosphere, maintaining the substrate at low temperature [179, 180] or performing a heating of the substrate during deposition [157, 181]. The original RGTO method, as well as the two modifications give rise to a very similar highly porous structure.

Catalytic metals can be introduced to enhance sensitivity and selectivity [182] after the metal oxidation through the thermal evaporation or sputter evaporation of small amounts of noble metal onto the RGTO metal-oxide film.

In the following a detailed description of the formation of SnO₂ RGTO films is given. Special emphasis will be done to the oxidation step and the influence

of an incomplete oxidation on the stability of the sensor and its evolution as source of drift of the sensor response.

4.3.1 General characteristics of the growth of SnO_2 RGTO films

4.3.1.1 Substrates used for RGTO growth

For the fundamental investigation of the RGTO method most of the films were prepared onto Si/SiO_2 and Al_2O_3 substrates neither with heater nor contact electrodes. So, some of the tin layers were deposited onto $5 \times 5 \text{mm}^2$ or $10 \times 10 \text{mm}^2$ Si substrates, which were previously thermally oxidised in order to form a thin isolating SiO_2 layer. The rest were deposited onto $3 \times 3 \text{mm}^2$ or $10 \times 10 \text{mm}^2$ Al_2O_3 substrates.

Whenever explicitly be not said, when electrical tests were planned on real sensors, the deposition was performed onto $3 \times 3 \text{mm}^2$ Al_2O_3 substrates developed at the Brescia University. In these substrates, the heating element was deposited on the backside of the substrate. It consisted in a Pt layer with meander shape and a thickness of $1 \mu\text{m}$, deposited by sputtering onto an area of $2.1 \times 2.4 \text{mm}^2$ with the substrate held at 300°C . On the substrate front side a gold layer with a thickness of $2.8 \mu\text{m}$ was deposited onto a $\text{Ti}_{0.1}\text{W}_{0.9}$ layer used as bonding pad. Finally, Pt comb-like (interdigitated) electrodes were deposited by sputtering. The electrical contacts were realized by bonding gold ribbons onto the bonding pads by a parallel gap welder. The resulting sensor was finally mounted on a TO8 socket with dimensions $12.75 \times 12.75 \times 16 \text{mm}^3$. Figure 14 shows the front and back sides of the sensor structure. In table VIII the power consumption of this substrate to reach the sensor operating temperature is presented [183].

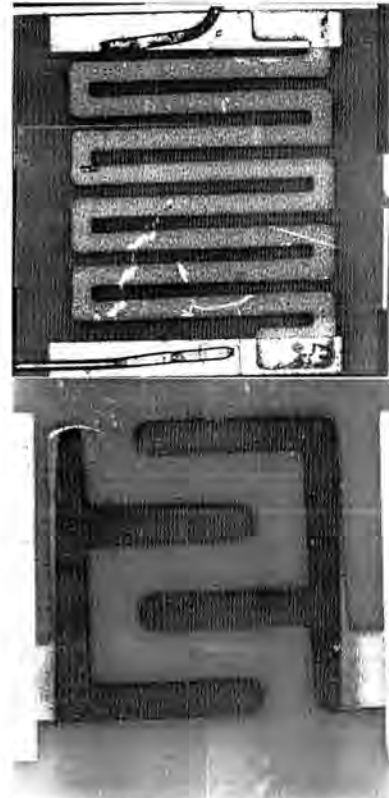


Figure 14: Heater (top) and interdigitated electrodes (bottom) in RGTO sensors.

Power (mW)	Temperature (°C)
400	200
520	250
650	300
790	350
930	400
1090	450
1250	500

Table VIII: Power consumption and temperature obtained for RGTO sensors.

4.3.1.2 Parameters for Sn deposition

The Sn deposition was performed in a r.f. sputtering system (Alcatel 450 SCM) from a pure tin target (Sn 99.9999% purity supplied by CERAC). A scheme of the deposition chamber of such sputtering plant is presented in figure 15. It can be seen that the substrates are maintained face down during the deposition step, 7-10cm away from the target. During deposition the substrate was maintained at room temperature or at a temperature of ~400°C. The parameters of the deposition were an incident r.f. power of 50 W, a deposition rate between 2.1 nm/s and 2.5 nm/s and an Ar pressure of 2×10^{-3} mbar.

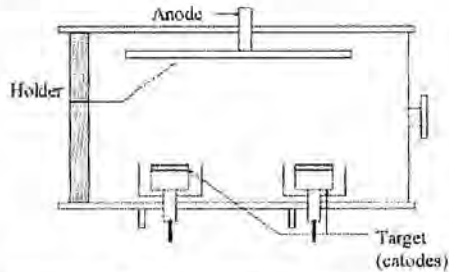


Figure 15: Scheme of the sputtering chamber.

The concrete type of substrate used during the deposition process, as well as the temperature of the substrate and the deposition rate for each sample will be given in the text in table form during the discussion.

4.3.1.3 The thermal oxidation cycle in RGTO

The oxidation was performed inside an oven (Heraeus furnace equipped with a Thermicon P temperature controller), being the oxidation ambient atmospheric air (no particular carrier gas was used). The temperature during the process was controlled by a thermocouple placed on the internal wall of the furnace, and the samples were placed 10cm apart from this wall, assuring a precision of about 10°C.

As is presented in figure 16, the complete oxidation cycle in RGTO consists of two steps, the samples being maintained in the furnace during the complete process. The first step is carried out at 250°C for 4h. The second step is done usually at 600°C for times up to 30h. The time to reach each stable temperature is usually 4 hours in order to avoid a fast evaporation of the metallic tin, especially in the first ramp. As will be discussed in the text, the first stabilisation at 250°C allows to obtain a first oxidation of the film.

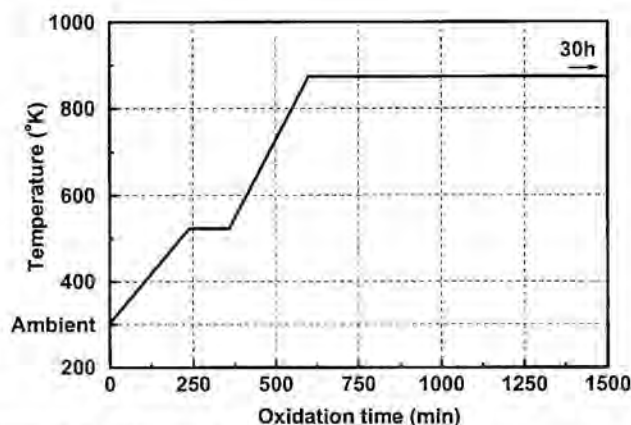


Figure 16: RGTO oxidation cycle.

4.3.2 Initial investigation of SnO_2 thin films grown by the RGTO technique

Once the RGTO method and the parameters of fabrication have been presented, a detailed overview of the characteristics of the films grown by this method will be given in the following. The analysis begins with the investigation of the deposition of tin, as this will be a fundamental parameter, because the rest of the process depends in principle to a large extent on the morphology of the Sn film obtained during the reothaxial growth. Afterwards, details such as the morphology of the film after the oxidation will be given, and the problem of the incomplete oxidation of tin will be outlined. The mechanisms occurring during the oxidation of tin will be given in the following sections.

4.3.2.1 Experimental results about the deposition of Sn

Table IX shows the set of samples fabricated in order to analyse the deposition of tin. None of the samples was deposited to be measured as sensor and, hence, without neither heater nor interdigitated electrodes. All of them correspond to

different thicknesses. Samples A, B, C, and D were deposited to analyse directly the influence of thickness, with the rest of parameters constant. So, these samples were deposited at 2.5nm/s and the substrate temperature during deposition was maintained at 400°C. The nominal thickness (corresponding to the sputtering time multiplied by the deposition rate) of sample E is 300nm, but the deposition rate was reduced to 2.1nm/s. The temperature of the substrate was also held at 400°C during deposition. Finally, in sample F the nominal thickness is 1000nm, and the deposition rate is the same as for sample E. However, the substrate was not heated during deposition.

RGTO						
Code	Material type	Size	Film type	Heater /IDC	Deposition	Oxidation
A	Sn/SiO ₂ /Si	10 x 10mm ²	1-Sn 50nm	No/No	T=400°C R=2.5nm/s; t=20s	—
B	Sn/SiO ₂ /Si	10 x 10mm ²	1-Sn 100nm	No/No	T=400°C R=2.5nm/s; t=40s	—
C	Sn/SiO ₂ /Si	10 x 10mm ²	1-Sn 200nm	No/No	T=400°C R=2.5nm/s; t=80s	—
D	Sn/SiO ₂ /Si	10 x 10mm ²	1-Sn 400nm	No/No	T=400°C R=2.5nm/s; t=160s	—
E	Sn/SiO ₂ /Si	10 x 10mm ²	1-Sn 300nm	No/No	T=400°C R=2.1nm/s; t=2min 23s	—
F	Sn/SiO ₂ /Si	10 x 10mm ²	1-Sn 1000nm	No	T=RT R=2.1nm/s; t=8min	—

Table IX: Set of samples fabricated to investigate the deposition of tin.

The plan-view SEM micrographs of samples A, B, C, D, E, and F, presented in figure 17, show that after the reothaxial growth the film never has a planar surface morphology. In the case of sample F, which was deposited with the substrate held at room temperature, irregular forms are developed due to the non-liquid character of the clusters (understood here as a group of atoms/molecules) and the low diffusion coefficient of the atoms on the substrate surface due to its low temperature. However, in samples A, B, C, D, and E, clusters with semi-spherical shape are formed because the binding energy of the 'condensate' atoms to each other is greater than their binding energy to the substrate. As the growth has occurred in the liquid state, surface tension determines the shape of the clusters (hereinafter called droplets) to take the form of truncated spheres. This is not the case if the film is grown in the solid state, as for sample F. The amorphous substrate makes the distribution spatially isotropic and avoids preferential orientation of the droplets.

The general characteristics of the liquid deposited samples are that after long deposition times, when a large quantity of Sn has been deposited, very large droplets of similar size exist, which are surrounded by smaller ones with higher size polydispersity forming a background. Moreover, denudes zones appear around large clusters (it is very well observed in sample E).

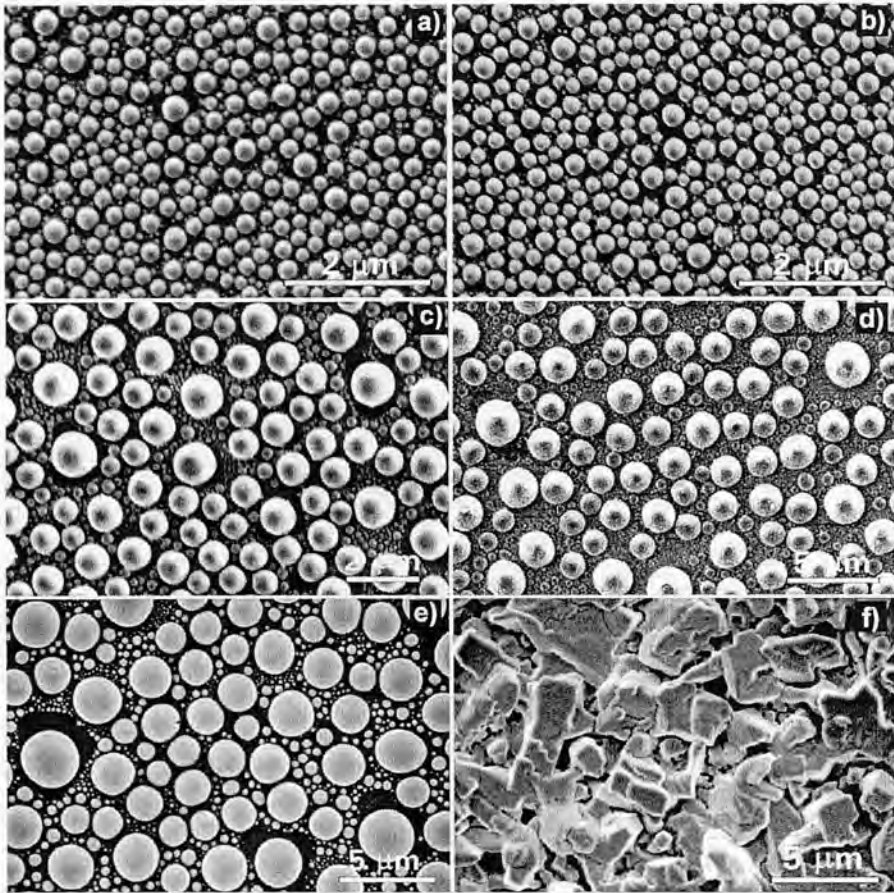


Figure 17: SEM images of the as deposited films. Images from (a) to (f) correspond to layers A to F.

The size distribution of the hemispheres of samples A through E is presented in figure 18. It can be observed that, as could intuitively be expected, the size distribution changes for every deposition time, the deposition rate being constant. In this case, the longer the deposition time is, the larger the hemisphere radius becomes and the spreader results the sphere size distribution. However, there is also a dependence on the deposition rate, because sample E corresponds to a lower nominal thickness than sample D and its size distribution is even more spreaded and shifted to higher sizes than that of sample D. In all cases where droplets are formed, it is observed that the size distribution is bimodal. It is formed by a power-law decay for

small sizes[†] (a tail) superimposed on a quasi-monodispersed, bell-shaped distribution peaked at the mean droplet size. The existence of these two parts in the droplet size distribution implies that there are two distinct mechanisms controlling the formation of small and large droplets.

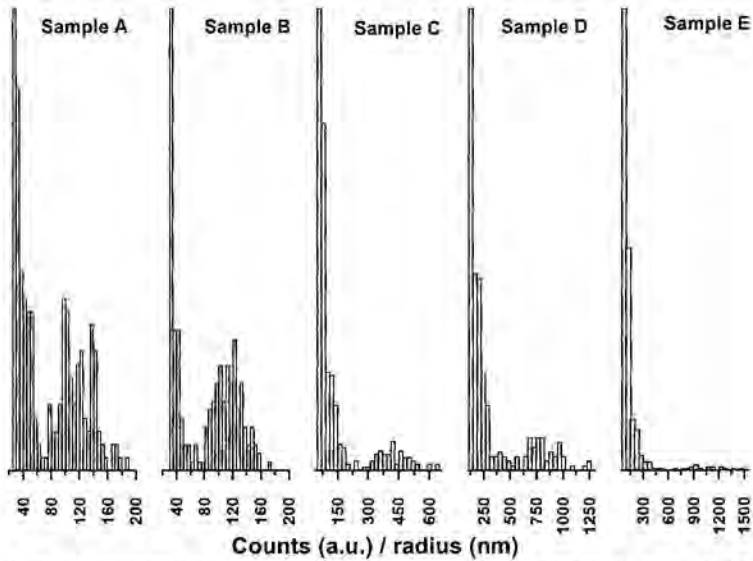


Figure 18: Histograms extracted from the SEM images of the samples A, B, C, D, and E. Note the similarity between the histograms of samples A and B, which is attributed to an error in the fabrication of the samples. In all cases it is observed a tail followed by a bell-shaped part in the distribution.

Because we will be interested mainly in the bell-shaped part of the histogram, better statistics for the large droplets have been obtained using public domain image processing software [184]. The obtained histograms, which were normalised to an area of 25x25µm², were fitted with a gaussian curve. The results of the fitting and the corresponding values for the centre (average radius $\langle R \rangle$) and height (number of particles corresponding to the droplets with radius $\langle R \rangle$) are presented in figure 19 and table X.

[†] Note that the sample statistics is a major problem, especially when dealing with measurements on small particles corresponding to the tail of the distribution. These arise mainly from SEM resolution and cut-off induced magnification problems. Therefore, the contribution of the smallest particles has been taken out from the histograms.

Sample	Deposition time (s)	$\langle R \rangle$ (nm)	$N_{\langle R \rangle}$	Dep. Time (s) *	$\langle R \rangle$ *
A	20 ($r=2.5\text{nm/s}$)	99.25	611.07		
B	40 ($r=2.5\text{nm/s}$)	105.71	1154.8		212.76
C	80 ($r=2.5\text{nm/s}$)	407.52	41.37		
D	160 ($r=2.5\text{nm/s}$)	719.50	13.32		

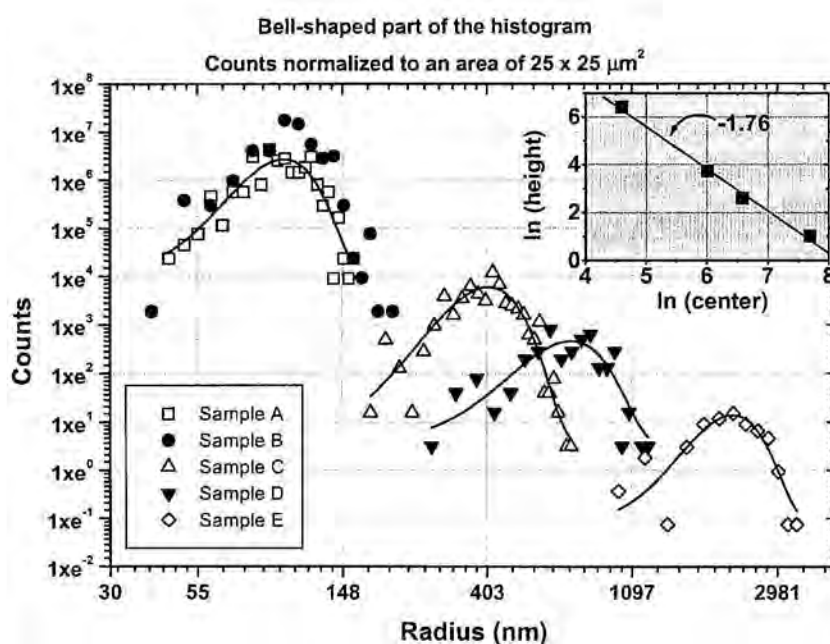
Table X: Results of the gaussian fit. * Calculated values of $\langle R \rangle$ in the case of sample B.

Figure 19: Size distribution in the bell-shaped part of the histogram after improved measurement. It is shown in the inset the linear fitting of the maximum of the size distribution (number of particles) as a function of the particle size corresponding to the maximum, i.e., the coordinates of the peaks of the histograms.

As can be observed in figure 19 and table X, the results obtained for sample B require special comments. Particularly it is important to note the similarity between the size distribution of samples A and B. According to the obtained average radius (99 and 105 nm for samples A and B, respectively) it seems that after doubling the deposition time maintaining constant the deposition rate, a significant change in the size of the particles does not occur. In principle we do not think that this is a consequence neither of the growth process itself nor of a statistics problem. The most plausible explanation for the observed distribution seems to be the location of the sample in the sputtering

chamber. Thus, the value obtained here for sample B will be not be considered in the following discussions of the *Chapter*.

From figure 19 (inset) it can be also observed (neglecting sample B) that some type of size ordering takes place, as in a doubly logarithmic plot of the histograms the values $N_{<R>}$ and $\langle R \rangle$, i.e., the peak of the histograms, are scaled according to a coefficient $\phi=1.76$. This suggest that the evolution of the system occurs in a similar fashion as deposition proceeds, independently of the deposition rate, i.e., the droplet size distribution can be scaled according to a mean size value and a power law. Further demonstrations of size ordering are obtained by the fact that the value $\sigma/\langle R \rangle$ for the bell-shaped part of the distribution, where σ is the standard deviation, saturates around 0.25.

Figure 20 presents an estimation of the percentage of the substrate covered by the Sn droplets taking into account droplets both in the tail and in the bell-shaped part of the size distribution. Sample B has not been taken into account because of the factors commented above. It can be observed that the coverage saturates asymptotically at a value around ~70%. The coverage of the substrate is always in the range 55-70% and is caused mainly by the particles forming the tail, especially for high deposition times. This substrate coverage is in agreement with that found by Hellmich et al. [167], around 80%.

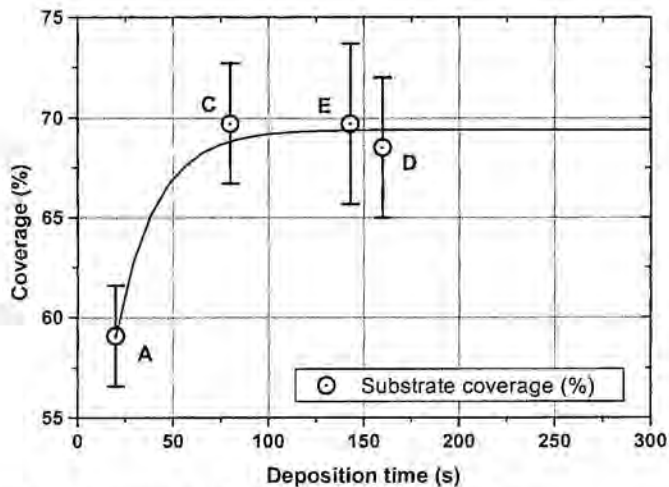


Figure 20: Percentage of the substrate covered by Sn droplets.

4.3.2.2 Kinetics of droplet nucleation

The problem of droplet nucleation on a substrate has been extensively reported in the literature, both experimental and theoretically, mainly through Monte-

Carlo computer simulations [185-188]. The most investigated phenomena related to coalescence of droplets is the analysis of breath figures obtained through the condensation of water on cold surfaces (see for example [189]). However, the analysis of other cases such as, for example, the deposition of liquid Sn on SiO_x [190, 191], Ga on GaAs [192], or In on InP [193] yield to a very similar morphology resulting from similar growth processes.

It has been claimed that the evolution of the system passes through three stages:

- 1) *Nucleation and growth of immobile individual droplets.* Nucleation can be heterogeneous or homogenous. In the former, the condensation of droplets occurs on impurities or imperfections. In the last, the droplets form by molecules combining together to form a small droplet which can grow spontaneously. As we are dealing with amorphous substrates it is expected that homogeneous nucleation takes place. The mean radius $\langle R_v \rangle$ corresponding to the mean volume follows during this stage a power law [190]:

$$\langle R_v \rangle \sim t^{1/3} \quad (1)$$

- 2) *Static coalescence of droplets,* in which $\langle R_v \rangle$ follows a different power law [190]:

$$\langle R_v \rangle \sim t^1 \quad (2)$$

As deposition and growth continues, the separation between droplets decreases and, upon contact, they coalesce to form larger droplets. In the liquid state the coalescence of two spherical droplets give rise to a new spherical droplet with no loss in volume (with mass conservation) [187]. The coalescence is driven by the surface tension, which tends to minimise the surface area of the liquid droplets. As proposed by Lewis et al. [194], the coalescence proceeds initially by the deformation of the two clusters in such a way to optimise the contact surface, i.e., without interdiffusion of one cluster into the other. At this stage of the coalescence, surface tension forces drive the hydrodynamic flow and, in a larger time scale, diffusion takes over and the mixing of the two initial clusters occurs. The new formed droplet will be located on a position which depends of the position and mass of the contributing ones, but its mobility results decreased as their size increases [195]. In general, during the deposition of droplets (of dimensionality $D=3$) on a substrate (with dimensionality $d=2$), when a droplet of radius r_i touches

or overlaps a droplet of radius r_2 , the new droplet formed is centered in the center of mass of the two original droplets[†], and has a radius r given by

$$r = (r_1^D + r_2^D)^{1/D} \quad (3)$$

During the coalescence of two large droplets, depleted regions are left behind. In this way, the possibility of two droplets of being in close proximity is reduced, which is in agreement with the SEM observations presented in figure 17 (note the lack of small droplets around a larger one after long deposition times, where new particles have not yet accumulated there as a consequence of the continuation of deposition). This process hinders the total coverage of the substrate, in agreement also with our observations. Moreover, as the resulting droplet after coalescence gains more material and grows larger than if it would only grow because of the arrival of atoms at the surface, the distribution of sizes results substantially broadened.

3) *Renucleation of small particles* in the areas cleaned by previous coalescence events (second generation of droplets). If the growth continues it passes thorough stages 1 and 2 and a new generation of droplets starts to appear.

In the deposition of tin maintaining the substrate at 400°C the process is identical to that outlined in stages 1, 2, and 3. However the values found for the coverage of the substrate and of the power of the power law corresponding to stage 2 differ from those presented in the literature. As commented above the power of the deposition time for a growing droplet resulting from coalescence should be 1. However, from figure 21, we obtain a value of 0.88 if the mean droplet radius is considered or 0.84 if the radius corresponding to the mean volume is considered instead. On the other hand, the substrate coverage reported in the literature after long deposition times is ~55%, while we found a tendency to reach the limit ~70%. However, it is reasonable to think that if our particles grow slowly, as corresponds to the power 0.88, the coverage of the substrate surface be higher, because fewer droplets have coalesced. Thus, our results up to this point are coherent. Nevertheless, the temperature of the substrate during deposition used in this work (400°C), which is four times higher than the used by Sondergard et al. [190], who reported a power of 0.92 and a coverage of 55% as due to static coalescence, should increase the diffusion of the particles belonging to the tail, thus promoting a higher coalescence rate and a lower substrate coverage. Therefore, other parameters have to influence the deposition and actuate reducing coalescence rate and lowering the mobility of the smaller droplets and atoms arriving to the substrate.

[†] In some models the new droplet is considered to be centered in the position of the larger droplet. In a realistic case where the new droplet is located should depend on the substrate temperature and substrate type.

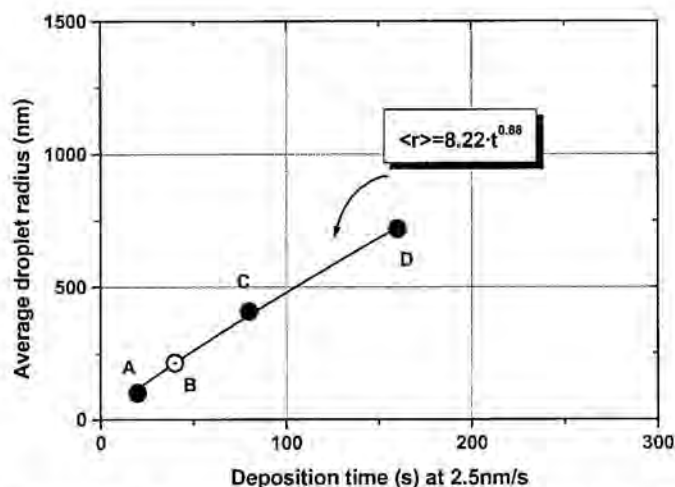


Figure 21: Average droplet radius as a function of the deposition time. The fitting indicates a dependency on the power of time of 0.88. Sample B has been located in this figure after the fitting. The obtained value of average droplet size is the written in table X.

The two most probable are:

■ *The annihilation of droplets due to evaporation.*

In the case that evaporation would take place, it seems evident and has been experimentally reported [190] that the smaller droplets should evaporate first. The evaporated material could:

- 1) Be lost
- 2) Be re-deposited on the larger droplets
- 3) Be re-deposited on the substrate again as small droplets

Options 1 and 2 would give rise to a lowering of the substrate coverage, which is opposite to the observed behaviour. The most probable is that a combination of 2 and 3 takes place, i.e., the material is re-deposited all over the substrate surface, being part of the material deposited on the larger droplets. Note that if only 3 would occur, the system would arrive to a stationary regime equivalent to the case in which evaporation does not occur. Anyway, the combination of 2 and 3 would give rise to a decrease of the coalescence rate and to an increase of the substrate coverage due to the large quantity of small droplets on it.

■ *The effects of the experimental set-up.*

As tin was deposited in all cases maintaining the substrate face down in the sputtering chamber, the effects of this experimental set-up might influence in two forms, limiting droplet growth and increasing surface coverage:

- 1) Reducing diffusion on the substrate (due to the competition of surface tension and gravity)
- 2) Competing with surface tension changing the shape of the droplet in such a form that there is no wetting.

If the hypothesis of Sondergard et al. is correct, i.e., they are dealing with static coalescence, our experimental set-up hinders in addition the coalescence of droplets, as it is impossible to obtain lower diffusion than in static coalescence. This is completely reasonable if diffusion is lowered enough, as the coalescence process involves the diffusion of at least one of the two coalescing droplets. However, surface coalescence can also be retarded by elongating the radius of the droplet in the direction perpendicular to the substrate with respect to the radius that the droplet would have in this direction if the substrate was placed face up.

Therefore, the final situation would be something like

- 1) Droplets of small size are nucleated homogeneously on the substrate.
- 2) Some of these droplets coalesce, giving rise to larger droplets. The rest remain on the substrate or evaporate. Deposition continues and 1 and 2 are repeated.
- 3) As a consequence of the experimental set-up the droplets acquire a shape different from that if the substrate was placed face up, i.e., the droplets are more elongated in the direction perpendicular to the substrate than if the sputtering was done with the substrate face up. This will retard the coalescence of droplets.
- 4) The competition of gravity and surface tension do not reduce surface diffusion and we have higher diffusion than in the case of Sondergard et al. due to the higher substrate temperature.

Comparing sample E with samples A through D, it can be deduced that the mechanism of growth is the same, being possible to obtain an equivalent deposition time to re-scale the size distribution. This implies that lowering of the deposition rate has exactly the same effect as increasing the deposition time. At this point, the difference between samples D and E can be attributed only to the different time that the particles arriving to the substrate and the smallest particles existing already on the substrate have to move before coalescing. If evaporation occurs in the smaller particles a lower deposition rate should promote more evaporation. This would produce a higher growth rate of the larger droplets, but never faster than due to the coalescence process itself. However, if the diffusion of the droplets is high due to the temperature of the substrate, more coalescence events can take place, with the consequent apparition of very large droplets after a sufficiently long deposition time. In addition, the coverage of the substrate should be by smaller droplets than if evaporation would not occur.

The scaling of the size distribution has been also previously reported [186, 187]. It has been claimed that the size distribution can be scaled according with:

$$N_s(t) \sim s^{-\theta} f\left(\frac{s}{S(t)}\right) \quad (4)$$

where $S(t)$ is the mean droplet volume defined as

$$S(t) = \frac{\sum s^2 N_s(t)}{\sum s N_s(t)} \quad (5)$$

s is the droplet volume and $N_s(t)$ the number of droplets of size s at time t . However, the theoretical value of $\theta=(D+d)/D$ is $5/3$ [186, 187], which differs substantially to the obtained value with our samples ($\theta \approx 0.58$). As commented above, the particular experimental set-up used in this work introduces an additional parameter, the gravitational force, which produces that the scaling law be also applicable but with a different coefficient θ . In our case, the scaling law is satisfied for the volume, as well as for the radius, as might be expected.

4.3.2.3 Morphology of the RGTO films after a complete oxidation cycle

For the initial investigation of the oxidation of Sn, samples A, B, C, and D have been oxidised for 30h, following the oxidation cycle described in section 5.3.1.3. The new samples obtained are presented in table XI.

RGTO						
Code	Material type	Size	Film type	Heater /IDC	Deposition	Oxidation
AT	SnO ₂ /SiO ₂ /Si	10 x 10mm ²	1-SnO ₂ 50nm	No/No	T=400°C R=2.5nm/s; t=20s	30h at 600°C
BT	SnO ₂ /SiO ₂ /Si	10 x 10mm ²	1-SnO ₂ 100nm	No/No	T=400°C R=2.5nm/s; t=40s	30h at 600°C
CT	SnO ₂ /SiO ₂ /Si	10 x 10mm ²	1-SnO ₂ 200nm	No/No	T=400°C R=2.5nm/s; t=80s	30h at 600°C
DT	SnO ₂ /SiO ₂ /Si	10 x 10mm ²	1-SnO ₂ 400nm	No/No	T=400°C R=2.5nm/s; t=160s	30h at 600°C

Table XI: Samples for the initial analysis of oxidation.

In figure 22 it is shown the aspect of the films after the thermal oxidation for 30h. It can be observed that the smooth morphology of the surface, consequence of the shape of the droplets, changes to spongy. Agglomerates of oxidised tin, distributed uniformly over the substrate, produce this spongy morphology. Such morphology is responsible for a large surface area, which is the preferred situation in a semiconductor gas sensor because the mechanism for gas sensing is related rather to surface reactions than to bulk changes. The spongy aspect of the agglomerates is strongly dependent on

the size of the starting Sn spheres in the sense that larger spheres give rise to more spongy agglomerates (compare the aspect of samples AT through DT). Therefore, a larger surface area is obtained for the nominally thicker samples, in which larger Sn spheres are present. In addition, it is clear that a spongier surface increases the connectivity between agglomerates, giving rise to a more continuous layer, which increases the conductivity of the film. The coverage of the substrate is now complete in the case of the thicker samples due to the growth induced under the oxidation process. The smaller droplets corresponding to the tail of the distribution are almost always hidden under the larger agglomerates.

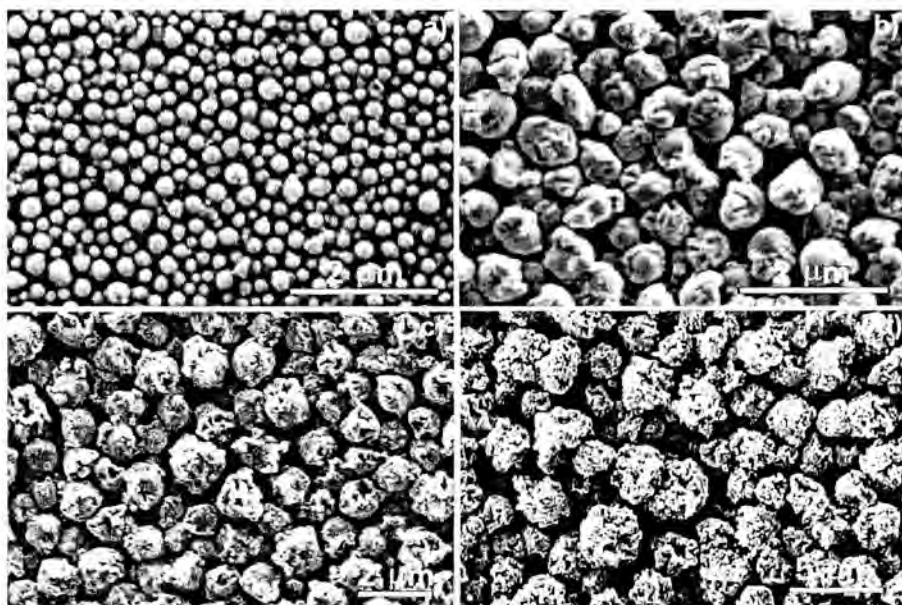


Figure 22: SEM images of the oxidised films. a) Sample AT, b) sample BT, c) sample CT, and d) sample DT.

The size distribution and size (radius) increase under oxidation are presented in figures 23 and 24. It is clearly observed that the larger the initial droplets are, the larger the size increment after oxidation is, ranging from ~15 to ~50%. Note that to elaborate figure 24, the value of the radius for sample B is the estimated one. As it is evident, the corresponding oxidised sample (BT) has an average radius that corresponds to this initial estimated value rather than to the radius extracted from the measurements. This demonstrates our initial assumption that sample B was not located in a proper place in the sputtering chamber.

Under cross section TEM observation the morphology of the spongy agglomerates is revealed (Figure 25). For the thinner starting layer (sample A), the oxidised film is formed by accumulations of small grains of size in the range

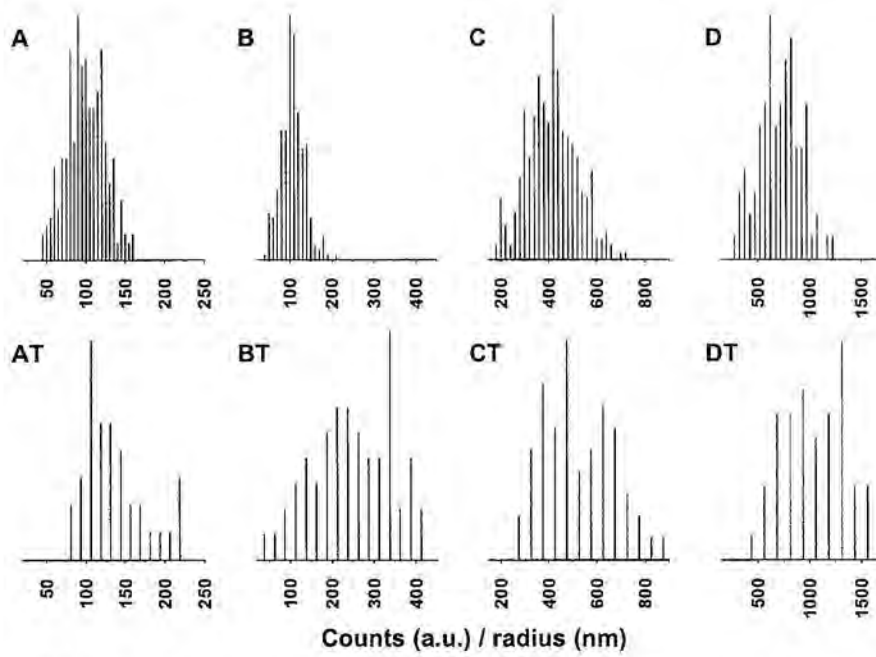


Figure 23: Size distribution of the oxidised films compared with those of the as deposited films.

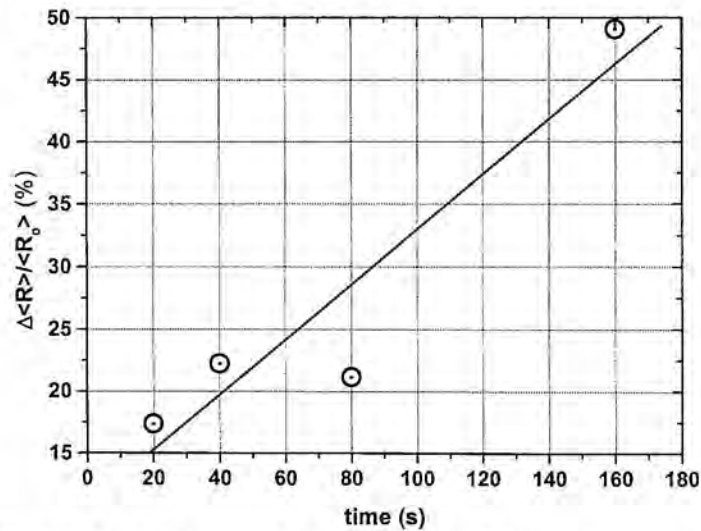


Figure 24: Relative increment of size after oxidation. The observed increment is extremely large compared with the expected.

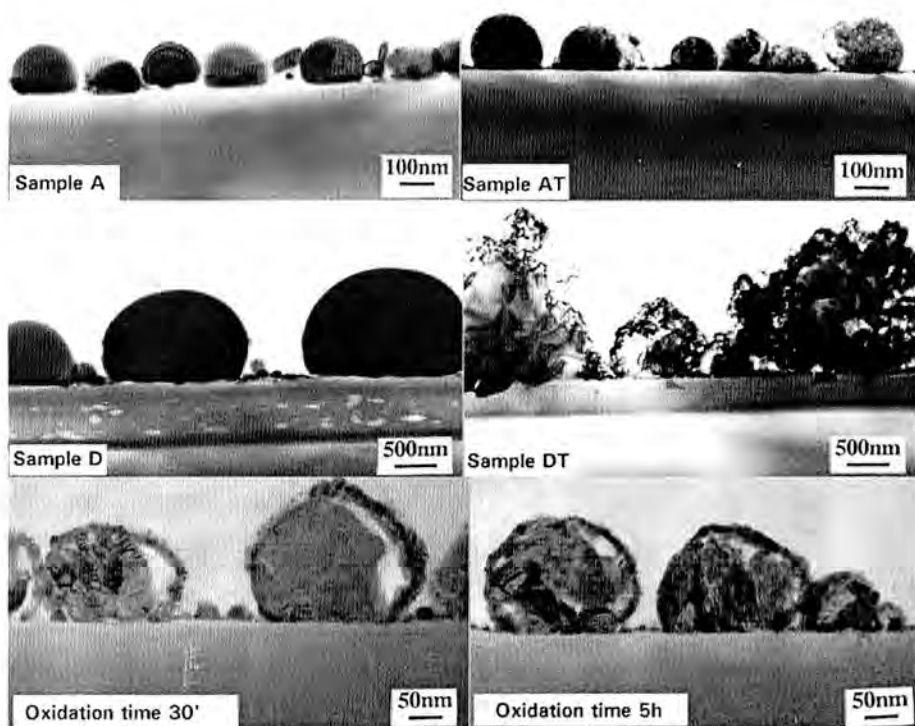


Figure 25: Cross-section TEM images of the as deposited tin samples A and D, and of the corresponding oxidised ones for 30h, AT and DT. They are shown also two intermediate states (30 min. And 5h) of the oxidation of sample A.

10-60nm. These accumulations present normally smooth surfaces and are not in contact. When the thickness increases the aspect of the accumulations are as shown in figure 25 for the sample DT. Large SnO_2 grains (as shown by electron diffraction) are covered by smaller grains of 10-20nm in size, which give rise to the spongy aspect observed by SEM. This result explains the unusual increase of size of the droplets in the transformation from Sn to SnO_2 observed in this work. In sample AT, the morphology is very little spongy and, as can be observed by TEM, the grains forming an agglomerate are touching one each other. So, a small increment of size occurs during the transformation (17%). For larger droplets, such as those appearing in sample D, the transformation gives rise to a very spongy morphology. In sample DT it is observed by TEM that the agglomerates are formed by small particles surrounding larger ones, but the smaller particles are not touching practically, giving rise to a higher size increase ~49%. These results are in agreement with other values reported in the literature (see for example 50% in [161]).

So, the size increase is due not only to the transformation under oxidation, which would suppose a theoretical increment of 10%, but also to the morphology of the surface after oxidation.

4.3.2.4 Level of oxidation after 30h in the oxidation cycle

In principle the phase transformation from Sn to SnO₂ can be extracted from the selected area electron diffraction patterns (SADP). The SADP of some of the droplets taken from samples A to D show that their crystalline structure

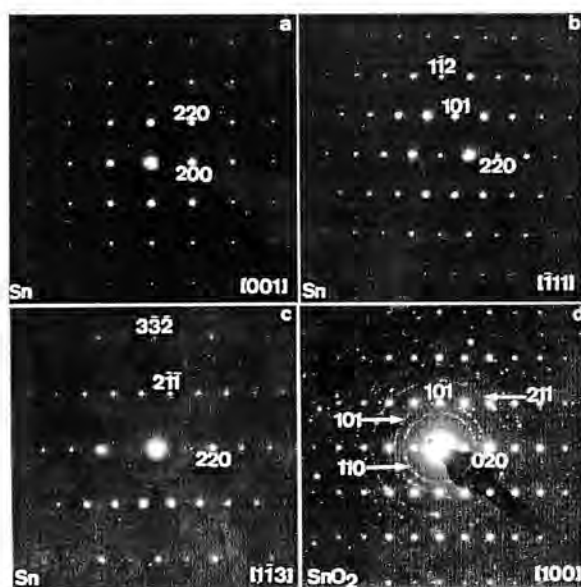


Figure 26: TED images of individual droplets in sample D ((a), (b), and (c)), and of a large agglomerate of sample DT (d). The zone axis is indicated in the bottom and right corner of each image. Image (d) shows spots corresponding to a large grains and rings corresponding to smaller ones.

one of SnO₂ (cassiterite). The SADP of one of the large agglomerates of sample D is presented in figure 26d. The polycrystalline character of the layer is visible through the appearance of diffraction rings, which are superimposed on the [100] zone axis of a large SnO₂ grain. Similarly that for the case of tin, the [100] reflection is attributed to double reflection.

Therefore it seems that the transformation from Sn to SnO₂ has been completed after the complete cycle of 30h even in the thicker film. However, in order to have better statistics and to assure the results obtained by TED, samples AT, BT, CT, and DT were examined by Raman spectroscopy. The spectra

corresponds to tetragonal tin with space group I41/amd (141) and lattice parameters $a=5.831\text{\AA}$ and $c=3.182\text{\AA}$. Some of these SADP corresponding to the sample D are presented on figure 26a-c, which are taken with the electron beam along different zone axes. It has to be mentioned that once the crystalline structure has been identified with confidence, the reflections [110] and $[\bar{1}\bar{1}0]$ have to be defined as due to double reflection effects, as they are forbidden in the tetragonal structure. After oxidation, the crystalline structure has been found to be the tetragonal rutile

corresponding to samples BT, CT and DT are presented in figure 27. It can be observed that in addition to the mode A_{1g} of the cassiterite appearing at ~636cm⁻¹, sample DT presents other anomalous and very intense bands in the lower wavenumbers region that do not correspond to SnO₂, but another intermediate oxidation phase. In fact the most intense of these bands starts to be visible already in sample CT.

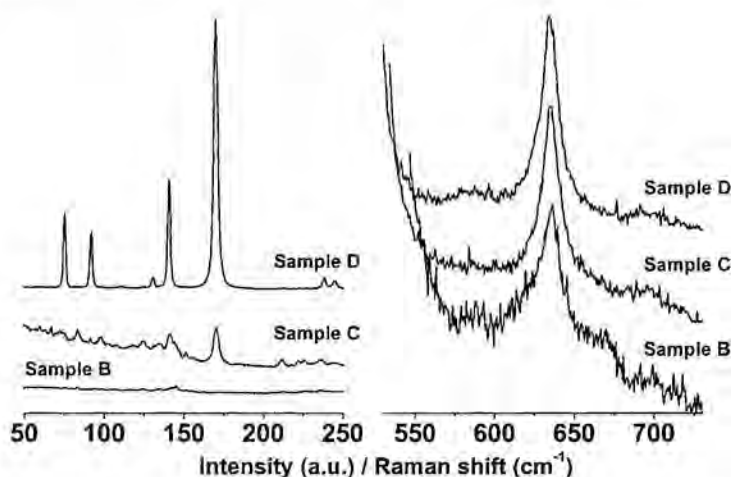


Figure 27: Raman spectra of the oxidised films BT, CT, and DT. The spectrum of sample AT is difficult to obtain because of the small thickness of the film. The spectra have been separated in two regions for better clarity.

Therefore, after oxidation for 30h films with nominal thickness larger than at least 200nm result incompletely oxidised. It seems clear that, as could intuitively be expected, larger droplets require longer times to reach a complete oxidation, i.e., to assure stoichiometric SnO₂. In the following parts of the *Chapter* we will investigate in detail the mechanism of oxidation of tin and the effects that an incomplete oxidation can produce in the response of the sensor.

4.3.3 Structural characterisation of the thermal oxidation of Sn

In order to investigate the oxidation of tin, new sets of samples were prepared. The objective is to analyse the complete oxidation cycle and, thus, the samples were located throughout it. The characterisation will include investigation up to very few nanometers of the structures, being required the use of HREM and thus samples of thickness ~50-100nm being optimal. In order to analyse the crystalline structure with higher statistics and to identify the possible phases appearing during the oxidation, Raman and XRD will be also used complementarily.

In this case thicker samples are optimal, namely ~300-500nm. The two sets of samples required for the investigations are presented in table XII and in figure 28.

RGTO						
Code	Material type	Size	Film type	Heater /IDC	Deposition	Oxidation
E	Sn/SiO ₂ /Si	10 x 10mm ²	1-SnO ₂ 92nm	No/No	T=400°C R=2.1nm/s; t=2min 23s	--
E240 E360 E420 E480 E540 E600 E720 E1200	SnO _x /SiO ₂ /Si					240 min 360 min 420 min 480 min 540 min 600 min 720 min 1200 min
G	Sn/SiO ₂ /Si	10 x 10mm ²	1-SnO ₂ 300nm	No/No	T=400°C R=2.3nm/s; t=40s	--
G360 G420 G440 G460 G500 G540 G600	SnO _x /SiO ₂ /Si					360 min 420 min 440 min 460 min 500 min 540 min 600 min

Table XII: Set of Sn and SnO₂ films grown by RGTO to investigate the oxidation process.

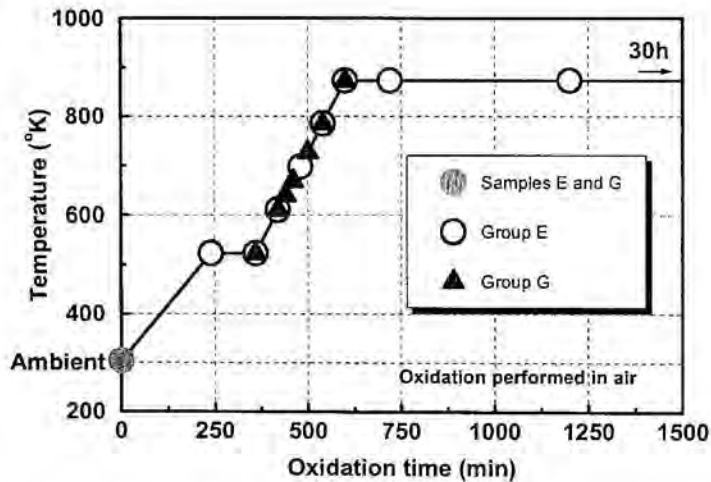


Figure 28: Distribution of the set of samples of table XII in the RGTO oxidation cycle.

4.3.3.1 Formation of the spongy agglomerates

In order to investigate the formation of the spongy agglomerates the group of samples G was used.

All that is needed to explain the way in which the spongy agglomerates are formed are the results presented in section 4.3.2.3 and the HREM images of figure 29. Figure 29a corresponds to a sample oxidised for 360min. After this time the droplet has been partially oxidised and some crystallites have been formed at the outer part. So, it is deduced from this image that oxidation begins at the surface of the droplets, as would be intuitively expected. At temperatures higher than 232°C the Sn droplets are liquid. So, when the temperature is high enough to allow oxygen to diffuse into the droplet, the surface begins to oxidise in random orientations (nuclei formation). These nuclei will grow further as oxidation continues, but not at the same rate, as oxygen diffusion depends of the crystallographic orientation of the formed solid crystallites.

As oxidation proceeds, several factors can cause the surface morphology to change from smooth to irregular. As can be observed in figure 29, when oxygen penetrates into the droplet, the growth of the nuclei is produced simultaneously to the centre of the droplet. So, two different casuistics can be found. In one, the crystallites are nucleated in different orientations and grow to the centre of the droplet, their simultaneous growth giving rise to the formation of planar defects when finally they get in contact. The second can take place when the crystallites grow in only one or few orientations, such as that observed in figure 29b. In this case, the spherical nature of the droplet will produce also the appearance of planar defects. As shown in figure 29b, the curvature of the Moiré's fringes on the surface of the grain, are indicative of a high deformation in the surface material. Thus, after further growth, it will be expected that planar defects appear as a consequence of strain.

On the other hand, additional sources of strain are also produced under the phase transformations occurring during the oxidation. Due to the liquid character of tin, no significant strain is expected between the oxidised and the non-oxidised regions. However, as will be discussed later, in general, the oxidation does not occur directly from Sn to cassiterite SnO₂, but passes mainly thorough another phase, namely SnO. Strain will arise mainly from the transformation of SnO into SnO₂ and by the presence of liquid Sn. So, the planar defects nucleated after the oxidation of the first external layers actuate as preferential locations for fracture when interior Sn of the droplet results oxidised because of oxygen diffusion, or when the transformation from SnO to SnO₂ occurs. Accordingly with this mechanism, it is worth to note that larger Sn spheres would produce more spongy agglomerates because this process of fracture could be repeated a higher number of times until the droplet becomes completely oxidised. Moreover, it is clear than both oxygen content in the oxidant atmosphere and

rate of temperature variation have to deeply influence the final structure of the agglomerates.

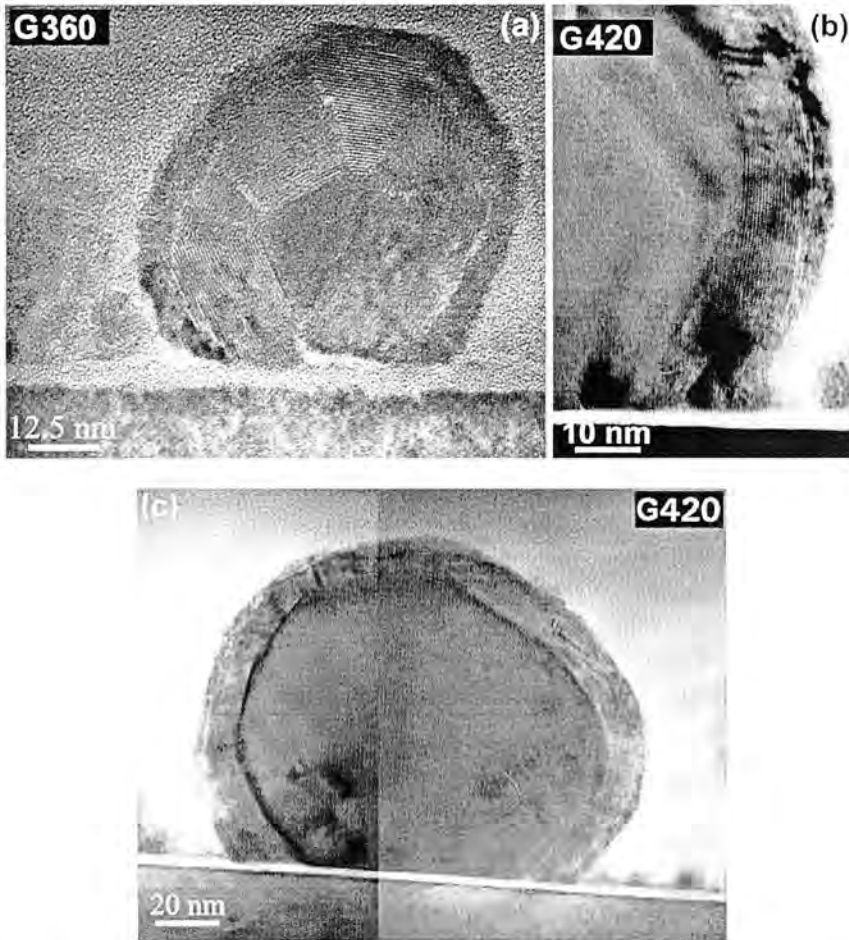


Figure 29: HREM images of samples G360 and G240. Image (c) is a composition of two images to show the complete exterior layer. Image (b) is a portion of image (c). In (b) a region of a partially oxidised Sn microsphere containing Moriree's fringes arising as a consequence of the curvature of the microsphere and the tensions produced between two coexisting phases is clearly observed.

Figure 30 shows the thickness of the oxidised layer after different periods in the oxidation ramp. The squares indicate an average value and the error bars the maximum and minimum thickness of the oxidised layer. In sample G600 almost all droplets are completely oxidised. For comparison it is presented also the theoretical

curve calculated according to values of the activation energy E_a and the diffusion coefficient D_o for $T=\infty$ in the diffusion of oxygen in tin calculated by Hellmich et al. [167]. To elaborate this curve the oxidation ramp used has to be taken into account. As it is clear there is no good fit between our experimental data and the theoretical ones. However it is the expected as Hellmich et al. did not take into account that:

- 1) Solid crystallites appear after some oxidation period, each one growing in random crystallographic orientations. If the diffusion coefficient has the expression:

$$D(T) = D_o e^{-E_a/kT}, \tag{5}$$

E_a does not depend of the orientation of the crystallites because the type of bonds that have to be broken is always the same for a given material. However, D_o depends of the crystallographic orientation because of the different density of bonds for each one of them.

- 2) Intermediate phases are formed, changing the activation energy during the oxidation process. It is clear that the energy needed to break Sn-Sn atoms will not be the same as the needed to break the same type of bonds in an intermediate oxidation phase nor Sn-O bonds. The D_o coefficient has to change also accordingly with the new phase formed.
- 3) Planar defects appear, where oxygen diffusion is presumably faster.
- 4) After some oxidation time and especially in large droplets (they used a nominal Sn thickness of 300nm) fracture of crystallites is produced. These crystallites are separated from the rest of the droplet, and hence, the thickness that oxygen has to diffuse to reach the interior material has changed spontaneously.

In order to fit our results we have started by considering the typical expression for the diffusion length and diffusion coefficient:

$$L(t) = \sqrt{D(T) \cdot t} \tag{6}$$

$$D(T) = D_o e^{-E_a/kT} \tag{7}$$

As the temperature during the process follows the RGTO oxidation cycle, the diffusion length for a complete cycle would be given by:

$$L^2 = \int D(t) dt = \int_0^{t_1} D(t) dt + \int_{t_1}^{t_2} D(t) dt + \int_{t_2}^{t_3} D(t) dt + \int_{t_3}^{t_4} D(t) dt \tag{8}$$

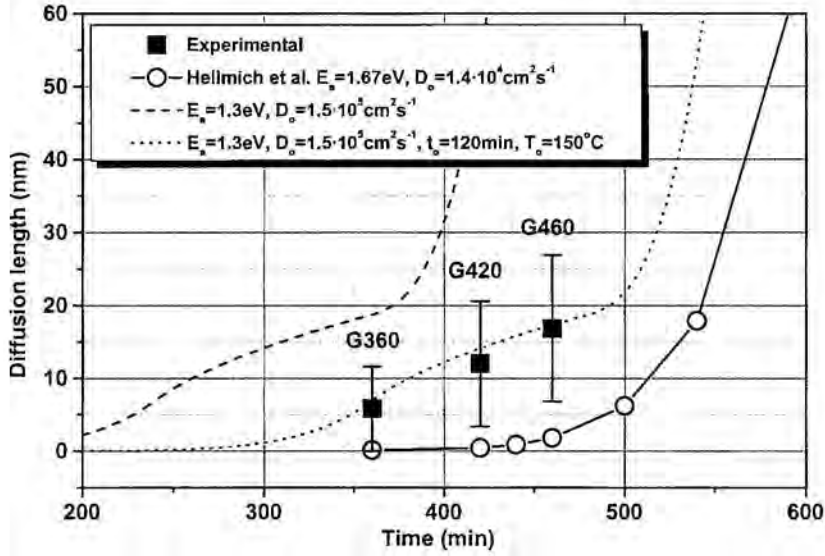


Figure 30: Thickness of the oxidised portion of the layer together with predicted values according to the literature. The fittings performed in this work are also presented.

where t_1 is the time to reach the first plateau, t_2-t_1 the duration of the first plateau, t_3-t_2 the duration of the second ramp, and t_4-t_3 the time that the sample is held at the temperature of the second plateau.

During the plateaus,

$$T = ct = T_a \tag{9}$$

and hence,

$$L^2_{a \rightarrow b} = \int_{t_a}^{t_b} D_o e^{-E_a/kT_a} dt = D_o e^{-E_a/kT_a} (t_b - t_a) \tag{10}$$

During the ramps,

$$T = T_a + ct \tag{11}$$

and hence,

$$L^2_{a \rightarrow b} = \int_{t_a}^{t_b} D_o e^{-E_a/k(T_a+ct)} dt \tag{12}$$

Making

$$p = \frac{E_a}{k(T_a + ct)} \tag{13}$$

$$dp = -\frac{E_a ck}{(kT_a + ckt)^2} dt = -\frac{ck}{E_a} p^2 dt \tag{14}$$

thus,

$$\begin{aligned} L^2_{a \rightarrow b} &= -\frac{D_o E_a}{ck} \int_{p_a}^{p_b} \frac{e^{-p}}{p^2} dp = \frac{D_o E_a}{ck} \left\{ \left. \frac{e^{-p}}{p} \right|_{p_a}^{p_b} - \int_{p_a}^{p_b} \frac{e^{-p}}{p} dp \right\} = \\ &= \frac{D_o E_a}{ck} \left\{ \left. \frac{e^{-p}}{p} \right|_{p_a}^{p_b} - \left[\ln p - \frac{p}{1!} + \frac{p^2}{2!} - \frac{p^3}{3!} + \dots \right] \right\}_{p_a}^{p_b} \end{aligned} \tag{15}$$

As this expression is very complicated to fit our results with only 3 points[†], we preferred to start with the values of D_o and E_a given by Hellmich et al. and fit by successive approximations our data. The results are also presented in figure 30. It can be seen that to fit our experimental data it is needed to add a third parameter. This parameter, t_o , is the time that the entire system needs to melt the tin, i.e., it has to be assumed that the entire system spends some energy to melt first the Sn droplets before the oxidation begins. The temperature associated to $t_o=120$ min. is $T_o=150^\circ\text{C}$, which agrees with the data reported by Sondergard et al. [190], for which tin droplets can be liquid. The values for D_o and E_a thus obtained are $1.5 \cdot 10^5 \text{cm}^2 \text{s}^{-1}$ and 1.3eV respectively.

Although these values differ substantially from those reported by Hellmich et al. we think that are a better approximation, because of the factors that, as commented above, they did not take into account. To these factors, the energy needed to melt the Sn droplets should be added. This last parameter might depend of the size of the initial droplets and, thus, change from sample to sample.

4.3.3.2 The thermal oxidation of Sn: XRD and Raman spectroscopy

The phase transformations occurring during the oxidation of Sn are illustrated in figures 31 and 32, which show respectively the X-ray diffraction and Raman spectra of the oxidised films belonging to the samples E group (the thicker films). The as-deposited layer consists of tetragonal tin (β -Sn) as is inferred from the X-ray

[†] A fourth point corresponding to sample G600 does not has to be considered because the sample is completely oxidised, and hence, other phenomena than the diffusion of oxygen in tin might be considered.

diffraction measurements. As shown in figure 31, the initial oxidation step corresponds to Sn transformed partially into romarchite SnO at 250°C. With increase of the oxidation time, the transformation continues further, as it is observed by the decrease in the intensity of the β -Sn reflections with respect to those of the SnO. After 540 minutes in the oxidation ramp (512°C) the maximum ratio of intensities between the romarchite and the Sn peaks, and so the maximum quantity of romarchite, is obtained. At the same time tetragonal SnO₂ with the cassiterite structure appears clearly. Further oxidation gives rise to a considerable increase of cassiterite, together with a reduction of both, Sn and SnO. Finally, after 2h at 600°C (sample E720), the SnO signal completely disappears, although some unoxidised metallic Sn remains. Further increase of the oxidation time at 600°C only produces an increase of the ratio SnO₂/Sn.

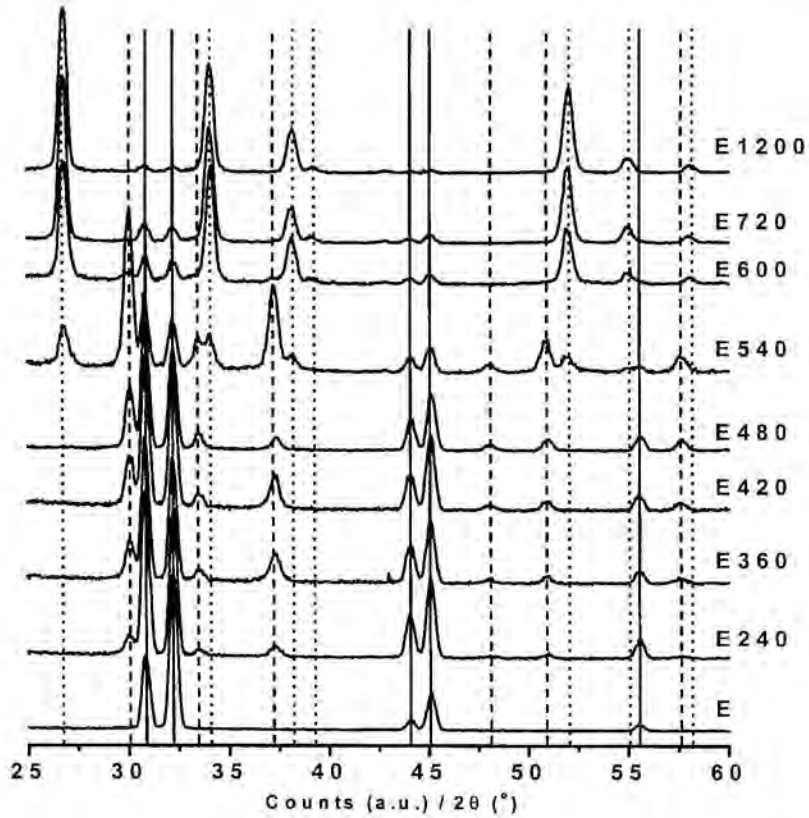


Figure 31: XRD diffractograms of the thicker samples. As shown, the oxidation of β -Sn begins with the formation of romarchite-SnO, which is transformed steeply into tetragonal SnO₂. Solid lines represent Sn, dashed lines SnO and dotted lines SnO₂.

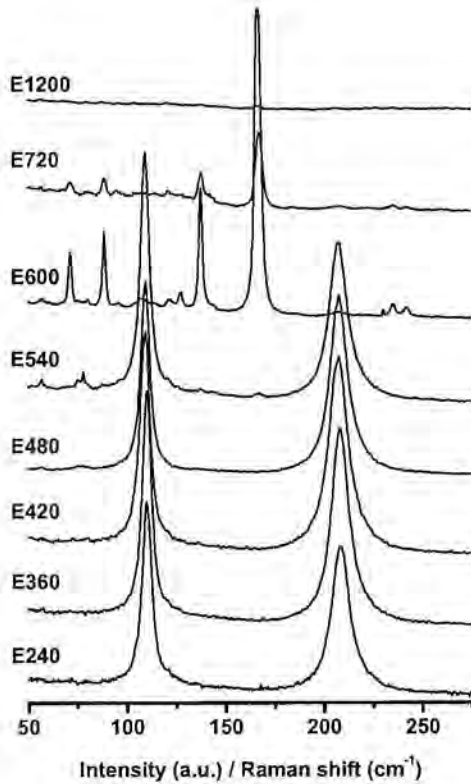


Figure 32: Raman spectra of the thicker samples in the region between 50 and 275 cm⁻¹. The bands at c.a. 109 and 208 cm⁻¹ correspond to SnO and the very intense bands at 71, 88, 137, and 166 cm⁻¹ to an intermediate compound between SnO and SnO₂. The A_{1g} mode of cassiterite observed in samples E720 and E1200 is not shown in the graph.

At the beginning and the end of the oxidation practically the same result is observed by Raman spectroscopy (figure 32). The Raman bands at 109 and 208 cm⁻¹ indicate that the transformation begins with the appearance of SnO with the romarchite structure. On the other hand, the appearance of the mode A_{1g} of the cassiterite at 632 cm⁻¹ in sample E600 indicates the presence of SnO₂, which results further increased as the oxidation proceeds. However, for temperatures above ~500°C other not well defined bands, corresponding to a phase not described by XRD, appear. These bands evolve towards a well defined structure at the end of the ramp (600°C). Their positions are observed at 71, 88, 137, and 166 cm⁻¹ and their intensities are very high compared with those of SnO. In order to identify the phase observed by Raman spectroscopy, additional XRD analysis of sample E600 were performed in a SIEMENS D-500 diffractometer, which has a higher angular resolution. As

shown in figure 33, a careful examination of the profile clearly shows the presence of several peaks at $2\theta = 27, 31.5, 32.5$ and 36.9° in the range from $2\theta = 24$ to 40° . According with these positions, three different structures could be possible, being two phases of Sn₃O₄ (PDF Cards Number 16-737 and 20-1293), and one phase of Sn₂O₃ (PDF Card Number 25-1259), making impossible to identify with confidence if only one of these compounds is present, two or all three. So, as has been previously presented in the literature [196, 147], we have to conclude with the existence of a SnO_x phase with intermediate composition between SnO and SnO₂.

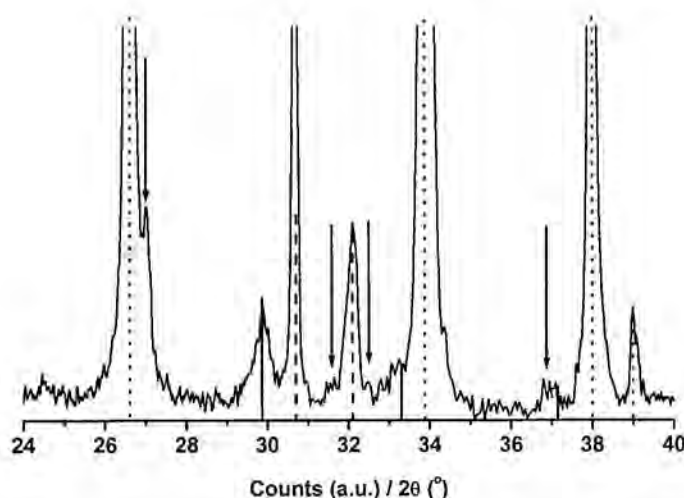
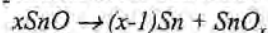


Figure 33: A detailed investigation of sample E600 shows the presence of anomalous shoulders and reflections not assigned to Sn (---), SnO (—) or SnO₂ (···). These reflections, marked by arrows indicate the presence of Sn₃O₄ or Sn₂O₃, being impossible the complete identification.

Thus, it is shown that during the thermal oxidation of Sn, the phase transformations produced in order to reach stoichiometric tin dioxide are SnO, an intermediate phase SnO_x having *x* ranging from 1.33 to 1.5, and finally SnO₂. However, according to the observations presented in this work, the Raman spectra of the intermediate phase would present four main bands located at 71, 88, 137, and 166 cm⁻¹, and not only the last two, as has been reported in other works [196, 197]. These bands present a very high Raman intensity in spite of the low intensity of the SnO_x reflections observed in the XRD profiles. Such intensities should be ascribed at these moments to enhancement due to a strong polarizability. Their origin as a consequence of resonance effects, involving the absorption of the laser excitation wavelength at 514.5nm (2.4eV), is discarded because the band gap for these structures will be probably intermediate between that of SnO at ~2.5eV and SnO₂ at ~3.6eV.

The process of oxidation for this system seems to be rather complex. In figure 34, the evolution of the different phases appearing during the oxidation is shown. Initially, the thermal oxidation of tin transforms partially Sn into SnO. After this initial stage, according with Geurts et al. [196], a disproportional reaction that decomposes SnO to metallic β-Sn and SnO₂ should occur above 300°C,



However, we observe (figure 34) that Sn is transformed progressively into SnO until the oxidation temperature arrives to ~600°C. At this point an abrupt decrease of SnO, together with the appearance of SnO₂ takes place. As reported by Moreno et al. [198],

the retardation of the decomposition reaction has been claimed to be produced by the existence of metal vacancies which create an effective local field that tends to order the crystal around that site, thus stabilising the SnO compound by strain coupling. However, contrarily to that is observed in figure 34, when the disproportional reaction occurs, a considerable increment of Sn should occur. The only plausible explanation to the small quantity of Sn and the no existence of SnO at temperatures above 600°C is that Sn reacts rapidly with oxygen to form SnO₂ at these temperatures (probably forming SnO as intermediate phase, which decomposes immediately). The fast decomposition of SnO and oxidation of Sn to form SnO₂ produce regions with an average composition between SnO and SnO₂ with a well defined structure, i.e., observable by XRD.

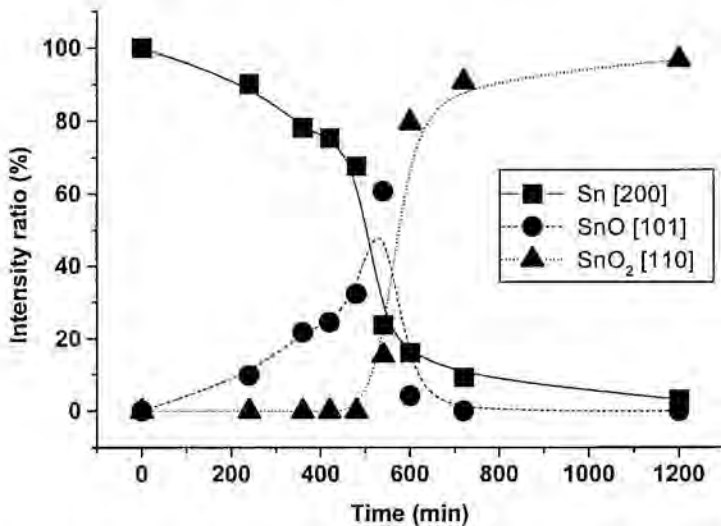


Figure 34: Evolution of the ratio of intensities of the most intense reflections of Sn, SnO and SnO₂ with respect to the sum of intensities. Without considering the different absorption coefficients this figure represents a measure of the percentage of each phase at each point of the oxidation ramp investigated in the group of thicker samples. The intermediate phase SnO_x has been omitted.

4.3.3.3 The thermal oxidation of Sn: Connection with the formation of agglomerates

As discussed before, the transformation of SnO into SnO₂ can be directly related with the formation of the spongy agglomerates and, probably the existence of liquid Sn takes also active part during the process.

A simple calculation taking into account the density of romarchite-SnO and cassiterite-SnO₂ gives rise to the determination of the volume occupied by a basic molecule in the romarchite ($V \approx 35.23 \text{ \AA}^3$) or in the cassiterite ($V \approx 35.93 \text{ \AA}^3$) lattice, giving rise to an expansion under transformation with a strain higher than 2%. This value, in general, is not very high. However, it could be possible that gives rise to fractures during the oxidation of RGTO films.

Comparing the summary of phase transformations in figure 34 and the SEM images of figure 35, it is found that the existence of these two phases and the formation of the agglomerates is intimately related. First, a smooth and spherical surface is obtained in the as deposited Sn (fig. 35a). During the oxidation, up to 480 min. (fig. 35b), the surface becomes more faceted due to the growth of SnO crystallites, and when SnO₂ appears after 540 min. of oxidation (figure 35c) a small surface roughness begins to appear. The increment of the oxidation time up to 600 and 720 min. only produces a more marked surface roughness (figures 35d and 35e). However, no differences exist when the oxidation proceeds further once all the SnO has disappeared (comparison of figures 35e and 35f for 720 and 1200 min. respectively). This result clearly shows that the origin of the agglomerates formation is mainly the transformation of SnO in SnO₂.

4.3.3.4 Influence of the temperature of deposition of tin in the final film

Because sometimes RGTO films are deposited at room temperature, it will be also interesting to analyse how the oxidation occurs in this case and compare with the case in which tin is deposited in the melted state. For this, sample F was oxidised using the normal RGTO cycle. The different times corresponding to different oxidation stages are presented in table XIII together with the nomenclature used for the samples for this study.

RGTO						
Code	Material type	Size	Film type	Heater /IDC	Deposition	Oxidation
F	Sn/SiO ₂ /Si	10 x 10mm ²	1-SnO ₂ 1000nm	No/No	T=RT°C R=2.1nm/s; t=8min	--
F240 F360 F480 F540 F720 F1200	SnO _x /SiO ₂ /Si					240 min 360 min 480 min 540 min 720 min 1200 min

Table XIII: Samples to analyse the oxidation of the tin film deposited at room temperature.

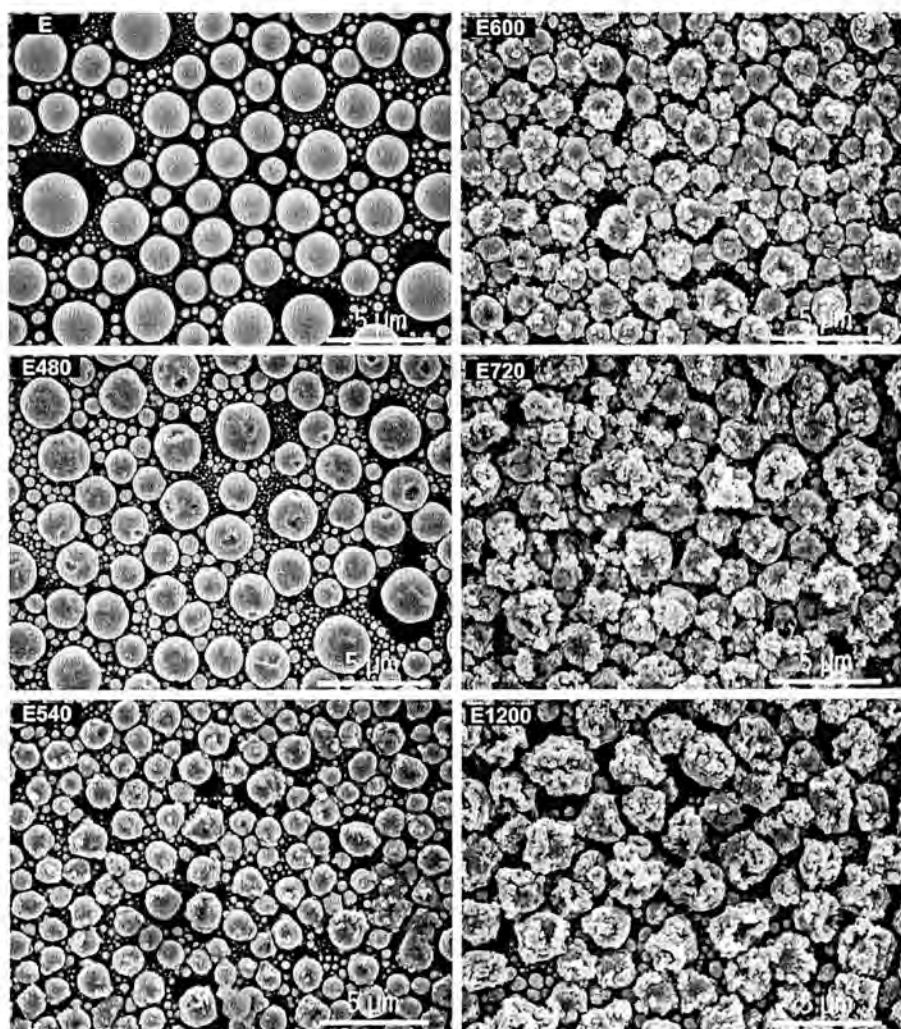


Figure 35: SEM images of the group of thicker samples.

The comparison of the Raman spectra for identical oxidation conditions (same history and final point in the oxidation cycle) indicates a similar oxidation process (see figure 32 for samples E and figure 36 for samples F). After 240 minutes of oxidation (samples E240 and F240) the temperature has arrived to 250°C. At this stage in both types E and F samples a transformation to SnO has taken place. The predominant phase is still SnO up to 540 minutes of oxidation (~512°C), where the SnO_x and SnO₂ phases appear. In the case of the group of samples F no signals of SnO are found at this stage. However, the no observation of SnO can be due to the higher thickness of the samples of group F. In both groups the transformation to SnO₂ occurs especially fast for temperatures above 600°C.

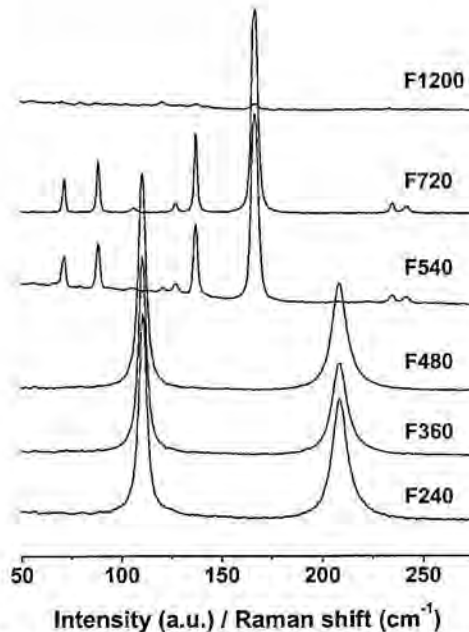


Figure 36: Raman spectra of the samples F in the region between 50 and 275cm⁻¹.

The optical absorption spectra of samples E and F is the typical of a metallic film, i.e., its optical absorption is nearly constant across the entire photon-energy range. After partial oxidation the spectra corresponds to that of a semiconductor, presenting absorption for photon-energy values lower than the band gap. This absorption evidently depends of the phase/s existing in the sample and evolves with time to that of SnO₂. By comparing the optical absorption spectra of selected stages in the RGTO scenario, i.e., after deposition and after 720 and 1200 minutes of oxidation (figure 37), it is clear that there is an excellent similitude between groups E and F. Thus, from the Raman and UVVIS spectra one can conclude that the phase transformations occurring during the thermal oxidation of Sn are independent of how Sn was deposited.

Finally, figure 38 shows the SEM images of group of samples F. From the slight change of the surface of the clusters, small signals of phase transformation can be found already for 240 minutes of oxidation. After 480 minutes the formation of nuclei at the surface of the clusters is well observed, and for longer oxidation times

($t > 540$ min.) the typical aspect of the agglomerates already seen in the group E develops. According to our previous observations for the samples deposited at 400°C, this would imply that SnO₂ has appeared, which is in agreement with the Raman results. Therefore, comparison of these images with those presented in figure 35, indicates that the formation of agglomerates occurs in the same manner for both groups.

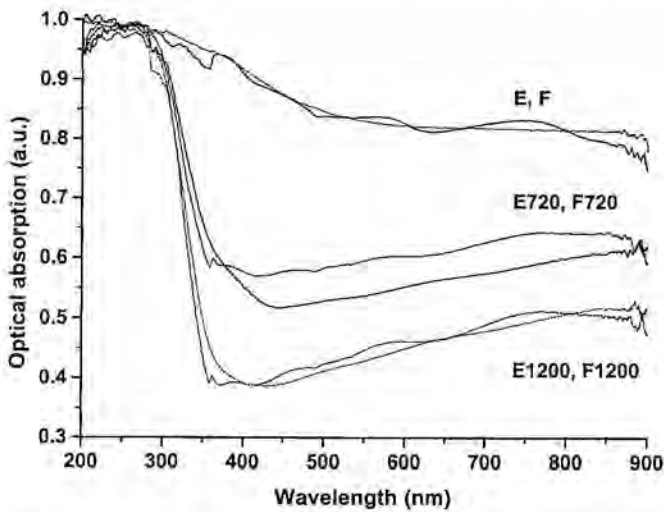


Figure 37: Comparison of the UV-VIS spectra of samples E and F oxidised for 720 and 1200 minutes.

So, the thermal oxidation of Sn occurs in a similar way independently of how Sn was deposited. In the case of a film deposited at a temperature higher than the metal melting point, metal droplets form. These droplets offer a higher front for oxygen diffusion than a relatively planar film and, hence, a faster oxidation could be expected. However, the mechanism of droplet coalescence leads to the formation of clusters of much larger thickness than if the film was planar and, hence, a retardation of the completion of oxidation. The early apparition of SnO₂ in samples F might be due to the fact that oxygen diffusion to the interior material is more difficult when the Sn films is not formed by droplets, the oxidation occurring then faster in the surface region. For temperatures $\sim 600^\circ\text{C}$ the high diffusion of oxygen and the decomposition of SnO makes indistinguishable if the deposition of the film was performed at 400°C or at room temperature.

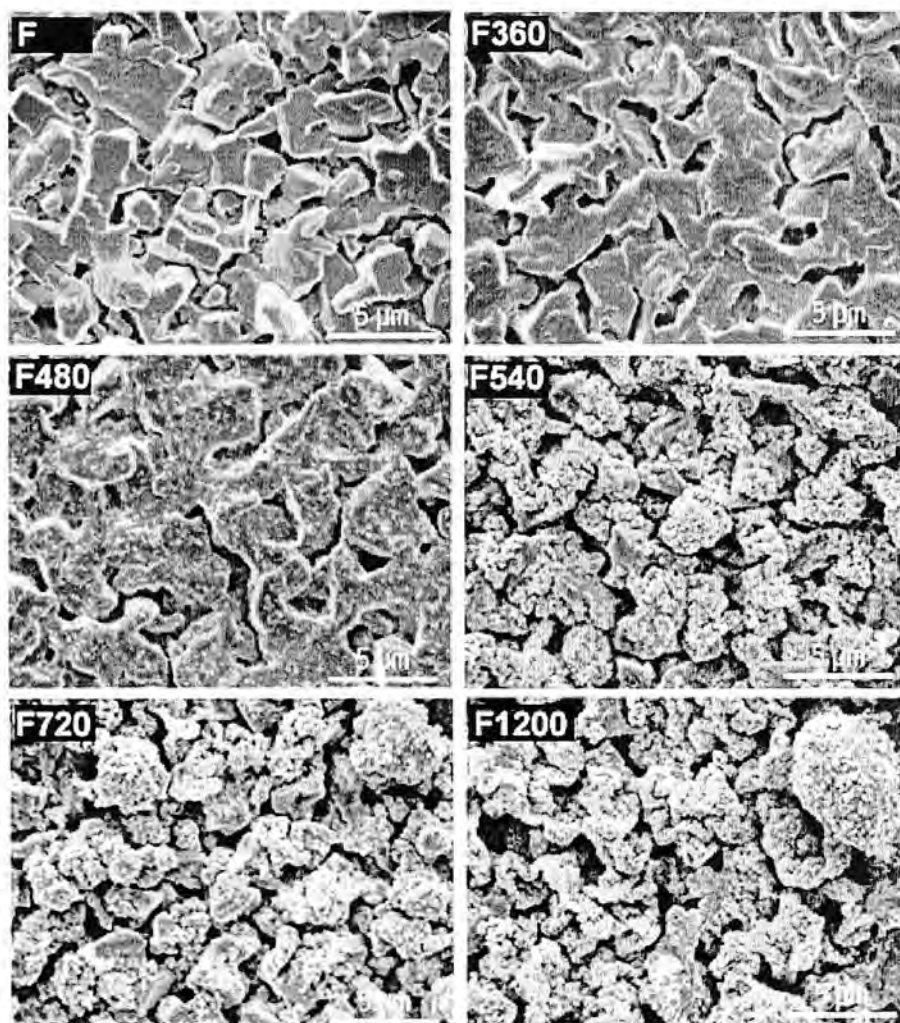


Figure 38: SEM images of the room temperature deposited sample, F, and the corresponding oxidised ones for 360, 480, 540, 720 and 1200 minutes.

4.3.3.5 Influence of an incomplete oxidation on gas sensor stability

It has been shown that in the case of SnO₂-RGTO layers, as well as for any other SnO₂ film formed through the thermal oxidation of tin droplets, large Sn clusters are preferred to be oxidised in order to form the active layer of gas sensors because of its higher surface area and better coverage of the substrate. However, this requires long oxidation periods that increase the risk of the microstructure damage. Then, if the oxidation periods are reduced, severe inhomogeneities occur in the oxidised film due to the Sn cluster size dispersion in the metallic film. As has been previously commented, incompletely oxidised regions have also been observed in other films prepared by other methods, such as the r.f. sputtering of SnO₂.

In order to analyse the influence of an incomplete oxidation on gas sensor stability three sensors were prepared (table XIV), namely SA, SB, and SC, which were thermally oxidised for 10 minutes at 450°C, 1h at 500°C, and 30h used the complete oxidation cycle. To perform electrical measurements the films were grown onto substrates equipped with a Pt meander heater on the backside and Pt interdigitated contacts on the sensor surface. After the initial measurements, the sensors were aged at a temperature ranging from 300 to 400°C in air for 47 days applying a constant voltage to the heater of the sensors.

RGTO						
Code	Material type	Size	Film type	Heater /IDC	Oxidation	Ageing
SA	SnO _x /SiO ₂ /Si	3 x 3mm ²	1-SnO ₂ 300nm	Yes/Yes	10 min at 450°C	47 days at 300-400°C
SB	SnO _x /SiO ₂ /Si	3 x 3mm ²	1-SnO ₂ 300nm	Yes/Yes	1h at 500°C	47 days at 300-400°C
SC	SnO _x /SiO ₂ /Si	3 x 3mm ²	1-SnO ₂ 300nm	Yes/Yes	30h at 600°C	47 days at 300-400°C

Table XIV: RGTO sensors.

Figure 39a shows the sensor response $\Delta G/G$ towards 100p.p.m. of CO at 400°C of sensors SA, SB, and SC as a function of the exposure time. The corresponding XRD analysis showing the state of oxidation is presented in figure 40a. As it is observed, for sensor SC, which is completely oxidised, the response is fast and it fully recovers to the value measured in air when the flow of pure air is restored. In the case of sensor SB, consisting of a mixture Sn, SnO and SnO₂, the response has not reached a stable value also after an exposure of 20 minutes. This is evident from the lack of the plateau observed in the $\Delta G/G$ behaviour of sensor SB, compared to that of sensor SC. Moreover, when the pure air flux is restored the conductance does not recover to the initial value. In the case of sensor SA, a drift in the response is observed, as can be deduced from the increase of the baseline with time. After the ageing treatment (figure 39b), the response behaviour with time has

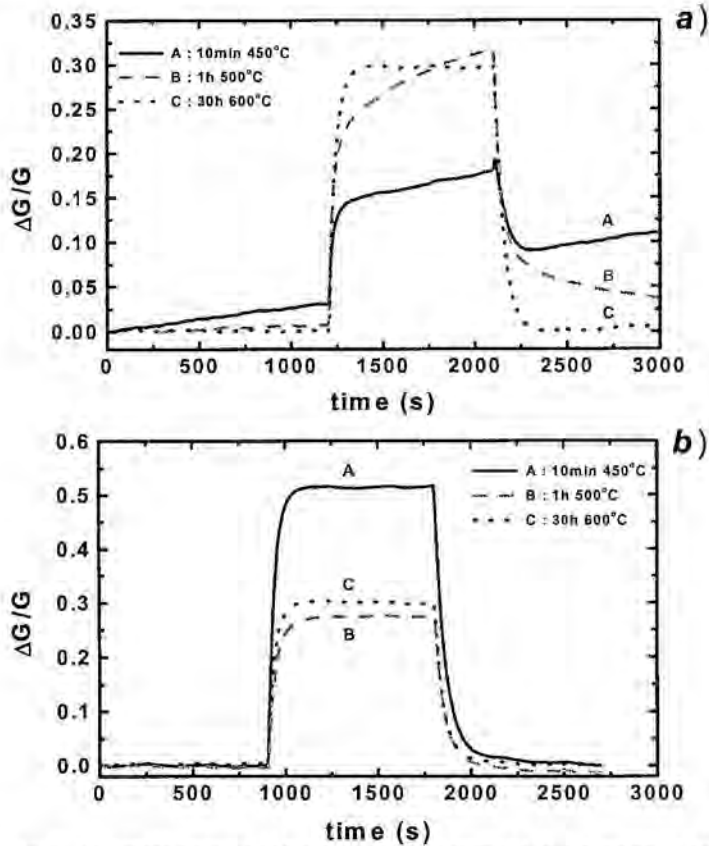


Figure 39: Sensor response ($\Delta G/G$) towards 100 ppm CO as a function of time measured at $T=400^\circ\text{C}$, before the long-term operation (top) and after (bottom).

dramatically improved. There is no baseline drift as that found in sensor SA in figure 40b and the response profile is quite sharp for all samples with a fast recovery. These findings indicate that the ageing process has contributed to stabilise the sensors and make the response more uniform within our set of specimens (the spread of response values measured for the three sensors reduces with ageing). However, these results reveal mainly that some type of important drift occurs during the first days of sensor operation.

According to the results presented in this work, mainly two different sources of sensor response drift arise from an incomplete oxidation:

- i) *Short term drifts:* When one sensor undergone a high temperature oxidation (600°C) for insufficient time is operated even at temperatures lower than usual (i.e., lower than $\sim 400^\circ\text{C}$), it is observed that the

reflections due to Sn are lost at the operating temperature because Sn at this temperature is liquid (see figure 41). If the sensor is calibrated at this stage of oxidation, such liquid content would give rise to an inductive behavior [199]. After further short time operation this signal would disappear as Sn will transform into SnO. Therefore, the predictions of the signal processing algorithms will be incorrect. The initial transformation of Sn into SnO should be included as a short-term drift and, as one of the origins for a bad calibration of sensors. Additional short-term drifts produced by the accommodation of the material during heating would also occur, although they would be more predictable [24].

- ii) *Short to Long term drifts:* As was discussed in the previous sections, once SnO appears, the transformation to SnO₂ and thus, the formation of the spongy agglomerates is produced very fast at temperatures in the range 500-600°C. As for temperatures below 540°C, SnO₂ was not detected, it is expected that at the usual temperatures of operation of the sensor (~400-500°C) the rate of this transformation be much more slow (i.e. probably one to two orders of magnitude longer than at 600°C). The short to long-term drifts thus caused would occur not only due to the phase transformation, but also due to the morphological changes taking place when the agglomerates form.

So, the overall improvement of the sensors behaviour, observed when comparing the plots in figure 39, is ascribed to the oxidation process induced by the ageing treatment. Even though the ageing temperature is well below the standard annealing temperature for this kind of sensors (600°C) full oxidation can be achieved on a long time scale. This is confirmed by X-ray diffraction experiments (figure 40) where the XRD pattern of SnO₂ cassiterite only is detected from all sensors after the ageing treatment.

Additional changes such as grain size growth and microstrain modification are expected to produce additional long-term drifts in the sensor response. In the particular case of RGTO-SnO₂ films once the agglomerates are created no detectable variations in the grain size are observed after 6 months of operation. This stability of the grain size can probably be attributed to the faceted morphology of the crystallites.

So, the easiest form of reduce instabilities is to deposit Sn clusters of limited size, even though it diminishes the final active surface area. As this would give rise a low coverage of the substrate, a multilayer procedure could be used without increasing significantly the total thermal budget of the structure, keeping the grain size small enough, and obtaining a high surface area. Concretely, it has been observed [200] that a three-step RGTO multilayer procedure produces active SnO₂ films for gas sensors which assure a total coverage and a range of resistance variation suitable for signal processing (<1MΩ). The final part of this chapter will be dedicated to the analysis of this multilayer RGTO process.

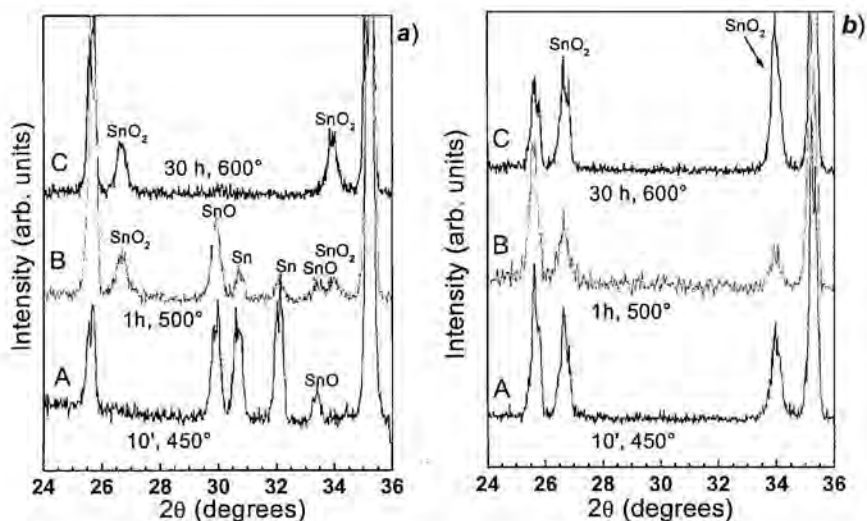


Figure 40: X-ray diffraction patterns of the oxidised tin layers after oxidation at 450 °C for 10 minutes (sensor SA); after oxidation at 500 °C for 1 hour (sensor SB); after oxidation at 600 °C for 30 hours (sensor SC). The left image corresponds to measurements before the long-term operation and the right figure after.

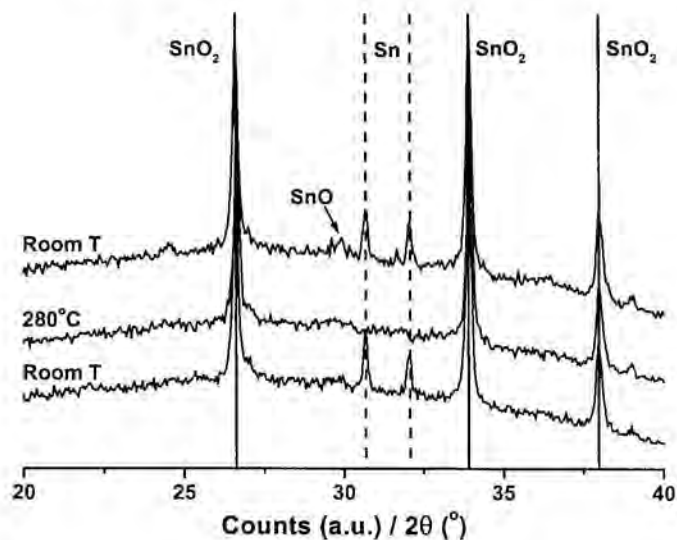


Figure 41: XRD profiles of sample E600 as obtained (bottom), at 280°C in a low temperature TTK chamber for XRD (medium) and at room temperature after the annealing (top). It is observed that the XRD reflections of Sn disappear at 280°C. After cooling the Sn profile recovers and small bands of SnO appear.

4.3.4 The multilayer RGTO technique

The principle of the multilayer process is to make successive deposition and oxidation steps on the same substrate. Therefore, a first RGTO film is formed and subsequent layers are grown on it. The conditions for deposition are the same as the used for monolayered films, and oxidation is performed using also the same oxidation cycle. Concretely, for a three-layers RGTO film the sequence of steps would be as follows:

- 1) d.c. sputtering of metallic Sn with the substrate held at 400°C.
- 2) oxidisation using the same oxidation cycle that for monolayers with $T_{max}=600^{\circ}C$.
- 3) sputtering of a second Sn layer
- 4) oxidisation as in step 2
- 5) sputtering of a third Sn layer
- 6) oxidisation as in steps 2 and 4

Next the multilayer RGTO technique will be analysed in some detail. We will investigate the evolution when passing from one to three multilayers, the intermediate stages, and compare the electrical behavior of mono and multilayer sensors. For this investigation we used the samples presented in tables XV and XVI.

From one to three multilayers						
Code	Material type	Size	Film type	Heater /IDC	Oxidation	Ageing
1M40AT	SnO ₂ /SiO ₂ /Si	10 x 10mm ²	1-RGTO 40nm	No/No	5h at 600°C	–
2M40BT	SnO ₂ /SiO ₂ /Si	10 x 10mm ²	2-RGTO 40nm	No/No	5h at 600°C	--
3M40CT	SnO ₂ /SiO ₂ /Si	10 x 10mm ²	3-RGTO 40nm	No/No	5h at 600°C	--
Intermediate stages						
1MSn40	Sn/SnO ₂ /SiO ₂ /Si	10 x 10mm ²	1-RGTO 40nm + 1-Sn 40nm	No/No	--	–
Influence of substrate roughness						
SENAu	SnO ₂ /Al ₂ O ₃	3 x 3mm ²	3-RGTO 120nm + 4.5nm of Au	Yes/Yes	30h at 600°C	yes

Table XV: Single and multilayers RGTO films.

Sensors						
Code	Material type	Size	Film type	Heater /IDC	Oxidation	Ageing
MONun1	SnO ₂ /Al ₂ O ₃	3 x 3mm ²	1-RGTO 240nm	Yes/Yes	5h at 600°C	--
MULun1	SnO ₂ /Al ₂ O ₃	3 x 3mm ²	3-RGTO 80nm	Yes/Yes	5h at 600°C	--
MULAu1	Au/SnO ₂ /Al ₂ O ₃	3 x 3mm ²	3-RGTO 80nm + 4.5nm of Au	Yes/Yes	5h at 600°C	--
MONun2	SnO ₂ /Al ₂ O ₃	3 x 3mm ²	1-RGTO 100nm	Yes/Yes	30h at 600°C	120 days
MULun2	SnO ₂ /Al ₂ O ₃	3 x 3mm ²	3-RGTO 100nm	Yes/Yes	30h at 600°C	85 days
MULAu2	Au/SnO ₂ /Al ₂ O ₃	3 x 3mm ²	3-RGTO 100nm + 4.5nm of Au	Yes/Yes	30h at 600°C	80 days

Table XVI: Multilayer RGTO sensors.

4.3.4.1 Description of film formation

The aspect of the first RGTO layer (figure 42) is similar to the results presented up to now: it is formed by agglomerates of grains surrounded by smaller ones. These agglomerates are separated from each other and do not cover the substrate completely. When the second Sn layer is deposited onto the oxidised one, the Sn droplets move into the voids existing between neighbouring SnO_2 agglomerates (figure 42). After this process, the substrate becomes practically completely covered. The oxidation of this second layer does not cause an appreciable increase of the thickness of the film, while the grain size remains about 10-20nm at the surface of the agglomerates. The repetition of the RGTO process to form a third layer gives rise to the same morphology (figure 42), an increase in the layer thickness occurring from $\sim 180\text{nm}$, with surface roughness $\sim 160\text{nm}$, to $\sim 440\text{nm}$, with roughness also $\sim 160\text{nm}$. Furthermore, the size of the grains at the surface as well as at the interface region is in the nanometer range. The presence of interfaces between the different SnO_2 layers is not visible, as we can not really speak about layers.

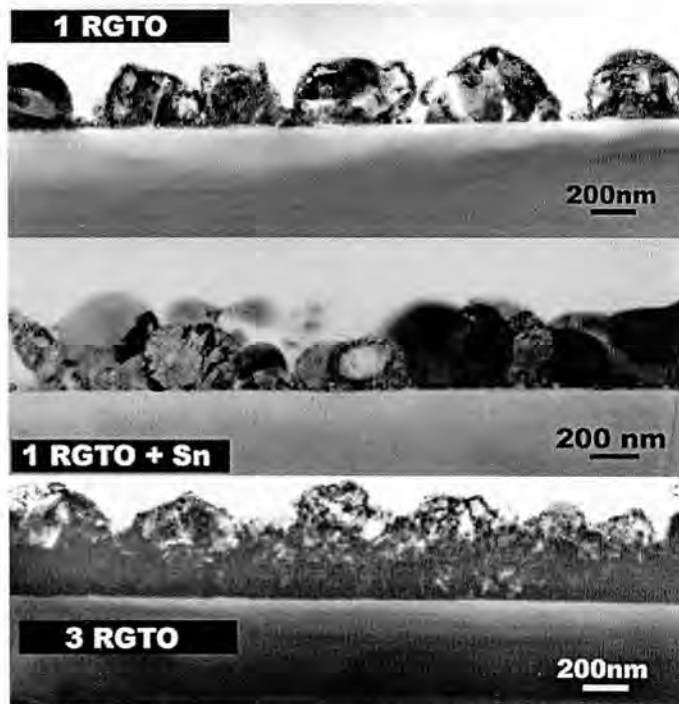


Figure 42: Cross-section TEM images of a single SnO_2 -RGTO film, the same film on which an additional Sn layer has been deposited, and a 3-step SnO_2 -RGTO multilayer. The images correspond to samples 1M40AT, 1MSn40, and 3M40CT, fabricated onto SiO_2/Si .

Thus, the multilayer RGTO technique is an effective method to maintain the grain size in the nanometer range (at least in the size of the agglomerates), as well to obtain a high surface area. Both factors can improve the sensing properties of this type of layers [201]. Moreover, the substrate is completely covered after two RGTO steps, thus improving the charge conduction between the sensor electrodes.

When RGTO films are deposited onto Al₂O₃ substrates (figure 43) surface morphology results more rough. However, this roughness is not referred to the agglomerates, but to the form in which these are distributed. As a consequence of the roughness of the substrate, in the deposit of melted Sn, the droplets are nucleated in the valleys formed by one or more Al₂O₃ grains. Thus coalescence of droplets occurs only in valleys. In order to allow droplets nucleated in different valleys to coalesce, a larger amount of Sn than in the case of a planar substrate has to be deposited. As a consequence of this, some regions of the Al₂O₃ result uncovered by Sn, remaining uncovered after oxidation. Therefore, higher resistances are expected for these films.

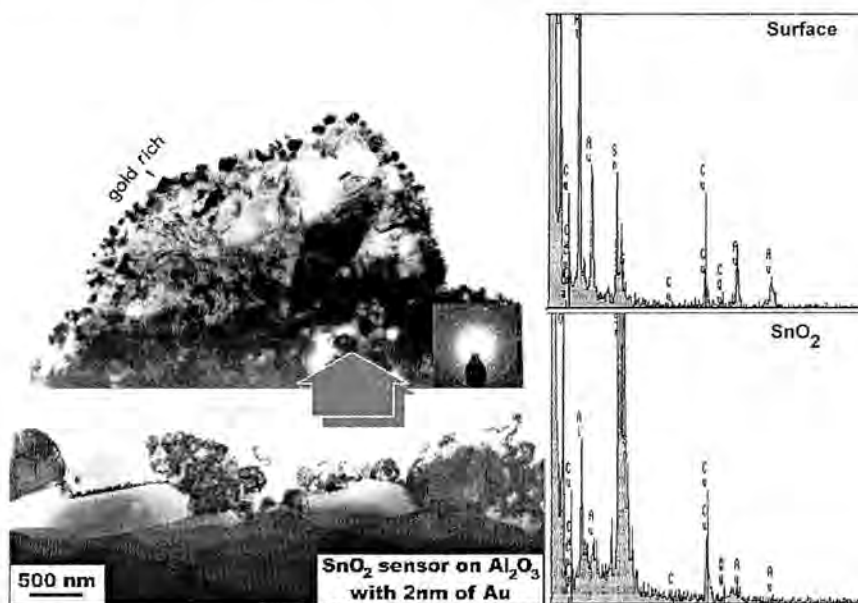


Figure 43: Sensor SENAu. Cross-section TEM images (left) and EDS spectra (right). The higher roughness with respect to the SnO₂ films grown on SiO₂/Si is evident. On the top of the SnO₂ film are visible Au particles, identified with confidence through the EDS spectra.

4.3.4.2 Improvement of the sensor characteristics with multilayered RGTO systems

For electrical tests, the sensors were located in a flow cell, where gases were passed at a total flow rate of 300ml/min. Humidification of the test gas was carried out by means of a saturation method. The baseline air with humidity concentration of 40% r.h. at 20°C was produced by mixing appropriate fractions of dry and saturated synthetic air. The sensor signal was defined as the voltage changes produced by the test gas relative to the signal baseline as detected by an electrometer. The changes in the sensor voltage were measured at an applied constant current of 1mA across the SnO₂ films. The sensor temperature was determined by the voltage across the Pt heater which was sputtered onto the backside of the alumina substrate.

The sensitivity $S=(R_{air}-R_{gas})/R_{gas}$ towards CO was measured at 400°C with concentrations ranging between 100 and 500ppm. Before the measurement, the sensors were held at 400°C for 4 hours in order to make a pre-heating and stabilise them.

The ageing of the sensors was performed at 400°C in ambient air. At fixed time intervals the sensors were placed inside the test chamber and their response to 250ppm of CO in air was tested.

The calibration curve to CO of the sensors of table XVI is presented in figure 44. The multilayered sensors (MULun1 and MULAu1) present an electrical resistance two order of magnitude lower than that of the monolayered sensor (MONun1). This has been previously attributed to the different density of grain boundary contacts and sintering necks evolving between the individual grains during the annealing of the two types of layers [200]. This lower resistance of multilayered films is very important to make the read-out through electronic circuitry easier. However, it is more likely to think that it is the higher connectivity of the multilayered films, which produce such decrease of resistance. Nevertheless, it should be noted that in the case of monolayer RGTO films, connectivity between agglomerates can be only obtained after oxidation of very thick Sn films, while it is easily obtained with multilayer processes and thinner individual films.

The sensor signal follows a power law dependence with [CO], i.e., $S\sim[CO]^\alpha$, with $\alpha=5\cdot 10^{-3}$, $1.755\cdot 10^{-3}$, and $5.75\cdot 10^{-4}$ for sensors MULAu1, MULun1, and MONun1, respectively. It can be observed that the sensor signal of sensor MONun1 is the lowest, while the multilayer of pure tin dioxide shows a response enhancement, which results further increased upon addition of gold. The same effect is observed when comparing the sensor response of sensors MULun2 and MULAu2 in figure 44. As is shown in figure 43, the deposition by sputtering of gold onto a SnO₂ film produces gold clusters onto the surface of the film, which act as catalyses for the reaction with the CO gas.

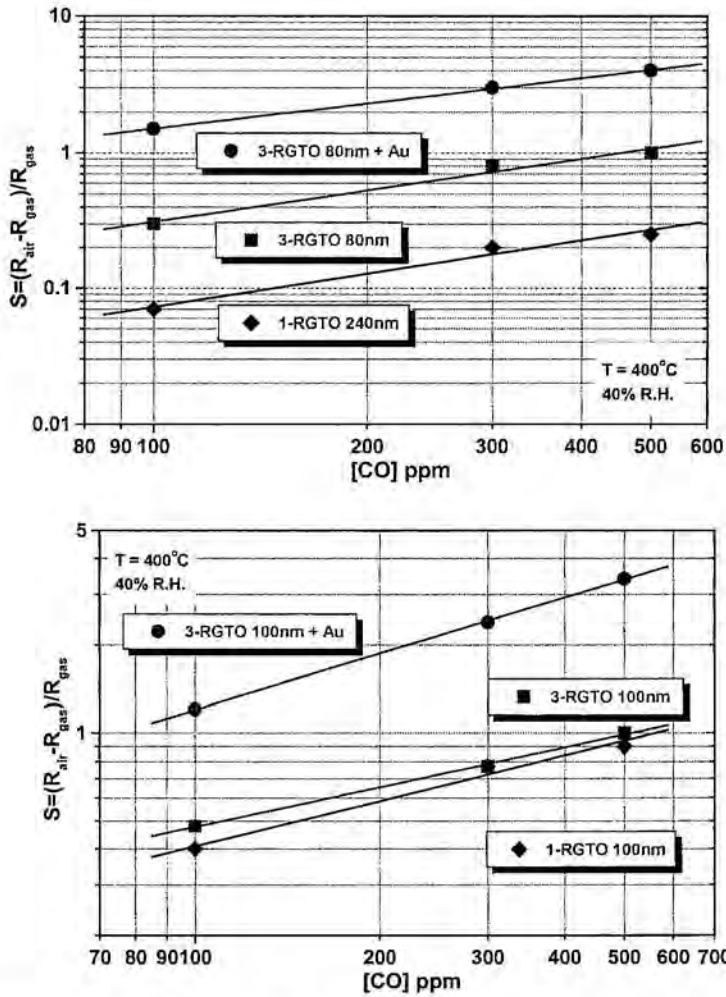


Figure 44: Comparison of sensor sensitivity to CO for sensors MONun1, MULun1, and MULAu1 (top), and sensors MONun2, MULun2, and MULAu2 (bottom). The top graph allow to compare sensitivity for the same thickness (240nm), changing the procedure of fabrication or by adding Au. The bottom graph allows to compare the influence of thickness and Au addition on sensor sensitivity.

For comparison of stability of mono and multilayer sensors, sensors MONun2, MULun2, and MULAu2 were used. By the examination of figure 45 one can observe that the resistance of the three sensors is stabilised after about three weeks of operation. However, the three-layered sensors have a more stable resistance in air. Concretely, its variation over the whole measurement period is about 152% for the undoped sensor and 110% for the Au doped sensor, while is ten

times higher (1052%) for the monolayer. It is plausible to think that all the three sensors follow an evolution based in microstrain changes. Even in the case of the monolayered sensor, it is expected that it will be completely oxidised, as its nominal thickness is only 100nm. However, if the same type of analysis would be performed on thicker films, other factors such as further oxidation and reorganisation of nanocrystals in the film would occur.

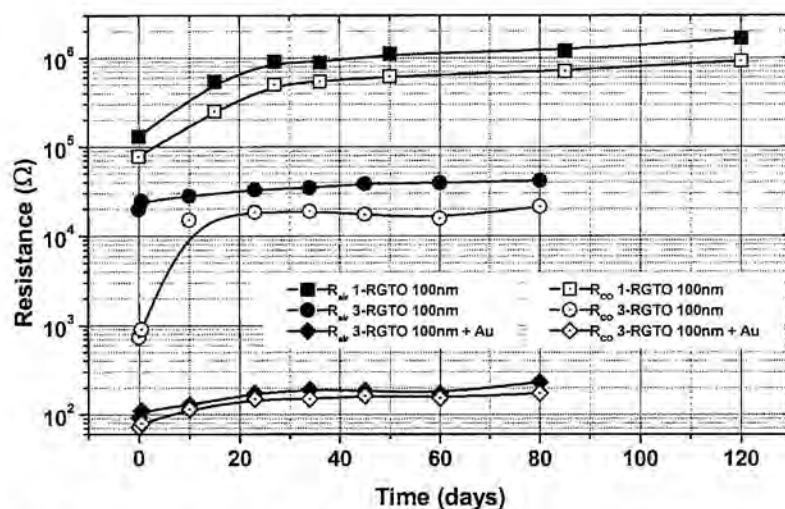


Figure 45: Evolution of resistance in air and in CO over 80 (MULun2 and MULAu2) or 120 days (MONun2).

4.4 Conclusions

The analysis of thin films performed in this chapter is of fundamental importance in the understanding of phenomena related to thin film formation and stability. The main conclusion is, probably, that stable films are obtained when they are formed by nanoparticles with defined shape and stoichiometry. Nevertheless, our analysis of IBAD and RGTO films has allowed concluding in certain characteristics of the growth processes basic to obtain reliable films for gas sensing. For IBAD, it was the annealing of the substrate during deposition. For RGTO, a sufficiently long oxidation performed on Sn films or the use of a multilayer growth. Nevertheless, the deep investigation of the complete RGTO method, including the deposition and oxidation of tin, has resulted in conclusions, very important in some cases, and interesting in others.

It has been found that in the deposition of tin at temperatures above its melting point, the mechanism of coalescence of tin droplets is predominant over any other mechanism taking place. The distribution of droplets, and specially the larger ones, occurs always in the same manner, independently of parameters such as the deposition rate. In this way, the evolution of the droplet size distribution with time is modified only by scale factors, its shape being similar at different stages of the deposition.

The oxidation of tin does not occur directly from Sn to SnO₂, but through intermediate phases, the most important being SnO. It has been shown that the oxidation begins at the surface of the droplets and that during the oxidation, it is the phase change from SnO to SnO₂, which produces the transformation of the morphology of the film. This new morphology has a spongy aspect, the degree of spongy being dependent of the size of the initial tin droplets. The complete mechanism of oxidation, described in detail in the *Chapter*, occurs exactly in the same manner, independently of how the tin was deposited. This last result is very important to extent the results presented in this work to other SnO₂ films grown in similar manner.

In what respects to the stability of RGTO films, the incomplete oxidation has been demonstrated as a important source for sensor calibration and future drifts. On one hand, the existence of Sn in the film produces a rapid and unexpected behaviour of the sensor when it is operated at usual sensing temperatures. On the other hand, when this Sn is oxidised, beyond the formation of new phases, morphological changes also take place, which will disturb the stability of the sensor in a longer time scale.

The problems outlined about the stability of RGTO sensors could be eliminated with longer oxidation periods. However, due to the actual interest in integration, an increase of the oxidation time is not appropriate. Thus, the multilayer RGTO technique has been analysed and shown to be effective in order to keep the grain size small enough without performing a long-term oxidation. In this way, the

thermal budget needed for the production of smart sensors is strongly reduced, which is a very important factor in order to avoid damages on the sensor and on the read-out electronics. Moreover, multilayered sensors present a better sensitivity to CO than monolayered sensors, which is increased with the addition of gold. Their resistance is also several orders of magnitude lower than in the case of single RGTO sensors, which has important implications in the read-out through electronic circuitry and represent a remarkable feature in view of large scale applications. In addition, and what is more important for the objective of this chapter, multilayered sensors present a significant improvement of stability. In particular, the sources of sensor instability produced by an incomplete oxidation are eliminated, even in relatively thick films.

4.5 REFERENCES

- [1] S.G. Ansari, P. Borojerdian, S.K. Kulkarni, S.R. Sainkar, R.N. Karekar, and R.C. Aiyer, Effect of thickness on H₂ gas sensitivity of SnO₂ nanoparticle-based thick film resistors, *Journal of Materials Science: Materials in Electronics* **7**, 267-270 (1996).
- [2] U. Dibbern, G. Kuersten, and P. Willich, Gas sensitivity, sputter conditions and stoichiometry of pure tin oxide layer, *Proc. 2nd Int. Meet. Chemical Sensors*, Bordeaux (France), pp. 127-130 (1986).
- [3] G. Sberveglieri, G. Faglia, S. Gropelli, P. Nelli, and A. Taroni, A novel PVD technique for the preparation of SnO₂ thin films as C₂H₅OH sensors, *Sensors and Actuators B* **7**, 721-726 (1992).
- [4] B. Flietner, and I. Eisele, Work function measurements for gas detection using tin oxide layers with a thickness between 1 and 200 nm, *Thin Solid Films* **250**, 258-262 (1994).
- [5] B.C. Tofield, State of the art and future prospects for solid state gas sensors, in *Solid State Gas Sensors*, pp. 198-238, ed. by P.T. Moseley, and B.C. Tofield, Adam Hilger, Bristol, 1987.
- [6] K. Liping, W. Ping, W. Xiaoxiang, and L. Jianping, The design of a new integrated gas sensor array based on FEA, *Technical Digest of the Seventh International Meeting on Chemical Sensors*, Beijing (China), pp. 91-93 (1998).
- [7] C. Cané, I. Gracia, A. Götz, L. Fonseca, E. Lora-Tamayo, M.C. Horrillo, I. Sayago, J.I. Robla, J. Rodrigo, and J. Gutierrez, On-line detection of gases with arrays of optimised micromachined tin oxide gas sensors, *Technical Digest of the Seventh International Meeting on Chemical Sensors*, Beijing (China), pp. 151-153 (1998).
- [8] F. Ménil, C. Lucat, H. Debéda, The thick-film route to selective gas sensors, *Sensors and Actuators B* **24-25**, 415-420 (1995).
- [9] M.A. Portnoff, R.G. Grace, A.M. Guzman, P.D. Runco, and L.N. Yannopoulos, *3rd IMCS '96* (1990).
- [10] C.H. Kwon, D.H. Yun, H.K. Hong, S.R. Kim, K. Lee, H.Y. Lim, and K.H. Yoon, Multilayered thick film gas sensor array for selective sensing by catalytic filtering technology, *Technical Digest of the Seventh International Meeting on Chemical Sensors*, Beijing (China), pp. 278-280 (1998).
- [11] A. Grisel, Integrated chemical sensor technology and related devices manufacturing, *Technical Digest of the Seventh International Meeting on Chemical Sensors*, Beijing (China), pp. 87-90 (1998).
- [12] S. Ehrmann, J. Jüngst, J. Goschnick, and D. Everhard, Application of a gas sensor microarray to human breath analysis, *Technical Digest of the*

- Seventh International Meeting on Chemical Sensors*, Beijing (China), pp. 214-216 (1998).
- [13] A. Grisel, and V. Demarne, in *Chemical Sensor Technology* vol. 1, ed. T. Seiyama, Kodansha LTD Tokio – Elsevier Science Publishers B.V. Amsterdam, 1988.
- [14] C. Perego, and G. Sberveglieri, Silicon micromachining and thin film technology for gas sensors fabrication, in *Sensors for Domestic Applications*, ed. A. D'Amico and G. Sberveglieri, World Scientific Publishing Co. Pte. Ltd., Singapore, pp. 217-225 (1995).
- [15] R. P. Lyle, and D. Walters, Commercialization of silicon-based gas sensors, *Digest of Technical Papers vol. 2 of the International Conference on Solid-State Sensors and Actuators*, Transducers'97, Chicago (USA), pp. 975-977 (1997).
- [16] W.Y. Chung, T.H. Kim, Y.H. Hong, and D.D. Lee, Characterization of porous tin oxide thin films and their application to microsensor fabrication, *Sensors and Actuators B* **24-25**, 482-485 (1995).
- [17] R.E. Cavicchi, J.S. Suehle, K.G. Kreider, B.L. Shomaker, J.A. Small, M. Gaitan, and P. Chaparala, Growth of SnO₂ films on micromachined hotplates, *Appl. Phys. Lett.* **66**(7), 812-814 (1995).
- [18] H.W. Shin, G.Lloyd, and J. Gardner, Combined resistive and calorimetric sensing of gases using a single silicon micromachined device, *Digest of Technical Papers vol. 2 of the International Conference on Solid-State Sensors and Actuators*, Transducers'97, Chicago (USA), pp. 935-938 (1997).
- [19] B. Ruhland, Th. Becker, and G. Müller, Gas-kinetic interactions of nitrous oxides with SnO₂ surfaces, *Sensors and Actuators B* **50**, 85-94 (1998).
- [20] Z. Tang, S.K.H. Fung, D.T.W. Wong, P.C.H. Chan, J.K.O. Sin, and P.W. Cheung, An integrated gas sensor based on tin oxide thin-film and improved micro-hotplate, *Sensors and Actuators B* **46**, 174-179 (1998).
- [21] L.Y. Sheng, Z. Tang, J. Wu, P.C.H. Chan, and J.K.O. Sin, A low-power CMOS compatible integrated gas sensor using maskless tin oxide sputtering, *Sensors and Actuators B* **49**, 81-87 (1998).
- [22] L.Y. Sheng, Z. Tang, J. Wu, P.C.H. Chan, and J.K.O. Sin, A low-power CMOS compatible integrated gas sensor using maskless tin oxide sputtering, *Digest of Technical Papers vol. 2 of the International Conference on Solid-State Sensors and Actuators*, Transducers'97, Chicago (USA), pp. 939-942 (1997).
- [23] A. Hierlemann, M. Schweizer-Berberich, U. Weimar, G. Kraus, A. Pfau, and W. Göpel, Pattern recognition and multicomponent analysis, in

- Sensors: update*, 1st ed., vol 2, Ed. by H. Baltes, W. Göpel, and J. Hesse, VCH, Weinheim, 120-180 (1996).
- [24] H.E. Endres, W. Göttler, H.D. Jander, S. Drost, G. Sberveglieri, G. Faglia, and C. Perego, A systematic investigation on the use of time-dependent sensor signals in signal-processing techniques, *Sensors and Actuators B* **24-25**, 785-789 (1995).
- [25] F. Allegretti, N. Butta, L. Cinquegrani, and S. Pizzini, A tin oxide semiconductor sensor for oxygen determination in the sub-ppm range, *Sensors and Actuators B* **10**, 191-195 (1993).
- [26] A. Galdikas, A. Mironas, and A. Setkus, Copper-doping level effect on sensitivity and selectivity of tin oxide thin-film gas sensor, *Sensors and Actuators B* **26-27**, 29-32 (1995).
- [27] I.S. Chuprakov, and A.R. Kaul, SnO₂ and Pd/SnO₂ based thin film gas sensors obtained by MOCVD, *Proc. Int. Meet. on Chem. Sens.* **5**, 683, Rome (1994).
- [28] R. Lalauze, C. Pijolat, S. Vincent, and L. Bruno, High-sensitivity materials for gas detection, *Sensors and Actuators B* **8**, 237-243 (1992).
- [29] R. Lalauze, N. Bui, and C. Pijolat, Interpretation of the electrical properties of a SnO₂ gas sensor after treatment with sulfur dioxide, *Sensors and Actuators* **6**, 119-125 (1984).
- [30] N. Butta, L. Cinquegrani, E. Mugno, A. Tagliente, and S. Pizzini, A family of tin oxide-based sensors with improved selectivity to methane, *Sensors and Actuators B* **6**, 253-256 (1992).
- [31] L. Bruno, C. Pijolat, R. Lalauze, Tin dioxide thin-film gas sensor prepared by chemical vapour deposition: Influence of grain size and thickness on the electrical properties, *Sensors and Actuators B* **18-19**, 195-199 (1994).
- [32] T. Honglin, Z. Yaohua, Q. Zhimei, and L. Minqiang, Pd-doped tin(IV) oxide-based thin-film gas sensors, *Proc. Int. Meet. on Chem. Sens.* **5**, 602, Rome (1994).
- [33] C.Y.B. Chu, S.Y. Zhao, P.H. Wei, and J.F. Lu, Characteristics of tin dioxide thin-film sensor for the detection of H₂S, *Sensors and Actuators B* **13-14**, 519-520 (1993).
- [34] T. Oyabu, Sensing characteristics of SnO₂ thin film gas sensor, *J. Appl. Phys.* **53**, 2785-2787 (1982).
- [35] R.M. Geatches, A.V. Chadwick, and J.D. Wright, Single crystal metal oxide gas sensors, *Sensors and Actuators B* **4**, 467-472 (1991).
- [36] G. Sanon, R. Rup, and A. Mansingh, Influence of thickness and substrate on the properties of SnO₂ films deposited by CVD, *Phys. Stat. Sol. A* **128**, 109-116 (1991).

- [37] A. Smith, J.M. Laurent, D.S. Smith, J.P. Bonnet, R. Rodriguez-Clemente, Relation between solution chemistry and morphology of SnO₂-based thin films deposited by a pyrosol process, *Thin Solid Films* **266**, 20-30 (1995).
- [38] S.G. Ansari, S.W. Gosavi, S.A. Gangal, R.N. Karekar, and R.C. Aiyer, Characterization of SnO₂-based H₂ gas sensors fabricated by different deposition techniques, *J. Mater. Sci.: Materials in Electronics* **8**, 23-27 (1997).
- [39] G. Sanon, R.R. Rup, and A. Mansingh, Growth and characterization of tin oxide films prepared by chemical vapour deposition, *Thin Solid Films* **190**, 287-301 (1990).
- [40] A. Mani, N. Karuppiyah, and R. Mahalingam, Microstructure of CVD-SnO₂ films, *Mat. Res. Bull.* **25**, 799-806 (1990).
- [41] M. Kanamori, K. Suzuki, Y. Ohya, and Y. Takahashi, Analysis of the change in the carrier concentration of SnO₂ thin film gas sensor, *Jpn. J. Appl. Phys.* **33**, 6680-6683 (1984).
- [42] T. Maruyama, and T. Morishita, Tin oxide thin films prepared by photochemical vapour deposition from tin(II) acetate, *Thin Solid Films* **251**, 19-22 (1994).
- [43] G. Sberveglieri, P. Nelli, G.P. Benussi, L.E. Depero, M. Zocchi, G. Rossetto, and P. Zanella, Enhanced response to methane for SnO₂ thin films prepared with the CVD technique, *Sensors and Actuators B* **15-16**, 334-337 (1993).
- [44] J.R. Brown, M.T. Cheney, P.W. Haycock, D.J. Houlton, A.C. Jones, and E.W. Williams, The gas-sensing properties of tin oxide thin films deposited by metallorganic chemical vapor deposition, *J. Electrochem. Soc.* **144**, 295-299 (1997)
- [45] S.W. Lee, P.P. Tsai, and H.D. Chen, H₂ sensing behavior of MOCVD-derived SnO₂ thin films, *Sensors and Actuators B* **41**, 55-61 (1997).
- [46] F. DiMeo, R.E. Cavicchi, S. Semancik, J.S. Suehle, N.H. Tea, J. Small, J.T. Armstrong, and J.T. Kelliher, In situ conductivity characterization of oxide thin film growth phenomena on microhotplates, *J. Vacuum Sci. and Technol.* **16**, 131-138 (1998).
- [47] M. Labeau, B. Gautheron, G. Delabouglise, J. Pena, V. Ragel, A. Varela, J. Roman, J. Martinez, J.M. Gonzalez-Calbet, M. Vallet-Regi, Synthesis, structure and gas sensitivity properties of pure and doped SnO₂, *Sensors and Actuators B* **15-16**, 379-383 (1993).
- [48] B. Gautheron, M. Labeau, G. Delabouglise, and U. Schmatz, Undoped and Pd-doped SnO₂ thin films for gas sensors, *Sensors and Actuators B* **15-16**, 357-362 (1993).

- [49] S. Manorama, G.S. Devi, and V.J. Rao, Hydrogen sulfide sensor based on tin oxide deposited by spray pyrolysis and microwave plasma Chem Vap Deposition, *Appl. Phys. Lett.* **64**, 3163-3165 (1994).
- [50] T. Ratcheva, I. Stambolova, and K. Konstantinov, Copper doped SnO₂ thin films for PH₃ detection, *Thin Solid Films* **217**, 187-192 (1992).
- [51] H.H. Afify, F.S. Terra, and R.S. Momtaz, Substrate temperature effects on the tin oxide films prepared by spray pyrolysis, *J. Mater. Sci.: Materials in Electronics* **7**, 149-153 (1996).
- [52] D.R. Acosta, E.P. Zironi, E. Montoya, and W. Estrada, About the structural, optical and electrical properties of Sson films produced by spray pyrolysis from solutions with low and high contents of fluorine, *Thin Solid Films* **288**, 1-7 (1996).
- [53] V. Vasu, and A. Subrahmanyam, Physical properties of sprayed SnO₂ films, *Thin Solid Films* **202**, 283-288 (1991).
- [54] I. Yagi, Y. Hagiwara, K. Murakami, and S. Kaneko, Growth of highly oriented SnO₂ thin films on glass substrate from tetra-n-butyltin by the spray pyrolysis technique, *J. Mater. Res.* **8**(7), 1481-1483 (1993).
- [55] D. Narducci, G. Girardi, and Ch. Piseri, Preparation, micromorphology and stability of tin oxide thin films, *Solid State Phenomena* **51-52**, 435-440 (1996).
- [56] Z.C. Orel, B. Orel, and M.K. Gunde, Spectrally selective SnO₂:F film on glass and black enamelled steel substrates: spray pyrolytical deposition and optical properties, *Solar Energy Materials and Solar Cells* **26**, 105-116 (1992).
- [57] M. Fujimoto, T. Urano, S. Murai, and Y. Nishi, Microstructure and X-ray study of preferentially oriented SnO₂ thin film prepared by pyrohydrolytic decomposition, *Jpn. J. Appl. Phys.* **28**(12), 2587-2593 (1989).
- [58] Z.C. Orel, B. Orel, and M.K. Gunde, Spectrally selective SnO₂:F film on glass and black enameled steel substrates: spray pyrolytical deposition and optical properties, *Solar Energy Materials and Solar Cells* **26**, 105-116 (1992).
- [59] H.H. Afify, R.S. Momtaz, W.A. Badawy, and S.A. Nasser, Some physical properties of fluorine-doped SnO₂ films prepared by spray pyrolysis, *J. Mater. Sci.: Materials in Electronics* **2**, 40-45 (1991).
- [60] U. Schmatz, G. Delabouglise, M. Labeau, and J. Garden, Electrical and microstructural studies of SnO₂ ceramics obtained by tin sulfate pyrolysis, *J. Electrochem. Soc.* **141**(11), 3254-3258 (1994).
- [61] J. Roman, J.C. Fabian, M. Labeau, G. Delabouglise, and M. ValletRegi, Synthesis, structure, and gas sensitivity properties of SnO₂-CuO mixture

- phase obtained by pyrolysis of an aerosol, *J. Mater. Res.* **12** (2), 560-565 (1997).
- [62] J.P. Zhang, and K. Colbow, Surface silver clusters as oxidation catalysts on semiconductor gas sensors, *Sensors and Actuators B* **40**, 47-52 (1997).
- [63] M. Rumyantseva, M. Labeau, G. Delabouglise, L. Ryabova, I. Kutsenok, and A. Gaskov, Copper and nickel doping effect on interaction of SnO₂ films with H₂S, *J. Mat. Chem.* **7** (9), 1785-1790 (1997).
- [64] M.D. Olvera, and R. Asomoza, SnO₂ and SnO₂:Pt thin films used as gas sensors, *Sensors and Actuators B* **45**, 49-53 (1997).
- [65] D. Briand, M. Labeau, J.F. Currie, and G. Delabouglise, Pd-doped SnO₂ thin films deposited by assisted ultrasonic spraying CVD for gas sensing: selectivity and effect of annealing, *Sensors and Actuators B* **48**, 395-402 (1998).
- [66] H. Gourari, M. Lumbreras, R. VanLandschoot, and J. Schoonman, Elaboration and characterization of SnO₂-Mn₂O₃ thin layers prepared by electrostatic spray deposition, *Sensors and Actuators B* **47**, 189-193 (1998).
- [67] P. Pasierb, and Z. Szklakski, Electrical properties of SnO₂/Pd thin film gas sensors, *Le Vide, les Couches Minces* **260**, 39 (1992).
- [68] G. Gaggiotti, A. Galdikas, S. Kaciulis, G. Mattogno, and A. Setkus, Surface chemistry of tin oxide based gas sensors, *J. Appl. Phys.* **76**, 4467-4471 (1994).
- [69] G. Gaggiotti, A. Galdikas, S. Kaciulis, G. Mattogno, and A. Setkus, Temperature dependencies of sensitivity and surface chemical composition of SnO_x gas sensors, *Sensors and Actuators B* **24-25**, 516-519 (1995).
- [70] H.P. Hübner, and E Obermeier, Reactively sputtered tin oxide thin-film gas sensors: correlation between fabrication parameters and CO-sensitivity, *Sensors and Actuators* **17**, 351-354 (1989).
- [71] C. Pijolat, P. Breuil, A. Methivier, and R. Lalauze, An electrical percolation model for tin dioxide polycrystalline thin films, *Sensors and Actuators B* **13-14**, 646-648 (1993).
- [72] F.J. Gutierrez, L. Ares, J.L. Robla, M.C. Horrillo, L. Sayago, J.M. Getino, and J.A. Agapito, NO_x tin dioxide sensors activities as a function of doped materials and temperature, *Sensors and Actuators B* **15-16**, 354-356 (1993).
- [73] G. Williams, and G.S.V. Coles, The influence of deposition parameters on the performance of tin dioxide NO₂ sensors prepared by radio-frequency magnetron sputtering, *Sensors and Actuators B* **24-25**, 469-473 (1995).

- [74] G. Sberveglieri, S. Gropelli, and G. Coccoli, Radio frequency magnetron sputtering growth and characterization of indium tin oxide (ITO) thin films for NO₂ gas sensors, *Sensors and Actuators* **15**, 235-242 (1988).
- [75] T. Sotomura, K. Ariga, and S. Sekido, SnO₂ sputtered film gas sensor, *Nat. Tech. Rep.* **29**, 137-144 (1983).
- [76] S.C. Chang, Thin film semiconductor NO_x sensor, *IEEE Trans. Electron Devices*, **ED-26**, 1875-1880 (1979).
- [77] H.P. Hübner, and S. Drost, Tin oxide gas sensors: an analytical comparison of gas sensitive and non gas-sensitive thin films, *Sensors and Actuators B* **4**, 463-466 (1991).
- [78] J. Klöber, M. Ludwig, and H.A. Schneider, Effects of thickness and additives on thin-film SnO₂ gas sensors, *Sensors and Actuators B* **3**, 69-74 (1991).
- [79] R. Sanjines, F. Levy, V. Demarne, and A. Grisel, Some aspects of the interaction of oxygen with polycrystalline SnO_x thin films, *Sensors and Actuators B* **1**, 176-181 (1990).
- [80] J.W. Gardner, H.V. Shurmer, and P. Corcoran, Integrated tin oxide sensors, *Sensors and Actuators B* **4**, 117-121 (1991).
- [81] D.S. Vlachos, C.A. Papadopoulos, and N. Avaritsiotis, Dependence of sensitivity of SnO_x thin-film gas sensors on vacancy defects, *J. Appl. Phys.* **80**(10) 6050-6054 (1996).
- [82] L.J. Meng, and M.P. dos Santos, The influence of oxygen partial pressure and total pressure (O₂ + Ar) on the properties of tin oxide films prepared by dc sputtering, *Vacuum* **45**(10) 1191-1195 (1994).
- [83] L.I. Popova, M.G. Michailov, and V.K. Gueorguiev, Structure and morphology of thin SnO₂ films, *Thin Solid Films* **40**, 107-112 (1989).
- [84] B. Stjerna, E. Olsson, and C.G. Granqvist, Optical and electrical properties of radio frequency sputtered tin oxide films doped with oxygen vacancies, F, Sb, or Mo, *J. Appl. Phys.* **76**(6), 3797-3817 (1994).
- [85] A. Galdikas, V. Jasutis, S. Kaciulis, G. Mattogno, A. Mironas, V. Olevano, D. Senuliene, and A. Setkus, Peculiarities of surface doping with Cu in SnO₂ thin film gas sensors, *Sensors and Actuators B* **43** 140-146 (1997).
- [86] O.V. Safonova, M.N. Rummyantseva, M. Labeau, and A.M. Gaskov, Effect of doping metals on the kinetics of interaction of SnO₂ thin films with oxygen, *J. Mater. Chem.* **8**(7), 1577-1581 (1998).
- [87] D. Rosenfeld, R. Sanjines, W.H. Schreiner, and F. Levy, Gas sensitive and selective SnO₂ thin polycrystalline films doped by ion implantation, *Sensors and Actuators B* **15-16**, 406-409 (1993).

- [88] G.N. Advani, Y. Komem, J. Hasenkopf, and A.G. Jordan, Improved performance of SnO₂ thin-film gas sensors due to gold diffusion, *Sensors and Actuators B* **2**, 139 (1982).
- [89] V. Lantto, and J. Mizsei, H₂S monitoring as an air pollutant with silver-doped SnO₂ thin-film sensors, *Sensors and Actuators B* **5**, 21-24 (1991).
- [90] H.J. Michel, H. Leiste, and J. Halbritter, Structural and electrical characterization of PVD-deposited SnO₂ films for gas-sensor applications, *Sensors and Actuators B* **24-25**, 568-572 (1995).
- [91] L. Promsong, and M. Sriyudthsak, Thin tin-oxide film alcohol-gas sensor, *Sensors and Actuators B* **24-25**, 504-506 (1995).
- [92] G. Williams, and G.S.V. Coles, NO_x response of tin dioxide based gas sensors, *Sensors and Actuators B* **15-16**, 349-353 (1993).
- [93] G.B. Barbi, J.P. Santos, P. Serrini, P.N. Gibson, M.C. Horrillo, and L. Manes, Ultrafine grain-size tin-oxide films for carbon monoxide monitoring in urban environments, *Sensors and Actuators B* **24-25**, 559-563 (1995).
- [94] I. Sayago, J. Gutierrez, L. Ares, J. Robla, M.C. Horrillo, J. Getino, J. Rino, and J.A. Agapito, The effect of additives in tin oxide on the sensitivity and selectivity to NO_x and CO, *Sensors and Actuators B* **26-27**, 19-23 (1995).
- [95] M.C. Horrillo, J. Gutiérrez, L. Arés, J. Robla, I. Sayago, J. Getino, and J.A. Agapito, The influence of the tin-oxide deposition technique on the sensitivity to CO, *Sensors and Actuators B* **24-25**, 507-511 (1995).
- [96] M. Di Giulio, G. Micocci, A. Serra, A. Tepore, R. Rella, and P. Siciliano, SnO₂ thin films for gas sensors prepared by r.f. reactive sputtering, *Sensors and Actuators B* **24-25**, 465-468 (1995).
- [97] U. Hofer, G. Kühner, W. Schweizer, G. Sulz, and K. Steiner, CO and CO₂ thin-film SnO₂ gas sensors on Si substrates, *Sensors and Actuators B* **22**, 115-119 (1994).
- [98] K. Steiner, U. Hofer, G. Kühner, G. Sulz, and E. Wagner, Ca- and Pt-catalysed thin-film SnO₂ gas sensors for CO and CO₂ detection, *Sensors and Actuators B* **24-25**, 529-531 (1995).
- [99] O. Merdrignac, P.T. Moseley, R. Peat, C.J. Soeld, and L. Sugden, The modification of gas-sensing properties of semiconducting oxides by treatment with ionizing radiation, *Sensors and Actuators B* **7**, 651-655 (1992).
- [100] G. Sulz, G. Kühner, H. Reiter, G. Uptmoor, W. Schweizer, H. Löw, M. Lacher, and K. Steiner, Ni, In and Sb implanted Pt and V catalysed thin-film SnO₂ gas sensors, *Sensors and Actuators B* **15-16**, 390-395 (1993).
- [101] H.K. Hong, H.W. Shin, H.S. Park, D.H. Yun, C.H. Kwon, K. Lee, K. Sung-Tae, and T. Moriizumi, Gas identification using micro gas sensor

- array and neural-network pattern recognition, *Sensors and Actuators B* **33**, 68-71 (1996).
- [102] P. Althainz, A. Dahlke, J. Goschnick, and H.J. Ache, Low temperature deposition of glass membranes for gas sensors, *Thin Solid Films* **241**, 344-347 (1994).
- [103] G.B. Barbi, and J. Santos-Blanco, Structure of tin oxide layers and operating temperature as factors determining the sensitivity performances to NO_x, *Sensors and Actuators B* **15-16**, 372-378 (1993).
- [104] I. Sayago, J. Gutierrez, L. Ares, J.L. Robla, M.C. Horrillo, J. Getino, J. Rino, and J.A. Agapito, Long-term reliability of sensors for detection of nitrogen oxides, *Sensors and Actuators B* **26-27**, 56-58 (1995).
- [105] G. Sberveglieri, G. Faglia, S. Groppelli, and P. Nelli, Methods for the preparation of NO, NO₂ and H₂ sensors based on tin oxide thin films, grown by means of the r.f magnetron sputtering technique, *Sensors and Actuators B* **8**, 79-88 (1992).
- [106] H. Löw, G. Sulz, M. Lacher, G. Kuhner, G. Uptmoor, H. Reiter, and K. Steiner, Thin-film In-doped V-catalysed SnO₂ gas sensors, *Sensors and Actuators B* **9**, 215-219 (1992).
- [107] K. Steiner, G Sulz, E. Neske, and E. Wagner, Laser annealing of SnO₂ thin-film gas sensors in single chip packages, *Sensors and Actuators B* **26-27**, 64-67 (1995).
- [108] T. Mochida, K. Kikuchi, T. Kondo, H. Ueno, and Y. Matsuura, Highly sensitive and selective H₂S gas sensor from RF sputtered SnO₂ thin film, *Sensors and Actuators B* **24-25**, 433-437 (1995).
- [109] K. Lee, D.H. Yun, H.S. Park, H.W. Shin, H.K. Hong, C.H. Kwon, and S.T. Kim, Thin-film micro-gas sensor for detecting CH₃SH, *Sens Mater* **7**, 35 (1995).
- [110] H.S. Park, H.W. Shin, D.H. Yun, H.K. Hong, C.H. Kwon, K. Lee, and S.T. Kim, Tin oxide micro gas sensor for detecting CH₃SH, *Sensors and Actuators B* **24-25**, 478-481 (1995).
- [111] D.Y. Godovski, A.A. Vasiliev, and E.V. Dorofeev, Analysis of hydrogen fluoride with SnO₂ gas sensors, *Sensors and Actuators B* **18-19**, 483-485 (1994).
- [112] H. Widischmann, and P. Mark, A model for the operation of thin film SnO_x conductance modulation carbon monoxide sensors, *J. Electrochem. Soc.* **126**, 627-633 (1979).
- [113] T.W. Capehart, and S.C. Chang, The interaction of tin oxide films with O₂, H₂, NO and H₂S, *J. Vac. Sci. Technol.* **18**, 393-397 (1981).
- [114] R. Huck, U. Bottger, D. Kohl, and G. Heiland, Spill-over effects in the detection of H₂ and CH₄ by sputtered SnO₂ films with Pd and PdO deposits, *Sensors and Actuators B* **1**, 176-181 (1990).

- [115] R.B. Cooper, G.N. Advani, and Jordan, Gas sensing mechanism in SnO₂ films, *J. Electron. Mater.* **10**, 455-472 (1981).
- [116] J. Zacheja, A. Schutze, A. Brauers, and D. Kohl, Fast detection of phenylarsine, a comparison of sputtered and sintered SnO₂ films, *Sensors and Actuators B* **4**, 355-358 (1991).
- [117] J. Zacheja, A. Schutze, A. Brauers, and D. Köhl, Detection of phenylarsine in air, *J. Cryst. Growth* **107**, 314-318 (1991).
- [118] J. Taftø, G. Rajeswaran, and P.E. Vanier, The local structure of amorphous SnO₂ by electron microscope techniques, *J. Appl. Phys.* **60**(2), 602-606 (1986).
- [119] H.J. Michel, H. Leiste, E. Nold, and J. Halbritter, Interface studies on magnetron-sputtered SnO₂-films, *Fresenius J. Anal. Chem.* **353**, 625-630 (1995).
- [120] U. Lampe, J. Gerblinger, and H. Meixner, Carbon-monoxide sensors based on thin films of BaSnO₃, *Sensors and Actuators B* **24-25**, 657-660 (1995).
- [121] U. Lampe, J. Gerblinger, and H. Meixner, Nitrogen-oxide sensors based on thin films of BaSnO₃, *Sensors and Actuators B* **26**, 97-98 (1995).
- [122] V. Demarne, A. Grisel, R. Sanjines, D. Rosenfeld, and F. Levy, Electrical transport properties of thin polycrystalline SnO₂ film sensors, *Sensors and Actuators B* **6-7**, 704-708 (1992).
- [123] K.H. Cha, H.C. Park, and K.H. Kim, Effect of palladium doping and film thickness on the H₂-gas sensing characteristics of SnO₂, *Sensors and Actuators B* **21**, 91-96 (1994).
- [124] M. Di Giulio, G. Micocci, R. Rella, P. Siciliano, and A. Tepore, Properties of reactively sputtered tin oxide films as CO gas sensors, *Sensors and Actuators B* **23**, 193-195 (1995).
- [125] A.E. Varfolomeev, A.L. Volkov, A.V. Eryshkin, V.V. Malyshev, A.S. Rasumov, and S.S. Yakimov, Detection of phosphine and arsine in air by sensors based on SnO₂ and ZnO, *Sensors and Actuators B* **7**, 727-729 (1992).
- [126] H. Nanto-H, T. Morita, H. Habara, K. Kondo, Y. Douguchi, and T. Minami, Doping effect of SnO₂ on gas sensing characteristics of sputtered ZnO thin film chemical sensor, *Sensors and Actuators B* **36**, 384-387 (1996).
- [127] J. Santos, P. Serrini, B. OBeirn, and L. Manes, A thin film SnO₂ gas sensor selective to ultra-low NO₂ concentrations in air, *Sensors and Actuators B* **43**, 154-160 (1997).
- [128] M.C. Horrillo, P. Serrini, J. Santos, and L. Manes, Influence of the deposition conditions of SnO₂ thin films by reactive sputtering on the

- sensitivity to urban pollutants, *Sensors and Actuators B* **45**, 193-198 (1997).
- [129] J. Mizsei, P. Sipila, and V. Lantto, Structural studies of sputtered noble metal catalysts on oxide surfaces, *Sensors and Actuators B* **47**, 139-144 (1998).
- [130] M. Egashira, Y. Shimizu, Y. Takao, and Y. Fukuyama, Hydrogen-sensitive breakdown voltage in the I-V characteristics of tin dioxide based Semiconductors, *Sensors and Actuators B* **33**, 89-95 (1996).
- [131] T. Brousse, and D.M. Schleich, Sprayed and thermally evaporated SnO₂ thin films for Ethanol sensors, *Sensors and Actuators B* **31**, 77-79 (1996).
- [132] R. Lalauze, P. Breuil, and C. Pijolat, Thin films for gas sensors, *Sensors and Actuators B* **3**, 175-182 (1991).
- [133] H. Torvela, C. Pijolat, and R. Lalauze, Dual response of tin dioxide gas sensors characteristic of gaseous carbon tetrachloride, *Sensors and Actuators B* **4**, 445-450 (1991).
- [134] V.M. Jimenez, A.R. Gonzalez-Elipe, J.P. Espinos, A. Justo, A. Fernandez, Synthesis of SnO and SnO₂ nanocrystalline powders by the gas phase condensation method, *Sensors and Actuators B* **31**, 29-32 (1996).
- [135] Y. Ionue, J. Matsuo, and K. Sato, Polarization effects of poled ferroelectric substrates upon surface conductivity changes in phthalocyanine and SnO₂ films following gas adsorption, *J. Chem. Soc. Faraday Trans.* **86**, 2611-2615 (1990).
- [136] R. Lalauze, and C. Pijolat, A new approach to selective detection of gas by an SnO₂ solid-state sensor, *Sensors and Actuators*, **5**, 55-63 (1984).
- [137] D. Kohl, and G. Heiland, Problems and possibilities of oxide and organic semiconductor gas sensors, *Sensors and Actuators* **8**, 227-233 (1985).
- [138] A. Lousa, S. Gimeno, and J. Martí, Preparation conditions of transparent and conductive SnO₂ thin films by reactive evaporation, *Vacuum* **45**(10), 1143-1145 (1994).
- [139] D. Nicolas, E. Souteyrand, and J.R. Martin, Gas sensor characterization through both contact potential difference and photopotential measurements, *Sensors and Actuators B* **44**, 507-511 (1997).
- [140] K.D. Schierbaum, U. Weimar, and W. Göpel, Comparison of ceramic, thick-film and thin-film chemical sensors based upon SnO₂, *Sensors and Actuators B* **7**, 709-716 (1992).
- [141] D.D. Lee, and W.Y. Chung, Gas-sensing characteristics of SnO_{2-x} thin film with added Pt fabricated by the dipping method, *Sensors and Actuators* **20**, 301-305 (1989).

- [142] S.P. Lee, Analysis of $\text{SnO}_{2-x}/\text{Pt}$ thin film for gas sensors, *Sensors and Actuators B* **13-14**, 504-505 (1993).
- [143] S.M. Rozati, S. Mirzapour, M.G. Takwale, B.R. Marathe, and V.G. Bhide, Effect of post-deposition heat-treatment on physical properties of tin oxide thin films prepared by an electron-beam evaporation technique, *J. Mater. Sci. Lett.* **12**, 949-951 (1993).
- [144] Y.K. Fang, and J.L. Lee, A tin oxide thin film sensor with high ethanol sensitivity, *Thin Solid Films* **169**, 51-56 (1989).
- [145] M.H.M. Reddy, S.R. Jawaleker, and A.N. Chandorkar, The effect of heat treatment on the structural properties of electron beam evaporated SnO_2 films, *Thin Solid Films* **169**, 117-126 (1989).
- [146] R. Banerjee, and D. Das, Properties of tin oxide films prepared by reactive electron beam evaporation, *Thin Solid Films* **149**, 291-301 (1987).
- [147] W.K. Choi, J.S. Cho, S.K. Song, Y.T. Kim, K.H. Yoon, H.J. Jung, and S.K. Koh, Preparation and characterization of tin oxide films by ion-assisted deposition, *Mat. Res. Soc. Symp. Proc.* **438**, 683-688 (1997).
- [148] W.K. Choi, H.J. Jung, and S.K. Koh, Chemical shifts and optical properties of tin oxide films grown by a reactive ion assisted deposition, *J. Vac. Sci. Technol. A* **14**(2), 359-366 (1996).
- [149] S.K. Song, W.K. Choi, J.S. Cho, H.J. Jung, D. Choi, J.Y. Lee, H.K. Baik, and S.K. Koh, Effect of oxygen ion energy and annealing in formation of tin oxide thin films, *Jap. J. Appl. Phys.* **36** (4A), 2281-2287 (1997).
- [150] W.K. Choi, S.K. Song, J.S., Cho, Y.S. Yoon, D. Choi, H.J. Jung, and S.K. Koh, H_2 gas-sensing characteristics of SnO_x sensors fabricated by a reactive ion-assisted deposition with/without an activator layer, *Sensors and Actuators B*. **40**, 21-27 (1997).
- [151] T. Aste, R. Botter, and D. Beruto, Double-layer granular SnO_2 sensors, *Sensors and Actuators B* **24-25**, 826-829 (1995).
- [152] G. Sberveglieri, S. Groppelli, and P. Nelli, Bismuth-doped tin oxide thin-film gas sensors, *Sensors and Actuators B* **3**, 183-189 (1991).
- [153] G. Sberveglieri, S. Groppelli, P. Nelli, and A. Camanzi, A new technique for the preparation of highly sensitive hydrogen sensors based on $\text{SnO}_2(\text{Bi}_2\text{O}_3)$ thin films, *Sensors and Actuators B* **5**, 253-255 (1991).
- [154] G. Sberveglieri, S. Groppelli, and P. Nelli, Highly sensitive and selective NO , and NO_2 sensor based on Cd-doped SnO_2 thin films, *Sensors and Actuators B* **4**, 457-461 (1991).
- [155] G. Sberveglieri, S. Groppelli, P. Nelli, and A. Camanzi, A new technique for the preparation of highly sensitive hydrogen sensors based on $\text{SnO}_2(\text{Bi}_2\text{O}_3)$ thin films, *Sensors and Actuators B* **5**, 253-255 (1991).

- [156] G. Sberveglieri, S. Gropelli, P. Nelli, C. Perego, G. Valdre, and A. Camanzi, Detection of sub-ppm H₂S concentrations by means of SnO₂(Pt) thin films, grown by the RGTO technique, *Sensors and Actuators B* **15-16**, 86-89 (1993).
- [157] V. Demarne, A. Grisel, A new SnO₂ low temperature deposition technique for integrated gas sensors, *Sensors and Actuators B* **15-16**, 63-67 (1993).
- [158] G. Sberveglieri, C. Perego, F. Parmigiani, G. Dinelli, and G. Quattroni, Sn_{1-x}Fe_xO_y: a new material with high carbon monoxide sensitivity, *Sensors and Actuators B* **20**, 163-167 (1994).
- [159] P. Bonzi, L.E. Depero, F. Parmigiani, C. Perego, G. Sberveglieri, and G. Quattroni, Formation and structure of tin-iron oxide thin film CO sensors, *J Mater Res* **9**, 1250-1256 (1994).
- [160] K.S. Yoo, N.W. Cho, H.S. Song, and H.J. Jung, Surface morphology and gas-sensing characteristics of SnO_{2-x} thin films oxidised from Sn films, *Sensors and Actuators B* **24-25**, 474-477 (1995).
- [161] T. Aste, D. Beruto, R. Botter, C. Ciccarelli, M. Giordani, and P. Pozzolini, Microstructural development during the oxidation process in SnO₂ thin films for gas sensors, *Sensors and Actuators B* **18-19**, 637-641 (1994).
- [162] G. Sberveglieri, S. Gropelli, P. Nelli, V. Lantto, H. Torvela, P. Romppainen, and S. Leppävuori, Response to nitric oxide of thin and thick SnO₂ films containing trivalent additives, *Sensors and Actuators B* **1**, 79-82 (1990).
- [163] G. Sberveglieri, G.P. Benussi, G. Coccoli, S. Gropelli, and P. Nelli, Reactively sputtered indium tin oxide polycrystalline thin films as NO and NO₂ gas sensors, *Thin Solid Films* **186**, 349-360 (1990).
- [164] G. Sberveglieri, Classical and novel techniques for the preparation of SnO₂ thin-film gas sensors, *Sensors and Actuators B* **6**, 239-247 (1992).
- [165] G. Sberveglieri, Recent developments in semiconducting thin-film gas sensors, *Sensors and Actuators B* **23**, 103-109 (1995).
- [166] P. Camagni, G. Faglia, P. Galinetto, C. Perego, S. Samoggia, G. Sberveglieri, Photosensitivity activation of SnO₂ thin film gas sensors at room temperature, *Sensors and Actuators B* **31**, 99-103 (1996).
- [167] W. Hellmich, Ch. Bosch-v. Braunmühl, G. Müller, G. Sberveglieri, M. Berti, and C. Perego, The kinetics of formation of gas-sensitive RGTO-SnO₂ films, *Thin Solid Films* **263**, 231-237 (1995).
- [168] A. Diéguez, A. Romano-Rodríguez, J.R. Morante, P. Nelli, L.E. Depero, L. Sangaletti, and G. Sberveglieri, Electron microscopy analysis of the RGTO technique for high sensitivity gas sensor development, *Inst. Phys. Conf. Ser.* **157**, 593-596 (1997).

- [169] G. Sberveglieri, G. Faglia, S. Gropelli, P. Nelli, and A. Camanzi, A new technique for growing large surface area SnO₂ thin film (RGTO technique), *Semicond. Sci. Technol.* **5**, 1231-1233 (1990).
- [170] H.E. Endres, W. Gottler, R. Hartinger, S. Drost, W. Hellmich, G. Muller, C. Bosch von Braunmuhl, A. Krenkow, C. Perego, and G. Sberveglieri, A thin-film SnO₂ sensor system for simultaneous detection of CO and NO₂ with neural signal evaluation, *Sensors and Actuators B* **36**, 353-357 (1996).
- [171] W. Hellmich, G. Muller, C. Bosch von Braunmuhl, T. Doll, and I. Eisele, Field-effect-induced gas sensitivity changes in metal oxides, *Sensors and Actuators B* **43**, 132-139 (1997).
- [172] B. Strickland, and C. Roland, Low-temperature growth and ion-assisted deposition, *Phys. Rev. B* **51**(8), 5061-5064 (1995).
- [173] J.S. Colligon, H. Kheyrandish, G. Carter, and M.C. Simmonds, The modification of alloys by low energy ion-assisted deposition, *Vacuum* **46**(8-10), 919-922 (1995).
- [174] S. Tamulevicius, and L. Pranevicius, Ion-beam-activated processes on the surface of solids, *Surface and Coatings Technology* **71**, 239-249 (1995).
- [175] Brite-Euram III: 12 Monthly Progress Report (NG-2-96), *Functional Nano-Scaled Materials for Long-Term Stable Gas Sensors (BE2-7303)*, (1997).
- [176] A. Diéguez, A. Romano-Rodríguez, J.R. Morante, U. Weimar, M. Schweizer-Berberich, and W. Göpel, Morphological analysis of nanocrystalline SnO₂ for gas sensor applications, *Sensors and Actuators B* **31**, 1-8 (1996).
- [177] A. Jain, A physical basis for stress reduction during ion beam assisted deposition, *Scripta Metallurgica et Materialia* **32**(4), 589-593 (1995).
- [178] R.P. Reade, S.R. Church, and R.E. Russo, Ion-assisted pulsed-laser deposition, *Rev. Sci. Instrum.* **66**(6), 3610-3614 (1996).
- [179] J.M. Bosc, Motorola Gas Sensor Qualification Overview, Motorola Device Data / Handbook, 4th ed., USA, 1.19-1.35 (1997).
- [180] T. Lee, V. Sarinan, R. Sharma, A. Peyre-Lavigne, *Am. Soc. Mech. Eng.* (11/1997).
- [181] V. Demarne, P. Lacombe, A. Grisel, *Proc. Int. Meet. on Chem. Sens. 5*, Rome, 1070 (1994).
- [182] G. Faglia, P. Nelli, and G. Sberveglieri, Frequency effect of highly sensitive NO₂ sensors based on RGTO SnO₂(Al) thin films, *Sensors and Actuators B* **18**, 497-499 (1994).
- [183] Brite-Euram III: Final technical report, *Functional Nano-Scaled Materials for Long-Term Stable Gas Sensors (BE2-7303)*, (1997).

- [184] NIH Image program (developed at the U.S. National Institutes of Health and available on the internet at <http://rsb.info.nih.gov/nih-image/>).
- [185] S. Cueille, and C. Sire, Droplet nucleation and Smoluchowski's equation with growth and injection of particles, *Phys. Rev. E* **57**(1), 881-901 (1998).
- [186] F. Family, and P. Meakin, Scaling of the droplet-size distribution in vapor-deposited thin films, *Phys. Rev. Lett.* **61**(4), 428431 (1988).
- [187] F. Family, and P. Meakin, Kinetics of droplet growth processes: Simulations, theory and experiments, *Phys. Rev. A* **40**(7), 3836-3854 (1989).
- [188] P. Meakin, Droplet deposition growth and coalescence, *Rep. Prog. Phys.* **55**, 157-240 (1992).
- [189] D. Beysens, and C.M. Knobler, Growth of breath figures, *Phys. Rev. Lett.* **57**(12), 1433-1436 (1986).
- [190] E. Sondergard, R. Kofman, P. Cheyssac, and A. Stella, Production of nanostructures by self-organization of liquid Volmer-Weber films, *Surf. Sci.* **364**, 467-476 (1996).
- [191] L. Haderbache, R. Garrigos, R. Kofman, E. Sondergard, and P. Chyssac, Numerical and experimental investigations of the size ordering of nanocrystals, *Surf. Sci.* **410**, L748-L756 (1998).
- [192] M. Zinke-Allmang, L.C. Feldman, and W. Van Saarloos, Experimental study of self-similarity in the coalescence growth regime, *Phys. Rev. Lett.* **68**(15), 2358-2361 (1992).
- [193] T.D. Lowes, and M. Zinke-Allmang, Cluster shape cycles during self-similar cluster growth, *Phys. Rev. B* **49**(23), 16678-16683 (1994).
- [194] L.J. Lewis, P. Jensen, and J.L. Barrat, Melting, freezing, and coalescence of gold nanoclusters, *Phys. Rev. B* **56**, 2248-2257 (1997).
- [195] C. Bréchnignac, Ph. Cahuzac, F. Carlier, M. de Frutos, and A. Masson, Size effects in nucleation and growth processes from preformed soft-landed clusters, *Phys. Rev. B* **57**, R2084-R2087 (1998).
- [196] J. Geurts, S. Rau, W. Richter, and F.J. Schmitte, SnO films and their oxidation to SnO₂: Raman scattering, IR reflectivity and X-ray diffraction studies, *Thin Solid Films* **121**, 217-225 (1984).
- [197] L. Sangaletti, L.E. Depero, B. Allieri, F. Pioselli, E. Comini, G. Sberveglieri, and M. Zocchi, Oxidation of Sn thin films to SnO₂, MicroRaman mapping and X-ray diffraction studies, *J. Mat. Res.* **13**, 2457-2460 (1998).
- [198] M.S. Moreno, A. Varela, and L.C. Otero-Díaz, Cation nonstoichiometry in tin-monoxide-phase Sn_{1-x}O with tweed microstructure, *Phys. Rev. B* **56**, 5186-5192 (1997).
- [199] N. Bârsan, Private communication.

- [200] L. Sangaletti, L.E. Depero, A. Diéguez, G. Marca, A. Romano-Rodríguez, J.R. Morante, and G. Sberveglieri, Microstructure and morphology of tin dioxide multilayer thin film gas sensors, *Sensors and Actuators B* **44**, 268-274 (1997).
- [201] L.E. Depero, A. Diéguez, J.R. Morante, C. Perego, A. Romano, L. Sangaletti, and G. Sberveglieri, Proceedings of the 10th conference on solid-state transducers, vol 2, p 409-412, September 8-11, 1996. Leuven, Belgium. Edited by Robert Puers.

CHAPTER 5

CONCLUSIONS



The fundamental properties of SnO₂ nanoparticles have been investigated by a wide set of structural characterisation techniques, including Transmission Electron microscopy, X-ray diffraction, Raman, Fourier Transform infrared, and X-ray photoelectron spectroscopies. The combined use of the different techniques has allowed a better understanding of the structural and vibrational properties of the material, as well as the development of a working methodology to analyse nanoparticle properties.

The analysis of the complete Raman spectrum of SnO₂ nanoparticles, has allowed to develop new non-destructive methodologies to extract an approximate value of the average grain size of SnO₂ powders. It has been developed a new procedure through which, based on the investigation of the Low-Frequency region of the spectrum, the complete nanoparticle size distribution can be obtained accurately. The successful application of this technique to nanoparticle size distribution in SnO₂ powders gives good promises for non-destructive characterisation of nanoparticle size distribution in gas sensors constituted by nanoparticles of very small size (~7nm for SnO₂). Other existing methods for nanoparticle size determination through the analysis of the Raman spectrum, such as the spatial correlation model, have been found to be applicable also in the case of SnO₂, at least for nanoparticle size larger than 8-10nm.

About stability of SnO₂ obtained by wet chemical methods, it is concluded that nanoparticles have to be calcinated at temperatures able to allow the desorption of water and hydroxyl groups. Associated to such desorption, it has been observed that faceting and reorganisation of the material takes place, giving rise to more stable particles. Simultaneously, a higher growth rate is observed. Hence, SnO₂ nanoparticles have to be calcinated at temperatures higher than 430-450°C. Moreover, for high sensitivity to NO₂ and low cross sensitivity to CO at low temperatures, particles have to be pure and calcinated at 1000°C. The better sensitivity of these nanoparticles has been attributed to the better state of their surface. On the other hand, the introduction of the metal additives Pt and Pd, facilitates oxygen adsorption and increases the sensitivity to CO. The additives are located mainly at the surface of the SnO₂ nanoparticles and are in oxidised state, as corresponds to the low loading performed. Their effect is to act as electronic sensitisers by creating centres in the band gap at the surface of the nanoparticles.

In addition to the typically treatments applied to improve the characteristics of SnO₂ based semiconductor gas sensors, such as calcination and noble metal addition,

grinding has been found to deeply influence the structural properties of the nanoparticles as well as their sensing capabilities. Grinding treatments have been found to be effective in reducing grain size even in a ~30%. When grinding is performed in large particles, reduction of grain size occurs via their breaking. As a consequence the nanoparticle size distribution can result broader. On the other hand, grinding of very small and hydrated particles, makes the ground powder to be more agglomerated. In such agglomerates, the desorption of water and hydroxyl groups is hindered, thus being limited atom migration and, thus, the processes for grain growth.

Nevertheless, improvement of the sensor characteristics have been found not to be directly related to the decrease of grain size, but to the modification of the SnO₂ surface. Although grinding depends on the procedure, combined grinding for 2 hours before and after calcination has been observed to give the better sensitivity results (to NO₂) in this work. The improvement of sensitivity to NO₂ and the lowering of sensitivity to CO has been attributed to the appearance of acceptor levels in the band gap, which make easy the adsorption of NO₂, so decreasing the places at the surface for oxygen adsorption and, hence, the sensitivity to CO.

Two current technologies for the fabrication of SnO₂ thin film gas sensors have been investigated, namely the Ion Beam Assisted Deposition of SnO₂ and the Reothaxial Growth and Thermal Oxidation of tin. A characterisation of the effects of deposition rate on the morphological properties of IBAD sensors has shown strong problems in the film structure associated to the parameters of deposition, like the presence of voids and stratified growth. However, it has been possible to reduce such problems by heating of the substrate during deposition.

A detailed investigation of the deposition of tin and of its thermal oxidation have been performed in RGTO. The deposition of tin, under conditions through which Sn remains liquid at the substrate surface, makes appear droplets of Sn of variable sizes. The size dispersion of such hemispheres, as well as the average size, have been found to increase with the quantity of deposited material. As the size of the Sn droplets is much larger than the nominal thickness expected if a planar film would develop, it is mandatory the recalculation of the oxidation times in order to obtain a complete oxidation. Moreover, the obtained morphology imposes a severe difficulty to oxidise completely and homogeneously the tin layer when short oxidation times are used, thus creating a lack of stability of the sensor response. The best solution proposed to solve this problem is to deposit smaller hemispheres on the substrate and repeat the procedure once oxidised, i.e., perform a multilayer procedure.

It has been found that the degree of oxidation deeply influences the stability characteristics of thermally oxidised SnO₂ films. The oxidation has been found to begin at the surface of the deposited Sn and proceed independently of the temperature of deposition of tin. The thermal oxidation of tin passes through mainly the intermediate formation of SnO before the obtaining of the final SnO₂. From the analysis of the first steps of the oxidation, the parameters reported in the literature for the diffusion of oxygen in tin have been improved, being $D_0=1.5 \cdot 10^5 \text{cm}^2 \text{s}^{-1}$ and $E_a=1.3 \text{eV}$. By using the thermal cycle of this work to oxidise tin, the particles forming the SnO₂ layer are of good crystalline quality and faceted, which ensures a good stability of the sensor, if the film is completely oxidised.

ANNEXES

ANNEX A: JPDS CARDS

JPDS cards are in general used as a standard for identification of phases by X-ray diffraction. Nevertheless, it has to be noted that *JPDS* cards are a standard only for the geometry used to obtain them. Thus, for example, in the INEL diffractometer used in this work, measurements were done by transmission (Debye-Scherrer), while in the SIEMENS diffractometer measurements are done by reflection (Bragg-Brentano). So, the intensities of the peaks appearing in one and other diffractometer are not comparable because in the first case there is absorption, between other factors. So, it has to be taken into account that relative intensities depend on configuration used for the measurement, the lines used as radiation and so on. So, the best is to make a reference profile of the same material which is going to be analysed (use a pattern).

The *JPDS* cards related to Sn and their oxides are presented below.

ANNEX A: JPDS CARDS

4- 673 JCPDS-ICDD Copyright (c) 1995 PDF-2 Sets 1-45 database Rad.= 1.54060 Quality: 1

		2-theta	Int.	h k l		
Sn						
		30.645	100	2	0	0
	Tin	32.019	90	1	0	1
		43.872	34	2	2	0
	Tin, syn	44.903	74	2	1	1
		55.332	17	3	0	1
Rad: CuK α Lambda: 1.54056 Filter: Ni d-sp:						
Cutoff: Int: Diffractometer I/Inc: 1.966						
Ref: Swanson, Tatge, Natl. Bur. Stand. (U.S.), Circ. 539, 1 24 (1953)						
		62.560	23	1	1	2
		63.783	13	4	0	0
		64.578	20	3	2	1
		72.416	15	4	2	0
		75.196	15	4	1	1
Sys: Tetragonal S.G.: I41/amd (141)						
	a: 3.831	b:	c: 3.182	A:	C: .5457	
	A:	B:	C:	Z: 4	mp: 231.9 deg.	
Ref: ibid.						
	D ₁ : 7.29	D ₂ :	SS/FDH: F29=70(.013,33)			
	ea:	nwb:	ey:	Sign:	2V:	
	Ref:					
		97.418	5	5	2	1
		103.275	5	2	1	3
		104.868	2	6	0	0
		111.663	3	3	0	3
		112.101	13	5	1	2
Color: Light gray metallic						
Pattern taken at 26 C. Sample was furnished by Johnson Matthey Company, Ltd.						
and annealed 12 hours at 160 C. CAS no.: 7440-31-5. Analysis (wt.%): Pb						
0.0012, Sb 0.001, Fe 0.00027, Cu 0.0002, As 0.0002, Bi 0.00012, S 0.0003, Sn						
99.997 (by difference), other form alpha-Sn (cubic). Space group given by						
Mark, Polanyi, I. Phys., 18 75-96 (1925). Color from Dana's						
System of Mineralogy, 7th Ed., 485. Sn type. PSC: t14. Mat: 118.69.						
Volume[CD]: 108.19.						

2-theta	Int.	h k l	2-theta	Int.	h k l	2-theta	Int.	h k l
130.976	10	5 3 2						
133.431	4	6 3 1						
144.590	6	6 4 0						
145.859	3	7 0 1						

Strong lines: 2.92/1 2.79/9 2.02/7 2.06/3 1.48/2 1.44/2 1.21/2 1.66/2

ANNEX A: JPDS CARDS

21-1250 DELETED JCPDS-ICDD Copyright (c) 1995 PDF-2 Sets 1-45 database Rad.# 1.54060 Quality: i

				2-theta	Int.	h k l		
SnO ₂				26.579	100	1	1	0
Tin Oxide				33.876	81	1	0	1
Cassiterite, syn				37.930	24	2	0	0
				38.976	5	1	1	1
				42.612	2	2	1	0
Rad: CuKα	Lambda: 1.54056	Filter: Ni	d-spr	51.753	63	2	1	1
Cutoff:	Int: Diffractometer	I/ICor:		54.759	17	2	2	0
Ref: Swanson, Tatge, Matl. Bur. Stand. (U.S.), Circ. 539, 1 54 (1955)				57.835	8	0	0	2
				61.891	15	3	1	0
				64.729	17	1	1	2
Sys: Tetragonal	S.G.: P42/mnm (136)							
a: 4.738	b:	c: 3.188		65.965	15	3	0	1
β:	β:	α:	α:	71.278	7	2	0	2
Ref: ibid.		2:	2:	76.690	11	3	2	1
				81.172	3	4	0	0
ax: 6.99	bx: 7.02	GS/FOM: F30=20(.031,49)		83.661	8	2	2	2
wa:	nw: 2.006	ey: 2.0772	Sign: + 2V:	87.199	3	3	3	0
Ref: Winchell, A., Winchell, H., Microscopic Character of Artificial Inorg. Solid Sub., 62 (1964)				89.724	8	3	1	2
				90.891	8	4	1	1
				93.335	3	4	2	0
				96.066	4	1	0	3
Color: White	Sample from Johnson, Matthey Co., Ltd. Their spectroscopic analysis showed no impurities greater than faint trace. X-ray pattern taken at 26 C. Optical data on specimen from Dana's System of Mineralogy, 7th Ed., 1 535.			108.273	8	4	0	2
	Opaque mineral optical data on specimen from Nwirasando mine, Uganda, RSM=11.5-12.4, Disp.=Std., VHM100=1168-1332, Ref.: IMA Commission on Ure Microscopy 00F. 02Ti type. Rutile group, rutile subgroup. Also called: tin stone. Also called: wood tin. PSC: tP6. To replace 1-637. Deleted by 41-1445, lower Fn, Bayliss, 8/90. Net: 150.69. Volume(CB): 71.57.			112.009	3	5	1	0
				114.811	3	3	3	2
				116.045	8	4	3	1
				121.725	7	3	0	3

2-theta	Int.	h k l	2-theta	Int.	h k l	2-theta	Int.	h k l
121.842	6		147.380	6	5 1 2			
130.563	6	5 2 1						
133.782	1	4 4 0						
137.641	4	3 2 3						
142.905	2	5 3 0						

Strong lines: 3.35/1 2.64/8 1.77/6 2.37/2 1.68/2 1.44/2 1.42/2 1.50/1

ANNEX A: JPDS CARDS

6- 393 JCPDS-ICDD Copyright (c) 1995 PDF-2 Sets 1-45 database Rad.= 1.54060 Quality: i

SnO		2-theta	Int.	h k l
Tin Oxide		18.277	10	0 0 1
Rhombohite, syn		29.869	100	1 0 1
		33.395	33	1 1 0
		37.153	14	0 0 2
		44.393	<1	1 0 2
Radi: CuKα Lambda: 1.5405 Filter: Ni d-sp:		47.808	14	2 0 0
Cutoff: Int: Diffractometer I/Icor:		50.765	25	1 1 2
Ref: Swanson et al., Natl. Bur. Stand. (U.S.), Circ. 539, 4 28 (1955)		57.402	25	2 1 1
		62.075	12	2 0 2
		62.540	12	1 0 3
Sys: Tetragonal S.G.: P4/nmm (129)		67.750	4	1 1 3
a: 3.802 b: c: 4.836 A: C: 1.2720		69.939	6	2 2 0
Ref: Ibid.		77.926	4	3 0 1
Dz: 6.40 Dz: SS/FDH: F30=36(.019,45)		79.157	4	0 0 4
w: 2.0 mB: ey: Sign: 2V:		79.710	4	3 1 0
Ref: Organ, Mandarino, Can. Mineral., 10 916 (1971)		81.952	6	2 2 2
		82.376	8	2 1 3
		85.928	2	1 0 4
Color: Black		88.633	4	1 1 4
Pattern taken at 26 C. Sample from Baker Chemical Company. Spectroscopic analysis: (0.01% Ca, Cu, Fe, Mg, Sb, Si; (0.001% Al, Ba, Ni, Pb. OPb type. Litharge group. PSC: tP4. Mwt: 134.69. Volume(CD): 69.91.		91.367	6	3 1 2
		96.774	4	3 2 1
		98.072	4	2 0 4
		101.249	2	3 0 3
		102.865	2	2 1 4
		105.548	<1	0 0 5

2-theta	Int.	h k l	2-theta	Int.	h k l	2-theta	Int.	h k l
108.240	4	4 0 0	129.293	4	3 1 4	148.576	2	4 1 3
110.572	4	1 0 5	129.894	4	4 2 0			
116.553	4	4 1 1	132.833	6	2 1 5			
117.970	4	2 2 4	145.674	2	0 0 6			
121.609	6	3 2 3	147.674	<1	4 2 2			

Strong lines: 2.99/1 2.69/4 1.80/3 1.60/3 2.42/1 1.99/1 1.49/1 1.48/1

ANNEX A: JPDS CARDS

25-1259 JCPDS-ICDD Copyright (c) 1995 PDF-2 Sets 1-45 database Rad.= 1.54060 Quality:

SnO	SnO:SnO	2-theta	Int.	h k l
2 3	2	10.781	12	0 1 0
Tin Oxide		16.161	41	1 0 0
		21.765	3	0 2 0
		23.967	12	0 0 1
		25.603	6	0 -1 1
Rad: Cu	Lambda: 2.28970	Filter: V	d-spt	
Culoff: Int: Diffractometer	I/Icor:			
Ref: Hurken, Trozel, Z. Anorg. Allg. Chem., 397 117 (1973)		26.998	100	0 1 1
		29.555	41	1 0 1
		31.601	50	0 -2 1
		32.256	25	1 1 1
		32.965	30	0 3 0
Sys: Triclinic	S.S.: Pk			
a: 5.457	b: 8.179	c: 3.714	a: 0.6672	C: 0.4541
A: 93.8	B: 92.3	C: 90.00	Z: 2	ap:
Ref: Ibid.				
Dx: 5.735	Dy: 5.900	SS/FOM: F30=3(.145,77)		
pa:	nb:	ey:	Sign:	ZV:
Ref:				
		42.257	1	-2 1 1
		43.760	1	2 1 1
		44.393	41	0 4 0
		45.163	41	-1 3 1
		47.072	41	-2 3 0
Formed by decomposition of SnO above 300 C. PSC: aP10. To replace 18-1386.				
Mt: 285.38. Volume[CD]: 165.27.				
		48.294	1	2 2 1
		47.212	2	0 0 2
		49.816	14	0 -1 2
		50.315	18	3 0 0
		51.192	4	0 1 2

2-theta	Int.	h k l	2-theta	Int.	h k l	2-theta	Int.	h k l
51.502	16	3 1 0	56.291	1	-3 -1 1	60.678	1	-3 2 1
52.455	25	0 4 1	58.601	2	0 -3 2			
55.078	6	2 -3 1	59.096	1	1 5 0			
55.785	3	-2 3 1	59.472	41	-3 -2 1			
55.697	12	1 4 1	59.769	4	-2 -1 2			

Strong lines: 3.50/1 2.83/5 2.72/3 2.77/3 1.74/3 2.45/2 2.43/2 1.81/2

ANNEX A: JPDS CARDS

16-737 JCPDS-ICDD Copyright (c) 1995 PDF-2 Sets 1-45 database Rad.= 1.54060 Duality:

				2-theta	Int.	h k l
Sn O						
3 4						
Tin Oxide				10.820	5	
				24.099	30	
				25.879	5	
				27.081	100	
				31.727	80	
Rad: CuK α	Lambda: 1.5405	Filter: Mono.	d-spi			
Cutoff:	Int: Visual	l/lcorr:		32.316	50	
Ref: Gauzzi, Ann. Chim. (Rome), 53 1503 (1963)				33.015	50	
				37.073	40	
				40.284	30	
				49.355	5	
Sys:	S.G.:					
a:	b:	c:	a:			
A:	B:	C:	Z:	50.020	40	
Ref:				50.494	40	
				51.690	30	
				52.683	30	
				52.847	5	
ax:	axB:	ay:	Sign:	53.245	10	
Ref:				55.081	40	
				58.075	5	
				58.765	5	
Wt: 420.07.				59.983	10	
				60.943	40	
				63.541	30	
				65.475	10	
				66.388	5	
				67.253	10	

2-theta	Int.	h k l	2-theta	Int.	h k l	2-theta	Int.	h k l
67.917	5		80.030	5				
68.173	5		80.678	30				
77.775	5							
78.690	5							
79.079	5							

Strong lines: 3.29/1 2.82/8 2.77/5 2.71/5 2.42/4 1.82/4 1.81/4 1.64/4

ANNEX A: JPDS CARDS

20-1293 JCPDS-ICDD Copyright (c) 1995 PDF-2 Sets 1-45 database Rad.= 1.54060 Quality:

Sn 0 3 4	2-theta	Int.	h k l
Tin Oxide	16.920	15	0 0 1
	18.315	30	1 0 0
	21.765	5	0 0 2
	26.998	25	1 1 1
	30.634	35	0 2 0
Rad: Lambda: Filter: d-sp:	31.624	15	0 -2 1
Cutoff: Int: Visual I/Icons:	32.019	30	-1 1 2
Ref: Lawson, Nature (London), 215 955 (1967)	32.197	5	0 0 3
Sys: triclinic S.G.: P1	32.890	100	1 1 2
a: 4.86 b: 5.88 c: 8.20 A: I: 2.16 C: sp:	33.883	50	
A: 93.00 B: 93.35 C: 91.00 I: 2.16 sp:			
Ref: Ibid.			
Dx: 6.451 Dx: SS/FOM: F9=4(.088,26)			
ea: mWB: ey: Sign: ZV:			
Ref:			
C.D. Cell: a=5.880, b=8.200, c=4.860, alpha=93.35, beta=91.00, gamma=93.00; a/b=0.7171, c/b=0.5927, S.G.=P1, -1. PSC: aP15.12. Mwt: 420.07. Volume[CB]: 253.56.			

Strong lines: 2.72/1 2.65/5 2.92/4 4.84/3 2.79/3 3.30/3 6.17/2 2.85/2



UNIVERSITAT DE BARCELONA



UNIVERSITAT DE BARCELONA

Departament d'Electrònica

CARACTERIZACIÓN ESTRUCTURAL PARA LA
OPTIMIZACIÓN DE SENSORES DE GAS
BASADOS EN SnO₂
(RESUMEN)

Tesis doctoral

Resumen en Castellano de la Memoria presentada por
Angel Diéguez Barrientos
para optar al grado de Doctor en Física

Directores: Prof. Joan Ramón Morante i Leonart
Dr. Albert Romano Rodríguez

Barcelona, Julio de 1999

PRÓLOGO

La tecnología actual de sensores de gases cubre los requisitos mínimos exigidos por el mercado en la mayoría de los casos. Sin embargo, presenta todavía ciertas limitaciones. Por lo tanto no es extraño que actualmente exista una amplia investigación en múltiples laboratorios de todo el mundo dirigida a la optimización de tales dispositivos. Hasta no hace muchos años, esta investigación sobre sensores de gas y catalizadores se realizaba empíricamente mediante métodos de ensayo y error. Actualmente, sin embargo, la investigación sistemática es cada vez más importante en la mejora de los sensores y a la hora de desarrollar nuevos principios. Así, la obtención de sensores de gas estables, con alta sensibilidad, estabilidad y bajo coste de producción en masa pasa a través de la investigación básica y por lo tanto a través de la caracterización estructural de materiales para construir nuevos dispositivos sensores o para mejorar los existentes. Con tal propósito se ha fundado en la CEE un programa en sensores de gas semiconductores bajo proyectos BRITE/EURAM, enfocado a desarrollar un amplio rango de sensores producidos mediante tecnologías de capa gruesa y capa delgada para la detección de gases inflamables y/o tóxicos. Las ventajas de tal programa incluyen la interacción entre universidades y fabricantes de sensores y ha sido el promotor básico de toda la investigación presentada en este trabajo.

El resumen de la memoria se ha estructurado como sigue. En el *Capítulo 1* resumido se presentan las aplicaciones fundamentales de los sensores de gas basados en óxido de estaño. A continuación se hace un breve resumen acerca de los principales métodos de obtención y de los principios de su funcionamiento. Finalmente se explica la forma mediante la cual pueden mejorarse sus características.

En el *Capítulo 2* se indican las técnicas de caracterización estructural usadas para el desarrollo del trabajo. No se incluye en el resumen de la memoria un resumen del *Capítulo 2* de la tesis, consistente en una explicación detallada del conjunto de técnicas de caracterización estructural, ya que está dedicado a nuevos usuarios y no es estrictamente necesario para entender el resto del trabajo.

Los *Capítulos 3* y *4* contienen todo el trabajo experimental realizado, así como las discusiones y conclusiones a las que se ha llegado. El *Capítulo 3* ha sido dedicado a los sensores de gas basados en SnO_2 fabricados en capa gruesa. La parte introductoria acerca de la fabricación de este tipo de sensores se ha trasladado en forma muy resumida al *Capítulo 1*. Así, en este *Capítulo 3* resumido se presentan únicamente los resultados del estudio. Desde el punto de vista de investigación fundamental de las propiedades del material, se presentan las características especiales de los espectros de infrarojo y Raman al tratar con nanopartículas de SnO_2 . Desde el punto de vista de la optimización del material sensor y por lo tanto del sensor, se incluye en este *Capítulo* el análisis realizado para la mejora del material mediante las aproximaciones comúnmente usadas en la mayoría de laboratorios, esto es, mediante tratamientos térmicos y mediante la introducción de

los aditivos metálicos Pt y Pd. Como método innovador para la mejora de este tipo de sensores se estudia el procedimiento de 'molido' del material precursor (o sea, del polvo de óxido de estaño).

El *Capítulo 4* ha sido dedicado por completo al estudio de sensores de gas basados en SnO₂ en capa delgada. Al igual que en el *Capítulo 3*, se ha trasladado la parte introductoria acerca de los métodos de fabricación al *Capítulo 1*, dejando para este *Capítulo 4* resumido únicamente los resultados experimentales. Se han analizado dos técnicas actuales de crecimiento: el depósito asistido con iones y la oxidación térmica del Sn tras depósito mediante pulverización catódica. Sin embargo, se ha profundizado considerablemente más en la segunda técnica, de la cual se realiza un estudio detallado del depósito del Sn y de su posterior oxidación.

En *Capítulo 5* se resumen las conclusiones principales del trabajo.

ÍNDICE

1. Introducción: Sensores de gas basados en SnO₂. Principios de funcionamiento.

1.1	Importancia de los sensores de gases.....	1
1.2	Fabricación de sensores de gas basados en SnO ₂	2
1.3	Principio de funcionamiento de los sensores de gas semiconductores (de SnO ₂).....	3
1.4	Posibilidades hacia la optimización en la detección.....	5
1.4.1	Optimización del material sensible: microestructura.....	5
1.4.2	Optimización del material sensible: introducción de aditivos.....	6
1.4.3	Optimización del sistema de detección.....	7

2. Técnicas de caracterización estructural.....9

3. Propiedades de nanopartículas de SnO₂. Sensores en capa gruesa.

3.1	Evolución general en función de la temperatura de calcinación.....	11
3.2	Modificación de la respuesta del sensor con tratamientos térmicos y aditivos. Introducción de Pt y Pd.....	15
3.3	Optimización de las características del sensor mediante molido del polvo de SnO ₂	18

4. Sensores en capa delgada. Oxidación del Sn

4.1	Optimización del SnO ₂ obtenido por IBAD.....	21
4.2	Estudio del depósito y oxidación del Sn: RGTO.....	23
4.2.1	Depósito del Sn por pulverización catódica.....	23
4.2.2	Oxidación térmica del Sn.....	25
4.2.3	Influencia de una incompleta oxidación en la estabilidad.....	28
4.2.4	El método RGTO multicapa.....	28

5. Conclusiones

CAPÍTULO 1

INTRODUCCIÓN:

SENSORES DE GAS BASADOS EN SnO₂.
PRINCIPIOS DE FUNCIONAMIENTO.

1.1 Importancia de los sensores de gases

El interés actual en sensores de gas está enfocado hacia dos ramas diferentes: su propio desarrollo y mejora, y la realización de sistemas y microsistemas en los cuales se combinan uno o varios sensores y la electrónica necesaria para su control y el acondicionamiento y en ocasiones tratamiento de la señal (sensores inteligentes). La existencia de tales sensores y sistemas aporta beneficios importantes para todos, desde el punto de vista de sus aplicaciones, entre otras, en:

- La conservación del medio ambiente, mediante la monitorización y control de las emisiones a la atmósfera, disminuyendo por ejemplo el efecto invernadero y la afluencia de enfermedades respiratorias.

- La mejora de la seguridad en el hogar, mediante detectores de gases inflamables y/o tóxicos.

- Ahorro energético, ya que permiten controlar la eficiencia de procesos como combustiones.

- Narices electrónicas. Dichos dispositivos, consistentes en uno o varios sensores de gas, permiten, mediante las convenientes técnicas de reconocimiento de olores, la identificación de volátiles presentes en una mezcla. Sus aplicaciones son ilimitadas, siendo actualmente la más importante el control de procesos de fermentación y calidad de la comida. Otras aplicaciones son la identificación de residuos y la diagnosis de ciertas enfermedades mediante el olor corporal.

Dado que las aplicaciones de los sensores de gas crecen continuamente y que cada vez se les exige un mayor perfeccionamiento para cumplir las legislaciones vigentes y las exigencias del mercado, para que un sensor de gas sea funcional es necesario que cumpla la mayoría de las siguientes condiciones:

- Alta sensibilidad
- Alta selectividad
- Alta estabilidad
- Poca dependencia con la humedad y la temperatura
- Buena reproducibilidad y fiabilidad
- Respuesta rápida
- Robustez
- Facilidad de calibración
- Dimensiones pequeñas (ser portátil)

Sin embargo, la mayoría de los sensores de gas de reducidas dimensiones (se excluyen por lo tanto los cromatógrafos de gases, entre otros), no presentan alguna o varias de las anteriores condiciones, siendo el mayor problema en el caso de los sensores basados en óxido de estaño la baja estabilidad, la alta dependencia con la humedad y temperatura y la baja selectividad, pues responden en gran medida

a numerosos gases. Por otra parte, su bajo precio los ha hecho los dispositivos predominantes en el mercado.

Algunos de estos problemas, como por ejemplo la selectividad, pueden mejorarse con el uso de varios sensores y la electrónica adecuada (no es necesario llegar a una nariz electrónica, que es un sistema específico y complejo). Sin embargo, el mejor camino para la mejora de las cualidades de los sensores de gas, así como para la mayoría de dispositivos, aunque no el más sencillo en la mayoría de los casos, es la caracterización conjunta estructural y eléctrica.

1.2 Fabricación de sensores de gas basados en SnO₂

Los métodos de fabricación de sensores de gas basados en óxido de estaño se pueden separar en dos grandes grupos en atención a la estructura final de la capa sensible (SnO₂). Así, se dividen usualmente en sensores en capa gruesa y sensores en capa delgada. Los primeros se caracterizan por presentar una estructura rugosa, mientras que los segundos por ser una capa densa formada por pequeños granos del material. Dado que el fenómeno de detección de gases está íntimamente relacionado con la superficie del material, no se usan monocristales a tal efecto, sino policristales.

Es de remarcar que los sensores en capa delgada también pueden presentar una estructura rugosa (por ejemplo los realizados mediante pulverización catódica de Sn y posterior oxidación o RGTO). De hecho, cuando la estructura de la capa es densa y no rugosa el sensor no debería catalogarse como resistivo o conductométrico, sino más bien como de efecto de campo.

Uno de los métodos de obtención de un sensor en capa gruesa más utilizados consiste en fabricar un polvo de SnO₂, el cual posteriormente se mezcla con un componente orgánico para formar una pasta. Esta pasta es pintada o impresa (*painting* o *printing*) sobre un sustrato que es térmica y eléctricamente aislante, en el cual previamente se han depositado los electrodos y el calefactor. En ocasiones en vez de pintar la pasta sobre el sustrato, es éste el que se moja en la pasta (*dipping*). Los electrodos son necesarios para la medición de la resistencia del sensor, y el calefactor para calentar el sensor y así facilitar ciertas reacciones o limpiar la superficie del sensor de ciertos componentes. El proceso más complicado en la fabricación del sensor mediante la metodología descrita es la fabricación del material activo, esto es, el polvo de SnO₂. En muchos casos se usa la técnica química de sol-gel, la cual permite obtener SnO₂ de gran pureza. Otro de los métodos más comunes para la obtención de un polvo de SnO₂ es la pulverización pirolítica (*spray pyrolysis*).

En el caso de los sensores en capa delgada, el óxido de estaño se 'crece' o deposita directamente sobre el sustrato. Los métodos de obtención se dividen generalmente en químicos y físicos. Las técnicas químicas más usuales son el depósito químico en fase vapor y pulverización pirolítica (*spray pyrolysis*). Las

físicas son la evaporación térmica o mediante electrones de SnO_2 , y la pulverización catódica (*sputtering*) en sus varias versiones (r.f., reactiva, ...) de SnO_2 . Es importante comentar que los problemas más importantes encontrados en los diferentes casos son la contaminación por alguno de los componentes de los compuestos reaccionantes (como Cl) en los métodos químicos, y la pobre estequiometría en el caso de los métodos físicos comentados.

1.3 Principio de funcionamiento de los sensores de gas semiconductores (de SnO_2)

Los sensores de gas semiconductores, incluyendo los que tienen como material activo el SnO_2 , basan su funcionamiento en un cambio de la resistencia del sensor cuando éste se expone a una variación de los gases (gas, concentración, ...) presentes en el ambiente. De esta forma la sensibilidad, S , de un sensor de óxido de estaño se define generalmente como la variación de resistencia con respecto a una resistencia de referencia, generalmente la resistencia en aire.

Para entender como ocurren estos cambios en la resistencia del sensor considérese la figura 1. En la figura 1a se pretende representar un material semiconductor tipo n , tal y como el SnO_2 , en el que el carácter n le viene dado por la existencia de uno o más niveles donadores (en el caso del SnO_2 introducidos por la existencia natural de vacantes de oxígeno). La superficie del material introduce estados dentro de la banda prohibida (figura 1b) que si están 'cargados' han de ser compensados eléctricamente creándose la correspondiente zona de depleción cerca de la superficie y barrera de potencial. Cuando una molécula, proveniente de un determinado gas en el ambiente, se adsorbe en dicha superficie, se produce un cambio tanto en la altura de la barrera como en la extensión de la región de depleción (figura 1c). Dicho cambio ocurre porque para que se realice la adsorción ha de haber un intercambio de carga entre la molécula, que posteriormente quedará ionizada, y el semiconductor. En el caso sencillo del oxígeno, O_2 , al adsorberse recoge electrones del semiconductor, disminuyendo la cantidad de electrones cerca de la superficie y quedando en forma ionizada tal como por ejemplo 2O^- (necesarios 2 electrones) o 2O^{2-} (necesarios 4 electrones). De esta forma se produce el aumento de la barrera de potencial en la superficie y el aumento de la resistencia del sensor. El hecho de que la molécula quede en forma ionizada implica que, además, puede producirse un cambio en la afinidad electrónica como consecuencia de la creación de dipolos en la superficie.

Desde un punto de vista electrónico la adsorción de una molécula cargada puede relacionarse con la creación de un nivel electrónico fijo en la superficie dentro de la banda prohibida. En el caso por ejemplo del oxígeno, comentado antes, se considera que su adsorción va acompañada de la introducción de niveles aceptadores, ya que para adsorberse es necesario que el semiconductor aporte electrones.

El estado usual de la superficie es tal que existen adsorbidas varias especies de oxígeno, generalmente O^- y O_2^- . Al llegar un gas reductor, como CO o H_2 , éste reacciona con el oxígeno adsorbido formando una nueva molécula (CO_2 , H_2O) que vuelve a la fase gas. En este proceso se libera o liberan los correspondientes electrones, disminuyendo la altura de la barrera y la extensión de la zona de deplexión. Evidentemente, la disminución de la altura de la barrera produce el correspondiente aumento en la conductividad de grano a grano y por lo tanto la disminución de la resistencia del sensor.

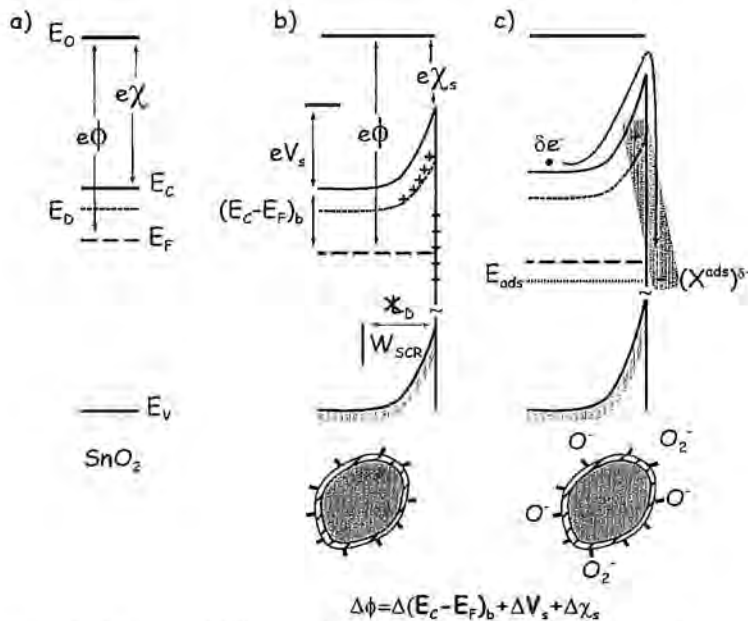


Figura 1: a) Esquema del diagrama de bandas de un semiconductor tipo n, tal y como el SnO_2 . b) Modificación del diagrama de bandas cerca de la superficie. c) Adsorción de oxígeno, produciéndose un aumento de la barrera Schottky, un incremento de la anchura de la zona de vaciamiento, y un cambio en la afinidad electrónica del semiconductor como consecuencia de la creación de dipolos entre la carga fija en la región de deplexión y la carga de las moléculas adsorbidas en la superficie.

Si bien es cierto que la explicación dada es bastante simplista, de ella se entiende el principio básico de funcionamiento de los sensores semiconductores de SnO_2 . Además, es evidente que la detección depende de manera importante de la actividad o captura de especies gaseosas, y por lo tanto de la cinética de las reacciones que tienen lugar en la fase gas y en la superficie del sensor. Por lo tanto, es de esperar, y de hecho se observa, una gran dependencia con la temperatura de operación del sensor. Por otra parte, los cambios en cada uno de los granos del

sensor han de ser medidos externamente a través de los electrodos, lo cual implica la consideración de los mecanismos de conducción predominantes entre granos (emisión termoiónica, túnel) y dependencia del tipo de contacto con los electrodos. Todo esto lleva a que el entender el funcionamiento real de un sensor de este tipo no sea tan sencillo como aquí se ha descrito.

1.4 Posibilidades hacia la optimización en la detección

Los problemas más importantes en el caso de sensores de gas conductométricos basados en SnO_2 son la estabilidad y la selectividad. La mejora de las características del sensor en estos dos aspectos pasa por la optimización del material sensible. Sin embargo, esto no quiere decir que sea la única forma, ya que la selectividad puede mejorarse también mediante el uso de varios sensores (con características diferentes) y la electrónica adecuada.

La mejora del material puede hacerse mediante el control de su estructura o mediante la introducción de aditivos, generalmente metales nobles como Pt o Pd;

1.4.1 Optimización del material sensible: microestructura

Como ya se ha comentado anteriormente, un buen material para ser aplicado en sensores de gas conductométricos, debe ser policristalino, ya que el fenómeno de detección es un fenómeno superficial. Esto quiere decir que cuanto mayor sea el área disponible para la adsorción del gas, mejor será, en general, la respuesta del sensor. Por lo tanto, será preferible disponer de materiales nanocristalinos, ya que la relación superficie/volumen disponible es inversamente proporcional al tamaño de grano.

Es importante, desde el punto de vista de mejora de la sensibilidad, que el gas pueda distribuirse por la superficie de los granos de óxido de estaño. De esta forma, presentarán, en general, sensibilidades más elevadas aquellos sensores en los que la capa tenga una estructura porosa. De todas formas, incluso en este caso, pueden existir diversos factores que impidan la difusión del gas hacia todas las regiones del sensor. Por otra parte, se ha de tener en cuenta que durante la operación del sensor el gas es adsorbido y desorbido, fenómenos que serán más lentos en un sensor con estructura porosa. Esto hace que, de forma general, sean los sensores formados por una capa de material denso los que presenten mejores tiempos de respuesta. Sin embargo, aunque el sensor presente una respuesta inicial rápida, si el gas intenta difundir en este material, la respuesta del sensor tardará en conseguir un estado estacionario.

Como se ha descrito, es muy relevante la estructura de la capa sensible, así como el tamaño de grano. Sin embargo la importancia del tamaño de grano es mayor de lo que se entiende de lo expuesto anteriormente. De acuerdo con la figura 1, cuando un gas tal y como el oxígeno o el NO_2 es adsorbido en la superficie de los

granos de SnO_2 , aparece la correspondiente barrera de potencial en la superficie y aumenta la anchura de la región de depleción. Si el grano es suficientemente pequeño, podría darse la situación en que el grano quede totalmente vacío de electrones ($L \leq 2W$, siendo L el tamaño de grano y W la anchura de la zona de carga espacial). Bajo estas condiciones se tiene un material altamente resistivo. Si la superficie del sensor es despoblada de parte de las moléculas adsorbidas, por ejemplo mediante la reacción de las mismas con gases reductores como CH_4 , CO , o H_2 , los granos del material pasan a una situación de no vaciamiento con la consiguiente disminución de resistencia del sensor. Un caso límite como el descrito sería de especial interés dado que los cambios de resistencia que se producen bajo la presencia de gases reductores son máximos.

1.4.2 Optimización del material sensible: introducción de aditivos

La forma más usual de modificar la sensibilidad de un sensor de óxido de estaño es mediante la introducción de metales nobles. Si los átomos del aditivo se colocan dentro de la red cristalina del SnO_2 lo que se consigue es un control sobre la capacidad de vaciamiento del material (dopaje). Sin embargo al introducir aditivos el resultado buscado es, generalmente, el control de la superficie y por lo tanto lo que se desea es que el aditivo se coloque en la superficie de los granos de SnO_2 . El contacto del aditivo (en forma metálica u oxidada) crea una barrera de potencial completamente determinada por la afinidad electrónica del semiconductor, la función de trabajo del metal y la densidad de estados superficiales localizados en la banda prohibida (figura 2).

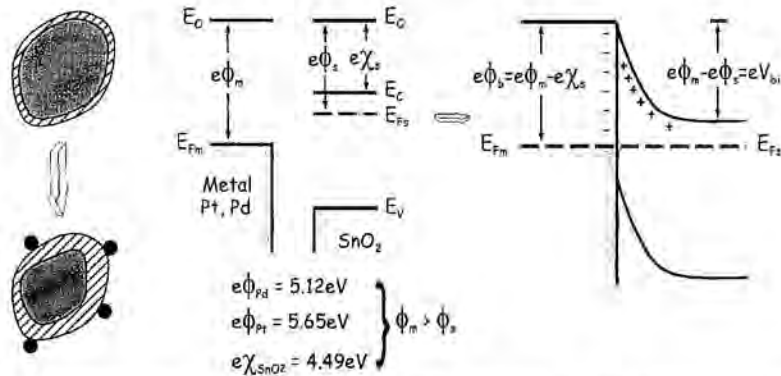


Figura 2: Introducción de aditivos en la superficie de los granos de SnO_2 (creación de barrera Schottky).

A partir de la situación anterior se describen en la literatura dos mecanismos diferentes mediante los cuales el material incrementa su respuesta a determinados gases:

i) *Activación química*: el metal colocado en la superficie, actúa como catalizador, esto es, facilita la adsorción del gas y la descomposición de las moléculas, de forma que una parte de la molécula descompuesta va hacia la superficie del soporte (SnO_2) y actúa como lo haría normalmente. Este es el caso del Pt en SnO_2 para gases como H_2 (figura 3a).

ii) *Activación electrónica*: Tras la adsorción del gas el estado químico del aditivo cambia, produciéndose el correspondiente cambio en la altura de la barrera de contacto entre el aditivo y el semiconductor y la variación de la extensión de la zona de carga espacial. Este es el caso típico del Pd, que se encuentra normalmente en forma oxidada (PdO) y cambia a estado metálico bajo la presencia de, por ejemplo H_2 (Figura 3b), o del Cu, que pasa a CuS bajo la presencia de H_2S .

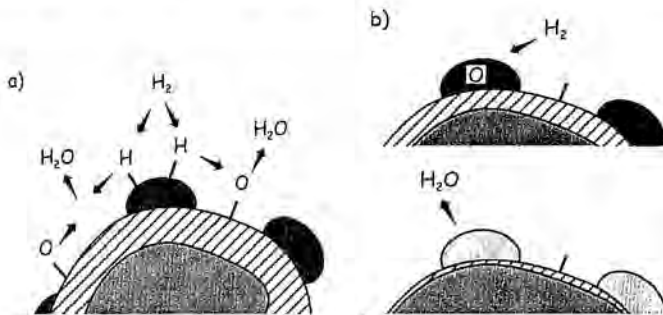


Figura 3: Esquema de los mecanismos de activación química (a) y electrónica (b).

Se ha de tener en cuenta, sin embargo, que en realidad ambos mecanismos pueden darse simultáneamente, pudiendo ser uno de ellos el dominante. Por otra parte, el comportamiento del aditivo es dependiente de la cantidad distribuida, de cómo se distribuye (tamaño de las partículas de aditivo), de sobre qué superficie del soporte se distribuye, etc. De hecho, dependiendo de la cantidad de aditivo, éste podría encontrarse siempre en estado oxidado aunque lo esperado fuese encontrarlo en estado metálico, y viceversa. El caso de control a través de la población de los niveles creados dentro de la banda prohibida por una cantidad muy pequeña de aditivo (varios átomos) debería considerarse como sensitivización electrónica.

1.4.3 Optimización del sistema de detección

Por lo que se ha dicho hasta ahora, la respuesta del sensor puede cambiarse mediante la introducción de aditivos, haciendo operar al sensor a diferentes temperaturas, mediante cambios en la estructura del material (tamaño de grano, densificación), lo cual podría llegar a variar los mecanismos de conducción, entre otras cosas, y mediante cambios en la configuración o material de los electrodos del sensor. La temperatura de operación del sensor no sólo afecta la velocidad de determinadas reacciones y procesos de difusión, sino también influye de manera

crítica sobre cuál o cuáles son las especies que se encontrarán sobre la superficie del material, esto es, O^- , O^{2-} , O_2^- para el oxígeno o H_2O o OH^- para el agua. La existencia de una u otra especie dominante depende de la temperatura y determina cuales serán los procesos dominantes en la respuesta del sensor (quimisorción, fisisorción, reacciones superficiales o reacciones con el volumen).

De acuerdo con lo anterior, con el fin de mejorar la selectividad, el sistema de detección puede optimizarse mediante el uso de varios sensores (una matriz de sensores), en ocasiones fabricados en un único circuito integrado. Para ello, con el uso de la circuitería adecuada se emplean:

- Sensores hechos con el mismo material
 - trabajando a diferentes temperaturas
 - impregnados con diferentes aditivos
 - de diferente grosor de la capa sensible
 - con diferente configuración o material para los electrodos
 - con diferentes tipos de filtros
 - ...

□ Sensores fabricados con materiales diferentes o incluso tipos de sensores diferentes.

La optimización del sistema de detección también pasa por la optimización del consumo de cada sensor, etc.

CAPÍTULO 2

TÉCNICAS DE CARACTERIZACIÓN
ESTRUCTURAL

La caracterización estructural llevada a cabo durante el desarrollo de este trabajo se ha realizado mediante microscopía electrónica de transmisión (TEM) y de barrido (SEM), difracción de rayos X (XRD), espectroscopía infraroja por transformada de Fourier (FTIR), espectroscopía Raman, y espectroscopía de fotoelectrones (XPS). De forma puntual se han realizado también experimentos de microanálisis (EDS) y de pérdidas de energía de electrones (EELS).

Las observaciones de microscopía electrónica de transmisión de polvos y de capas se realizaron en un microscopio electrónico Philips CM30 SuperTwin operado a 300 keV. Para la observación de polvos, éstos se dispersaron en etanol mediante ultrasonidos y posteriormente fueron depositados sobre membranas de carbono amorfas. Las secciones transversales y las preparaciones para observación en vista planar de las capas y sensores de SnO₂ se obtuvieron mediante pulido mecánico y adelgazamiento iónico con iones de Argón.

Las medidas de EELS se realizaron en un microscopio electrónico de transmisión *Philips CM200 FEG* (filamento de emisión de campo) operado a 200kV.

Las medidas de SEM se hicieron en un microscopio electrónico de barrido *Jeol JSM 840* con filamento de LaB₆, operado a una tensión suficientemente baja para evitar la carga de la muestra (~15kV) y en un microscopio electrónico de barrido *Hitachi S-2300* operado en las mismas condiciones.

Las medidas de difracción de rayos X de polvos se realizaron en un difractómetro de polvo *SIEMENS D-500* con radiación CuK α , detector por centelleo y monocromador secundario de grafito. Se realizaron en este instrumento medidas a alta temperatura, para las cuales se usó una cámara TTK (-193<T<250°C). Algunas medidas se realizaron en un difractómetro de polvo INEL, usando radiación CuK α , en configuración de Debye-Scherrer, con un detector 120° 2 θ y un monocromador primario de cuarzo para eliminar la radiación K α_1 . Los perfiles de difracción de capas y sensores se obtuvieron en ocasiones usando incidencia rasante en un difractómetro Philips MRD con un monocromador secundario de grafito, usando radiación CuK α y un detector proporcional.

Los espectros de FTIR se realizaron principalmente en transmisión en un espectrómetro BOMEM MB-120. Los espectros se midieron a temperatura ambiente usando incidencia normal. Para la medida de polvos en el rango 400-4000cm⁻¹ se obtuvieron pastillas de KBr con una pequeña cantidad de polvo de acuerdo con el método usual. Para las medidas en el rango 200-400cm⁻¹ se realizó el mismo proceso con pastillas de polietileno. Los espectros de absorbancia se obtuvieron usando como referencia una muestra adecuada (KBr o polietileno para polvos y Si o Al₂O₃ para las capas).

Las medidas de espectroscopía Raman se realizaron en configuración de retrodifusión (*backscattering*) con un espectrómetro Jobin-Yvon T64000 acoplado a un microscopio óptico Olympus en el caso de medidas en microcámara. La fuente de excitación fue un láser de iones de Argón operando a longitudes de onda de 457.0nm,

488.0nm, y 514.5nm, La potencia usada fue la necesaria para que no tuviesen lugar efectos térmicos (~2mW sobre la muestra con 514.5nm y objetivo 100x).

Para espectroscopia de fotoelectrones se uso un espectrómetro *Perkin-Elmer PHI 5500* con lineas de emisión $AlK\alpha$ (1486.6eV) o $MgK\alpha$ (1253.6eV).

CAPÍTULO 3

PROPIEDADES DE NANOPARTICULAS DE
SnO₂. SENSORES EN CAPA GRUESA

Los objetivos principales de este capítulo son, por una parte, analizar las propiedades fundamentales de las nanopartículas de SnO_2 . De este análisis se extraerán resultados importantes a añadir al conocimiento general sobre este material, así como metodologías a seguir en la caracterización de sensores de gases fabricados con tales nanopartículas. Por otra parte, optimizar la respuesta (sensitividad, selectividad, estabilidad) de sensores en capa gruesa de SnO_2 . Para ello, partiendo de un óxido de estaño hidratado obtenido mediante sol-gel, se han realizado experimentos de calcinación de las nanopartículas, a temperaturas entre 250 y 1000°C, en los cuales en ocasiones se han introducido los aditivos metálicos Pt y Pd. Como método innovador se ha estudiado la influencia de un molido del óxido precursor (óxido hidratado) y del óxido calcinado, tanto estructural como eléctricamente.

El proceso de fabricación de los polvos caracterizados se presenta de forma esquemática en la figura 1. En la figura 2 se presenta el conjunto de muestras usadas para la realización de este capítulo. Todas las muestras presentadas en la figura 2 se realizaron en forma de polvo. Sin embargo, salvo en el caso del estudio del molido del material, con aquéllas calcinadas a 450, 800, o 1000°C, se fabricaron sensores. Dichos sensores fueron hechos sobre sustratos cilíndricos y planos, mediante impresión, tal y como se explicó en el capítulo 1. Para el estudio del molido del precursor o bien del óxido calcinado, se fabricaron sensores sobre sustratos planos con polvos calcinados a 1000°C durante 8h en los cuales se realizó el molido bien durante 2 horas antes de la calcinación, o bien durante 2 horas después de la calcinación, o bien ambos molidos.

3.1 Evolución general en función de la temperatura de calcinación

Un polvo de SnO_2 hidratado en el que no se ha realizado ningún tratamiento de calcinación está formado por nanopartículas ($\sim 3\text{nm}$) altamente aglomeradas y que presentan una red cristalina desordenada con un alto contenido de humedad (agua y grupos hidroxilo). Al calcinar este polvo se produce:

- el incremento del tamaño de partícula ($\sim 16\text{nm}$ a 450°C, $\sim 110\text{nm}$ a 1000°C).
- una dispersión de los tamaños de las partículas asimétrica entorno al valor medio, siendo mayor hacia tamaños de partícula grandes
- la disminución del desorden en la red cristalina
- la desaglomeración del polvo
- el facetaje de las partículas
- disminución cualitativa de la densidad de defectos
- pérdida de humedad

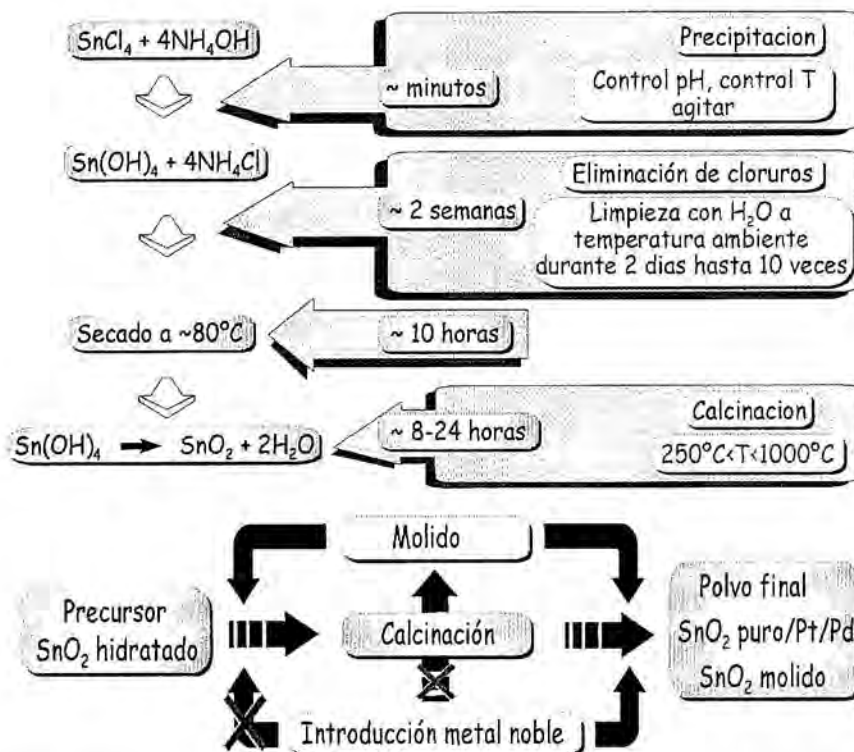


Figura 1: Procedimiento seguido para fabricar las nanopartículas de SnO₂ mediante el método de sol-gel. Se dan los tiempos orientativos para realizar cada paso con el fin de indicar lo largo del proceso. En la parte superior se muestra cómo se obtiene el precursor hidratado y en la inferior la obtención del polvo final, incluyendo la posible introducción de aditivos y el posible molido del polvo. Los caminos marcados con una cruz roja son posibles pero no se han tratado en este trabajo.

Tales cambios ocurren paulatinamente hasta llegar a la temperatura de ~430-450°C, a partir de la cual los cambios suceden de una manera mucho más rápida. En particular, se observa que la disminución de H₂O en el polvo llega a ser del 80% a 430°C y la de grupos OH⁻ del 55%. La pérdida de humedad en el polvo, juntamente con el incremento de energía térmica suministrada a los átomos que forman las nanopartículas, son los responsables de la modificación del resto de parámetros, como desorden, facetaje, o crecimiento rápido de tamaño de grano.

Como resultado del análisis se observa que el espectro Raman y el de infrarrojo presentan características diferentes de las asociadas a un monocristal o a un policristal con tamaño de grano grande. En particular en el espectro de infrarrojo se observa una dependencia de los modos de vibración del material con la forma de las partículas. El espectro Raman, que se presenta en la figura 3, muestra dos regiones que no se observan normalmente. A bajas frecuencias se observan varias bandas, de

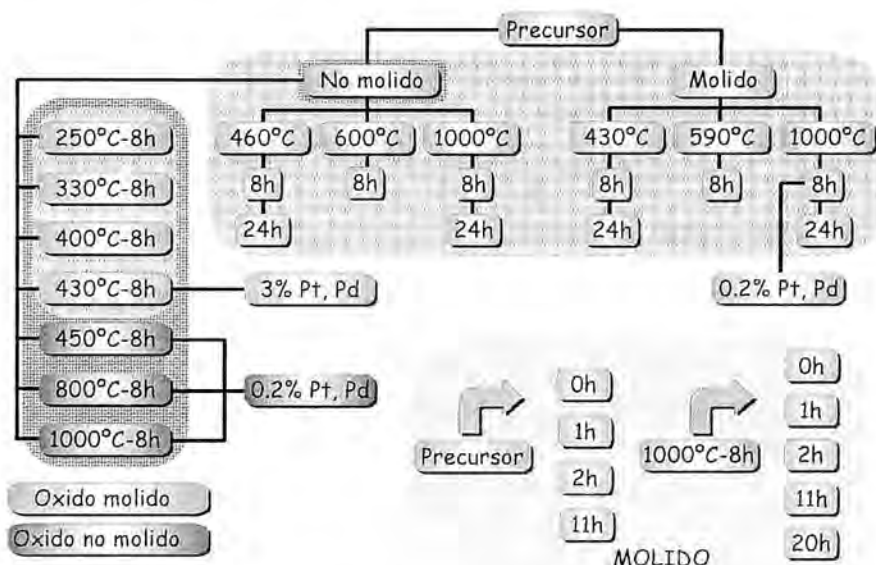


Figura 2: Esquema de las muestras investigadas en este capítulo agrupadas por:: i) investigación de la temperatura y tiempo de calcinación, ii) investigación de la introducción de aditivos, y iii) investigación del proceso de molido del precursor hidratado y/o del polvo tras la calcinación.

las que se considera una como principal dada la dificultad experimental del análisis. Esta banda puede ser asociada directamente al pequeño tamaño de las partículas, el cual permite una vibración completa de la nanopartícula como un todo al interaccionar con la radiación incidente. Al estar dicha banda relacionada con el tamaño de las partículas, es posible extraer la distribución de tamaños de grano en el polvo, tal y como se muestra en la figura 4. Con el mismo fin, pero no de forma tan precisa, es posible también aplicar en el caso del SnO₂ los modelos existentes relacionados con el confinamiento de fonones (modelo de correlación espacial para partículas de distinta geometría).

Por otra parte, en la región entre 475 y 775cm⁻¹ aparecen varias bandas, cuya intensidad (o área bajo la banda) depende también del tamaño de las partículas. Dichas bandas están asociadas con la capa desordenada existente en la superficie de todo material. Al tratarse de granos muy pequeños, la contribución de esta capa es importante y visible mediante espectroscopía Raman. Así, de acuerdo con los espectros de la figura 3, es posible determinar un grosor medio para esta capa distorsionada entorno a 1.1nm, lo cual es completamente razonable. Cabe comentar que tal capa podría ser influyente en el proceso de detección de gases, pues éste es un fenómeno principalmente superficial.

Aparte de lo comentado, de acuerdo con el estudio realizado y gracias a las diversas técnicas de caracterización estructural empleadas, se demuestra que la única

técnica de las empleadas que asegura una buena determinación en el tamaño de nanopartículas es la microscopía electrónica de transmisión. En ocasiones, otras técnicas como la difracción de rayos X y la espectroscopía Raman pueden dar resultados aproximados. Sin embargo, la última permite obtener la distribución de tamaños en el caso de partículas con tamaño inferior a ~ 7 nm de manera no destructiva, lo cual es de especial interés para aplicar en sensores.

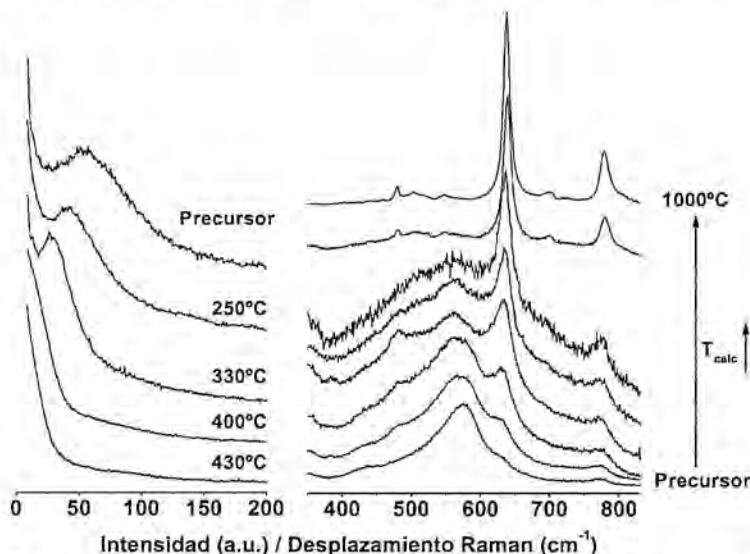


Figura 3: Espectros Raman de los polvos calcinados hasta 1000°C por 8h. Los espectros han sido divididos en la regiones de baja (izquierda) y alta frecuencia (derecha). No se observaron bandas adicionales en zonas no presentadas en esta figura.

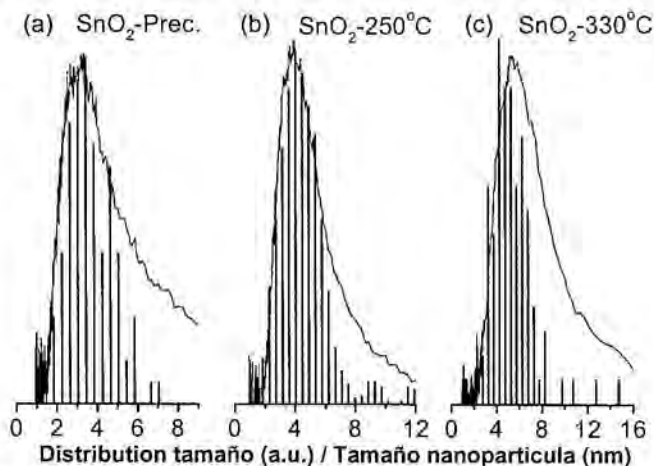


Figura 4: Comparación de la distribución de tamaño de partícula extraída por Raman (línea continua) y TEM (histograma).

3.2 Modificación de la respuesta del sensor con tratamientos térmicos y aditivos. Introducción de Pt y Pd

La resistencia de los sensores calcinados a diferentes temperaturas y con diferentes aditivos es evidentemente diferente. Como se representa en la figura 5, puede observarse como comportamiento general:

- El incremento de la resistencia con el incremento de la temperatura de calcinación (tamaño de partícula).
- El aumento de la resistencia, con respecto al material puro, al introducir Pt y Pd.

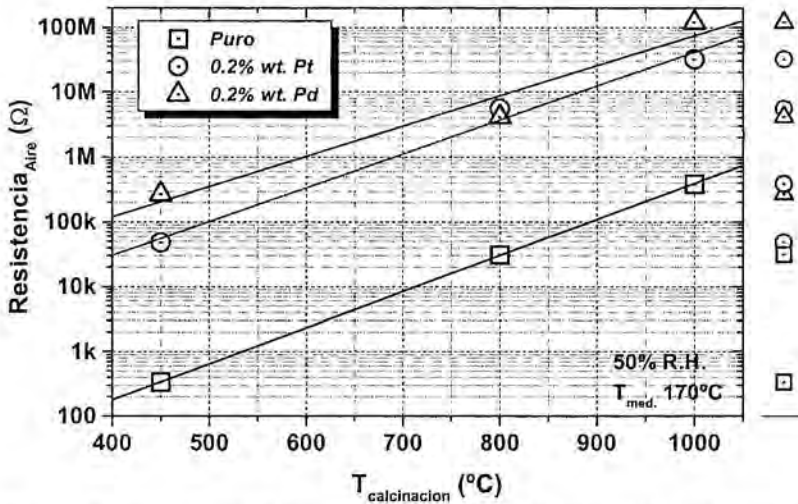


Figura 5: Resistencia en aire de los sensores calcinados a 450, 800 y 1000 $^{\circ}\text{C}$, sin introducir aditivos y con 0.2% wt. de Pt o Pd. Los resultados presentados han sido escogidos como representativos y corresponden a medidas realizadas a 170 $^{\circ}\text{C}$ bajo condiciones de humedad relativa del 50%. Medidas realizadas en la Universidad de Tübingen.

Si se considera el sensor como formado por cadenas paralelas de granos localizadas entre los electrodos, puede obtenerse que la resistencia debería ser inversamente proporcional al tamaño de grano. Es obvio que tal resultado no se observa en la figura 5 y que por lo tanto los resultados obtenidos atienden a un origen diferente.

Las diferentes resistencias a tener en cuenta en el sensor son:

- i) la resistencia de contacto con los electrodos, R_c ,
- ii) la resistencia en el interior de cada grano, R_i , y

- iii) la resistencia entre los diferentes granos, esto es, en las fronteras de grano, R_{fg} .

De acuerdo con lo expuesto en el *Capítulo 1*, los granos del sensor presentan en su superficie una región de deplexión, altamente resistiva por lo tanto. De esta forma, la contribución de las fronteras de grano es dominante frente al resto de contribuciones. Tal resistencia puede escribirse como:

$$R_{fg} \propto \frac{e^{qV_s/kT}}{n_{in}} = R_o e^{(E_c - E_F)_{in}/kT} e^{qV_s/kT} \tag{1}$$

donde se tiene en cuenta que los portadores han de saltar una barrera de potencial V_s al pasar de grano a grano y que la cantidad de portadores disponibles son los que hay en el volumen del grano, n_{in} . n_{in} vendrá determinada por la distancia entre el nivel de Fermi y la banda de conducción en el interior del grano.

De la anterior expresión se deduce que las variaciones de resistencia pueden ser debidas al movimiento del nivel de Fermi y por lo tanto de la densidad de portadores, o a la modificación de la altura de la barrera a través del cambio del estado de carga de las interficies.

En la tabla I se indican los cambios necesarios en la concentración de electrones y altura de la barrera necesarios para provocar las variaciones de resistencia observadas. Para ello se ha supuesto una concentración de donadores $N_D \sim 10^{16} \text{cm}^{-3}$ para el polvo puro calcinado a 1000°C (cuyas propiedades son más cercanas a las de un cristal perfecto). Incluso para este valor de N_D , muy inferior a los típicamente observados ($N_D \sim 10^{18} - 10^{19} \text{cm}^{-3}$) es evidente que es mucho más factible la variación de la altura de la barrera. Tal resultado es apoyado por el hecho de que los granos de SnO_2 están bien formados incluso a 450°C y por lo tanto no son de esperar cambios en la concentración de portadores tan importantes como los que se muestran en la tabla I.

$T_{\text{calcificación}} (^{\circ}\text{C})$	450	800	1000	1000 (Pt)	1000 (Pd)
$R(\Omega) \sim \frac{1}{N_D} e^{qV_s/kT}$	~300	~30K	~400K	~30M	~100M
$\frac{R_{T2}}{R_{T1}} \sim \frac{N_{T1}}{N_{T2}}$ $N_{T2} \sim N_{T1} R_{T1} / R_{T2} \text{ (cm}^{-3}\text{)}$	$1 \cdot 10^{19}$	$1 \cdot 10^{17}$	$1 \cdot 10^{16}$	$7.5 \cdot 10^{17}$	$2.5 \cdot 10^{18}$
$(V_{T2} - V_{T1}) \sim \frac{kT}{q} \ln \left\{ \frac{R_{T2}}{R_{T1}} \right\} \text{ (eV)}$	-0.18	-0.064	--	0.108	0.138

Tabla I: Resistencia, R, concentración de portadores, N, y altura de la barrera, V, necesarios para modelizar el cambio de resistencia con la temperatura de calcinación y la introducción de aditivos. Los valores de resistencia de referencia corresponden a una temperatura de medida, T_1 , de 170°C .

En cuanto a la sensibilidad de estos sensores, en la figura 6 se representa a modo de resumen la respuesta a 230°C a 100ppm de CO y a 2ppm de NO₂. Puede verse que con el fin de obtener un buen sensor para NO₂ es mejor que el material sea puro y calcinado a altas temperaturas. Por otra parte, una buena respuesta a CO se obtiene mediante la introducción de Pt o Pd habiendo calcinado el polvo a 450°C.

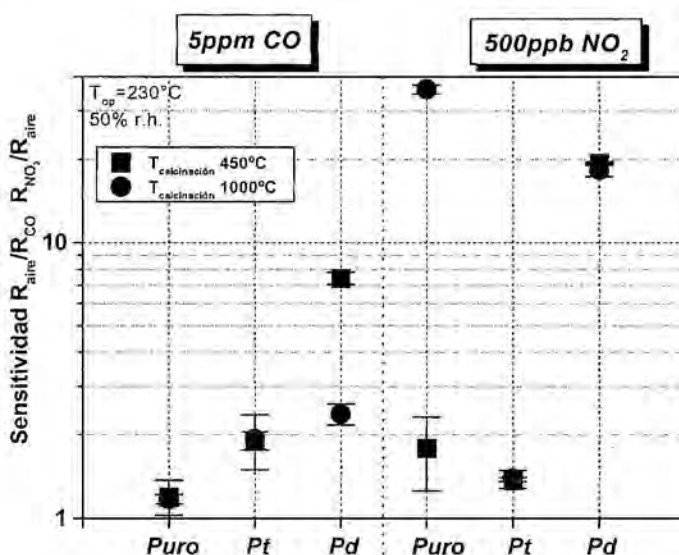


Figura 6: Respuesta de sensores planos en capa gruesa a CO y NO₂ medida a ~230°C. Medidas realizadas en la Universidad de Tübingen.

Parece ser que una buena superficie, tal y como la que existe tras calcinar a 1000°C es óptima para la detección de un gas oxidante como el NO₂, mientras que para la reacción de CO es necesario que el Pt o Pd ayuden a fijar oxígeno en la superficie.

Las medidas de sensibilidad y de resistencia en aire apuntan a que los aditivos se encuentran en la superficie de los granos de SnO₂. Dicho resultado se confirma a través de la caracterización estructural mediante TEM, Raman y XPS. Concretamente, se deduce además de las medidas de XPS que ambos aditivos se encuentran en estado oxidado en la superficie, tal y como corresponde a la pequeña cantidad introducida.

Los resultados obtenidos indican que la modificación en la respuesta de los sensores tras la introducción de Pt o Pd ocurre mediante sensitización electrónica a través de la población de los niveles creados dentro de la banda prohibida en la superficie de las nanopartículas de SnO₂.

3.3 Optimización de las características del sensor mediante molido del polvo de SnO_2

La caracterización mediante TEM llevada a cabo demuestra que el molido del material antes o después de la calcinación lleva a la disminución del tamaño de las nanopartículas (figura 7).

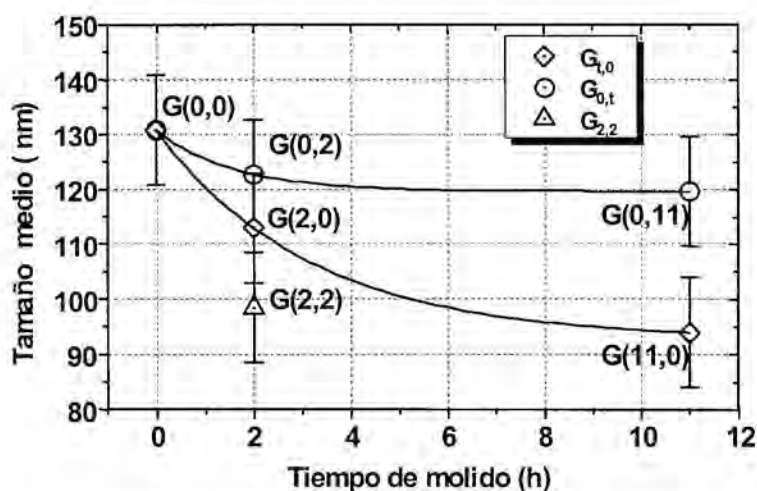


Figura 7: Evolución del tamaño de grano medio en función del tiempo de molido extraída por TEM. Las barras verticales representan la dispersión de tamaños respecto al tamaño medio. Cada muestra ha sido indicada en la forma $G(t_1, t_2)$, donde t_1 es el tiempo de molido antes de calcinar y t_2 el de después de calcinar. La calcinación fue hecha a 1000°C durante 8h.

La disminución del tamaño de grano tras calcinar es debida a la rotura de las nanopartículas por impacto, bien con las bolas de ZrO_2 usadas para el molido, bien con las paredes, o bien con otras nanopartículas. Sin embargo, no es posible determinar si la rotura es producida en el impacto o tras el impacto, cuando se libera la tensión sobre el grano. La rotura de las nanopartículas lleva a que se observe una distribución bimodal de tamaños de grano. Por otra parte, se observa que molidos por tiempos superiores a 11h no resultan muy efectivos.

La disminución del tamaño de grano observada en los polvos calcinados cuando el molido se realiza antes de calcinar es debida a la mayor aglomeración del precursor (figura 8). Esta mayor aglomeración puede ser debida al mayor contenido de agua de éste. Durante la calcinación, al estar el polvo más aglomerado, es más difícil liberar el agua contenida, con lo que el grano crece más difícilmente. Por otra parte, al crecer los granos individuales dentro de un aglomerado puede ser que éstos se separen y no reciban aporte de material de otros aglomerados, siendo más difícil

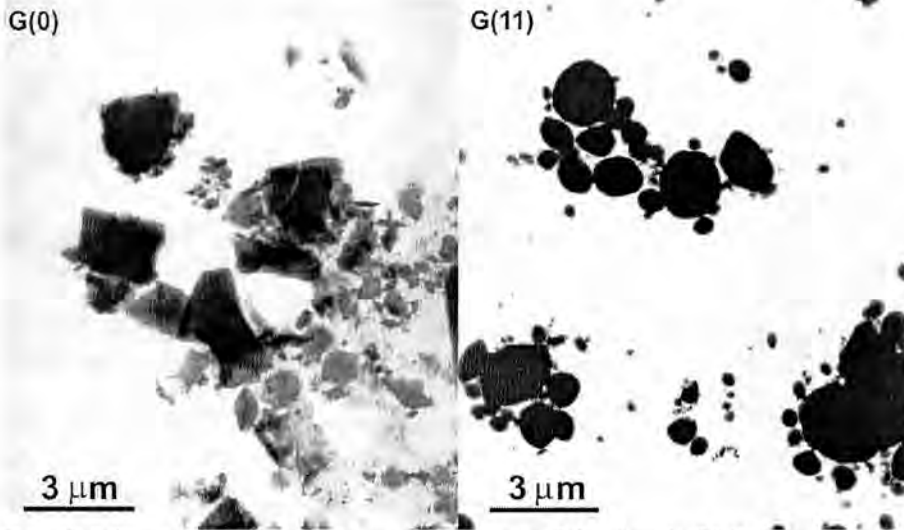


Figura 8: Imágenes de TEM de los precursores de SnO_2 , antes, G(0) y después, G(11), del molido.

el crecimiento del grano por encima de un cierto límite. De nuevo, el procedimiento de molido seguido parece no ser muy efectivo para tiempos superiores a 11h.

El molido más efectivo es el combinado, antes y después de calcinar, mediante el cual se consiguen reducciones de tamaño de grano tras 2h de molido entorno al 25%. Como el polvo es calcinado a 1000°C , es de esperar que el sensor sea altamente estable.

Respecto del punto de vista eléctrico, se observa que la resistencia en aire de un sensor en el cual se ha realizado el molido durante 2 horas después de calcinar, se incrementa un orden de magnitud. Cuando el molido se realiza por 2 horas antes y después de calcinar el incremento es de unos 2 ordenes de magnitud. Tal variación de resistencia no puede ser explicada en función del cambio de tamaño de grano únicamente. La única explicación razonable, que va de acuerdo con la caracterización por XPS, es que se produce un cambio en la superficie de las nanopartículas, esto es, se introducen nuevos estados en la banda prohibida localizados en la superficie de las nanopartículas. La introducción de tales estados explicaría, además, las curvas de sensibilidad a CO y NO_2 presentadas en la figura 9.

Parece ser que el molido tras calcinar reduce la sensibilidad al CO, y el molido antes de calcinar aumenta la sensibilidad al NO_2 a bajas temperaturas. Por otra parte, el molido del material hace que la respuesta de los sensores siga el mismo tipo de comportamiento, como se deduce del hecho que las curvas de sensibilidad sean paralelas en el caso de los sensores B y C (figura 9).

De acuerdo con estos resultados es plausible pensar que el molido introduce nuevos lugares (estados superficiales) que facilitan la adsorción de moléculas tales como el NO_2 . La introducción de estos nuevos estados puede dificultar la adsorción

de oxígeno, ya que la cantidad de lugares para su posible adsorción disminuye, de forma que la reacción con el CO se dificulta.

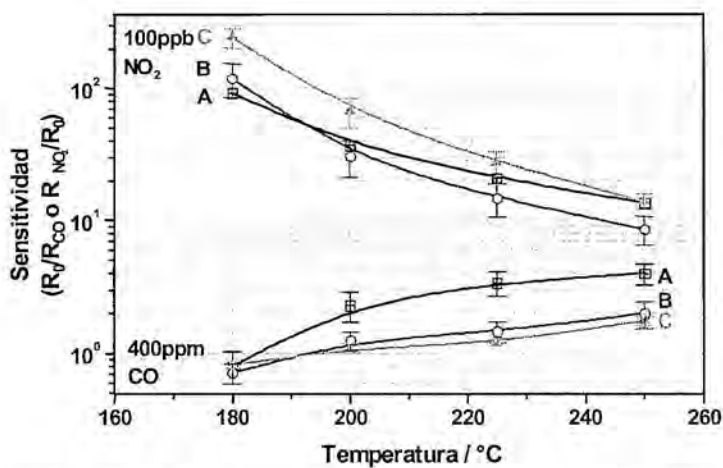


Figura 9: Respuesta de los sensores a 400ppm de CO y 100ppb de NO₂. Todos los sensores han sido calcinados a 1000°C durante 8h. En el sensor A no se ha realizado ningún molido. En el sensor B se realizó el molido durante 2 horas tras calcinar. En el sensor C se realizó el molido durante 2 horas antes y después de calcinar el polvo. Medidas realizadas en la Universidad de Tübingen.

CAPÍTULO 4

SENSORES EN CAPA DELGADA. OXIDACIÓN
DEL Sn.

En este capítulo se analizan sensores fabricados en capa delgada mediante dos métodos de interés actual. Por una parte se estudia el depósito de SnO_2 mediante evaporación de electrones asistida por iones de oxígeno (IBAD). Por otra parte se estudia el depósito de estaño por pulverización catódica y su posterior oxidación (RGTO). Ambos métodos pretenden solucionar la pobre estequiometría obtenida en capas fabricadas mediante métodos físicos. En el caso de capas depositadas por IBAD, se pretende al bombardear con iones de oxígeno la superficie del material recientemente depositado:

- i) Aportar la cantidad de oxígeno necesaria para obtener una estequiometría correcta, y
- ii) Estimular la reacción en la superficie mediante el bombardeo.

Por otra parte, con el método RGTO se pretende eliminar una etapa que normalmente es necesaria en capas obtenidas mediante pulverización catódica, esto es, la posterior oxidación del material para conseguir la estequiometría correcta. Para ello, se incluye esta oxidación directamente en el método. Así, el método RGTO consiste básicamente en:

- i) El depósito de Sn. Éste se realiza normalmente a una temperatura superior a la temperatura de fusión del Sn ($T > 250^\circ\text{C}$).
- ii) La posterior oxidación del estaño depositado. Para ello se introduce la capa de Sn en un horno en el que el ambiente es aire y se realiza la oxidación en dos etapas. La primera etapa se lleva a cabo a 250°C durante 4 horas. La segunda a 600°C durante el tiempo necesario, el cual depende del grosor de la capa de Sn depositada. Para llegar a cada temperatura de las indicadas se emplean rampas de 4 horas de duración.

Desde el punto de vista de la morfología obtenida, ambos tipos de sensores son muy diferentes. Los primeros presentan una estructura de capa densa, mientras que los segundos presentan una estructura muy porosa. Así, aunque ambos son considerados sensores basados en cambio de resistencia, aquéllos obtenidos mediante IBAD deberían ser enmarcados dentro del grupo de los sensores basados en efecto de campo.

4.1 Optimización del SnO_2 obtenido por IBAD

El parámetro fundamental estudiado en este tipo de capas ha sido la velocidad de depósito, la cual se varió entre 0.8 y 1.9 \AA/s . El resto de parámetros se mantuvieron fijos. Así, el depósito se realizó manteniendo constante la temperatura del sustrato a 35°C , la presión a $1.5 \cdot 10^{-4} \text{ mbar}$, y la tensión y densidad de corriente del haz de iones a 400V y 1.41 mA/cm^2 , respectivamente.

Como se muestra en la figura 1, a pesar del pequeño tamaño de grano obtenido en la mayoría de los casos ($\sim 7 \text{ nm}$), el material obtenido no presenta unas

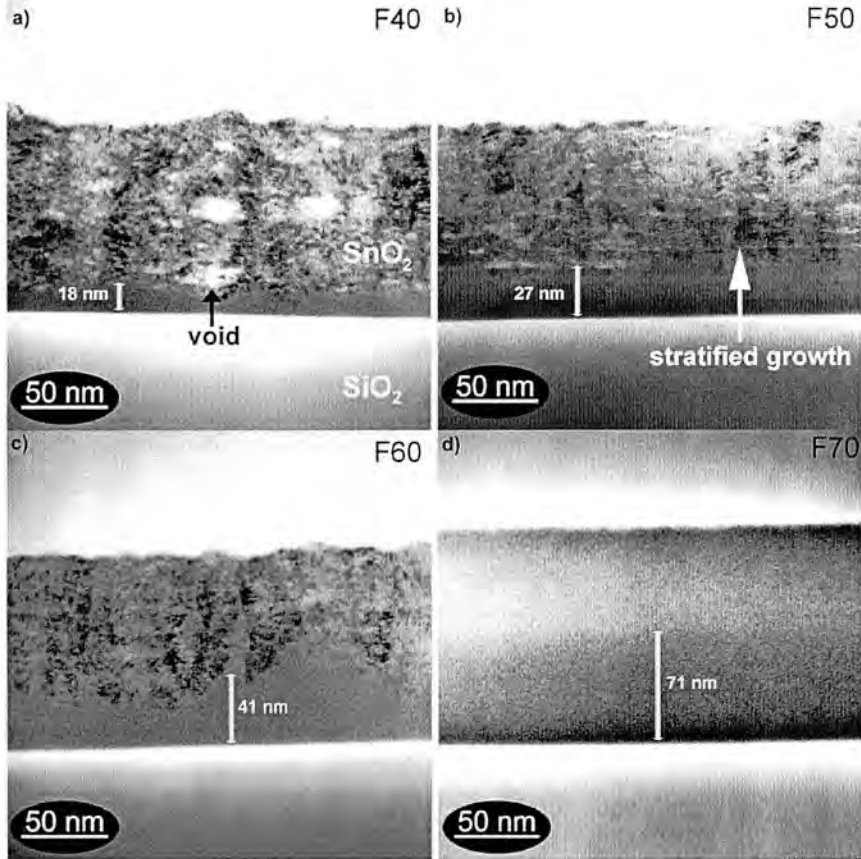


Figura 1: Imágenes de TEM en sección transversal de las muestras depositadas a una velocidad de 0.8 \AA/s (a), 1.0 \AA/s (b), 1.3 \AA/s (c), and 1.9 \AA/s (d).

características mínimas para ser usado como material sensible en un sensor de gas debido principalmente a que no es uniforme:

- Aparece una región amorfa en la interficie $\text{SnO}_2/\text{SiO}_2$ cuyo grosor depende de la velocidad de depósito.
- Aparecen regiones dentro de la capa en las que no existe material o éste tiene una composición muy rica en oxígeno.
- Se observa un crecimiento estratificado.

Dichas inhomogeneidades producirán variaciones en la respuesta del sensor con el tiempo, lo cual es evidentemente no deseado. De hecho, tratamientos térmicos realizados en estas capas modifican substancialmente su estructura,

principalmente cristalizando el material amorfo y provocando la aparición de una gran densidad de defectos en esas regiones

En principio, el origen de la no uniformidad del material puede ser debido a la falta de la movilidad suficiente del material depositado para reorganizarse y cristalizar adecuadamente. Por este motivo, se propone realizar un calentamiento del sustrato durante el depósito, el cual resulta efectivo en uniformizar el material, tal y como se observa en la figura 2.

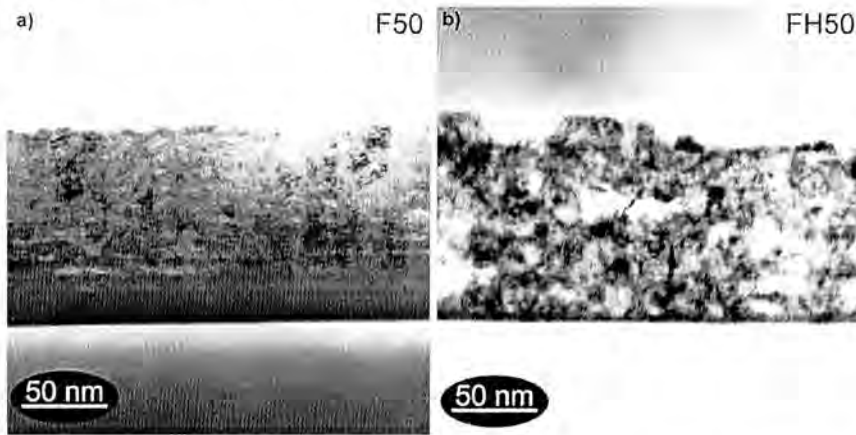


Figura 2: Comparación de una capa de SnO₂ depositada sin calentar el sustrato durante el depósito (a) y con el calentamiento simultáneo del sustrato (b).

4.2 Estudio del depósito y oxidación del Sn : RGTO

4.2.1 Deposito del Sn por pulverización catódica

La morfología de las capas obtenidas tras el depósito de Sn depende de a qué temperatura se realice el depósito y la cantidad de material depositado. Como puede verse en la figura 3, el depósito de Sn a temperatura superior a la de fusión produce que éste tome la forma de esferas truncadas sobre la superficie del sustrato. Dicha morfología se desarrolla, al evolucionar en fase líquida, dado que existe suficiente movilidad sobre la superficie del sustrato debido a la activación térmica y a que el Sn tiende a enlazarse con él mismo antes que con el material del sustrato. Es un ejemplo más de formas comúnmente desarrolladas en muchas superficies, tales como las gotas de vapor de agua en un cristal.

La distribución de tamaño de 'gotas' de Sn presenta una forma bimodal formada por una cola exponencial decreciente en función del tamaño de partícula, para las gotas pequeñas, y de una distribución en forma de campana (gausiana) para

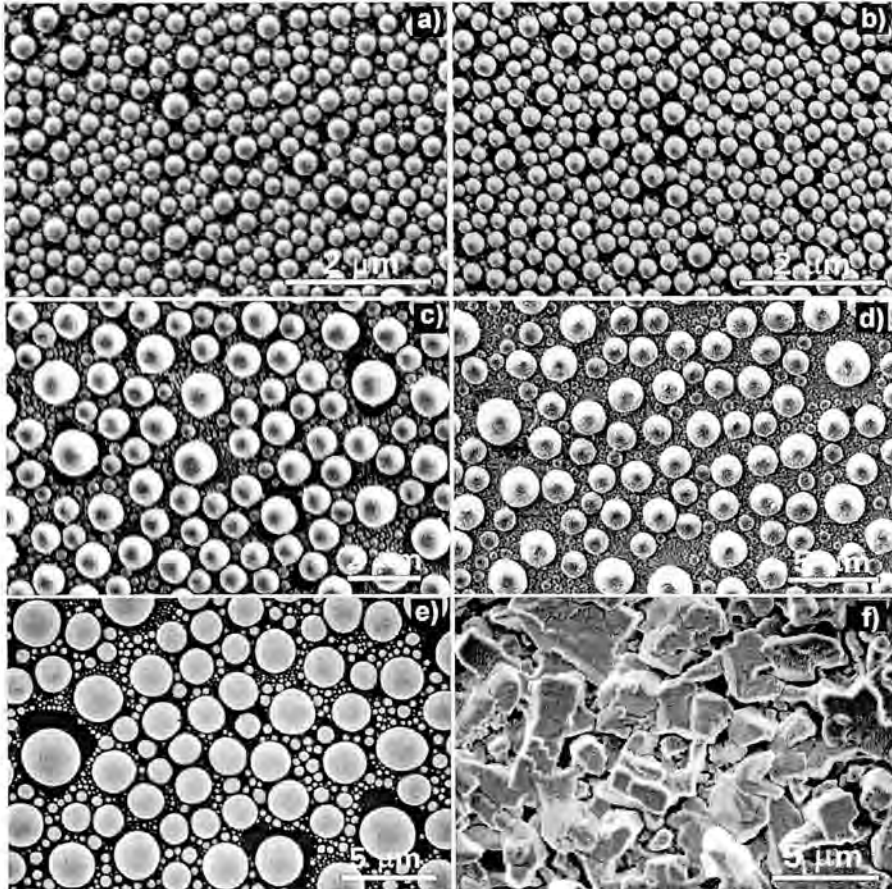


Figura 3: Imágenes de microscopía electrónica de barrido de capas de Sn depositadas a temperatura superior a la de fusión del Sn de grosor nominal: a) 50nm depositados a 2.5nm/s, b) 100nm depositados a 2.5nm/s, c) 200nm depositados a 2.5nm/s, d) 400nm depositados a 2.5nm/s, e) 300nm depositados a 2.1nm/s. La imagen (f) corresponde a una capa depositada a temperatura ambiente con grosor nominal de 1000nm depositada a 2.1nm/s.

las gotas grandes. Cuanto más material se deposita, mayor es el tamaño medio de las gotas y más ancha es la distribución. Sin embargo, siempre se mantiene el mismo proceso de crecimiento a través de coalescencia. A pesar de la similitud con otros sistemas, pueden observarse diferencias debidas principalmente a la temperatura a la que se ha realizado el depósito y a la geometría usada.

Un resultado importante desde el punto de vista de la posterior oxidación de ésta 'capa' es el hecho de que el recubrimiento del sustrato tiende a un valor estable entorno al 70%. Esto es así debido al mencionado mecanismo de

coalescencia. Al coalescer dos gotas, la nueva se coloca en una posición nueva que depende de la masa de ambas gotas y su antigua posición. En este desplazamiento quedan zonas vacías sobre el substrato (como puede verse en la figura 3) que vuelven a ser ocupadas por nuevas gotas de tamaño pequeño, y de ahí la existencia de la cola exponencial. También es importante desde el punto de vista de la posterior oxidación que el tamaño de las gotas no corresponde con el grosor nominal que se pretendía obtener y que por lo tanto los tiempos de oxidación deberán ser mayores de lo previsto.

El depósito a temperatura ambiente provoca que aparezcan regiones irregulares pero no con forma esférica.

4.2.2 Oxidación térmica del Sn

En las imágenes de la figura 4 pueden observarse los cambios morfológicos que tiene lugar durante la oxidación del Sn. Tales cambios son prácticamente independientes de la temperatura a la cual fue depositado el Sn.

La oxidación comienza por la superficie del Sn, formándose pequeños núcleos oxidados en la misma. Como puede verse en la figura 5, tales núcleos crecen hacia el interior de la gota de estaño (o equivalente). Debido a la interacción de los diferentes núcleos creciendo hacia el interior y a la existencia de diferentes fases intermedias en la conversión de Sn a SnO₂, se desarrolla una estructura porosa (la competencia entre los diversos núcleos provoca tensiones capaces de 'romper' el material y desarrollar una estructura porosa). Tal estructura es muy deseada en sensores de este tipo, tal y como se explicó en el *Capítulo 1*. Sin embargo, no todas las capas presentan la misma rugosidad. Cuanto mayor sea el tamaño de las gotas de estaño, mayor es la rugosidad obtenida tras largos periodos de oxidación. De esta forma, una gota suficientemente grande presenta una estructura, tras la oxidación parcial, en la que pequeños cristales (~20nm) rodean un núcleo cristalino no totalmente oxidado mucho mayor. Estos nanocristales se han separado parcialmente del cúmulo inicial por fractura, proporcionando la distribución de dichas partículas el aspecto poroso observado por SEM. Las capas depositadas a temperatura ambiente siguen el mismo mecanismo. Sin embargo, el tamaño final de los nanocristales podría ser diferente, dada la distinta forma del Sn depositado, la cual podría permitir el crecimiento mucho mayor de los núcleos hacia el interior antes de producirse la fractura.

La oxidación pasa por diferentes fases intermedias. De estas fases la única que se puede identificar con seguridad es SnO, la cual comienza a aparecer durante la primera etapa de la oxidación (figura 6). Así, durante el ciclo de oxidación, inicialmente el Sn se transforma principalmente a SnO. A temperaturas ~600°C ocurre la descomposición del SnO en Sn y SnO₂. A partir de este momento, la rápida oxidación del Sn a estas temperaturas hace que la fase predominante sea el SnO₂. El hecho de que se haya relacionado la porosidad de las capas oxidadas con la

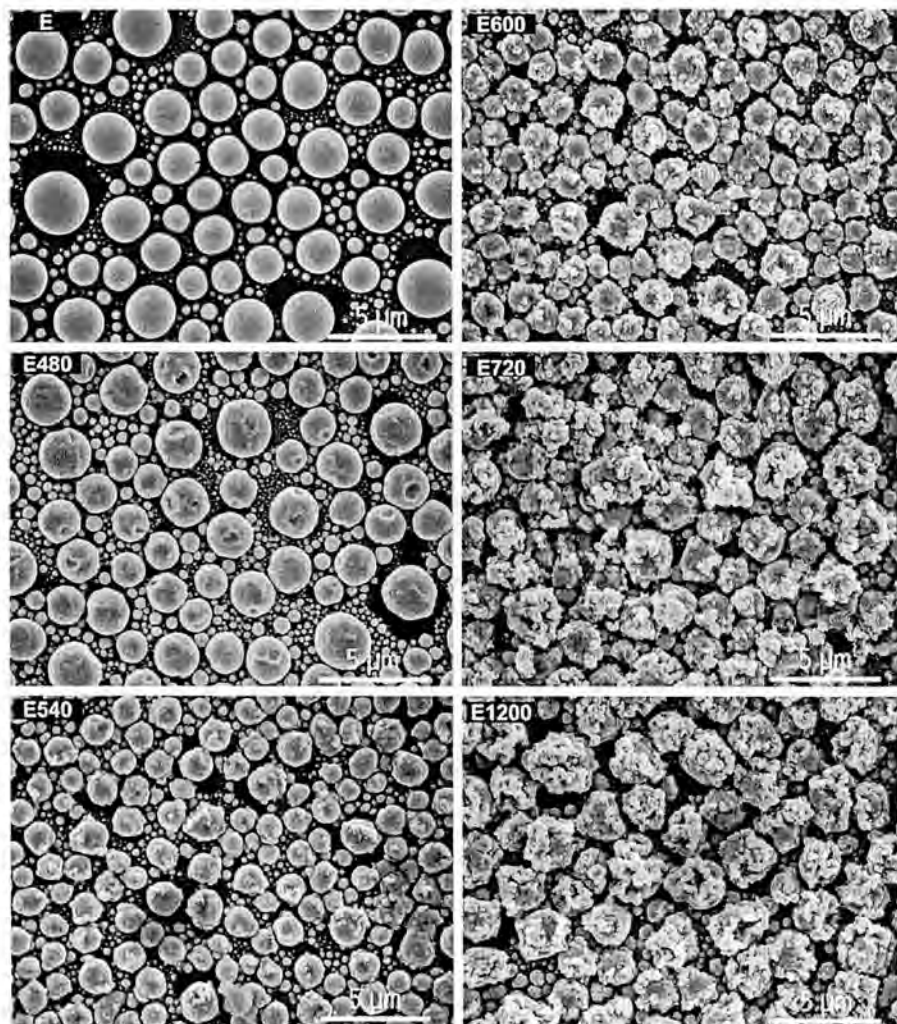


Figura 4: Imágenes de SEM de las capas parcialmente oxidadas. En cada imagen se indica el tiempo en el ciclo de oxidación. Así, de arriba a abajo y de izquierda a derecha, las imágenes corresponden a la capa inicial de estaño de 300nm, oxidación durante 480 minutos, 540 minutos (512°C), 600 minutos (600°C), 720 minutos (600°C), y 1200 minutos (600°C).

presencia de diferentes fases es debido a que no hay cambios en la rugosidad una vez es consumido el SnO.

Se ha descubierto que la oxidación del Sn ocurre más rápidamente de lo que inicialmente se pensaba. A esto contribuyen:

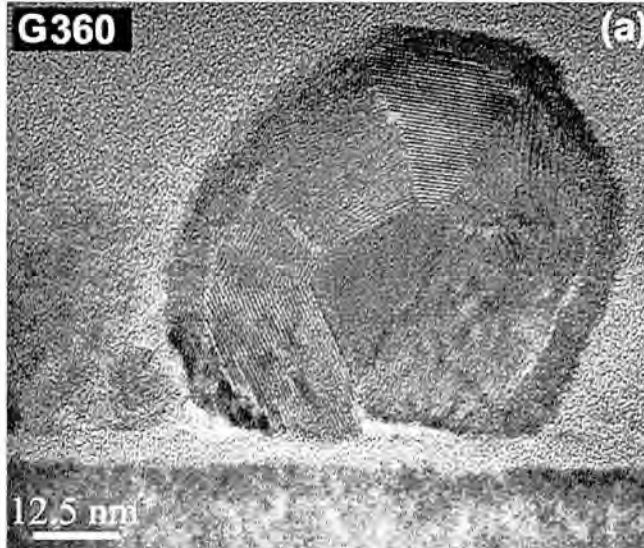


Figura 5: Imagen de alta resolución de una gota de estaño parcialmente oxidada (360 minutos en el ciclo de oxidación).

□ El desarrollo de núcleos oxidados que crecen hacia el interior generando zonas de contacto entre los diferentes cristales por donde la difusión del oxígeno para oxidar el material interior puede ocurrir más fácilmente.

□ La separación de dichos cristales con el progreso de la oxidación, dejando parcialmente libre de material una superficie que inicialmente no lo estaba.

Sin embargo, la inspección directa mediante TEM del grosor oxidado en las primeras etapas, permite obtener parámetros aproximados de la difusión del oxígeno en el estaño. Así, se observa que es necesario tener en cuenta que de acuerdo con el ciclo de oxidación empleado, el Sn es inicialmente fundido, cosa que ocurre a 150°C, tras 120 minutos en el ciclo. A partir de este punto la difusión del oxígeno puede aproximarse por una ley

$$L(t) = \sqrt{D(T) \cdot t} \quad (1)$$

$$D(T) = D_0 e^{-E_a/kT} \quad (2)$$

siendo los valores obtenidos de $D_0 = 1.5 \cdot 10^5 \text{ cm}^2 \text{ s}^{-1}$ y $E_a = 1.3 \text{ eV}$.

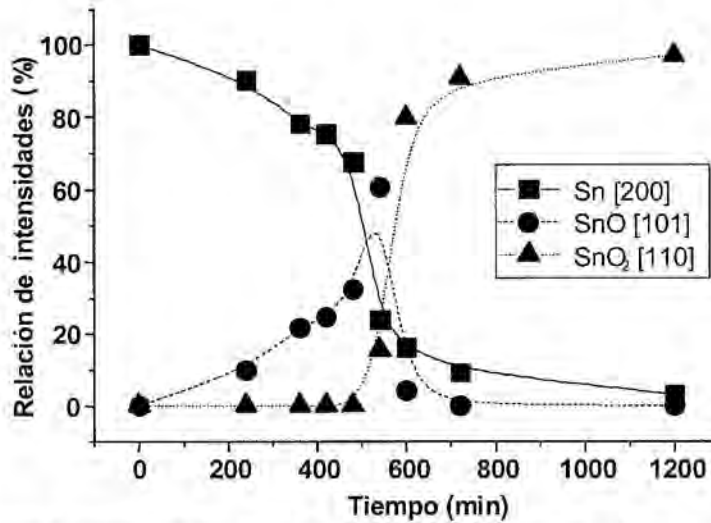


Figura 6: Evolución de la relación de intensidades de las reflexiones más importantes de Sn, SnO y SnO₂ en el espectro de rayos X, con respecto a la suma de intensidades. Sin considerar los diferentes coeficientes de absorción, ésta figura representa el porcentaje de cada fase en cada punto del ciclo de oxidación.

4.2.3 Influencia de una incompleta oxidación en la estabilidad

Como se ha visto, en ocasiones es necesario un largo ciclo de oxidación para oxidar completamente una capa de Sn. Si la capa está oxidada de forma incompleta se producen variaciones en la respuesta del sensor, como puede observarse en la figura 7. Dichas variaciones son debidas principalmente a una oxidación del sensor durante su operación, lo cual implica cambio de fase del material y cambio morfológico.

4.2.4 El método RGTO multicapa

Con el fin de reducir los periodos de oxidación es posible realizar un método multicapa. De tal forma, cada capa individual puede ser más delgada y fácil de oxidar completamente, evitando así las variaciones en la respuesta del sensor. Para ello se realiza el proceso de RGTO descrito sucesivas veces. La mejora obtenida no sólo concierne a la estabilidad del sensor, sino además mejora su respuesta (sensitividad).

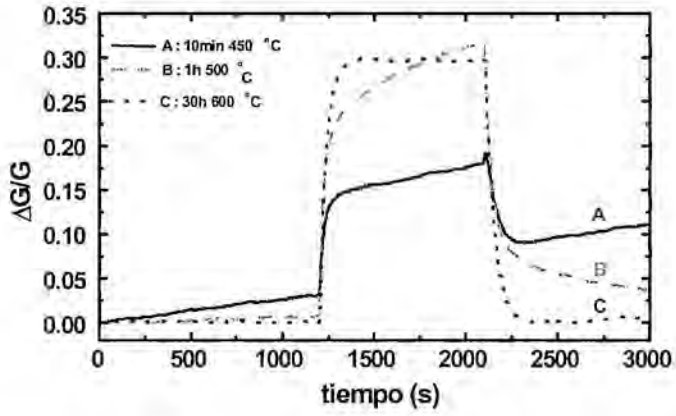


Figura 7: Respuesta de diferentes sensores fabricados por RGTO a 100 ppm de CO en función del tiempo. El sensor A fue oxidado durante 10 minutos a 450°C, el sensor B durante 1 hora a 500°C, y el sensor C durante 30 horas a 600°C. Los sensores A y B presentan una variación significativa en su respuesta en el tiempo. Puede verse claramente, por ejemplo, que la respuesta es diferente en ausencia de CO, antes y después del pulso de gas.

CAPÍTULO 5

CONCLUSIONES

La investigación de las propiedades fundamentales de nanopartículas de SnO_2 , y especialmente el análisis de su espectro Raman, ha permitido desarrollar nuevos métodos de obtención del tamaño medio de grano. A partir de la investigación de la región de baja frecuencia, se ha desarrollado un nuevo procedimiento a través del cual es posible extraer no sólo el tamaño medio sino la distribución completa de tamaños de grano de forma no destructiva y precisa. Dicha nueva técnica es de especial interés para ser aplicada en la caracterización de sensores de gas formados por nanopartículas de tamaño muy pequeño ($\sim 7\text{nm}$ para el SnO_2). Sin embargo, la comparación de las diferentes técnicas de caracterización estructural usadas para extraer el tamaño de nanopartícula demuestra que para los tamaños de grano usuales en el caso de sensores de gases la microscopía electrónica de transmisión es una técnica obligatoria.

Respecto a la estabilidad del SnO_2 obtenido por métodos químicos como sol-gel, se concluye que las nanopartículas han de ser calcinadas a temperaturas que permitan la desorción de agua y grupos hidroxilo. Asociado a tal desorción se ha observado que ocurren el facetaje y la ordenación de la red cristalina del material, dando lugar a partículas más estables. De esta forma, se ha encontrado que las nanopartículas de SnO_2 han de ser calcinadas a temperaturas mayores que $430\text{-}450^\circ\text{C}$. Además, se ha visto que para tener una alta sensibilidad a NO_2 y baja sensibilidad a CO , a bajas temperaturas, las partículas han de ser puras y calcinadas a 1000°C . Por otra parte, la introducción de los aditivos metálicos Pt y Pd facilita la absorción del oxígeno y aumenta la sensibilidad a CO . Los aditivos se colocan en la superficie de las nanopartículas de SnO_2 . La pequeña cantidad introducida de tales aditivos produce únicamente la creación de niveles dentro de la banda prohibida en la superficie. El mecanismo de activación es mediante sensitización electrónica.

Además de los tratamientos aplicados típicamente en sensores de gases basados en SnO_2 , tales como calcinación e introducción de aditivos metálicos, se ha observado que el molido del polvo de SnO_2 modifica de manera importante las propiedades estructurales de las nanopartículas y los mecanismos de sensibilidad. Se ha visto que el molido del material efectuado es efectivo para reducir el tamaño de grano incluso en un 30%. Sin embargo, la mejora de las características del sensor no está directamente relacionada con la disminución del tamaño de grano, sino con la modificación de la superficie de las nanopartículas de SnO_2 . Particularmente se ha observado que un molido combinado durante 2 horas antes y después de la calcinación es el que proporciona una mejor sensibilidad al NO_2 . Este efecto se atribuye a la aparición de niveles dentro de la banda prohibida que facilitan la absorción de NO_2 , disminuyendo así los lugares para la absorción de oxígeno, y por lo tanto la sensibilidad al CO .

Se han estudiado dos tecnologías actuales para la fabricación de sensores en capa delgada de SnO₂, que son el depósito de SnO₂ asistido por iones (IBAD) y la oxidación de Sn tras depósito por pulverización catódica (RGTO). La caracterización de los efectos de la velocidad de depósito en las propiedades morfológicas de los sensores fabricados mediante IBAD ha mostrado problemas importantes tales como la presencia de regiones amorfas en la capa de SnO₂ y crecimiento estratificado. Sin embargo, ha sido posible reducir tales problemas mediante el calentamiento del sustrato durante el depósito.

Se ha realizado una investigación detallada del depósito de Sn por pulverización catódica, principalmente a temperatura superior a la de fusión del Sn, y de su oxidación térmica. El depósito de Sn bajo condiciones en las cuales permanece líquido en la superficie del sustrato hace que éste se distribuya formando esferas truncadas de tamaños variables. La dispersión de tamaños de tales gotas, así como el tamaño medio, incrementa con el material depositado. Esta morfología implica la oxidación de gotas de tamaño mucho mayor que el esperado en el caso del depósito de una capa plana, y por lo tanto obliga a recalcular los tiempos necesarios para la completa oxidación. La mejor solución propuesta para conseguir una oxidación completa sin ser necesarios largos tratamientos térmicos es depositar pequeñas gotas sobre el sustrato, oxidar, y repetir el procedimiento, esto es realizar un procedimiento multicapa.

Se ha observado que el grado de oxidación influye de manera importante en la estabilidad de los sensores obtenidos mediante oxidación térmica del Sn. Se ha visto que la oxidación comienza en la superficie del Sn depositado y procede independientemente de la temperatura de depósito de la capa. Mediante oxidación térmica, antes de obtenerse la capa final de SnO₂, tiene lugar principalmente la formación intermedia de SnO. Del estudio de las primeras etapas de la oxidación se han deducido los parámetros para la difusión del oxígeno en el estaño de $D_o=1.5 \cdot 10^5 \text{cm}^2 \text{s}^{-1}$ y $E_a=1.3 \text{eV}$. Mediante RGTO, las nanopartículas que forman la capa de SnO₂ son de buena calidad cristalina y facetadas, lo cual asegura una buena estabilidad, perturbada únicamente por la reorganización de las nanopartículas como consecuencia de los tratamientos térmicos, siempre que la capa esté totalmente oxidada.

La introducción de aditivos metálicos mejora las características sensitivas de los sensores fabricados mediante sol-gel así como de los sensores fabricados mediante RGTO. Sin embargo, se ha observado que el método de introducción del aditivo metálico determina substancialmente el efecto final del aditivo. Así, métodos “energéticos”, como los usados en las capas delgadas, y altas dosis dan lugar a cúmulos metálicos capaces de actuar como activadores químicos o electrónicos. En cambio, métodos “poco energéticos”, como la impregnación, y bajas dosis implican

la única posibilidad de sensitización electrónica a través del control de los estados superficiales o interfaciales creados por el aditivo.